Promotional Effect of Support Materials in the Three-Way Catalysis of Supported Metal Catalysts

（担持金属系三元触媒における担体促進効果）

井　元

Graduate School of Chemical Sciences and Engineering

Hokkaido University

2022

Table of contents

Chapter 1 General Introduction 1

1.1 Environmental issues of automotive emissions 2

1.2 Three-way catalysts (TWCs) for DeNOx system 3

1.3 Aim of this thesis 5

1.4 Outline of thesis 8

References 11

Chapter 2 Promotional effect of La in the Three-Way Catalysis of La-loaded Al_2O_3 Supported Pd Catalysts (Pd/La/Al_2O_3)

2.1 Introduction 14

2.2 Experimental 16

2.3 Results and discussions 23

2.4 Conclusion 46

References 47

Chapter 3 Mechanistic study on three-way catalysis over Pd/La/Al_2O_3 with high La loading

3.1 Introduction 52

3.2 Experimental 53

3.3 Results and discussions 56

3.4 Conclusion 68

References 69

Chapter 4 Roles of the Basic Metals La, Ba and Sr as Additives in Al_2O_3 supported Pd-based Three-Way Catalysts

4.1 Introduction 73

4.2 Experimental 75

4.3 Results and discussions 78

4.4 Conclusion 95

References 96

Chapter 5 Role of Ba in an-Al_2O_3-Supported Pd-based Catalyst under Practical Three-Way Catalysis Conditions

5.1 Introduction 102

5.2 Experimental 104

5.3 Results and discussions 106

5.4 Conclusion 122

References 123

Chapter 6 Promoting Effect of Basic Metal Additives on DeNOx Reactions over Pt-based Three-Way Catalysts

6.1 Introduction 129

6.2 Experimental 130

6.3 Results and discussions 134

6.4 Conclusion 158

References 159

Chapter 7 Effect of Oxygen Storage Materials on the Performance of Pt-based Three-Way Catalysts

7.1 Introduction 164

7.2 Experimental 166

7.3 Results and discussions 170

7.4 Conclusion 191

References 193

Chapter 8 General conclusion 200

Chapter 1

General Introduction

1. General Introduction

1.1 Environmental issues of automotive emissions

Worldwide industrialization has resulted in the increase of use of automotive vehicles thanks to their flexibility and individual mobility. However, this also leads to the increase of automotive emissions, which was pointed out as one of the causes of environmental issues.[1]

The main pollutants present in automotive emissions include carbon monoxide (CO), nitrogen oxides (NO_x), and hydrocarbons (HC).[2,3] The poisoning effect of CO has been well-known that CO can have an impact on the visual ability and mental function. NO_x and hydrocarbons, when exposed to the sunlight, would generate smog via a photochemical process, which continues to harm human health.[4,5] Meanwhile, nitric oxide (NO) also reacts with the moisture in air to produce nitric acid which is a serious cause of acid rain. Nitrogen dioxide (NO_2), which is insoluble, can decrease lung function of human and induce severe health effects.[1]

Due to these harmful effects of pollutants present in automotive emissions, regulations have been established to limit the exhaust emission.[1,2,6,7] As shown in **Figure 1**, the automotive emissions have been significantly reduced by now and will be even strengthened in the near future.[4] Although after-treatment systems, which are used to chemically treat the exhaust gases generated by engine, contribute significantly to the control of automotive emissions, they are just sufficient to meet the current emission regulations. The development of more efficient after-treatment systems is still needed to fulfill the future severe emission regulation.

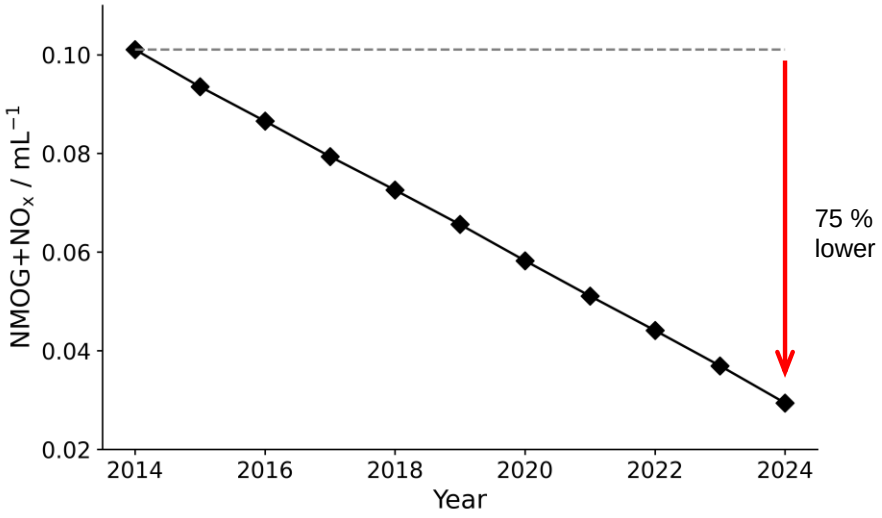

Figure 1. Fleet average non-methane organic gases plus NO_x emission limit of passenger and small trucks under low emission vehicles (LEV III) and Tier 1.

1.2 Three-way catalysts (TWCs) for DeNOx system

The technologies of after-treatment systems can be classified into oxidizing catalytic converter, three-way catalytic converter, oxidizing catalytic converter, selective catalytic converter etc.[8] Among these after-treatment technologies, three-way catalytic converter is one of the most efficient methods for gasoline engines of which the emissions are normally with stoichiometric composition. [9–11]

Catalysts used in three-way catalytic convertor has been developed for more than 40 years since the catalysts were firstly commercialized in U.S. and Japan in 1974.[12] Nowadays, the three-way catalysts were widely used in gasoline-powder vehicles to control the automotive emissions by reducing the NO_x with the simultaneous oxidation of CO and HC into their harmless products N_2, CO_2, and H_2O, as shown in **Scheme 1**.

Scheme 1. Three-way catalytic convertor

Figure 2 shows typical dependence of the three-way catalytic performance on the air-to-fuel ratio.[4] Herein, the parameter λ is defined to measure the working condition of three-way catalysts. Three-way catalysts normally function under stoichiometric atmosphere, where λ equals to 1. When λ <1, the exhaust is deficient in O_2 (rich) and three-way catalysts are ineffective for the oxidation of CO and HC, when λ > 1, the exhaust is in excess of O_2 (lean) and the reduction of NO_x to N_2 are suppressed significantly.

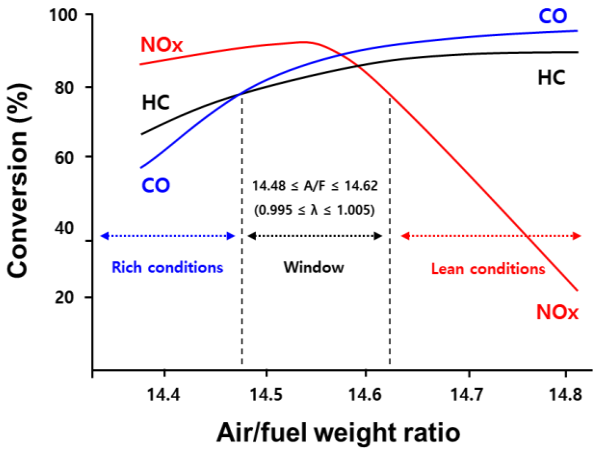

Figure 2. Typical dependence of three-way catalytic performance on air-to-fuel ratio

Modern three-way catalysts consist of (1) high surface area support, (2) oxygen storage materials, (3) platinum group metals (PGMs) including Pt, Pd, and Rh, as active components, and (4) other metal oxides, as shown in in **Scheme 2**.[11] In practical application, the catalyst powder containing these components are coated on a ceramic or stainless honeycomb substrate to improve the mass and heat transfer and decrease the pressure drop.[13]

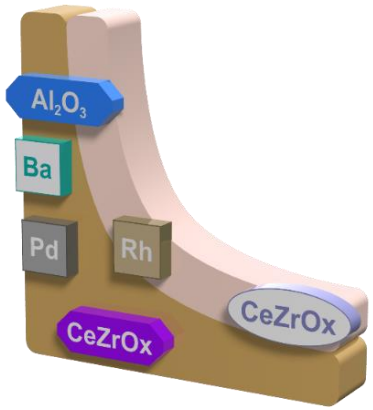

Scheme 2. Components of typical modern three-way catalysts.

1.3 Aim of this these

In this thesis, I focused on the development of efficient support materials to maximize the efficiency of platinum group metals (PGMs) for three-way catalysts:

1. Promotional effect of basic metal additives in Al_2O_3-supported Pt-based and Pd-based three-way catalysts.
2. Effect of oxygen storage materials in Pt-based three-way catalysts

1.3.1 Promotional effect of basic metal additives in Al_2O_3-supported Pt-based and Pd-based three-way catalysts.

γ-Al_2O_3 is one of the most frequently used support materials for three-way catalysts thanks to its high surface area, remarkable mechanical strength, and excellent thermal stability.[11] However, γ-Al_2O_3 can transform into relative stable θ phase at temperature as high as 800 °C and to stable α phase at even higher temperature.[14] Under practical working conditions, γ-Al_2O_3 can transform into α-Al_2O_3 when exposed to temperature as high as 1000 °C, leading to the decrease of surface area and the aggregation of supported platinum group metals.[15] As a result, suppression of the phase transformation of γ-Al_2O_3 is of great importance to sustain the three-way catalysts with good catalytic performance.

Basic metals are often added to the three-way catalysts to enhance the thermal stability of Al_2O_3.[16–19] Shinjoh reported that rare earth and alkaline earth metals are effective for increasing γ-to-α phase transformation temperature of Al_2O_3, leading to the enhancement of its thermal stability.[14] Oudet and co-workers concluded that rare earth metals in three-way reacted with Al_2O_3 at high temperature to form aluminate compound, inhibiting the transformation of γ-Al_2O_3 into α-phase.[20] However, only limited studies have been carried out to investigate the promotional effect of basic metals on the catalytic performance of three-way catalysts.

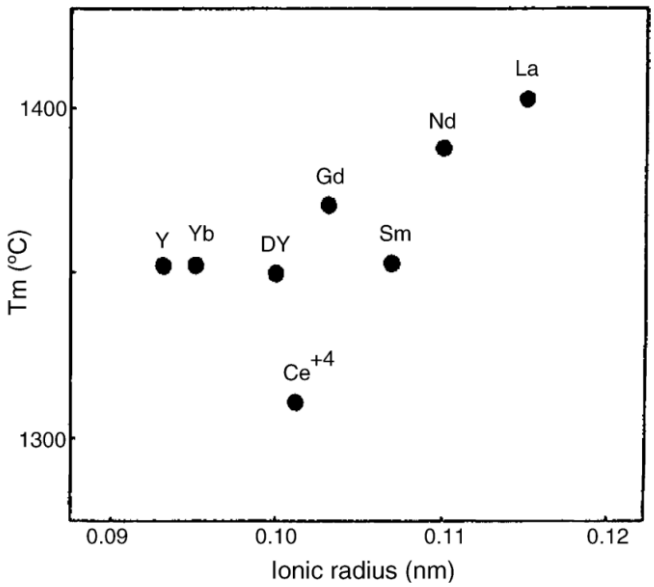

Figure 3. Transformation temperature of Al_2O_3 modified with various rare earth metals.

As an example, Muraki et al. reported that the addition of La favored the NO_x chemisorption, leading to the selective reduction of NO_x rather than O_2.[21–23] Sekiba and co-workers observed that the introduction of La_2O_3 and BaO into $Pd/CeO_2/Al_2O_3$ catalyst enhanced its catalytic performance for NO conversion under reducing conditions.[24] Kobayashi et al. confirmed that the ability to three-way catalytic performance of Pd-based catalysts were improved following the addition of basic elements, including La, Ba, and Sr.[25]

Compared to the Pd-based three-way catalysts, Pt-based catalysts have attracted less attention in recent years. Burch and Watling investigated the effects of basic metals, such as La and Ba, on the reduction of NO_x by C_3H_6 and found that basic metal additives enhanced the three-way catalytic performance of Pt-based catalysts under lean conditions. [26] Shinjoh et al. confirmed that Ba species in Pt-based three-way catalysts promoted the reduction of NO by C_3H_6 by weakening the chemisorption of hydrocarbon, thereby allowing the catalytic reaction to proceed smoothly. [27]

Although these studies are critical in the three-way catalysis field, our understanding of the role played by basic metal additives is still insufficient. It would be significantly beneficial to investigate the role played by basic metal additives in three-way catalytic reactions especially under practical conditions in order to develop effective support materials to maximize the efficiency of platinum group metals.

1.3.2 Effect of oxygen storage materials in Pt-based three-way catalysts

Three-way catalysts show high efficiency at conditions close to the stoichiometric atmosphere

point, while show poor performance under conditions deviating from stoichiometric feed composition as shown in **Figure 2**. However, under real three-way catalytic conditions nowadays, the feed composition of three-way convertor fluctuate significantly between rich and lean conditions because of an engine fuel-cut operation that was introduced relatively recently to improve the fuel efficiency of engine.[28]

Oxygen storage materials (OSMs), such as CeO_2 and CeO_2-ZrO_2 solid solution, are widely used in three-way catalysts to control the air-fuel ratios that deviate from stoichiometric conditions.[29,30] That is because ceria in three-way catalysts adsorbs and releases oxygen in response to the fluctuation of air-fuel ratio in exhaust gases, due to redox reaction between Ce^{4+} and Ce^{3+} as shown in **Scheme 3**.[11] Zr^{4+} are introduced into lattice of CeO_2 to enhance thermal stability, oxygen mobility, and the amount of surface oxygen vacancies in PGMs-based catalysts.[31–33] Nagai et al. reported that Pt–O–Ce bond formed by the Pt-support interaction acts as an anchor and inhibit the aggregation of Pt particles at high temperature.[34] Kubaka and co-workers compared catalytic performance of Al_2O_3-supported and CeO_2-ZrO_2-supported Pd catalysts, where the averaged Pd particle size, and found that CeO_2-ZrO_2-supported Pd catalyst promoted the conversion of NO and CO more efficiently.[31] Although these findings are critical in the three-way catalysis field, the fundamental understanding of effect of OSM on the performance of three-way catalysts is still insufficient, particularly under conditions related to real modern three-way catalysis operations, where deviations from stoichiometric conditions (i.e., fuel cut and acceleration) are often encountered. Comprehensive studies are required to further understand the behavior of PGM-based catalysts loaded on OSM supports during three-way catalysis in order to develop efficient support materials.

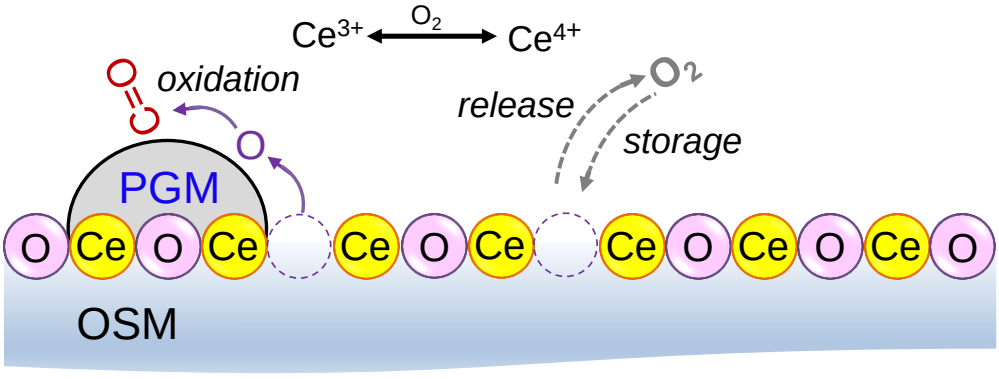

Scheme 3. Possible processes involved in the OSM-supported PGM catalysts.

1.4 Outline of Thesis

This thesis focuses on development of efficient catalysts for three-way catalysts. The objectives of this thesis are to elucidate the role played by basic metal additives and oxygen storage material in PGM-supported three-way catalysts. The thesis will show the promotion effect of basic metal additives, such as La, Ba, or Sr, in the Pd-based three-way catalysts (Chapter 2,3,4,5) and in the Pt-based three-way catalysts (Chapter 6). The effect of oxygen storage materials in Pt-based three-way catalysts is shown in Chapter 7.

Chapter 2 demonstrates the promotional effect of La in $Pd/La(x)/Al_2O_3$ (x = 0, 5, 15, 30wt%) catalysts for TWC reactions using a combination of kinetic and spectroscopic measurements as well as theoretical calculations. The obtained results show that the supported metallic Pd particles on La-containing Al_2O_3 supports are more electron deficient than those on pristine Al_2O_3, which results in a higher reactivity toward NO and a suppression of the poisoning effect of CO. As a result, a higher NO conversion efficiency is attained over these $Pd/La/Al_2O_3$ catalysts. In addition to investigations using powdered catalyst samples, we prepared and examined monolithic honeycomb catalyst samples in TWC reactions, which revealed a superior $DeNO_x$ performance for $Pd/La/Al_2O_3$ compared to Pd/Al_2O_3. Moreover, we investigated the optimal La loading for TWC reactions and found that a loading of 15 wt%, which is higher than that for the conventionally used industrial catalysts $Pd/La(5)/Al_2O_3$ (La = 5wt%) optimized to keep the high specific surface area, is more effective for the TWC process. As this study is a collaborative academic and industrial effort, we have also performed a practical test using a commercial vehicle. The results show that the catalytic system containing $Pd/La(15)/Al_2O_3$ exhibits improved conversions for the exhaust gasses including NO_x, CO, and HC compared to the one containing $Pd/La(5)/Al_2O_3$. Our results thus indicate that the loading of La in $Pd/La/Al_2O_3$ catalysts should be tuned depending on the application systems. This tuning should consider a balance between the support stability in terms of the surface area and the promotional effect in the TWC process.

Chapter 3 further shows the promotional effect of La in $Pd/La/Al_2O_3$ (x = 5, 15, and 30 wt%) in three-way catalytic process. La was found to enhance the NO conversion effectively via disproportionation reaction to yield surface nitrite species and gas-phase N_2O. A higher loading amount of La (15 wt%) favored the stable dispersion of Pd nanoparticles against sintering and in turn, retained a higher catalytic activity in $Pd/La(15)/Al_2O_3$ during the $DeNO_x$ process after the aging treatment.

Chapter 4 extent the metal additives to La, Ba, and Sr and shows their role in Pd-based three-way catalytic system using various spectroscopic and kinetic methods. Metallic Pd^0 species on Sr/Al_2O_3 and Ba/Al_2O_3 supports were found to be more electron-rich compared with those on

pristine Al_2O_3, whereas those on La/Al_2O_3 were more electron-deficient. Consequently, $Pd/La/Al_2O_3$ showed a lessened CO poisoning effect during NO reduction reactions. Evaluations were performed using powdered catalysts as well as monolithic honeycomb catalysts under conditions simulating actual use. $Pd/La/Al_2O_3$ was observed to promote the catalytic reduction of NO most efficiently, while $Pd/Ba/Al_2O_3$ exhibited the highest activity for the oxidations of CO and C_3H_6. The present data suggest that the optimal metal additive for a Pd-based TWC will be determined by the specific application. The selection of such metals should take into account not only the stability but also the promotional effect during the exhaust purification process.

Chapter 5 demonstrates the role of Ba in an Al_2O_3-supported Pd-based catalyst under practical thee-way catalysis conditions. The addition of Ba was found to reduce all of the emissions considered (NO_x, CO, and non-methane hydrocarbons) in the vehicle exhaust gas; it also suppressed supported-metal aggregation, which is a requirement of a high-performance catalyst. In addition, IR studies using model powder catalysts revealed that the efficient formation of intermediate surface nitrate species and their subsequent reactions with reductant gases, such as CO, H_2, and C_3H_6 (as a hydrocarbon), play key roles in reducing emissions. This process is akin to the NO_x storage and reduction (NSR) mechanism commonly used to control diesel emissions.

Chapter 6 shows the promoting effect of basic metal additives on NO reduction over Pt-based three-way catalysts. The catalytic activities of the $Pt/M/Al_2O_3$ catalysts for NO, CO, and total hydrocarbons were superior to those of Pt/Al_2O_3; moreover, Ba enhanced the catalytic activity of Pt-based catalysts more efficiently than La and Sr. The Pt^0 species loaded on Ba/Al_2O_3 were more electron-rich than those loaded on Al_2O_3, thereby promoting NO dissociation into N and O atoms, as revealed by the AP-XPS results. Moreover, the efficient formation of intermediate surface NO_x species, including nitrites and nitrates, and their reactivities toward reductant gases, such as H_2 or CO, were critical for promoting the effect of Ba on the NO reduction reaction.

Chapter 7 demonstrates the effect of oxygen storage materials, including CeO_2 and CeO_2-ZrO_2 solid-solutions having different ceria contents, on the performance of Pt-based three-way catalysts. Pt^0 species loaded on OSMs having a higher ceria content were found to be more electron-deficient. The increasing the ceria content in fresh OSM-supported Pt catalysts (Pt/OSMs) enhanced not only the formation of nitrite species and their reactivity toward CO but also the resistance to CO poisoning during NO–CO reactions. Both Ce and Pt species in Pt/OSM catalysts are involved in NO–CO reactions through their redox cycles. The obtained results also show that the hydrothermal ageing treatment resulted in the aggregation of Pt particles and lattice contraction of CeO_2 in Pt/OSMs, causing severe degradation of the redox ability of Pt and Ce

species and reducing the promoting effect of ceria on the formation of nitrites and their reactivity toward CO.

Chapter 8 is the general summary. support materials play an important role in enhancing the catalytic efficiency of PGM-based catalysts in three-way catalysts. Basic metal additives, such as La, Ba, and Sr, which are used widely in three-way catalysts to enhance the thermal stability of support materials, were found to enhance the catalytic performance efficiently via modifying the electronic state of metallic Pt/Pd species and enhancing the formation of reactive intermediate.

Reference

(1) Brijesh, P.; Sreedhara, S. EXHAUST EMISSIONS AND ITS CONTROL METHODS IN COMPRESSION IGNITION ENGINES: A REVIEW. *International Journal of Automotive Technology* **2013**, *14* (2), 195–206.

(2) Weiss, M.; Bonnel, P.; Kühlwein, J.; Provenza, A.; Lambrecht, U.; Alessandrini, S.; Carriero, M.; Colombo, R.; Forni, F.; Lanappe, G.; le Lijour, P.; Manfredi, U.; Montigny, F.; Sculati, M. Will Euro 6 Reduce the NO x Emissions of New Diesel Cars? - Insights from on-Road Tests with Portable Emissions Measurement Systems (PEMS). *Atmos Environ* **2012**, *62*, 657–665.

(3) Datye, A. K.; Votsmeier, M. Opportunities and Challenges in the Development of Advanced Materials for Emission Control Catalysts. *Nat Mater* **2020**, *20*, 1049–1059.

(4) Farrauto, R. J.; Deeba, M.; Alerasool, S. Gasoline Automobile Catalysis and Its Historical Journey to Cleaner Air. *Nat Catal* **2019**, *2*, 603–613.

(5) Roy, S.; Baiker, A. NOx Storage-Reduction Catalysis: From Mechanism and Materials Properties to Storage-Reduction Performance. *Chem Rev* **2009**, *109*, 4054–4091.

(6) Bielaczyc, P.; Woodburn, J.; Szczotka, A. An Assessment of Regulated Emissions and CO2 Emissions from a European Light-Duty CNG-Fueled Vehicle in the Context of Euro 6 Emissions Regulations. *Appl Energy* **2014**, *117*, 134–141.

(7) Catalysis in Motion. *Nature Catalysis 2019 2:7* **2019**, *2* (7), 553–553.

(8) Granger, P.; Parvulescu, V. I. Catalytic NOx Abatement Systems for Mobile Sources: From Three-Way to Lean Burn After-Treatment Technologies. *Chem Rev* **2011**, *111*, 3155–3207.

(9) Shelef, M.; McCabe, R. W. Twenty-Five Years after Introduction of Automotive Catalysts: What Next? *Catal Today* **2000**, *62*, 35–50.

(10) Matsumoto, S. Recent Advances in Automobile Exhaust Catalysts. *Catal Today* **2004**, *90* (3–4), 183–190.

(11) Wang, J.; Chen, H.; Hu, Z.; Yao, M.; Li, Y. A Review on the Pd-Based Three-Way Catalyst. *Catal Rev Sci Eng* **2015**, *57*, 79–144.

(12) Twigg, M. v. Progress and Future Challenges in Controlling Automotive Exhaust Gas Emissions. *Appl Catal B* **2007**, *70*, 2–15.

(13) Twigg, M. v. Catalytic Control of Emissions from Cars. *Catal Today* **2011**, *163*, 33–41.

(14) Shinjoh, H. Rare Earth Metals for Automotive Exhaust Catalysts. *J Alloys Compd* **2006**, *408–412* (December 2004), 1061–1064.

(15) Arai, H.; Machida, M. Thermal Stabilization of Catalyst Supports and Their Application to High-Temperature Catalytic Combustion. *Appl Catal A Gen* **1996**, *138*, 161–176.

(16) Suhonen, S.; Valden, M.; Pessa, M.; Savimäki, A.; Härkönen, M.; Hietikko, M.; Pursiainen, J.; Laitinen, R. Characterization of Alumina Supported Pd Catalysts Modified by Rare Earth Oxides Using X-Ray Photoelectron Spectroscopy and X-Ray Diffraction: Enhanced Thermal Stability of PdO in Nd/Pd Catalysts. *Appl Catal A Gen* **2001**, *207*, 113–120.

(17) Klingstedt, F.; Karhu, H.; Kalantar Neyestanaki, A.; Lindfors, L. E.; Salmi, T.; Väyrynen, J. Barium Promoted Palladium Catalysts for the Emission Control of Natural Gas Driven Vehicles and Biofuel Combustion Systems. *J Catal* **2002**, *206*, 248–262.

(18) Takayama, A.; Kurokawa, T.; Nakayama, H.; Katoh, T.; Nagata, M. Effect of Ba and La Additives to the Pd Layer of a Pd:Rh TWC. In *SAE Technical Papers*; SAE International, 2017; Vol. 2017-March.

(19) Wakabayashi, R.; Tomita, A.; Kimura, T. A Robust Mesoporous Al_2O_3-Based Nanocomposite Catalyst for Abundant NOx Storage with Rational Design of Pt and Ba Species. *Chemistry – A European Journal* **2021**, *27*, 6706–6712.

(20) Oudet, F.; Courtine, P.; Vejux, A. Thermal Stabilization of Transition Alumina by Structural Coherence with $LnAlO_3$ (Ln = La, Pr, Nd). *J Catal* **1988**, *114* (1), 112–120.

(21) Muraki, H.; Shinjyoh, H.;Fujitani, Y.; Muraki, H.; Shinjoh, H.; Fujitani, Y. Effect of Lanthanum on the NO Reduction over Palladium Catalysts. *Appl Catal* **1986**, *22*, 325–335.

(22) Muraki, H. ; H.; Shinjoh, H. ; H.; Sobukawa, H. ; H.; Yokota, K. K. ;; Fujitani, Y. Palladium-Lanthanum

Catalysts for Automotive Emission Control. *Industrial and Engineering Chemistry Product Research and Development* **1986**, *25* (2), 202–208.
(23) Muraki, H.; Yokota, K.; Fujitani, Y. Nitric Oxide Reduction Performance of Automotive Palladium Catalysts. *Appl Catal* **1989**, *48*, 93–105.
(24) Sekiba, T.; Kimura, S.; Yamamoto, H.; Okada, A. Development of Automotive Palladium Three-Way Catalysts. *Catal Today* **1994**, *22*, 113–126.
(25) Kobayashi, T.; Yamada, T.; Kayano, K. Effect of Basic Metal Additives on NOx Reduction Property of Pd-Based Three-Way Catalyst. *Appl Catal B* **2001**, *30* (3–4), 287–292.
(26) Burch, R.; Watling, T. C. The Effect of Promoters on Pt/Al_2O_3 Catalysts for the Reduction of NO by C_3H_6 under Lean-Burn Conditions. *Appl Catal B* **1997**, *11*, 207–216.
(27) Shinjoh, H.; Tanabe, T.; Sobukawa, H.; Sugiura, M. Effect of Ba Addition on Catalytic Activity of Pt and Rh Catalysts Loaded on γ-Alumina. *Top Catal* **2001**, *16*, 95–99.
(28) Machida, M.; Ueno, M.; Omura, T.; Kurusu, S.; Hinokuma, S.; Nanba, T.; Shinozaki, O.; Furutani, H. CeO2-Grafted Mn-Fe Oxide Composites as Alternative Oxygen-Storage Materials for Three-Way Catalysts: Laboratory and Chassis Dynamometer Tests. *Ind Eng Chem Res* **2017**, *56* (12), 3184–3193.
(29) Kim, G. Ceria-Promoted Three-Way Catalysts for Auto Exhaust Emission Control. *Industrial and Engineering Chemistry Product Research and Development* **1982**, *21* (2), 267–274.
(30) Tagliaferri, S.; Köppel, R. A.; Baiker, A. Influence of Rhodium- and Ceria-Promotion of Automotive Palladium Catalyst on Its Catalytic Behaviour under Steady-State and Dynamic Operation. *Appl Catal B* **1998**, *15* (3–4), 159–177.
(31) Kubacka, A.; Iglesias-Juez, A.; di Michiel, M.; Newton, M. A.; Fernández-García, M. Influence of the Ce–Zr Promoter on Pd Behaviour under Dynamic CO/NO Cycling Conditions: A Structural and Chemical Approach. *Physical Chemistry Chemical Physics* **2013**, *15* (22), 8640–8647.
(32) Shang, H.; Wang, Y.; Cui, Y.; Fang, R.; Hu, W.; Gong, M.; Chen, Y. Catalytic Performance of Pt–Rh/CeZrYLa+LaAl with Stoichiometric Natural Gas Vehicles Emissions. *Chinese Journal of Catalysis* **2015**, *36* (3), 290–298.
(33) Schmitt, R.; Nenning, A.; Kraynis, O.; Korobko, R.; Frenkel, A. I.; Lubomirsky, I.; Haile, S. M.; Rupp, J. L. M. A Review of Defect Structure and Chemistry in Ceria and Its Solid Solutions. *Chem Soc Rev* **2020**, *49* (2), 554–592.
(34) Nagai, Y.; Hirabayashi, T.; Dohmae, K.; Takagi, N.; Minami, T.; Shinjoh, H.; Matsumoto, S. Sintering Inhibition Mechanism of Platinum Supported on Ceria-Based Oxide and Pt-Oxide-Support Interaction. *J Catal* **2006**, *242*, 103–109.

Chapter 2

Promotional effect of La in the Three-Way Catalysis of La-Loaded Al_2O_3 Supported Pd Catalysts (Pd/La/Al_2O_3)

2.1 Introduction

Three-way catalysis (TWC) is regarded as the most extensively used method for controlling automotive emissions.[1–3] Much effort has been devoted to the design and development of effective catalytic materials for the TWC process, and the catalysts explored contain a variety of metals that include platinum group metals (PGMs) and other earth-abundant metals such as Fe, Ni, and Cu.[4–9] Although catalysts that contain these non-noble metal components have recently been intensively studied, practical systems still need large amounts of PGMs, such as Pd, Rh, and Pt in order to meet the very strict regulations for controlling exhaust gas emissions.[10–13] Modern commercial three-way catalysts generally consist of Pd- and Rh-based catalysts,[14,15] and therefore, the design and development of effective catalytic supports is necessary in order to maximize the activity of PGMs, especially Pd and Rh.

Among various candidates for TWC supports, La-loaded Al_2O_3 (La/Al_2O_3) is one of the most well-known and used industrial supports.[1] This is mainly due to its high specific surface area, mechanical strength, and high thermal stability.[16] Although Muraki and co-workers have reported the positive effect on the catalytic reduction of NO_x ($DeNO_x$) caused by the addition of La on Al_2O_3-based supports in the 1980s,[17–19] this research topic has not been pursued systematically in order to obtain mechanistic insight into the effect of using La/Al_2O_3 supports on the TWC processes. The authors argued that the addition of La (1) enhances the chemisorption of NO_x, which in turn leads to the selective reduction of NO_x, rather than O_2 and (2) suppresses the strong adsorption of hydrocarbons (HC) on Pd, which results in an efficient reduction of NO_x.[17–20] It should be noted here that similar promotional effects were observed upon addition of alkaline earth metals to the Pd-based catalysts.[21-23] It was also proposed by Muraki and co-workers that the high $DeNO_x$ activity of $Pd\text{-}La_2O_3/Al_2O_3$ under rich (reducing) conditions is due to the high catalytic performance of La oxides for steam-reforming and water gas shift (WGS) reactions that produce H_2, leading to a facile reduction of NO by the generated H_2.[18] Following these pioneering studies, Graham and Logan investigated the chemisorption of NO on a Pd(100) surface with over-layers of La_2O_3 and Al_2O_3.[23,24] They reported that at 300 K, NO partially dissociates on interfaces of Pd with La_2O_3 but not with Al_2O_3, suggesting that La_2O_3 enhances the dissociative adsorption of NO on the Pd surface. Sekiba and coworkers also observed that the introduction of La improves the TWC activity and attributed this higher activity to suppression of the strong adsorption of HC.[25] Skoglundh and co-workers have studied the addition of La to Pd/Al_2O_3 catalysts by a stepwise impregnation method, and observed a promotional effect of La for the conversion of NO under reducing conditions.[26] They proposed that this superior $DeNO_x$ activity of the $Pd/La/Al_2O_3$ catalysts relative to that of Pd/Al_2O_3 is caused by the formation of Pd-La oxides that promote the

reduction of NO by CO. These investigations represent seminal discoveries in this research field. However, the fundamental understanding of the role of La addition in improving the catalytic performance of La/Al_2O_3-supported Pd is still insufficient compared to its industrial importance. Comprehensive studies are necessary to further understand the behavior of Pd catalysts for TWC supported on La/Al_2O_3 supports. It should be pointed out here that most studies except the aforementioned reports have focused on the effect of La on the stability of the support, and not on the $DeNO_x$ activity. Therefore, the optimal La loading for industrial TWC processes is considered to be 3-5 wt% given that the thermal stability is maximized for this loading amount.

Recently, we have studied the role of La in La(5)/Al_2O_3 (La loading = 5 wt%) supports for Pd catalysts (Pd/La(5)/Al_2O_3) toward a NO–CO reaction,[27] which is one of the model reactions for the $DeNO_x$ chemistry.[28,29] The Pd/La(5)/Al_2O_3 catalyst, which contains a conventionally used amount of La, was employed for this purpose. The obtained results show that the introduction of La significantly enhances the catalytic activity toward the NO–CO reaction as a result of the efficient generation of nitrite species on the catalyst surface, and their reactivity toward CO as a reactant. It should also be informative to examine the role of La for TWC reactions under practical conditions, and it is anticipated that a more effective loading amount of La could potentially be identified for the Pd/La/Al_2O_3-catalyzed TWC reactions than that used for conventional industrial catalysts.

In this study, we have furthermore investigated the role of La in TWC process and the most effective loading amount of La for TWC reactions; we discovered that a loading of 15 wt%, which is higher than that for the conventional industrial catalysts (La = 3–5 wt%) optimized to retain the high specific surface area, is highly effective for the TWC process. The developed catalyst (Pd/La(15)/Al_2O_3) has been mounted in a commercial vehicle with a 1.5-L gasoline engine and evaluated on a LA-4 mode test cycle for practical applications. The results of various kinetic and spectroscopic studies, including *in situ* FT-IR, XAFS, and near ambient pressure X-ray photoelectron spectroscopy (NAP-XPS) in combination with density functional theory (DFT) calculations, show that Pd^0 species on the La/Al_2O_3 support are more electron deficient than Pd on Al_2O_3 in the absence of La, which leads to a higher reactivity toward NO at low temperature and a suppression of the poisoning effect of CO.

2.2 Experimental Section

2.2.1 Preparation of materials and catalysts

Commercially available γ-Al_2O_3 was used as the Al_2O_3 support, and the addition of La to the Al_2O_3 support was carried out as described in our previous study.[27] An aqueous solution that contains $La(NO_3)_3$ was impregnated onto the Al_2O_3 support. This was followed by drying at 120 °C for 2 h, and subsequent calcination in air at 600 °C for 2 h to yield La(x)/Al_2O_3 (x = La loading; x = 5, 15, 30 wt%). Pd/La(x)/Al_2O_3 (x = 5, 15, 30 wt%) and Pd/Al_2O_3 were prepared according to the following impregnation method: 5 g of La(x)/Al_2O_3 (or Al_2O_3) and 100 mL of an aqueous solution containing $Pd(NH_3)_2(NO_2)_2$ (obtained from Kojima Kagaku) were added to a 500 mL glass vessel. The solution was stirred for 15 min (200 rpm) at room temperature, before it was evaporated to dryness at 50 °C, dried at 90 °C (12 h), and calcined in air at 300 or 500 °C (3 h). It should be noted here that the average diameter of the Pd particles (determined by CO adsorption experiments) was adjusted to 3–4 nm by optimizing the calcination temperature. Subsequently, the catalysts were prepared by H_2 reduction of the calcined catalyst powders in a tube vessel under H_2 flow (20 mL/min) at 500 °C (0.5 h). Pd/Al_2O_3 was prepared in the same manner. Unless otherwise noted, the samples after the H_2 reduction were used for the various characterization experiments. Before each catalytic or *in situ* spectroscopic experiment, the samples were reduced again under 10% H_2/He flow (100 mL/min) at 400 °C (0.5 h).

Monolithic honeycomb catalysts were generated by coating a slurry, which was prepared from the calcined catalyst powders (1 wt% Pd), an inorganic binder, and water, onto a cordierite honeycomb (25.4 mmφ × 50 mm, 400 cells/in^2; NGK Insulators, Ltd.). This was followed by drying in air at 120 °C for 1 h and subsequent calcination at 600 °C for 2 h. The thus prepared honeycomb catalysts contained about 60 g L^{-1} of coated catalyst powder, commensurate with a total Pd loading of 0.06 g/L.

Monolithic honeycomb catalysts were aged for 4 h at 1000 °C under hydrothermal redox conditions, i.e., rich (reducing), lean (oxidizing), and stoichiometric atmospheres. The gas compositions for rich (3% CO, 3% H_2, 10% H_2O, and N_2 balance), stoichiometric (10% H_2O and N_2 balance), and lean (3% O_2, 10% H_2O, and N_2 balance) atmospheres were applied with programmed intervals of 180 s for rich, 10 s for stoichiometric, 180 s for lean, and 10 s for stoichiometric conditions. The flow rate was set to 3 L/min, which corresponds to space velocity (SV) = 7,200 h^{-1}.

2.2.2 Catalyst characterization

X-ray diffraction (XRD) measurements were conducted using Cu-Kα radiation on a Rigaku

Miniflex. AUTOSORB 6AG (Yuasa Ionics Co.) was used for the N_2 adsorption measurements. Bright-field scanning transmission electron microscope (BF-STEM) images and high-angle annular dark-field STEM (HAADF-STEM) images were collected using a JEM-ARM200F microscope (JEOL). CO-adsorption experiments were performed at -20 °C using BELCAT (MicrotracBEL). Temperature-programmed reduction by H_2 (H_2-TPR) were carried out using BELCAT. For that purpose, samples were mounted in a quartz cell and heated at a temperature gradient of 10 °C min^{-1} under 5% H_2/Ar flow (20 mL min^{-1}). The gas was passed through molecular sieves (MS4Å) in order to remove water. A thermal conductivity detector (TCD) was used to detect the quantity of H_2. ^{27}Al magic angle spinning (MAS) NMR measurements were carried out on a Bruker DSX-300 spectrometer operating at 300 MHz with a 4 mm rotor. XPS measurements were performed on a JEOL JPS-9010MC (MgKα). Binding energies were calibrated with respect to C_{1s} at 285.0 eV.

2.2.3 *In situ* infrared (IR) spectra

In situ IR measurements were performed at 200 °C using a JASCO FT/IR-4200 with a Mercury-Cadmium-Telluride (MCT) detector. Samples (40 mg) were pressed to make pellets (ϕ = 20 mm), which were placed in the quartz IR cell having CaF_2 windows connected to a gas flow system. The pellets were heated under a flow of 10% H_2/He (100 mL min^{-1}) at 400 °C for 0.5 h prior to the measurements. After cooling to 200 °C under the He flow, 1.0% NO/He was introduced for 600 s, before the gas was switched to He in order to allow the residual NO gas to exit. A reference spectrum, recorded at 200 °C under a flow of pure He, was subtracted from each measured spectrum.

2.2.4 (*In situ*) X-ray absorbance fine structure (XAFS) spectra

La K-edge XAFS spectra were recorded in transmittance mode at the BL14B2 beamline (operated at 8 GeV) of SPring-8 with a Si(311) double crystal monochromator (proposal 2018A1757). Samples were sealed in polyethylene cells in air, and the spectra were measured at room temperature. The EXAFS analysis was carried out using the REX ver. 2.5 program (RIGAKU). The Fourier transformation of the k^3-weighted EXAFS was carried out over a k range of 3–12 $Å^{-1}$. The curve-fitting analysis was performed using the REX ver. 2.5 program and the parameters for each shell were provided by FEFF6.

In situ Pd K-edge XAFS spectra were measured in transmittance mode at the BL14B2 beam line of SPring-8 with a Si(311) double crystal monochromator (proposal 2018B1768). A high-sampling-rate TCD GC (490 Micro GC; Agilent Technologies Inc.) was used for the quantitative analysis of NO, CO, N_2O, and N_2. A mass spectrometer (BELMass; MicrotracBEL

Corp.) was used to monitor the eluent gas. 400 mg of the samples (Pd/Al_2O_3 or $Pd/La(15)/Al_2O_3$) in pellet form (φ: 10 mm) were introduced into a quartz cell with Kapton film windows and gas lines connecting to the GC. The catalyst was pretreated under 5% H_2/He flow (200 mL min^{-1}) at 400 °C for 0.5 h, followed by cooling to 200 °C. Subsequently, 0.5% NO/He, 0.5% CO/He, and 0.5%NO+0.5%CO/He (800 mL min^{-1}) were introduced into the cell for 30 min (10 min intervals of He purge between each gas). The SV for the *in situ* Pd K-edge XAFS measurements was ~ 30, 000 h^{-1}. The EXAFS analysis was carried out as described above.

2.2.5 Near-ambitious-pressure X-ray photoelectron spectra (NAP-XPS)

NAP-XPS experiments were conducted at the beamline 13B of the Photon Factory (PF) at the High Energy Accelerator Research Organization (KEK).[30] A powder $Pd/La(15)/Al_2O_3$ catalyst with a Pd loading amount of 20 wt% was used for ease of the experiments. The promotion effect of La was confirmed for this high-Pd-loading sample by carrying out NO–CO reactions (**Figure 1**). The powder catalyst, which was reduced under 10% H_2/He flow (100 mL min^{-1}) at 500 °C for 0.5 h, was once dispersed in deionized water and deposited on a Si substrate by a drop-and-dry method. The prepared substrate was then introduced into the XPS chamber. A K-type thermocouple was directly attached to the sample to measure the operating temperature. Prior to the measurement, the sample pellet was pretreated again under a CO atmosphere at 400 °C for 0.5 h. For safety reasons, CO was used as a reducing gas instead of H_2. After cooling to 50 °C, NO (100 mTorr) was introduced and the spectra were measured. All core-levels (Al 2p, C 1s, Pd 3d, N 1s) measurements were recorded continuously using a fixed photon energy (550 eV). Calibration of the binding energy was carried out using the Al 2p level (74.3 eV). The obtained XPS intensities were normalized in order to remove the effect of attenuation caused by the introduced gases. XPS spectra were analyzed using the software “fitt” by convolution of the Lorentzian and Gaussian functions with a linear background.

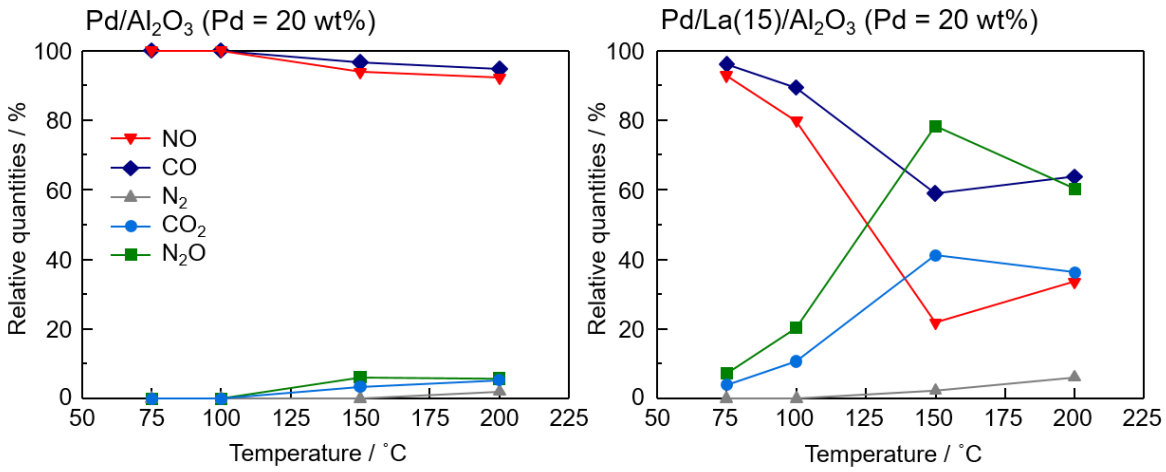

Figure 1. Catalytic conversions of NO and CO in the NO–CO reaction over powder forms of Pd/Al_2O_3 and $Pd/La(15)/Al_2O_3$ with 20 wt% Pd loading. Conditions: 0.5% CO, 0.5% NO, He balance; Catalyst amount = 10 mg, $W/F = 1.0\times10^{-4}$ g·min·cm^{-3}.

2.2.6 Catalytic reactions

Catalytic reactions on the powdered catalysts were carried out in a flow reactor. 15 mg of the catalyst was placed in a reactor using quartz wool in the catalyst bed. After the reduction of the catalyst under 10% H_2/He flow (100 mL min^{-1}) for 0.5 h, the catalyst was cooled to 125 °C and the catalytic NO–CO reaction was started by supplying a gas mixture containing CO (0.5%) and NO (0.5%), as well as He balance at 100 mL·min^{-1} (W/F corresponds to 1.5×10^{-4} g·min·cm^{-3}). Conversions and yields of the gasses were determined by GC analysis (Shimadzu GC-8A with a SHINCARBON ST column). The yields were calculated based on the following equation.

$$NO + CO \rightarrow 0.5\ N_2 + CO_2 \qquad (1)$$

Catalytic reactions on the honeycomb form catalysts were carried out in a flow reactor using MEXA-series (Horiba Ltd.). The catalysts were placed in a tubular-type reactor, and their catalytic performance was investigated by supplying a gas mixture typically containing 0.6% CO, 420 ppm C_3H_6, 0.2% H_2, 0.1% NO, 0.6% O_2, 15% CO_2, 10% H_2O, and N_2 balance (λ = 1) at SV = 100,000 h^{-1}. Conversions of NO, C_3H_6, and CO were monitored by using an exhaust gas analyzer (ABB, AO-2020). Before each catalytic activity test, the honeycomb catalyst was pre-treated under a flow of the aforementioned gas at 400 °C for 0.5 h. The □ values were calculated using the following equation and the further details on the gas composition were listed in **Table 1** and **Table 2**.

$$\lambda = \frac{O_{\square} + 0.5CO + 0.5H_{\square}O + CO_{\square} + 0.5NO}{0.5H_{\square} + CO + 1.5C_{\square}H_{\square} + 0.5H_{\square}O + CO_{\square}} \quad (2)$$

amount = 10 mg, W/F = 1.0×10^{-4} g·min·cm^{-3}.

Table 1. Composition of the simulated exhaust gas mixtures for TWC light-off tests.

□	CO / %	C_3H_6 / ppm	H_2 / %	NO / %	O_2 / %	CO_2 / %	H_2O / %	N_2 / %
0.95	2.4	420	0.8	0.1	0.6	15	10	balance
1.00	0.6	420	0.2	0.1	0.6	15	10	balance
1.05	0.6	420	0.2	0.1	1.65	15	10	balance

Table 2. Composition of the simulated exhaust gas mixtures for □ sweep tests.

□	CO / %	C_3H_6 / ppm	H_2 / %	NO / %	O_2 / %	CO_2 / %	H_2O / %	N_2 / %
0.95	2.40	420	0.80	0.1	0.60	15	10	balance
0.96	1.95	420	0.65	0.1	0.60	15	10	balance
0.97	1.60	420	0.53	0.1	0.60	15	10	balance
0.98	1.25	420	0.42	0.1	0.60	15	10	balance
0.99	0.95	420	0.32	0.1	0.60	15	10	balance
1.00	0.60	420	0.20	0.1	0.60	15	10	balance
1.01	0.60	420	0.20	0.1	0.80	15	10	balance
1.02	0.60	420	0.20	0.1	1.00	15	10	balance
1.03	0.60	420	0.20	0.1	1.22	15	10	balance
1.04	0.60	420	0.20	0.1	1.42	15	10	balance
1.05	0.60	420	0.20	0.1	1.65	15	10	balance

Practical tests using a commercial vehicle were carried out as follows. The catalysts (Pd/La(15)/Al_2O_3 or Pd/La(5)/Al_2O_3) were used in a Pd-Rh three-way catalyst with a double-layered structure. The Pd and Rh catalyst washcoats were coated on a 1.0-L ceramic monolith with a cell density of 600 in^{-2}.[31] The bottom layer consisted of Pd supported on a washcoat of the La(x)/Al_2O_3 (x = 5 or 15 wt%), a Ce-Zr mixed oxide, and Ba carbonate. The washcoat loading of the bottom layer was ~150 g/L with a Pd loading of 3 g/L. The top layer consisted of Rh supported on a washcoat of another Ce-Zr mixed oxide and La(5)/Al_2O_3. The washcoat loading of the top layer was ~60 g/L with a Rh loading of 0.3 g/L. The thus prepared three-way catalysts were bench-aged using a 1.8-L gasoline engine with a peak temperature of 950 °C for 75 hours. The aged catalysts were mounted in a commercial vehicle with a 1.5-L engine, and the vehicle emission test of LA-4 driving cycle (city cycle of US Federal and California) were conducted. The concentrations of NO_x (NO + NO_2), CO, and the total hydrocarbons (THC), as well as the catalyst-bed temperature and air-to-fuel ratio (AFR) were monitored by employing a Horiba MEXA series.

2.2.7 DFT calculations

All spin-polarized calculations were conducted using Vienna *Ab Initio* Simulation Package (VASP),[32,33] using projector-augmented wave potentials[34] and the Perdew-Burke-Ernzerhof (PBE)

functional.[35] The DFT-D3 method with Becke-Johnson damping dispersion correction was employed to take into account the dispersion interaction.[36,37] The original γ-Al_2O_3(100) surface structure was modelled according to a previous study by Raybaud and co-workers (**Figure 2**).[38] The structural model contains a (2 x 2) supercell, a four-layer-thick slab, and 10 Å of vacuum with 160 atoms (lattice parameters for the surface: a = 10.97 Å, b = 16.54 Å). The slab model was calculated with 2 × 1 × 1 k-points mesh and an energy cutoff of 400 eV. The (100) surface was employed in this study because it is the most stable surface for γ-Al_2O_3. The first two layers of □-Al_2O_3 relative to the surface were allowed to relax for the geometry optimization, while the two bottom layers were fixed. The criterion of the convergence was set to F_{max} < 0.03 eV/Å, where F_{max} is the maximum force that acts on the mobile atoms. For Pd_{13} clusters, the new biplanar (NBP) model was employed.[38] The adsorption energy of Pd_{13} on the alumina support (E_{ads}) can be calculated according to:

$$E_{ads} = E(Pd_{13}/Support) - E(Pd_{13}) - E(Support) \quad (3)$$

where $E(Pd_{13}/Support)$, $E(Pd_{13})$, and $E(Support)$ refer to the electronic energy of the supported system, the Pd_{13} cluster, and the support slab without the Pd_{13} cluster, respectively. In addition, interaction energies of the Pd_{13} clusters and the alumina support are defined by:

$$E_{int} = E(Pd_{13}/Support) - E(Pd_{13}') - E(Support') \quad (4)$$

where $E(Pd_{13}')$ is the energy of the Pd_{13} cluster having the deformed geometry after its adsorption on the support surface, and $E(Support')$ is the energy of the surface fragment having the deformed geometry after adsorption of the Pd_{13} cluster. Deformation energies are defined by the following Eqs. (5) and (6) for the support and the Pd_{13} cluster, respectively. They enable quantifying the influence of the shape adaptation on the adsorption event. Eqs. (7) and (8) describe the total deformation energy, which links the adsorption, interaction, and deformation energies.

$$E_{def\_Support} = E(Support') - E(Support) \quad (5)$$

$$E_{def\_Pd13} = E(Pd_{13}') - E(Pd_{13}) \quad (6)$$

$$E_{def\_total} = E_{def\_Support} + E_{def\_Pd13} \quad (7)$$

$$E_{ads} = E_{int} + E_{def\_total} \quad (8)$$

Bader charge analyses were carried out on the same system.

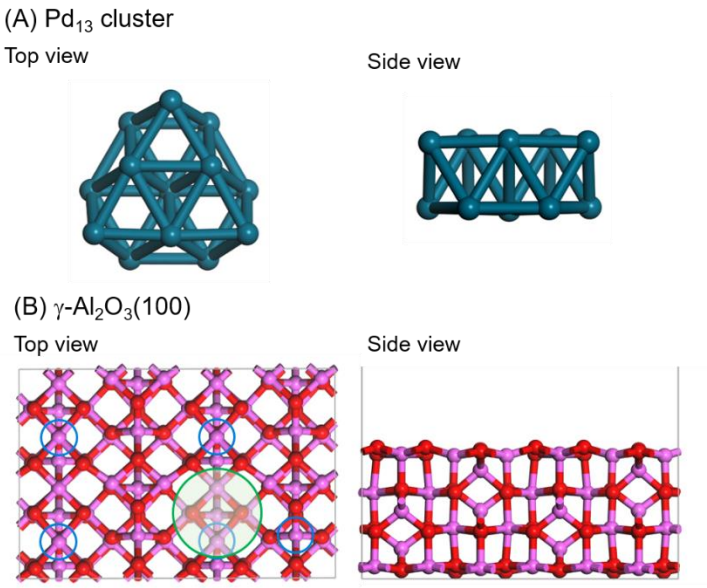

Figure 2. Structure models for the (A) Pd_{13} cluster and (B) γ-Al_2O_3(100). Al, O, and Pd atoms are shown as purple, red, and dark-blue balls, respectively. Locations where Al atoms are substituted with La atoms are marked by blue circles. The adsorption site for the Pd_{13} cluster is marked by the green circle.

2.3. Results and discussion

2.3.1 Catalysts characterization

The preparation conditions and the average Pd particle diameters for the Pd/Al_2O_3 catalyst and a series of $Pd/La(x)/Al_2O_3$ (x = 5, 15, 30 wt%) catalysts used in this study are summarized in **Table 3**. It should be noted here that some information and data for Pd/Al_2O_3 and $Pd/La(5)/Al_2O_3$ were taken from our previous report.[27] Catalysts containing Pd particles with an average diameter of 3–4 nm were prepared by optimizing the calcination temperature prior to the H_2 reduction process. Powder XRD patterns of the $Pd/La(x)/Al_2O_3$ catalysts show peaks assignable to γ-Al_2O_3 (**Figure 3A**).[27] This result indicates that all the Al_2O_3 and $La(x)/Al_2O_3$ supports used in this study are mainly comprised of the γ-Al_2O_3 phase.[27] However, the peak intensities decreased for samples containing higher proportions of La, indicating that these are of lower crystallinity compared to pristine γ-Al_2O_3. Peaks assignable to La_2O_3, $LaAlO_3$, or Pd species were not observed.[27] The ^{27}Al MAS NMR spectra (**Figure 3B**) of all catalysts exhibit two features at approximately 13 and 73 ppm, which were attributed to Al^{3+} cations in octahedral and tetrahedral coordination environments, respectively.[39–41] Pentacoordinated Al species that are typically observed at 35-40 ppm were not observed in our experiments. Reference compound $LaAlO_3$ exhibited only one peak at 12 ppm, indicating that it contains exclusively Al species that are octahedrally coordinated by oxygen. These ^{27}Al MAS NMR results are consistent with the XRD results, and thus corroborate that our catalysts are comprised predominantly of the γ-Al_2O_3 phase. N_2 adsorption isotherms are given in **Figure 3C**. The BET specific surface areas (S_{BET}) of the Pd/Al_2O_3 and $Pd/La(x)/Al_2O_3$ catalysts are summarized in **Table 3**. The S_{BET} gradually decreased with increasing La loading. XPS analyses were carried out for $La(15)/Al_2O_3$ and $LaAlO_3$, as shown in **Figure 3D**. The XPS spectra exhibit signals that correspond to $3d_{5/2}$ and $3d_{3/2}$ core levels and their satellite peaks.[27,42] $La(15)/Al_2O_3$ shows the main $3d_{5/2}$ peak at ~834.3 eV, which is higher than those seen in the spectrum for $LaAlO_3$ (~833.4 eV) and La_2O_3 (~833.9 eV),[27] suggesting that the La species in $La(15)/Al_2O_3$ are well dispersed.[27,42,43] H_2-TPR profiles of Pd/Al_2O_3, $La(15)/Al_2O_3$, and $Pd/La(15)/Al_2O_3$, which were measured under a 5% H_2/Ar flow (30 mL/min), are shown in **Figure 4**. The peak assignable to the reduction of PdO_x species at ca. 150 ˚C shifted to higher temperatures upon introduction of La in the support. This observation indicates that the introduction of La prevents the reduction of PdO_x species.

Table 3. Preparation conditions and textual properties of Pd/Al_2O_3 and $Pd/La(x)/Al_2O_3$.

Catalyst	$T_{calcination}$ / ˚C	$T_{H2\ reduction}$ / ˚C	S_{BET}[a] / $m^2\ g^{-1}$	Pd particle diameter[b] / nm
Pd/Al_2O_3[c]	500	500	156	3.4
$Pd/La(5)/Al_2O_3$[c]	500	500	148	3.1

$Pd/La(15)/Al_2O_3$	500	500	129	3.7
$Pd/La(30)/Al_2O_3$	300	500	74	3.8

[a] Determined by N_2 adsorption. [b] Estimated by CO adsorption at -20 ˚C. [c] The information and data for Pd/Al_2O_3 and $Pd/La(5)/Al_2O_3$ were taken from our previous report.[27]

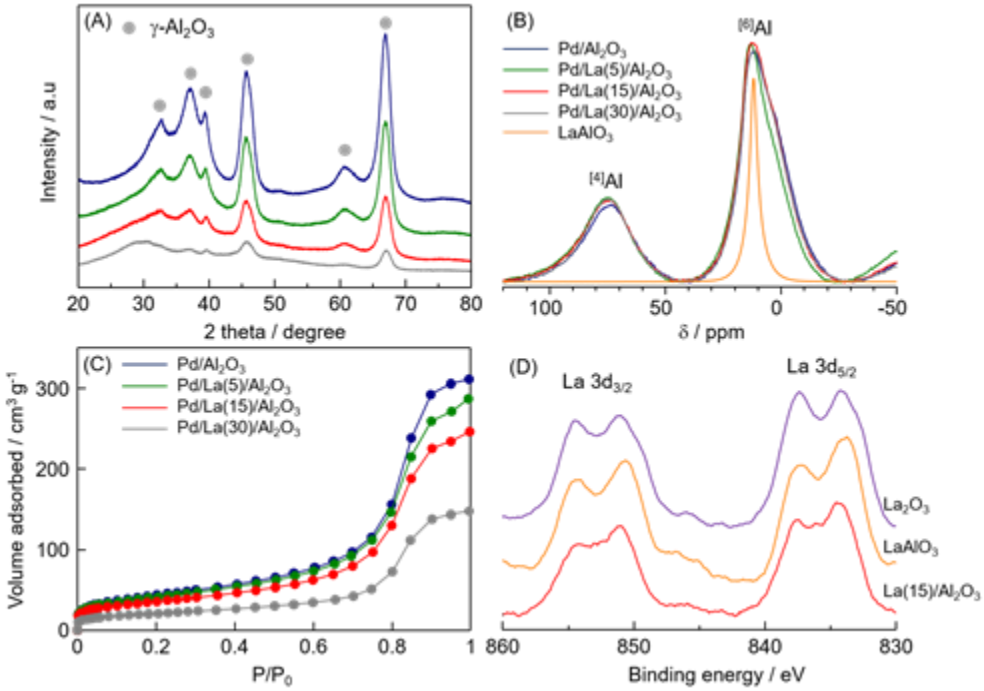

Figure 3. (A) XRD patterns of $Pd/La(x)/Al_2O_3$ (x = 5, 15, 30 wt%). (B) ^{27}Al MAS NMR spectra of Pd/Al_2O_3, $Pd/La(x)/Al_2O_3$ (x = 5, 15, 30 wt%), and $LaAlO_3$. (C) N_2 adsorption isotherms of $Pd/La(x)/Al_2O_3$ (x = 15, 30 wt%). (D) XPS spectra of $La(15)/Al_2O_3$ and $LaAlO_3$ (La 3d region).

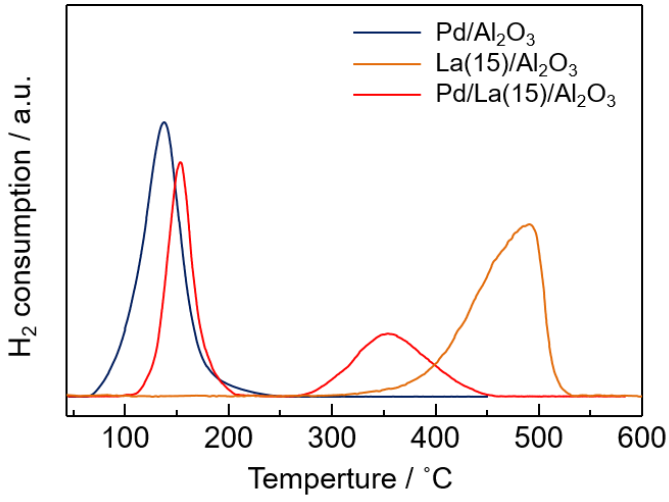

Figure 4. H_2-TPR profiles of Pd/Al_2O_3, $La(15)/Al_2O_3$, and $Pd/La(15)/Al_2O_3$ measured under a 5% H_2/Ar flow (30 mL/min). Heating rate = 10 ˚C min^{-1}.

La(15)/Al_2O_3 and Pd/La(15)/Al_2O_3 were subjected to HAADF-STEM measurements. La in La(15)/Al_2O_3 is atomically dispersed, as shown in **Figures 5** and **6**. This result is consistent with earlier findings for a similar La/Al_2O_3 system.[27,44–47] Moreover, the obtained images show that Pd nanoparticles in Pd/La(15)/Al_2O_3 exhibit an average particle size of 3–4 nm. The results of the La K-edge XAFS analysis for the Pd/La(x)/Al_2O_3 samples (x = 15 and 30 wt%) and their reference compound ($LaAlO_3$) are shown in **Figure 7**. $LaAlO_3$ is a perovskite material with a cubic structure. The first coordination environment around La consists of 12 O atoms with the same distance.[44] The EXAFS Fourier transform for $LaAlO_3$ shows La–Al and La–La at approximately 2.9 and 3.5 Å, respectively. For the Pd/La(x)/Al_2O_3 (x = 15, 30 wt%) samples, two peaks were observed at ca. 1.2 and 2.0 Å. It has been reported that the peak at 2.0 Å is due to La–O bonds, while the smaller peak arises from a side lobe of the La–O bonds due to the nonlinearity of their phase shifts.[44] The same feature was observed for Pd/La(5)/Al_2O_3 (data not shown).[27] A curve-fitting analysis of the EXAFS spectra is summarized in **Table 4**, which shows that the spectra of all Pd/La(x)/Al_2O_3 samples comprise only one La–O contribution. These results suggest that La is highly dispersed, which is in accordance with the aforementioned results of the XRD, XPS, and STEM measurements.

Pd K-edge XAFS measurements for Pd/Al_2O_3 and Pd/La(15)/Al_2O_3 (**Figure 8 and Table 5**) were carried out under a flow of 5% H_2/He at 200 °C after H_2 reduction at 400 °C. EXAFS Fourier transforms of Pd/Al_2O_3 and Pd/La(15)/Al_2O_3 showed only one distinct peak, which corresponds to the Pd–Pd bonds, indicating that the Pd species in Pd/Al_2O_3 and Pd/La(15)/Al_2O_3 are in metallic states. On the other hand, the XANES spectra showed that the edge position for Pd/La(15)/Al_2O_3 is slightly positively shifted compared to that of Pd/Al_2O_3, even though their Pd particle sizes are almost identical.

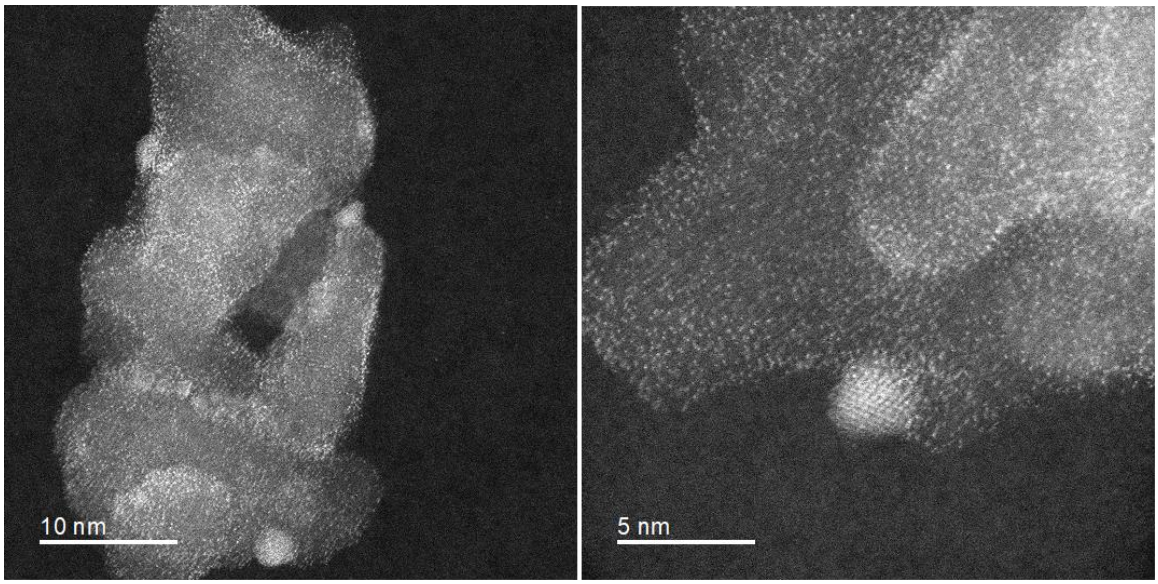

Figure 5. HAADF-STEM images of Pd/La(15)/Al_2O_3.

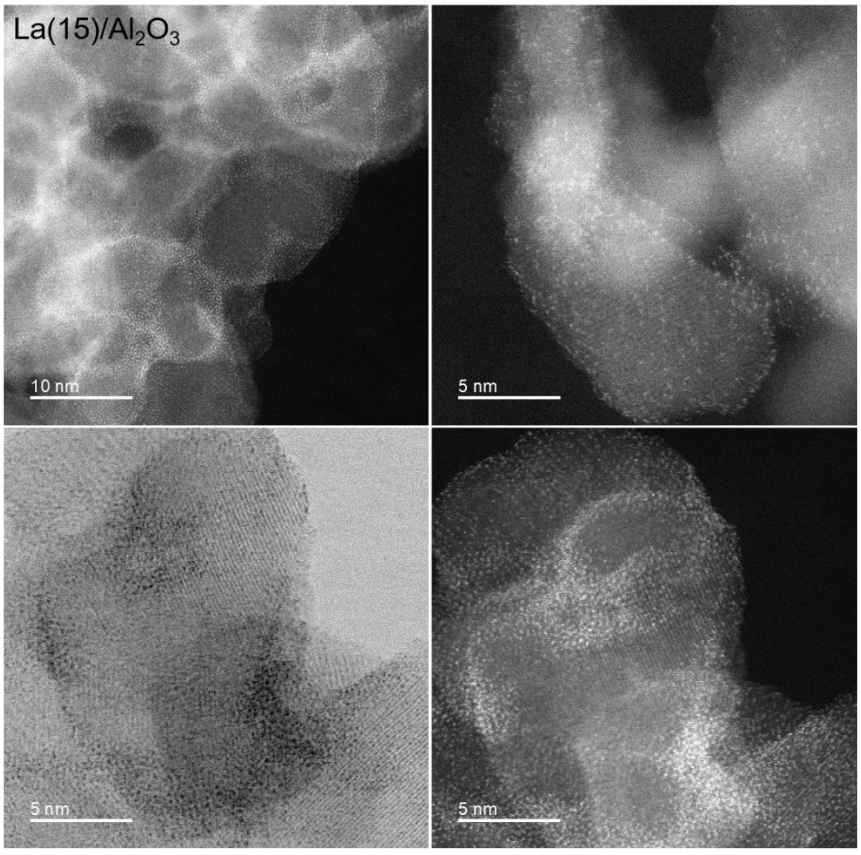

Figure 6. BF- and HAADF-STEM images of La(15)/Al_2O_3.

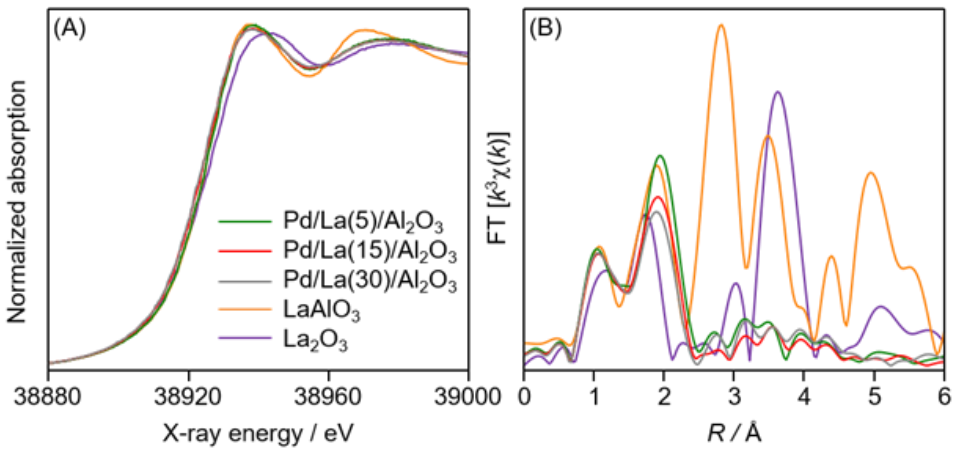

Figure 7. La K-edge (A) XANES spectra and (B) k^3-weighted EXAFS Fourier transforms of fresh samples of Pd/La(x)/Al_2O_3 (x = 15 and 30 wt%), together with those of a reference compound $LaAlO_3$. The spectra were recorded at room temperature in air.

Table 4. Curve-fitting analysis of La K-edge EXAFS of fresh samples of Pd/La(x)/Al_2O_3 (x = 5, 15, 30 wt%).

Sample	Shell	CN [a]	*R* (Å) [b]	σ (Å) [c]	R_f (%) [d]
Pd/La(5)/Al_2O_3 [e]	La–O	3.6	2.59	0.09	0.9
Pd/La(15)/Al_2O_3	La–O	3.2	2.58	0.10	0.2
Pd/La(30)/Al_2O_3	La–O	2.9	2.56	0.10	0.4

[a] Coordination number. [b] Bond distance. [c] Debye-Waller factor. [d] Residual factor. [e] The original XAFS spectrum for Pd/La(5)/Al_2O_3 used for this curve-fitting analysis was taken from our previous report.[S1]

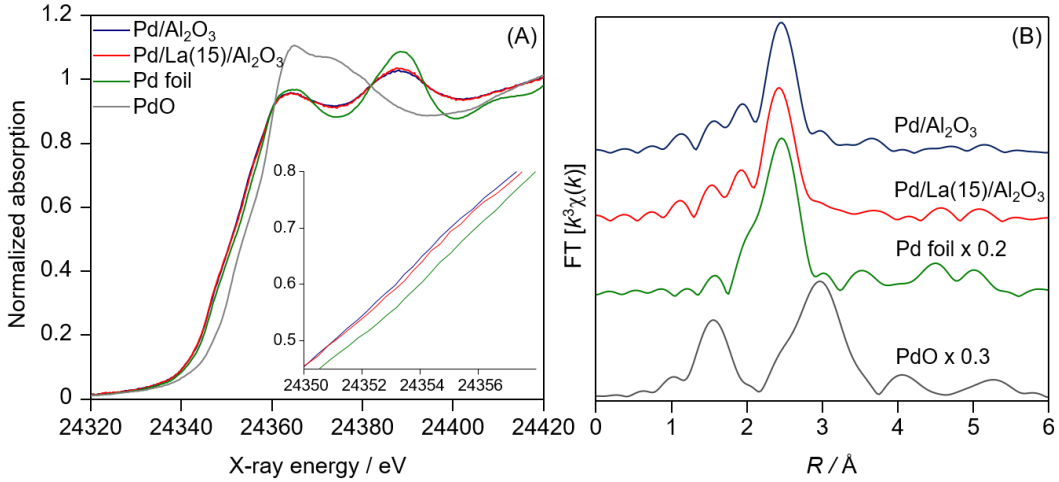

Figure 8. *In situ* Pd K-edge (A) XANES spectra and (B) k^3-weighted EXAFS Fourier transforms of Pd/Al_2O_3, Pd/La(15)/Al_2O_3, Pd foil, and PdO. The spectra of Pd/Al_2O_3 and Pd/La(15)/Al_2O_3 were collected under a flow of 5% H_2/He (200 mL/min) at 200 °C after H_2 reduction at 400 °C. The spectra of Pd foil and PdO were collected at room temperature in air.

Table 5. Curve-fitting analysis of the Pd K-edge EXAFS of Pd/Al_2O_3 and Pd/La(15)/Al_2O_3.

Sample	Shell	CN [a]	*R* (Å) [b]	σ (Å) [c]	R_f (%) [d]
Pd/Al_2O_3	Pd–Pd	3.1	2.67	0.11	1.1
Pd/La(15)/Al_2O_3	Pd–Pd	3.3	2.67	0.10	1.1

[a] Coordination number. [b] Bond distance. [c] Debye-Waller factor. [d] Residual factor.

To further study the electronic properties of Pd on the La-modified Al_2O_3 surfaces, DFT calculations were employed. We modelled La_5-Al_2O_3 by substituting five superficial Al atoms with La atoms. For the choice of the substituted Al atoms, we examined all possible permutations of substitution and confirmed that the chosen model is the most stable. The optimized structures for Pd_{13}/Al_2O_3, La_5-Al_2O_3, and Pd_{13}/La_5-Al_2O_3 are shown in **Figure 9**. For Pd_{13}/Al_2O_3, E_{def_Pd13}, E_{ads}, and E_{int} values of 1.45, -5.60, and -7.05 eV, respectively, were determined. For Pd_{13}/La_5-Al_2O_3 on the other hand, we determined values of 1.24, -6.05, and -7.29 eV. These results show that the

addition of La could potentially lead to a stabilization of Pd on the support. Moreover, we calculated the average Bader charge of Pd_{13} for Pd_{13}/Al_2O_3 (-0.036) and Pd_{13}/La_5-Al_2O_3 (-0.015), which indicates that Pd^0 species on La/Al_2O_3 is more electron deficient than Pd on pristine Al_2O_3. This result is in consistent with the aforementioned results of the Pd K-edge XAFS measurements.

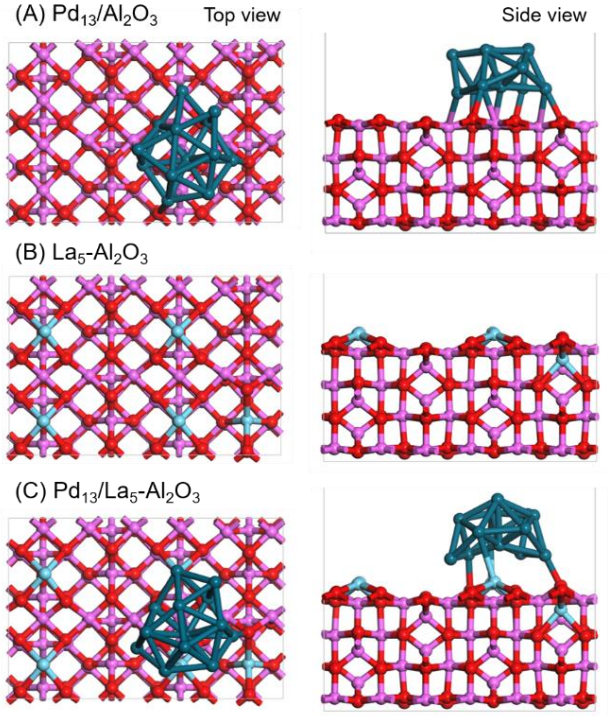

Figure 9. Optimized structures for (A) Pd_{13}/Al_2O_3, (B) La_5-Al_2O_3, and (C) Pd_{13}/La_5-Al_2O_3. Al, O, Pd, and La atoms are shown as purple, red, navy, and light blue balls, respectively.

2.3.2 Promotional effect of La on the NO reduction activity

NO–CO reactions with a powdered sample of $Pd/La(15)/Al_2O_3$ were performed as shown in **Figure 10A**. It should be noted here that the relative quantities refer to the reactants (NO and CO) and were obtained from eqn. (1). $Pd/La(15)/Al_2O_3$ shows a higher catalytic activity than Pd/Al_2O_3 and a comparable activity to $Pd/La(5)/Al_2O_3$ (NO conversion at 150 °C = 33.6% for $Pd/La(15)/Al_2O_3$ and 36.2% for $Pd/La(5)/Al_2O_3$).[27] This result confirms that La addition onto Al_2O_3 affects not only the stability, but also the catalytic activity in the NO–CO reaction.[27] In order to further investigate the role of La in the NO–CO reaction, reaction orders with respect to NO and CO were determined for $Pd/La(15)/Al_2O_3$ and Pd/Al_2O_3 from the steady-state reaction rate in a stream of NO and CO with different partial pressures (**Figure 10B**). It should be noted that the reaction rates were determined at an NO conversion < 30%. Reactions involving CO are often of negative order with respect to CO.[46,48] The strong binding of CO to the metal surface is usually

commensurate to catalyst inhibition, i.e., CO acts as a catalyst poison that needs to desorb prior to the reaction, which in turn leads to negative-order kinetics for such reactions on PGMs. This phenomenon was also observed for Pd/Al_2O_3, where the reaction order with respect to CO is -0.28, indicating that CO acts as a poison for Pd. Conversely, for $Pd/La(15)/Al_2O_3$, the reaction order with respect to CO is positive (+0.35), which indicates that CO is not a catalyst poison for $Pd/La(15)/Al_2O_3$. Similar behavior was observed by Datye and co-workers for the oxidation of CO with O_2 over a Pd (2.5 wt%) catalyst supported by La/Al_2O_3 (4 wt% La_2O_3; W. R. Grace (MI-386)).[46] They attributed this to single atom nature of the Pd species. In addition, it is well known that the back-donation from the transition metal surface to the adsorbate CO strongly contributes to the adsorption strength.[49,50] This contribution is weakened when Pd is positively charged, thus leading to a weaker adsorption of CO. Consequently, CO does not act as a catalyst poison for $Pd/La(15)/Al_2O_3$. We have also examined the adsorption energy of CO by using DFT calculations (**Figure 11**). The adsorption energy of CO on Pd_{13}/La_5-Al_2O_3 (E_{ads} = -2.18 eV for a hollow site and -1.62 eV for an ontop site) are smaller than those on Pd_{13}/Al_2O_3 (E_{ads} = -2.40 eV for a hollow site and -2.24 eV for an ontop site). It should also be noted here that the most stable structures were employed for this investigation for each model and adsorption site. This result also suggests that the addition of La leads to a weaker adsorption of CO. The reaction orders with respect to NO over $Pd/La(15)/Al_2O_3$ (+0.43) and Pd/Al_2O_3 (+0.83) showed a value for $Pd/La(15)/Al_2O_3$ that is in accordance with the results obtained by the *in situ* IR spectroscopy reported in our previous study,[27] which suggests that the promotional effect of La arises from the efficient generation of nitrite species on the catalyst surface and from their reactivity toward CO.

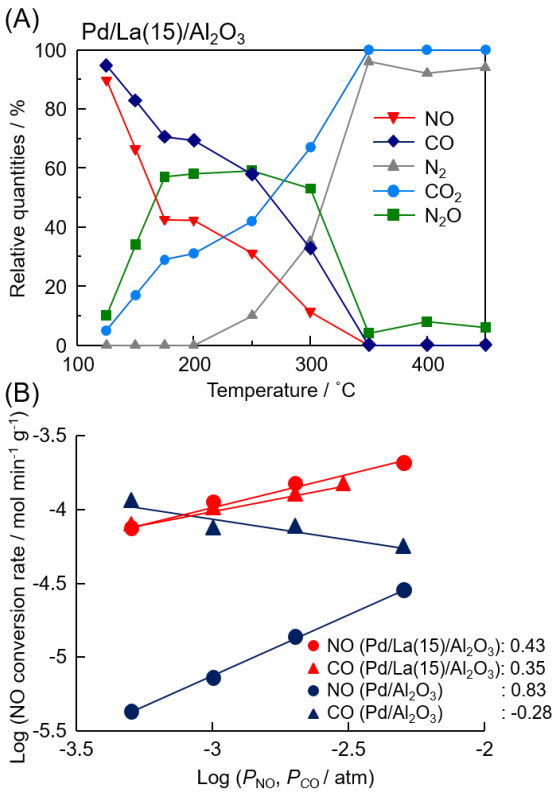

Figure 10. (A) Catalytic NO–CO reaction over a powdered sample of Pd/La(15)/Al_2O_3. Conditions: 0.5% CO, 0.5% NO, He balance; Catalyst weight = 15 mg. (B) Partial pressure dependence of the conversion rate of NO and the reaction order in the NO–CO reaction over powdered samples of Pd/La(15)/Al_2O_3 and Pd/Al_2O_3 at 150 ˚C. Conditions: 0.05–0.5% CO, 0.05–0.5% NO, He balance.

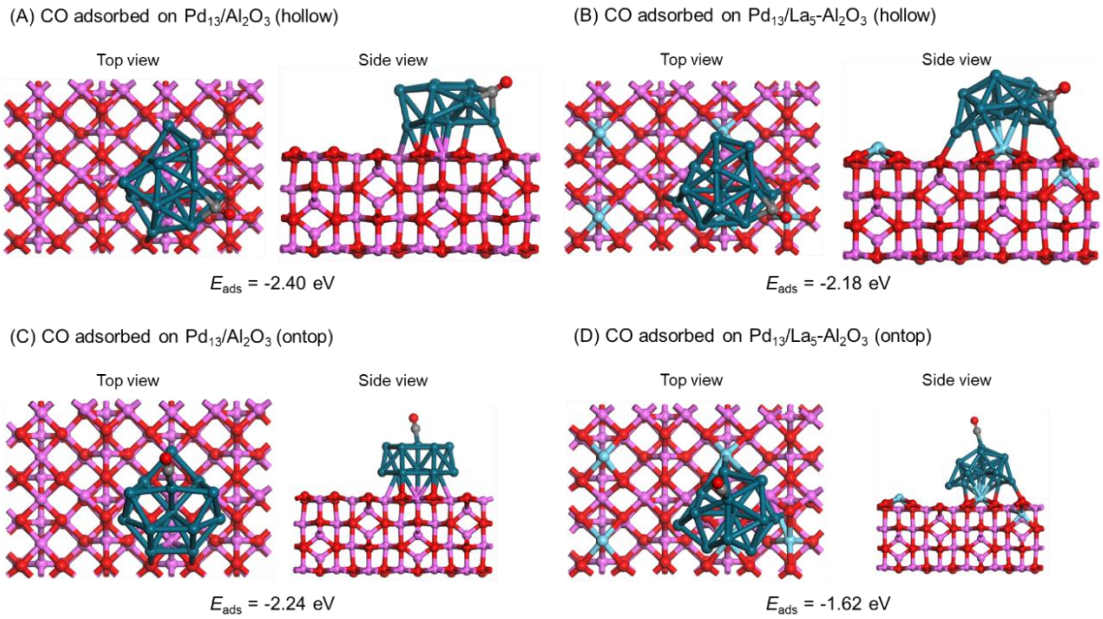

Figure 11. Adsorption energies of CO on (A,C) Pd_{13}/Al_2O_3, (B,D) Pd_{13}/La_5-Al_2O_3. The most stable adsorption structures for each adsorption mode (hollow and ontop) are shown.

In order to get further insights into the effect of La on the reactivity of Pd/Al_2O_3 and $Pd/La(15)/Al_2O_3$ toward NO, *in situ* Pd-K edge XAFS measurements were carried out under a flow of NO, CO, NO+CO at 200 °C after H_2 reduction at 400 °C.[51] For that purpose, 0.5% NO/He, 0.5% CO/He, and 0.5%NO+0.5%CO/He (800 mL min^{-1}) were introduced consecutively into the cell (30 min for each gas). The SV for the *in situ* Pd K-edge XAFS measurements was ~ 30,000 h^{-1}. **Figure 12** shows the corresponding XANES and the FT of the k^3-weighted EXAFS (without correction of the phase shift) of Pd/Al_2O_3 and $Pd/La(15)/Al_2O_3$ measured under a flow of 0.5% NO/He. The XANES of $Pd/La(15)/Al_2O_3$ show that the absorption edge shifts to higher energy upon introduction of NO. The FT of the k^3-weighted EXAFS spectra show that a peak corresponding to Pd–Pd (ca. 2.5 Å) decreased while a peak corresponding to Pd–O (ca. 1.6 Å) increased, indicating that Pd is oxidized by NO. During that event, N_2O was formed over the $Pd/La(15)/Al_2O_3$ catalyst as detected by the high-sampling-rate thermal conductivity detector GC (**Figure 13A**). The Pd^0 fraction ($Pd^0/(Pd^0+Pd^{II})$), derived from the linear combination fitting on the XANES analysis, also showed the original Pd species was oxidized by the introduced NO (**Figure 13B**). The Pd^0 fraction 30 min after the introduction of NO was determined to be 0.58. Subsequently, the partly oxidized Pd species were reduced by the introduction of CO and the Pd species adopted an almost metallic state (Pd^0 fraction = 0.86) 30 min after the introduction of CO. It should be noted here that the formation of CO_2 was detected upon introduction of CO. Moreover, the Pd species remained almost unchanged under a flow of 0.5%NO+0.5%CO/He gas, and N_2O, N_2, and CO_2 were detected as the gas-phase products. The coordination numbers for the Pd–Pd shells ($CN_{Pd–Pd}$) were obtained from a curve-fitting analysis of the EXAFS (**Figure 13C**). The $CN_{Pd–Pd}$ values decreased under a flow of NO, while a subsequent introduction of CO led to an increase of the $CN_{Pd–Pd}$, which is consistent with the results of the XANES analysis. These results indicate that the Pd species undergo a redox cycle in the presence of NO as an oxidizing gas and in the presence of CO as a reducing gas during the NO–CO reaction. A comparison with Pd/Al_2O_3 revealed the same redox behavior of the Pd species upon introduction of the reactant gasses. The changes to the Pd^0 fraction upon introduction of NO was smaller than that observed in $Pd/La(15)/Al_2O_3$, suggesting that the presence of La induces efficient oxidation of Pd by NO. On the other hand, the $CN_{Pd–Pd}$ value for Pd/Al_2O_3 was smaller than that for $Pd/La(15)/Al_2O_3$. We also discovered that the Pd–O contribution did not appear in the FT of the k^3-weighted EXAFS spectra of Pd/Al_2O_3. These results suggest that metallic Pd species were oxidized for Pd/Al_2O_3 upon

introduction of NO, albeit that PdO species were not formed, which stands in contrast to the case of Pd/La(15)/Al_2O_3. This could potentially be interpreted in terms of the highly dispersed nature of the Pd species on the Al_2O_3 support without La after the NO treatment for 30 min. In order to establish conditions identical to those in the XAFS analysis, we exposed Pd/Al_2O_3 to a flow of 0.5% NO/He at 200 ˚C, and subsequently recorded HAADF-STEM images (**Figure 14**). Although only Pd nanoparticles were observed for the fresh Pd/Al_2O_3 sample, highly dispersed Pd species including individual Pd atoms were observed for the sample after the NO treatment. As such highly dispersed Pd species should not form PdO species with definite Pd–O bonds, the Pd–O contribution did not appear for Pd/Al_2O_3. This interpretation would imply that La stabilizes the supported Pd particles. It is worth mentioning here that Cargnello and co-workers have recently reported similar phenomena for Pd/Al_2O_3 catalysts during the catalytic oxidation of methane.[52] The authors have reported that the supported Pd nanoparticles lose activity for the oxidation of methane by decomposition into inactive single atoms.

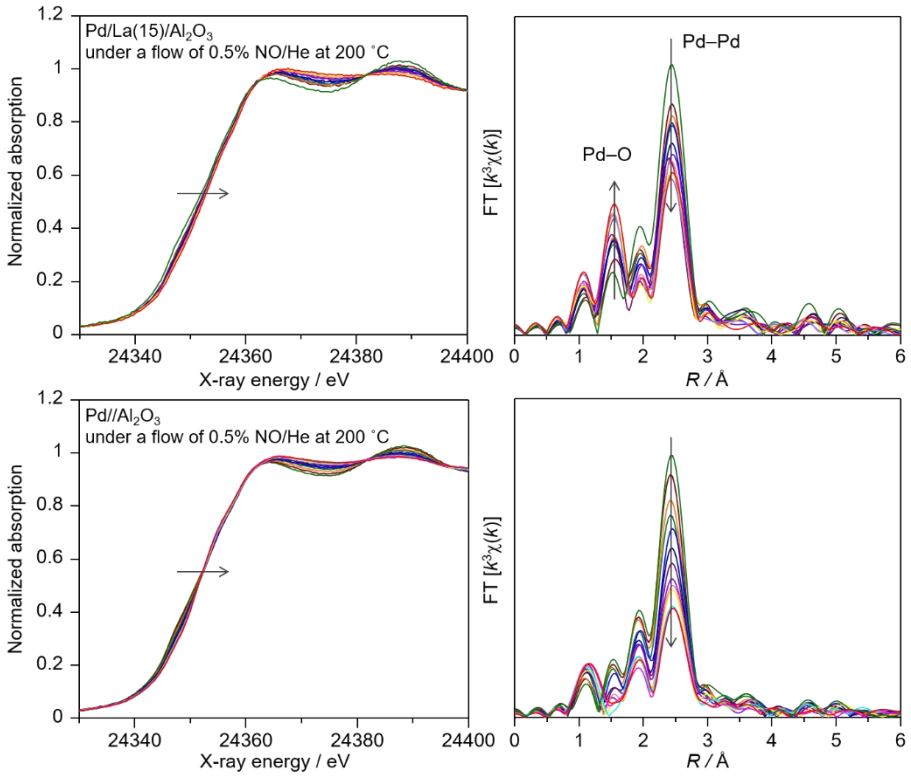

Figure 12. *In situ* Pd K-edge XANES spectra and k^3-weighted EXAFS Fourier transforms of Pd/La(15)/Al_2O_3, performed under a flow of 0.5% NO/He (800 mL/min) at 200 °C after H_2 reduction at 400 °C.

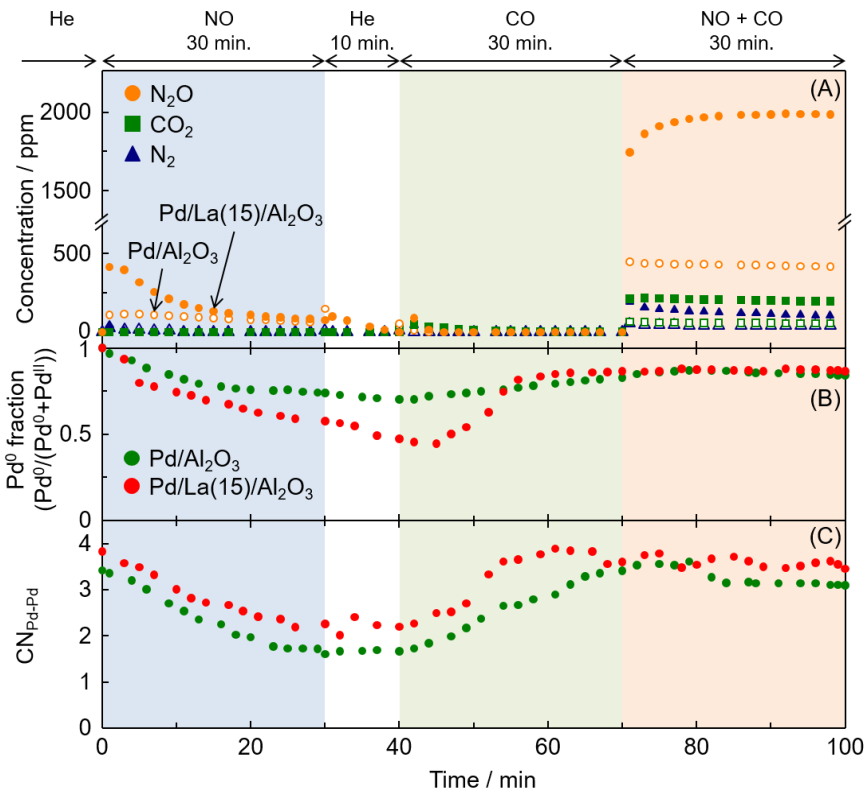

Figure 13. Results of the *in situ* Pd K-edge XAFS measurements. Changes in (A) the product concentrations in the gas phase, (B) fraction of Pd^0, and (C) $CN_{Pd–Pd}$ under a flow of NO, CO, and NO+CO at 200 °C.

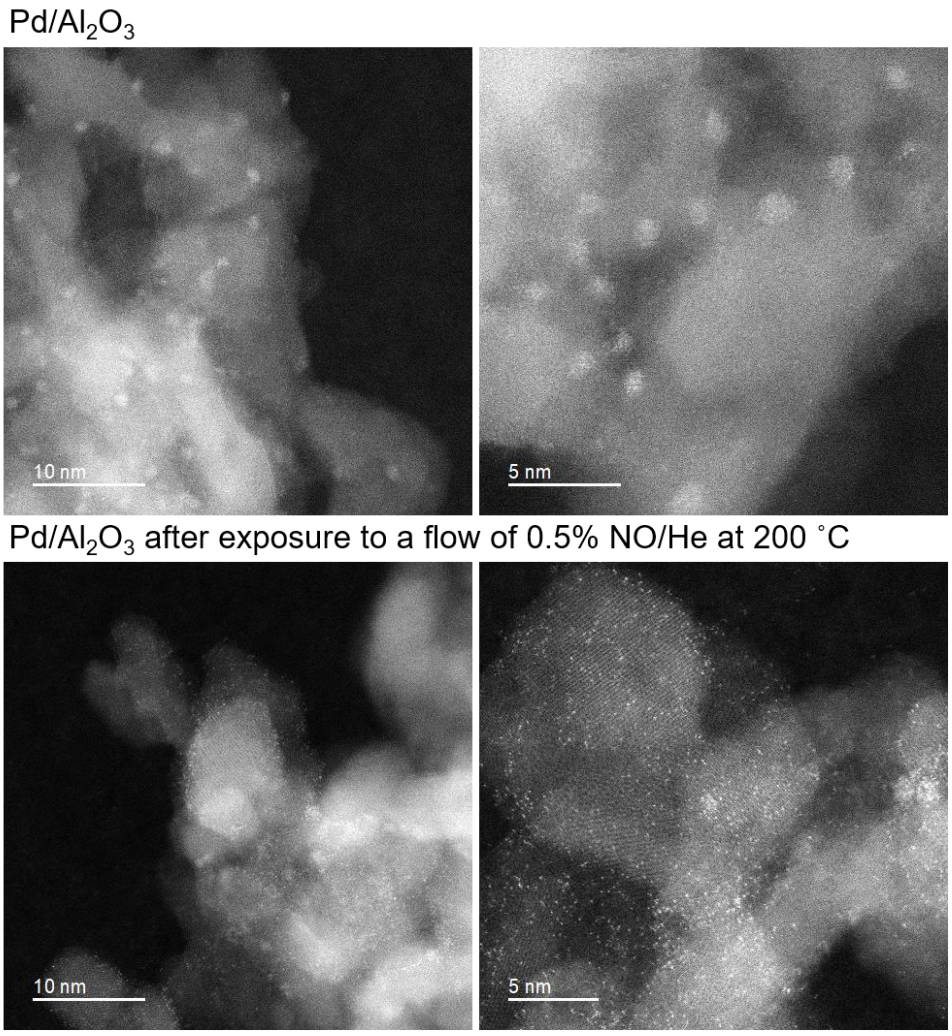

Figure 14. HAADF-STEM images of Pd/Al_2O_3 before and after exposure to a flow of 0.5% NO/He at 200 ˚C.

Subsequently, temperature-programmed surface reactions (TPSRs) were conducted in order to gain further insight into the reactivity of $Pd/La(15)/Al_2O_3$ and Pd/Al_2O_3 toward NO (**Figure 15**). After the pretreatment with H_2, the catalyst was exposed to 0.5 % NO/He flow for 10 min at 40 °C. After purging under He for 30 min, the catalyst was then heated to 500 °C in a flow of He (10 °C min^{-1}), and the gas-phase products were monitored by mass spectrometry. Although no obvious signals due to products such as N_2O and N_2 were observed below 100 °C over Pd/Al_2O_3, $Pd/La(15)/Al_2O_3$ produced N_2O even below 100 °C, which corroborates the notion that the presence of La induces higher reactivity of Pd toward NO at lower temperature. **Figure 16** shows the *in situ* IR spectra of species adsorbed on $Pd/La(15)/Al_2O_3$, Pd/Al_2O_3, and $La(15)/Al_2O_3$ after the introduction of NO at 50 °C. Various kinds of adsorbed NO_x species appear in the 1100-1800 cm^{-1} region after the introduction of NO.[27] Specifically, peaks that were attributed to nitrite arise at

ca. 1192 and 1230 cm^{-1}.[27,53] The intensities of these absorption peaks over Pd/La(15)/Al_2O_3 are much higher than those observed over Pd/Al_2O_3, indicating that higher amounts of surface nitrite species are generated over Pd/La(15)/Al_2O_3. Also, these peaks were virtually negligible over La(15)/Al_2O_3, i.e., in the absence of Pd nanoparticles, indicating the importance of the combination of Pd nanoparticles and La(15)/Al_2O_3 as a support. The absorption bands at ca. 1293 cm^{-1} can be assigned to both nitrates and nitrites.[27,53] The bands in the 1300-1650 cm^{-1} region appeared due to the presence of a variety of nitrate species with different adsorption modes.[27,54,55] The bands in the 1600-1800 cm^{-1} region were assigned to free nitrate ions[27,53] and/or to Pd-adsorbed NO.[27,53,56] The combined results of the NO-TPSR and the *in situ* IR spectroscopy suggest that the disproportionation reaction of NO over Pd/La(15)/Al_2O_3 affords nitrous oxide and nitrite even at low temperatures (< 100 ˚C).

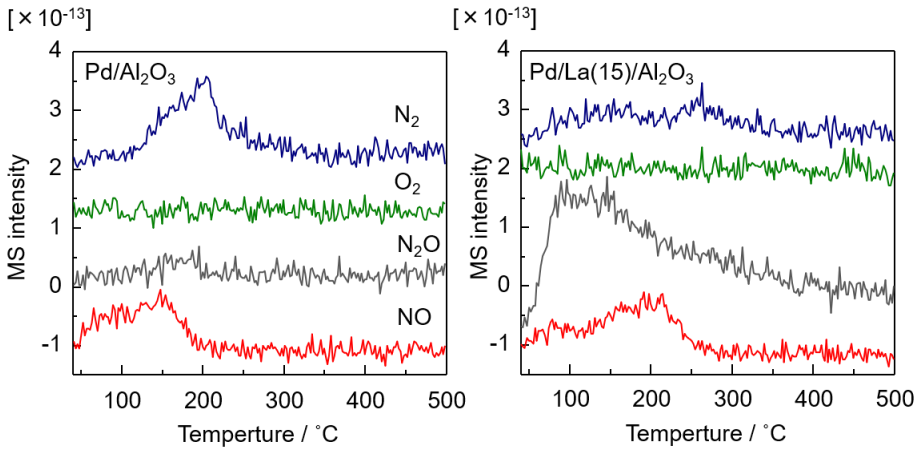

Figure 15. NO TPSR experiments for Pd/La(15)/Al_2O_3 and Pd/Al_2O_3. After the pretreatment with H_2, a catalyst was exposed to 0.5 % NO/He flow for 10 min at 40 °C. After purging in He for 30 min, the catalyst was heated to 500 °C in a flow of He (10 °C min^{-1}).

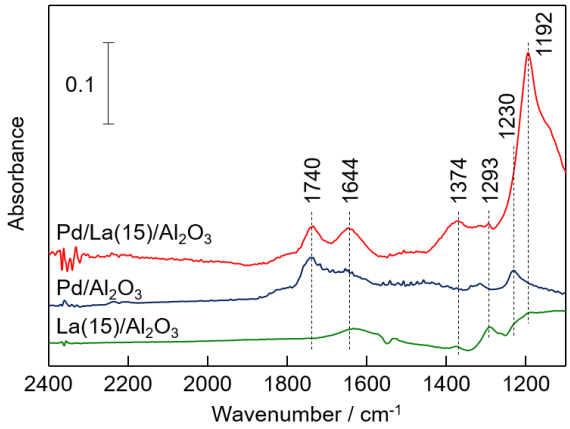

Figure 16. *In situ* IR spectra of species adsorbed on Pd/La(15)/Al_2O_3, Pd/Al_2O_3, and La(15)/Al_2O_3

at 50 ˚C. Spectra were recorded under He flow after the NO feed.

In order to obtain further insights into the NO-activation process over Pd/La(15)/Al_2O_3, NAP-XPS measurements were carried out. For this purpose, a powdered sample of a high-Pd-loaded Pd/La(15)/Al_2O_3 catalyst (Pd loading: 20 wt%), for which the promotional effect of La was confirmed by NO–CO reactions (**Figure 1**), was used for ease of the experiments. It should be noted here that the average Pd particle size for this Pd/La(15)/Al_2O_3 catalyst was determined to be 12.2 nm by a CO-adsorption measurement at -20 ˚C. After the pretreatment, the sample was cooled to 50 °C, and subsequently, NO (100 mTorr) was introduced. **Figure 17** shows an XPS spectrum of the N 1s region for Pd/La(15)/Al_2O_3, measured under an NO atmosphere (100 mTorr). The spectrum of the NO-adsorbed Pd/La(15)/Al_2O_3 contains four peaks at ca. 404, 401, 398, and 393 eV, which can be assigned to the surface-adsorbed nitrite (NO_2^-), molecularly adsorbed NO species (NO_{ad}), atomic nitrogen (N_{ad}), and NO species bound on the Si substrate, respectively.[57,58] The presence of the peak associated with N_{ad} indicates that NO is dissociated over Pd/La(15)/Al_2O_3 even at 50 °C. We also confirmed that the nitrite species is formed in accordance with the results of *in situ* IR study.

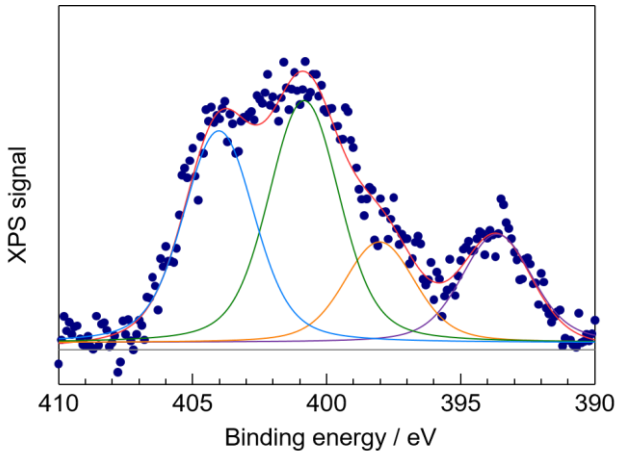

Figure 17. N 1s XPS spectrum of Pd/La(15)/Al_2O_3 (Pd loading: 20 wt%), measured upon exposure to NO (100 mTorr) at 50 ˚C. Navy dots: raw spectrum; red line: sum; blue line: surface-adsorbed nitrite (NO_2^-); green line: molecularly adsorbed NO (NO_{ad}); yellow line: atomic nitrogen (N_{ad}); purple line: NO species bound on the Si substrate; grey line: background.

2.3.3 Three-way catalytic reactions using monolithic honeycomb catalysts

Results of TWC light-off tests over monolithic honeycomb forms of Pd/La(x)/Al_2O_3 (x = 0, 5, 15, 30 wt%) catalysts are shown in **Figure 18**. The catalytic performances were evaluated in light-off mode under 1-Hz perturbated gasses between □ = 0.95 and □ = 1.05 at SV = 100,000 h^{-1}. Gas mixtures used for this test contained 0.6-2.4% CO, 420 ppm C_3H_6, 0.2% H_2, 0.1% NO, 0.6-1.65% O_2, 15% CO_2, 10% H_2O, and N_2 balance. It should be noted here that the honeycomb catalyst was pre-treated under a flow of the aforementioned gas at 400 °C for 0.5 h prior to each catalytic activity test. The conversion of NO, CO, and C_3H_6, which was continuously monitored, showed that the efficiency of Pd/La(15)/Al_2O_3 to remove these gasses was higher than that of Pd/Al_2O_3, indicating that La efficiently promotes the TWC reaction. In addition, the activity of Pd/La(15)/Al_2O_3 was comparable or slightly higher for the conversion of NO than that of the conventional Pd/La(5)/Al_2O_3 catalyst. We also observed that Pd/La(30)/Al_2O_3 exhibited lower activity for the TWC process, which demonstrates that an overloading with La is ineffective. Furthermore, the durability of these catalysts was studied using aged catalysts (for procedural details, see the Experimental Section). This is a highly important investigation, as in practice, catalysts are exposed to very harsh conditions, which they should ideally withstand for a long time. Although their activity decreased by the aging treatment, the aged Pd/La(15)/Al_2O_3 monolithic honeycomb catalyst still exhibited better performance than the other catalysts. This result suggests that Pd/La(15)/Al_2O_3, whose La loading is higher than that for the conventionally used industrial catalysts (La = 3–5wt%) optimized to keep high specific surface area, could potentially serve as a highly effective promoter for TWC processes even after hydrothermal aging.

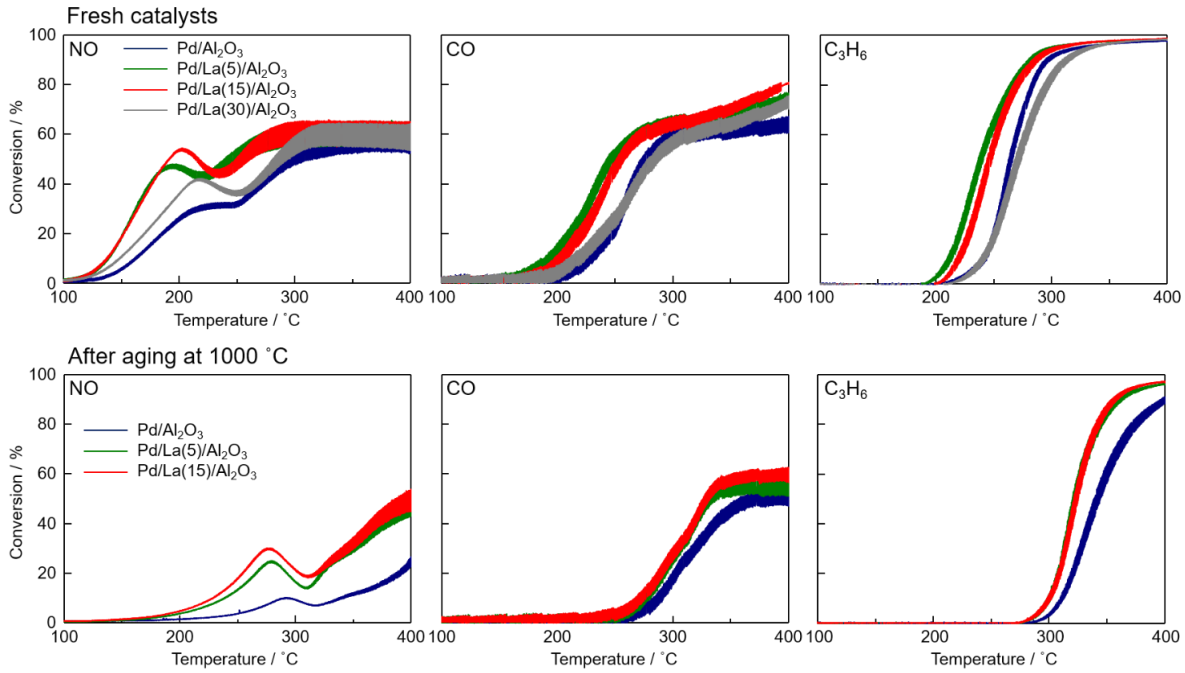

Figure 18. NO, CO, and C_3H_6 conversions for TWC light-off tests over the fresh and aged $Pd/La(x)/Al_2O_3$-coated honeycomb catalysts (x = 0, 5, 15, 30 wt%) under 1-Hz perturbated gasses between λ = 0.95 and λ = 1.05. Heating rate: 25 ˚C/min; Gas: CO (2.4-0.6%), C_3H_6 (420 ppm), H_2 (0.8%), NO (0.1%), O_2 (0.6-1.65%), CO_2 (15%), H_2O (10%), N_2 balance; SV = 100,000 h^{-1}.

The catalysts, after aging at 1000 °C for 4 h, were also characterized by XRD and N_2 adsorption techniques (**Figure 19**). It should be noted that the powdered catalysts were subjected to the aging treatment and analyzed for this purpose. Powder XRD patterns of the $Pd/La(x)/Al_2O_3$ (x = 0, 5, 15, 30 wt%) catalysts after aging at 1000 °C for 4 h (**Figure 19A**) show peaks assignable to $LaAlO_3$ in the diffraction patterns of $Pd/La(15)/Al_2O_3$ and $Pd/La(30)/Al_2O_3$, whereas these peaks were virtually negligible for the conventionally used catalyst $Pd/La(5)/Al_2O_3$. Peaks due to La_2O_3, Pd_3La alloy, or La_4PdO_7 were not seen in any of the XRD patterns.[59,60] S_{BET} values for the aged catalysts were determined from N_2-adsorption isotherms and are summarized in **Figure 19B** together with those of the fresh samples. $Pd/La(5)/Al_2O_3$ retained the highest S_{BET} value after hydrothermal aging; this is consistent with previous studies on the La/Al_2O_3 system, which focused on retaining high surface areas for their designated purpose as TWC supports.

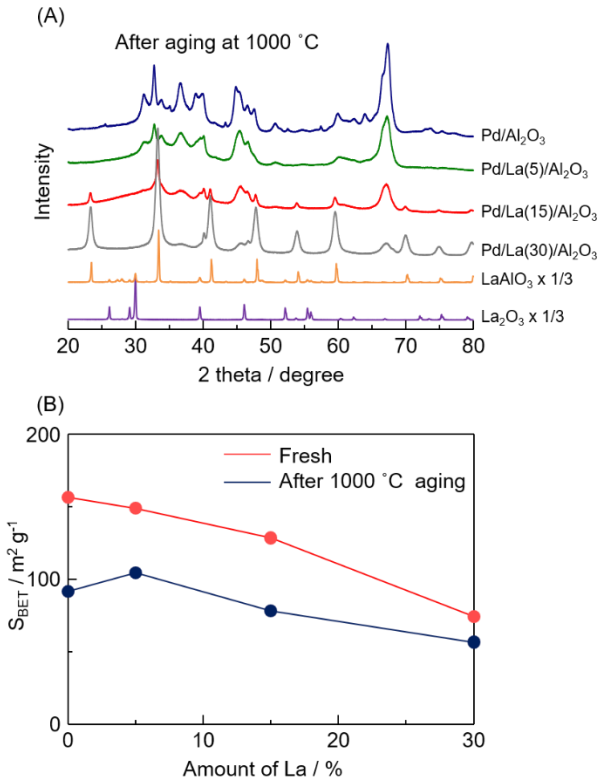

Figure 19. (A) XRD patterns of aged Pd/La(x)/Al_2O_3 (x = 0, 5, 15, 30 wt%). (B) S_{BET} of fresh and aged Pd/La(x)/Al_2O_3(x = 0, 5, 15, 30 wt%). S_{BET} for fresh Pd/Al_2O_3 and Pd/La(5)/Al_2O_3 were taken from our previous report.[27]

La K-edge XAFS measurements were carried out to further examine the local structure of La after hydrothermal aging (**Figure 20**). The results of a curve-fitting analysis of the EXAFS are summarized in **Table 6**. Pd/La(5)/Al_2O_3 revealed only two peaks at ca. 1.2 and 2.0 Å, even after aging. Again, the peak at 2.0 Å is due to the La–O bonds, while the other smaller peak is a side lobe of La–O due to the nonlinearity of their phase shifts.[44] A curve-fitting analysis showed that Pd/La(5)/Al_2O_3 contains only a La–O contribution after hydrothermal aging at 1000 °C. In contrast, La–Al and La–(O)–La contributions, which appear at ca. 2.9 and 3.5 Å in the EXAFS Fourier transforms, respectively, were observed for Pd/La(15)/Al_2O_3 and Pd/La(30)/Al_2O_3 after hydrothermal aging. Curve-fittings with both La–O and La–Al afforded better fits. These results indicate the formation of $LaAlO_3$ for Pd/La(15)/Al_2O_3 and Pd/La(30)/Al_2O_3 after hydrothermal aging at 1000 °C for 4 h. This result is in agreement with those of the aforementioned XRD measurements.

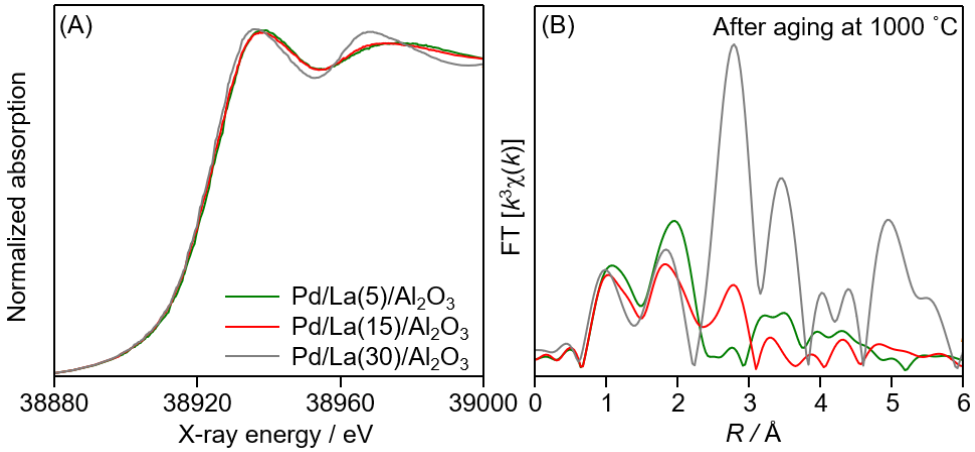

Figure 20. La K-edge (A) XANES spectra and (B) k^3-weighted EXAFS Fourier transforms of the aged samples. All spectra were recorded at room temperature.

Table 6. Curve-fitting analysis of La K-edge EXAFS of the aged Pd/La(x)/Al_2O_3 (x = 5, 15, 30 wt%).

Sample	Shell	CN [a]	*R* (Å) [b]	σ (Å) [c]	R_f (%) [d]
Pd/La(5)/Al_2O_3	La–O	2.6	2.57	0.04	0.1
Pd/La(15)/Al_2O_3	La–O	2.7	2.58	0.11	0.3
	La–Al	1.0	3.08	0.07	
Pd/La(30)/Al_2O_3	La–O	2.3	2.62	0.09	0.7
	La–Al	3.3	3.11	0.05	

[a] Coordination number. [b] Bond distance. [c] Debye-Waller factor. [d] Residual factor.

Figure 21 compares the conversion of NO, CO, and C_3H_6 at 300 °C of the studied honeycomb catalysts in the range λ = 1.05-0.95. The conversions were recorded after keeping each lambda condition for 1 min in order to examine the steady-state catalytic activity under these conditions. The conversion of NO occurred efficiently in the rich region (0.95 ≤ □ < 1), where excess reducing gasses are present. We observed that Pd/La(15)/Al_2O_3 exhibited high NO-removal efficiency and its activity is comparable to Pd/La(5)/Al_2O_3 throughout the □ range tested in this investigation. On the other hand, the conversion of CO and C_3H_6 reached more than 80% in the lean region (1 < □ ≤ 1.05), where oxidation processes are preferred in the presence of excess O_2. Pd/La(15)/Al_2O_3 and Pd/La(5)/Al_2O_3 showed higher activity than Pd/La(30)/Al_2O_3 and Pd/Al_2O_3, which is consistent with the aforementioned investigations and demonstrates that i) La promotes the TWC process and that ii) an overload of La has a negative effect. It should also be noted here that Pd/La(5)/Al_2O_3 exhibited a slightly higher catalytic activity than Pd/La(15)/Al_2O_3 for the conversion of CO and C_3H_6.

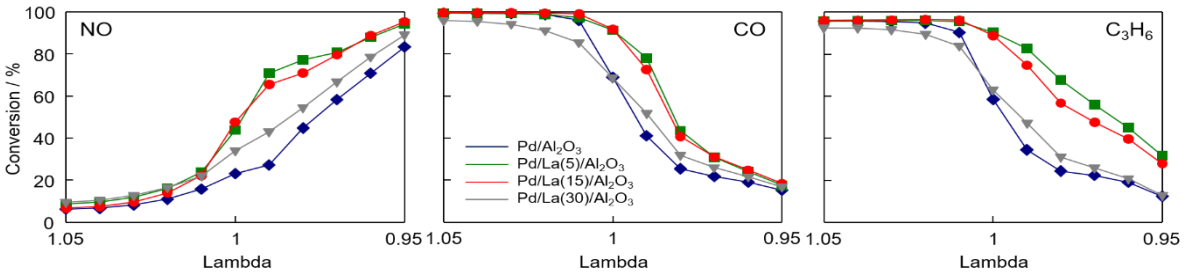

Figure 21. Lambda sweep performance for the conversion of NO, CO, and C_3H_6 on the honeycomb model catalysts formed by coated Pd and alumina support materials (λ = 1.05-0.95). Conversions were recorded after retaining each lambda condition for 1 min.

Under realistic TWC conditions, the λ value fluctuates between low (rich) and high (lean) values.[61] It is thus highly important that the TWC catalysts can operate and efficiently remove the exhaust gases under such transient conditions and are able to follow the rapid changes of the λ conditions. Therefore, we investigated the λ-switching performance for NO, CO, and C_3H_6 on the honeycomb model catalysts (**Figure 22**). We started the investigation under lean conditions (λ = 1.05), before we switched to rich conditions, and finally changed again to lean conditions. It should be noted here that there are detection delays, which are due to the experimental setup (1.0 s for NO and 3.2 s for CO relative to C_3H_6). During the first change from lean to rich, the NO conversion over Pd/Al_2O_3 occurred faster than over the other catalysts, including $Pd/La(15)/Al_2O_3$. In contrast, for the subsequent change from rich to lean, a high NO conversion was retained the longest over $Pd/La(15)/Al_2O_3$. In addition, the NO conversion over Pd/Al_2O_3 gradually decreased under rich conditions, suggesting that CO acts as a poison for Pd as observed for the NO–CO reaction. These results indicate that the promotional effect of La i) is particularly effective under rich conditions, and ii) can be ineffective under lean conditions as Pd on $La(15)/Al_2O_3$ is more difficult to reduce than Pd on Al_2O_3 without La.

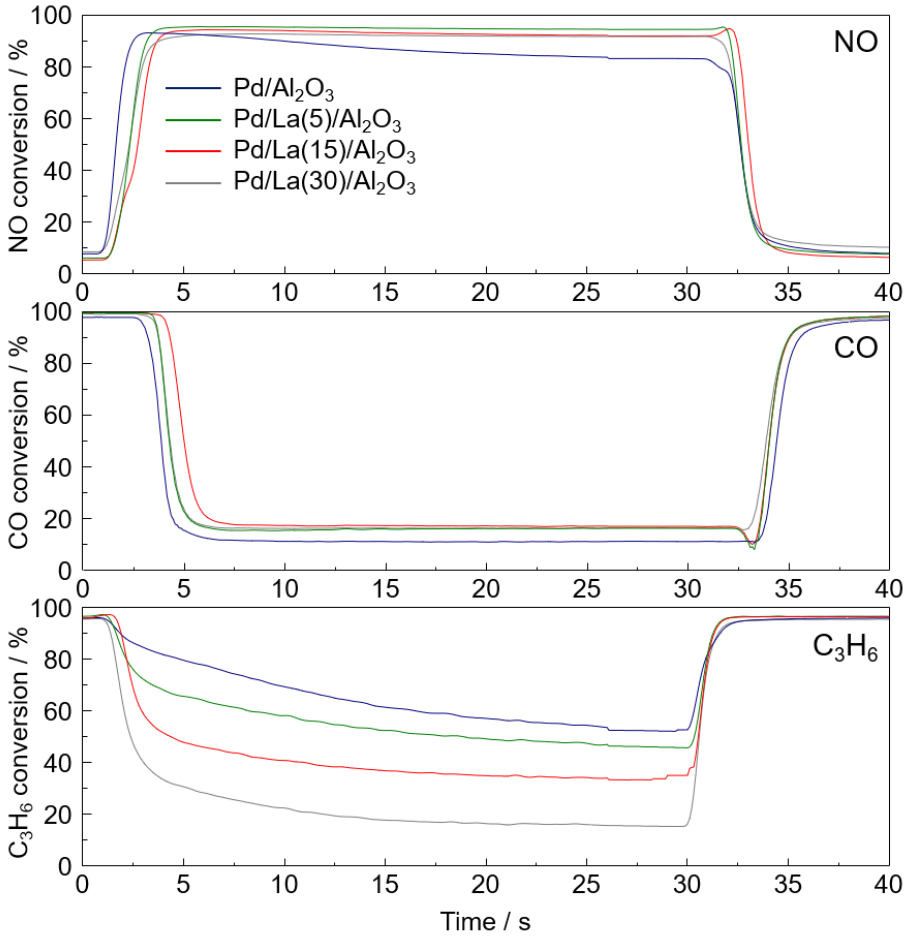

Figure 22. Lambda-switching performance for NO, CO, and C_3H_6 on the honeycomb model catalysts formed by coated Pd and alumina support materials upon lambda jumps (λ = 1.05-0.95). The time variation of the conversion rate was recorded with a data collection rate of 10 Hz. It should be noted here that there are detection delays due to the experimental setup (1.0 s for NO and 3.2 s for CO relative to C_3H_6).

Finally, practical tests using a commercial vehicle were carried out in order to confirm the applicability and potentially superior performance of Pd/La(15)/Al_2O_3 relative to the conventionally used catalyst Pd/La(5)/Al_2O_3. For this purpose, Pd-Rh three-way catalysts with a double-layered structure containing either Pd/La(15)/Al_2O_3 or Pd/La(5)/Al_2O_3 were prepared and bench aged for 75 h using a 1.8-L gasoline engine with a peak temperature of 950 °C. Subsequently, the catalysts were mounted in a commercial vehicle with a 1.5-L engine and evaluated according to the vehicle emission test of the LA-4 driving cycle. **Figure 23** shows the accumulated and transient emissions of NO_x, CO, and the total HC monitored at the tailpipe, as well as the AFR, and the catalyst-bed temperature together with the associated vehicle speed. **Figure 24** shows the corresponding transient emissions during the selected period (700-1000 s) for clarity. We observed that NO_x is

mainly emitted during the acceleration of the vehicle for both practical tests. On the other hand, CO and HC are emitted during the deceleration of the vehicle, i.e., under AFR-rich conditions (AFR < 14.6) just after an excessive intake of air (fuel cut). Compared to the driving test using the conventional catalyst (Pd/La(5)/Al_2O_3; green line), the catalytic system including Pd/La(15)/Al_2O_3 (red line) shows improved conversions for all exhaust gasses. In particular, the conversion of NO_x was significantly improved by the incorporation of the increased amount of La.

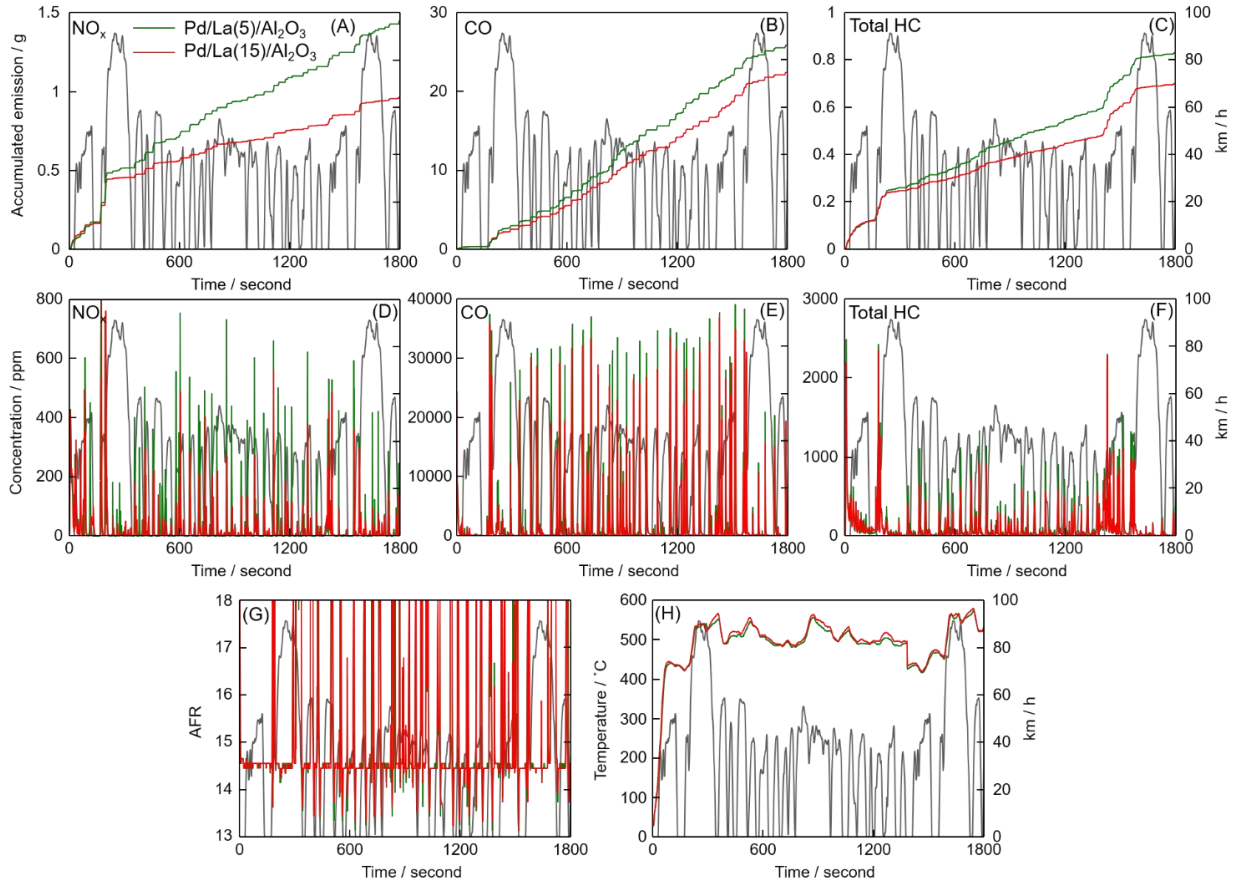

Figure 23. Accumulated emission of (A) NO_x, (B) CO, and (C) the total HC, monitored at the tailpipe during a LA-4 driving cycle (city cycle of US Federal and California) with a vehicle containing a 1.5-L gasoline engine and a Pd-Rh three-way catalysts with Pd/La(5)/Al_2O_3 (green) or Pd/La(15)/Al_2O_3 (red). Corresponding transient emission of (D) NO_x, (E) CO, and (F) the total HC. (G) AFR, and (H) catalyst bed temperature.

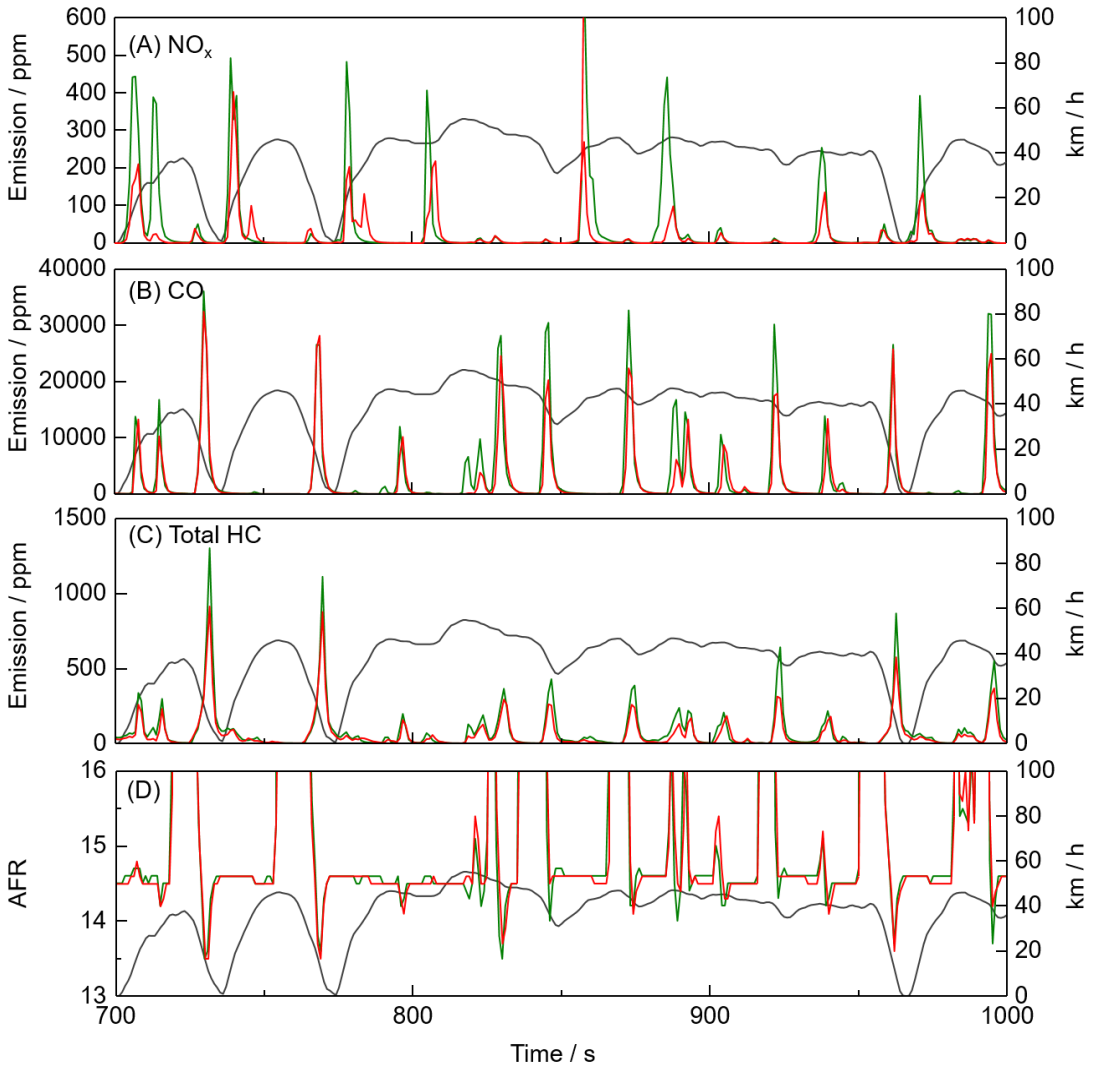

Figure 24. Transient emission of (A) NO_x, (B) CO, and (C) the total HC together with (D) AFR, monitored at the tailpipe during a LA-4 driving cycle (city cycle of US Federal and California) using a vehicle with a 1.5-L gasoline engine and a Pd-Rh three-way catalyst containing Pd/La(5)/Al_2O_3 (green) or Pd/La(15)/Al_2O_3 (red).

2.4 Conclusions

We have investigated the promotional effect of La in Pd/La(x)/Al_2O_3 (x = 0, 5, 15, 30wt%) catalysts for TWC reactions using a combination of kinetic and spectroscopic measurements as well as theoretical calculations. The obtained results show that the supported metallic Pd particles on La-containing Al_2O_3 supports are more electron deficient than those on pristine Al_2O_3, which results in a higher reactivity toward NO and a suppression of the poisoning effect of CO. As a result, a higher NO conversion efficiency is attained over these Pd/La/Al_2O_3 catalysts. In addition to investigations using powdered catalyst samples, we prepared and examined monolithic honeycomb catalyst samples in TWC reactions, which revealed a superior DeNO_x performance for Pd/La/Al_2O_3 compared to Pd/Al_2O_3. Moreover, we investigated the optimal La loading for TWC reactions and found that a loading of 15 wt%, which is higher than that for the conventionally used industrial catalysts Pd/La(5)/Al_2O_3 (La = 5wt%) optimized to keep the high specific surface area, is more effective for the TWC process. As this study is a collaborative academic and industrial effort, we have also performed a practical test using a commercial vehicle. The results show that the catalytic system containing Pd/La(15)/Al_2O_3 exhibits improved conversions for the exhaust gasses including NO_x, CO, and HC compared to the one containing Pd/La(5)/Al_2O_3. Our results thus indicate that the loading of La in Pd/La/Al_2O_3 catalysts should be tuned depending on the application systems. This tuning should consider a balance between the support stability in terms of the surface area and the promotional effect in the TWC process.

References

(1) Wang, J.; Chen, H.; Hu, Z.; Yao, M.; Li, Y. A Review on the Pd-Based Three-Way Catalyst. *Catal. Rev.* **2015**, *57*, 79–144.

(2) Matsumoto, S. Recent Advances in Automobile Exhaust Catalysts. *Catal. Today* **2004**, *90*, 183–190.

(3) Shelef, M.; McCabe, R. W. Twenty-Five Years after Introduction of Automotive Catalysts: What Next? *Catal. Today* **2000**, *62*, 35–50.

(4) Yamamoto, T.; Tanaka, T.; Kuma, R.; Suzuki, S.; Amano, F.; Shimooka, Y.; Kohno, Y.; Funabiki, T.; Yoshida, S. NO Reduction with CO in the Presence of O_2 over Al_2O_3-Supported and Cu-Based Catalysts. *Phys. Chem. Chem. Phys.* **2002**, *4*, 2449–2458.

(5) Yoshida, H.; Yamashita, N.; Ijichi, S.; Okabe, Y.; Misumi, S.; Hinokuma, S.; Machida, M. A Thermally Stable Cr-Cu Nanostructure Embedded in the CeO_2 Surface as a Substitute for Platinum-Group Metal Catalysts. *ACS Catal.* **2015**, *5*, 6738−6747.

(6) Satsuma, A.; Ueda, K.; Ito, Y.; Ang, C. A.; Ohyama, J. Automotive Three Way Catalytic Activity of Fe–Ni/Ceria. *Chem. Lett.* **2015**, *44*, 703–705.

(7) Ueda, K.; Ohyama, J.; Satsuma, A. Investigation of Reaction Mechanism of NO-C_3H_6-CO-O_2 Reaction over $NiFe_2O_4$ Catalyst. *ACS Omega* **2017**, *2*, 3135−3143.

(8) Koga, H.; Tada, K.; Hayashi, A.; Ato, Y.; Okumura, M. High NO_x Reduction Activity of an Ultrathin Zirconia Film Covering a Cu Surface: A DFT Study. *Catal. Letters* **2017**, *147*, 1827–1833.

(9) Hosokawa, S.; Matsuki, K.; Tamaru, K.; Oshino, Y.; Aritani, H.; Asakura, H.; Teramura, K.; Tanaka, T. Selective Reduction of NO over Cu/Al_2O_3: Enhanced Catalytic Activity by Infinitesimal Loading of Rh on Cu/Al_2O_3. *Mol. Catal.* **2017**, *442*, 74–82.

(10) Iwachido, K.; Onodera, T.; Miyamoto, K. NO_x Trap Catalyst Technologies and Exhaust Emission Control to Expand Lean Burn Operation for Gasoline Engine Application. *Rev. Automot. Eng.* **2010**, 127–132.

(11) Machida, M.; Ueno, M.; Omura, T.; Kurusu, S.; Hinokuma, S.; Nanba, T.; Shinozaki, O.; Furutani, H. CeO_2-Grafted Mn-Fe Oxide Composites as Alternative Oxygen-Storage Materials for Three-Way Catalysts: Laboratory and Chassis Dynamometer Tests. *Ind. Eng. Chem. Res.* **2017**, *56*, 3184−3193.

(12) Suarez-Bertoa, R.; Astorga, C. Impact of Cold Temperature on Euro 6 Passenger Car Emissions. *Environ. Pollut.* **2018**, *234*, 318–329.

(13) Li, L.; Zhang, N.; Huang, X.; Liu, Y.; Li, Y.; Zhang, G.; Song, L.; He, H. Hydrothermal Stability of Core-Shell $Pd@Ce_{0.5}Zr_{0.5}O_2/Al_2O_3$ Catalyst for Automobile Three-Way Reaction. *ACS Catal.* **2018**, *8*, 3222−3231.

(14) Gandhi, H. S.; Graham, G. W.; McCabe, R. W. Automotive Exhaust Catalysis. *J. Catal.* **2003**, *216*, 433–442.

(15) Kang, S. B.; Nam, I. S.; Cho, B. K.; Kim, C. H.; Oh, S. H. Kinetic Model for Modern Double-Layered Pd/Rh TWC as a Function of Metal Loadings and Mileage. *Chem. Eng. J.* **2015**, *278*, 328–338.

(16) Nishio, Y.; Ozawa, M. Thermal Stability and Microstructural Change of Lanthanum Modified Alumina Catalytic Support. *J. Ceram. Soc. Japan* **2007**, *115*, 633–636.

(17) Muraki, H.; Shinjoh, H.; Fujitani, Y. Effect of Lanthanum on the No Reduction over Palladium Catalysts. *Appl. Catal.* **1986**, *22*, 325–335.

(18) Muraki, H.; Shinjoh, H.; Sobukawa, H.; Yokota, K.; Fujitani, Y. Palladium-Lanthanum Catalysts for Automotive Emission Control. *Ind. Eng. Chem. Prod. Res. Dev.* **1986**, *25*, 202–208.

(19) Muraki, H.; Yokota, K.; Fujitani, Y. Nitric Oxide Reduction Performance of Automotive Palladium Catalysts. *Appl. Catal.* **1989**, *48*, 93–105.

(20) Shinjoh, H. Rare Earth Metals for Automotive Exhaust Catalysts. *J. Alloys Compd.* **2006**, *408–412*, 1061–1064.

(21) Shinjoh, H.; Isomura, N.; Sobukawa, H.; Sugiura, M. Effect of Alkaline Addition on Hydrocarbon Oxidation Activities of Palladium Three-Way Catalyst. *Stud. Surf. Sci. Catal.* **1998**, *116*, 83–91.

(22) Kobayashi, T.; Yamada, T.; Kayano, K. Effect of Basic Metal Additives on NO x Reduction Property of Pd-Based Three-Way Catalyst. *Appl. Catal. B Environ.* **2001**, *30*, 287–292.
(23) Graham, G. W. NO Chemisorption on Supported Pd. *Surf. Sci.* **1992**, *268*, 25–35.
(24) David Logan, A.; Graham, G. W. NO Chemisorption on Pd(100) with Ultra-Thin Overlayers of Oxidized La and Al. *Surf. Sci. Lett.* **1992**, *277*, L47–L51.
(25) Sekiba, T.; Kimura, S.; Yamamoto, H.; Okada, A. Development of Automotive Palladium Three-Way Catalysts. *Catal. Today* **1994**, *22*, 113–126.
(26) Skoglundh, M.; Johansson, H.; Löwendahl, L.; Jansson, K.; Dahl, L.; Hirschauer, B. Cobalt-Promoted Palladium as a Three-Way Catalyst. *Appl. Catal. B Environ.* **1996**, *7*, 299–319.
(27) Toyao, T.; Jing, Y.; Kon, K.; Hayama, T.; Nagaoka, S.; Shimizu, K. Catalytic NO–CO Reactions over La-Al_2O_3 Supported Pd: Promotion Effect of La. *Chem. Lett.* **2018**, *47*, 1036–1039.
(28) Valden, M.; Keiski, R. L.; Xiang, N.; Pere, J.; Aaltonen, J.; Pessa, M.; Maunula, T.; Savimäki, A.; Lahti, A.; Härkönen, M. Reactivity of Pd/Al_2O_3, Pd/La_2O_3-Al_2O_3 and Pd/$LaAlO_3$ Catalysts for the Reduction of NO by CO: CO and NO Adsorption. *J. Catal.* **1996**, *161*, 614–625.
(29) Takagi, N.; Ishimura, K.; Miura, H.; Shishido, T.; Fukuda, R.; Ehara, M.; Sakaki, S. Catalysis of Cu Cluster for NO Reduction by CO: Theoretical Insight into the Reaction Mechanism. *ACS Omega* **2019**, *4*, 2596–2609.
(30) Toyoshima, A.; Kikuchi, T.; Tanaka, H.; Mase, K.; Amemiya, K.; Ozawa, K. Performance of PF BL-13A, a Vacuum Ultraviolet and Soft X-Ray Undulator Beamline for Studying Organic Thin Films Adsorbed on Surfaces. *J. Phys. Conf. Ser.* **2013**, *425*, 152019−152022.
(31) Aderhold, D.; Haynes, A. G.; Spencer, M. L. W.; Winterborn, D. J. W. Monolith Coating Apparatus and Method Therefor. *US Pat.* **2013**, *US6599570B*.
(32) Kresse, G.; Furthmüller, J. Efficient Iterative Schemes for Ab Initio Total-Energy Calculations Using a Plane-Wave Basis Set. *Phys. Rev. B - Condens. Matter Mater. Phys.* **1996**, *54*, 11169–11186.
(33) Kresse, G.; Furthmüller, J. Efficiency of Ab-Initio Total Energy Calculations for Metals and Semiconductors Using a Plane-Wave Basis Set. *Comput. Mater. Sci.* **1996**, *6*, 15–50.
(34) Blöchl, P. E. Projector Augmented-Wave Method. *Phys. Rev. B* **1994**, *50*, 17953–17979.
(35) Perdew, J. P.; Burke, K.; Ernzerhof, M. Generalized Gradient Approximation Made Simple. *Phys. Rev. Lett.* **1996**, *77*, 3865–3868.
(36) Grimme, S.; Antony, J.; Ehrlich, S.; Krieg, H. A Consistent and Accurate Ab Initio Parametrization of Density Functional Dispersion Correction (DFT-D) for the 94 Elements H-Pu. *J. Chem. Phys.* **2010**, *132*, 154104.
(37) Grimme, S.; Ehrlich, S.; Goerigk, L. Effect of the Damping Function in Dispersion Corrected Density Functional Theory. *J. Comput. Chem.* **2011**, *32*, 1456–1465.
(38) Hu, C. H.; Chizallet, C.; Mager-Maury, C.; Corral-Valero, M.; Sautet, P.; Toulhoat, H.; Raybaud, P. Modulation of Catalyst Particle Structure upon Support Hydroxylation: Ab Initio Insights into Pd_{13} and Pt_{13}/γ-Al_2O_3. *J. Catal.* **2010**, *274*, 99–110.
(39) Kwak, J. H.; Hu, J.; Lukaski, A.; Kim, D. H.; Szanyi, J.; Peden, C. H. F. Role of Pentacoordinated Al^{3+} Ions in the High Temperature Phase Transformation of γ-Al_2O_3. *J. Phys. Chem. C* **2008**, *112*, 9486–9492.
(40) Düvel, A.; Romanova, E.; Sharifi, M.; Freude, D.; Wark, M.; Heitjans, P.; Wilkening, M. Mechanically Induced Phase Transformation of γ-Al_2O_3 into α-Al_2O_3. Access to Structurally Disordered γ-Al_2O_3 with a Controllable Amount of Pentacoordinated Al Sites. *J. Phys. Chem. C* **2011**, *115*, 22770–22780.
(41) Wischert, R.; Florian, P.; Copéret, C.; Massiot, D.; Sautet, P. Visibility of Al Surface Sites of γ-Alumina: A Combined Computational and Experimental Point of View. *J. Phys. Chem. C* **2014**, *118*, 15292−15299.
(42) Boukha, Z.; Fitian, L.; López-Haro, M.; Mora, M.; Ruiz, J. R.; Jiménez-Sanchidrián, C.; Blanco, G.; Calvino, J. J.; Cifredo, G. A.; Trasobares, S.; Bernal, S. Influence of the Calcination Temperature

on the Nano-Structural Properties, Surface Basicity, and Catalytic Behavior of Alumina-Supported Lanthana Samples. *J. Catal.* **2010**, *272*, 121–130.

(43) Ferrandon, M.; Björnbom, E. Hydrothermal Stabilization by Lanthanum of Mixed Metal Oxides and Noble Metal Catalysts for Volatile Organic Compound Removal. *J. Catal.* **2001**, *200*, 148–159.

(44) Yamamoto, T.; Hatsui, T.; Matsuyama, T.; Tanaka, T.; Funabiki, T. Structures and Acid-Base Properties of La/Al_2O_3- Role of La Addition to Enhance Thermal Stability of γ-Al_2O_3. *Chem. Mater.* **2003**, *15*, 4830–4840.

(45) Wang, S.; Borisevich, A. Y.; Rashkeev, S. N.; Glazoff, M. V.; Sohlberg, K.; Pennycook, S. J.; Pantelides, S. T. Dopants Adsorbed as Single Atoms Prevent Degradation of Catalysts. *Nat. Mater.* **2004**, *3*, 143–146.

(46) Peterson, E. J.; DeLaRiva, A. T.; Lin, S.; Johnson, R. S.; Guo, H.; Miller, J. T.; Kwak, J. H.; Peden, C. H. F.; Kiefer, B.; Allard, L. F.; Ribeiro, F. H.; Datye, A. K. Low-Temperature Carbon Monoxide Oxidation Catalysed by Regenerable Atomically Dispersed Palladium on Alumina. *Nat. Commun.* **2014**, *5*, 4885.

(47) Wang, H.; Dong, J.; Allard, L. F.; Lee, S.; Oh, S.; Wang, J.; Li, W.; Shen, M.; Yang, M. Single-Site Pt/La-Al_2O_3 Stabilized by Barium as an Active and Stable Catalyst in Purifying CO and C_3H_6 Emissions. *Appl. Catal. B Environ.* **2019**, *244*, 327–339.

(48) Berlowitz, P. J.; Peden, C. H. F.; Goodman, D. W. Kinetics of CO Oxidation on Single-Crystal Pd, Pt, and Ir. *J. Phys. Chem.* **1988**, *92*, 5213–5221.

(49) Gajdoš, M.; Eichler, A.; Hafner, J. CO Adsorption on Close-Packed Transition and Noble Metal Surfaces: Trends from Ab Initio Calculations. *J. Phys. Condens. Matter* **2004**, *16*, 1141–1164.

(50) Zeinalipour-Yazdi, C. D.; Cooksy, A. L.; Efstathiou, A. M. CO Adsorption on Transition Metal Clusters: Trends from Density Functional Theory. *Surf. Sci.* **2008**, *602*, 1858–1862.

(51) Asakura, H.; Hosokawa, S.; Ina, T.; Kato, K.; Nitta, K.; Uera, K.; Uruga, T.; Miura, H.; Shishido, T.; Ohyama, J.; Satsuma, A.; Sato, K.; Yamamoto, A.; Hinokuma, S.; Yoshida, H.; Machida, M.; Yamazoe, S.; Tsukuda, T.; Teramura, K.; Tanaka, T. Dynamic Behavior of Rh Species in Rh/Al_2O_3 Model Catalyst during Three-Way Catalytic Reaction: An Operando X-Ray Absorption Spectroscopy Study. *J. Am. Chem. Soc.* **2018**, *140*, 176–184.

(52) Goodman, E. D.; Johnston-Peck, A. C.; Dietze, E. M.; Wrasman, C. J.; Hoffman, A. S.; Abild-Pedersen, F.; Bare, S. R.; Plessow, P. N.; Cargnello, M. Catalyst Deactivation via Decomposition into Single Atoms and the Role of Metal Loading. *Nat. Catal.* **2019**, *2*, 748–755.

(53) Pieta, I. S.; García-Diéguez, M.; Herrera, C.; Larrubia, M. A.; Alemany, L. J. In Situ DRIFT-TRM Study of Simultaneous NOx and Soot Removal over Pt-Ba and Pt-K NSR Catalysts. *J. Catal.* **2010**, *270*, 256–267.

(54) Chi, Y.; Chuang, S. S. C. Infrared and TPD Studies of Nitrates Adsorbed on Tb_4O_7, La_2O_3, BaO, and MgO/g-Al_2O_3. *J. Phys. Chem. B* **2000**, *104*, 4673–4683.

(55) Lietti, L.; Daturi, M.; Blasin-Aubé, V.; Ghiotti, G.; Prinetto, F.; Forzatti, P. Relevance of the Nitrite Route in the NO_x Adsorption Mechanism over Pt-Ba/Al_2O_3 NO_x Storage Reduction Catalysts Investigated by Using Operando FTIR Spectroscopy. *ChemCatChem* **2012**, *4*, 55–58.

(56) Haneda, M.; Kintaichi, Y.; Nakamura, I.; Fujitani, T.; Hamada, H. Effect of Surface Structure of Supported Palladium Catalysts on the Activity for Direct Decomposition of Nitrogen Monoxide. *J. Catal.* **2003**, *218*, 405–410.

(57) Polzonetti, G.; Alnot, P.; Brundle, C. R. The Adsorption and Reactions of NO_2 on the Ag(111) Surface. I. XPS/UPS and Annealing Studies between 90 and 300 K. *Surf. Sci.* **1990**, *238*, 226–236.

(58) Ueda, K.; Isegawa, K.; Amemiya, K.; Mase, K.; Kondoh, H. Operando NAP-XPS Observation and Kinetics Analysis of NO Reduction over Rh(111) Surface: Characterization of Active Surface and Reactive Species. *ACS Catal.* **2018**, *8*, 11663−11670.

(59) Kim, D.; Woo, S.; Lee, J.; Yang, O. The Role of Lanthanum Oxide on Pd-only Three-way Catalysts Prepared by Co-impregnation and Sequential Impregnation Methods. *Catal. Letters* **2000**, *70*, 35–

41.
(60) Takayama, A.; Kurokawa, T.; Nakayama, H.; Katoh, T.; Nagata, M. Effect of Ba and La Additives to the Pd Layer of a Pd:Rh TWC. *SAE Tech. Pap.* **2017**, 2017-01–0922.
(61) Farrauto, R. J.; Heck, R. M. Catalytic Converters: State of the Art and Perspectives. *Catal. Today* **1999**, *51*, 351–360.

Chapter 3

Mechanistic Study on Three-Way Catalysis over $Pd/La/Al_2O_3$ with high La Loading

3.1 Introduction

Three-way catalysis (TWC) is an effective method for the removal of nitrogen oxides (NO_x), carbon monoxide (CO), and hydrocarbons (HCs) from automotive emissions.[1–3] Numerous studies have focused on the development of high-performing catalysts that contain platinum group metals (PGMs), such as Pd, Pt, and Rh, and other abundant transition metals for the TWC process.[4–11] Although PGM-free catalysts are highly desirable for the TWC process, owing to the high cost and limited resources of PGMs, real-life applications require the use of PGMs to meet strict regulations for engine emissions.[6,12–14] Most three-way catalysts now contain a combination of Rh and Pd.[15,16] Therefore, the development of effective catalyst supports is highly required to enhance the catalytic performance of PGMs (Rh and Pd).[17–19]

Much effort has been devoted to modifying catalyst supports to maximize the performance of Pd and Rh. Among these methods, the addition of La to Al_2O_3 to yield La/Al_2O_3 is widely used because it improves thermal stability and mechanical strength.[20,21] However, the role of La in $Pd/La/Al_2O_3$ in the TWC reaction has not been clearly understood.[22–24] Previously, we investigated the role of La in $Pd/La/Al_2O_3$ catalysts for $DeNO_x$ processes.[25,26] The results showed that $Pd/La/Al_2O_3$ was more effective in removing NO_x than Pd/Al_2O_3. The metallic Pd species loaded on La/Al_2O_3 were observed to be more electron-deficient than those on pristine Al_2O_3, which led to suppression in CO poisoning during the $DeNO_x$ reaction. In addition, $Pd/La(15)/Al_2O_3$, with an increased La loading, was more efficient than the conventionally used $Pd/La(3–5)/Al_2O_3$ in removing NO_x in the reactions tested, including the vehicle emission test.

As a continuation of our previous studies on $Pd/La/Al_2O_3$ with high La loading, in the present study, we further investigated the origin of the promotional effect of La and studied the effect of La on the catalytic durability. The obtained results showed that the conversion of NO was more efficiently catalyzed by $Pd/La/Al_2O_3$ via a disproportionation reaction pathway to form gas-phase N_2O and nitrite surface species. The aged $Pd/La(15)/Al_2O_3$ catalyst, which has a lower specific surface area than the conventionally employed $Pd/La(5)/Al_2O_3$, is more effective for stabilizing the Pd dispersion and retaining better catalytic activity after aging.

3.2 Experimental method

3.2.1 Preparation of materials and catalysts

La was loaded onto γ-Al_2O_3 using $La(NO_3)_3$ according to a previously reported procedure,[25,26] and the prepared supports were designated as La(x)/Al_2O_3 (x = 5, 15, and 30 wt%). The corresponding supported Pd (1 wt%) catalysts were prepared by impregnation using aqueous $Pd(NH_3)_2(NO_2)_2$ as a precursor, followed by calcination in air at 500 °C for 3 h and H_2 reduction at 500 °C for 0.5 h. The samples pretreated with H_2 were employed for characterizations unless otherwise noted. Prior to each catalytic and *in situ*/*operando* spectroscopic experiment, the samples were reduced again under 10% H_2/He (100 mL min^{-1}) gas flow at 400 °C for 0.5 h.

Monolithic honeycomb catalysts were prepared by coating a water slurry containing the calcined catalyst powders and an inorganic binder onto a cordierite honeycomb (25.4 mmφ × 50 mm, 400 cells/in^2), followed by drying at 120 °C for 1 h and subsequent calcination at 600 °C for 2 h.

The honeycomb catalysts were subjected to an aging treatment at 800 °C for 4 h under hydrothermal redox conditions. The treatment was performed with perturbation cycles of 180 s (3% H_2, 3% CO, 10% H_2O, and N_2 balance), 10 s (10% H_2O and N_2 balance), 180 s (3% O_2, 10% H_2O, and N_2 balance), and 10 s for rich, stoichiometric, lean, and another stoichiometric atmosphere, respectively. The total flow rate of the feeding gas was 3 L/min (space velocity = 7200 h^{-1}).

3.2.2 Catalyst characterization

X-ray diffraction (XRD) studies were conducted using a Rigaku Miniflex. N_2 adsorption was conducted at 77 K on an AUTOSORB 6AG (Yuasa Ionics Co.). High-angle annular dark-field scanning transmission electron microscopy (HAADF-STEM) images were obtained using a JEM-ARM200F microscope (JEOL), operating at 200 kV. The particle size of Pd was determined based on CO-chemisorption at −20 °C using BELCAT (MicrotracBEL). ^{27}Al magic angle spinning (MAS) nuclear magnetic resonance (NMR) spectra were recorded using a Bruker DSX-300 spectrometer (300 MHz) with a high-speed 4 mm rotor.

3.2.3 *In situ*/*operando* infrared (IR) analysis

In situ/*operando* IR spectra were recorded by Fourier transform (FT)-IR using a JASCO 4200 instrument with a MCT detector. Samples (40 mg) were pressed to obtain self-supporting pellets (ϕ = 20 mm), which were placed in a quartz IR cell with CaF_2 windows connected to a conventional gas flow system. The composition of the effluent gas was analyzed using a mass spectrometer (BELMass, MicrotracBEL).

3.2.4 (*In situ*/*operando*) X-ray absorption spectroscopy (XAS)

La K-edge XAS spectra were measured in transmittance mode at SPring-8 (BL14B2) using a Si(311) double crystal monochromator (proposal 2018A1757). Athena (ver. 0.9.25) was used for data analysis. The Fourier transform of the k^3-weighted extended X-ray absorption fine structure (FT-EXAFS) was conducted within the k range of 3–12 $Å^{-1}$. Curve-fitting was performed using the Artemis program, and the related parameters were provided by FEFF8.3.[27]

Pd L_3-edge XAS measurements were conducted in fluorescence mode at the B branch of the BL27SU beamline at SPring-8 using a Si(111) double crystal monochromator (proposal 2019B1156). The measurements were conducted under vacuum after sample preparations using a glove box filled with Ar.

Operando Pd K-edge XAS spectra were measured in fluorescence mode at the BL14B2 beamline with a Si(311) double crystal monochromator (proposal 2018A1757). A gas chromatography (GC) equipped with thermal conductivity detector (490 Micro GC; Agilent Technologies Inc.) was used for the quantitative analysis of N_2, N_2O, CO_2, and CO. Samples of Pd/Al_2O_3 or $Pd/La(15)/Al_2O_3$ (15 mg) in pellet form (ϕ: 10 mm) diluted by boron nitride (BN) were introduced into a quartz cell. The catalyst was pretreated under 10% H_2/He flow (100 mL/min) at 400 °C for 0.5 h and cooled to 200 °C. Subsequently, 0.5% NO/He and 0.5% CO/He (100 mL/min) were introduced into the cell, respectively. The space velocity (SV) for the *operando* Pd K-edge XAS measurements was ~ 100,000 h^{-1}.

3.2.5 Catalytic reactions

The catalytic activity of the powder catalysts was measured in a tubular continuous-flow reactor. The outlet gas composition was quantified by GC (Shimadzu GC-8A with a SHINCARBON ST column). The conversion of NO was calculated based on the amounts of N_2 and N_2O produced.

The catalytic activity of the honeycomb catalysts during the $DeNO_x$ reaction was investigated in a flow reactor using MEXA series (Horiba Ltd.) under NO–CO and TWC conditions. The feed composition employed during the NO–CO reaction was 0.1% NO and 0.1% CO balanced with N_2 at SV = 100,000 h^{-1}. The catalytic activity test was performed from 100 to 400 °C at a heating rate of 25 °C min^{-1}. Prior to the measurement of the catalytic activity for the NO–CO reaction, the catalyst block was pretreated under the aforementioned NO–CO gas from 30 to 400 °C at a heating rate of 25 °C min^{-1} and cooled to 100 °C under a flow of N_2.

Catalytic reactions on the honeycomb catalysts were conducted using a MEXA series (Horiba Ltd.). Catalytic performance was evaluated by feeding a gas mixture comprising CO, C_3H_6, H_2, NO, O_2, CO_2, H_2O, and balanced N_2 with different lambda at SV = 100,000 h^{-1}. The λ values were calculated using Equation (1). The catalyst was pretreated under a flow of the simulated exhaust

gas (λ = 1) at 400 °C for 0.5 h. The composition of the feeding gas for TWC light-off tests was perturbed at a frequency of 1 Hz between lambdas of 0.95 and 1.05, which is listed in **Table 1**.

$$\lambda = \frac{O_2 + 0.5CO + 0.5H_2O + CO_2 + 0.5NO}{0.5H_2 + CO + 1.5C_3H_6 + 0.5H_2O + CO_2} \quad (1)$$

Table 1. The simulated exhaust gas composition for TWC tests.

λ	CO/%	C_3H_6/ppm	H_2/%	NO/%	O_2/%	CO_2/%	H_2O/%	N_2
0.95	2.4	420	0.8	0.1	0.6	15	10	balance
1.00	0.6	420	0.2	0.1	0.6	15	10	balance
1.05	0.6	420	0.2	0.1	1.65	15	10	balance

3.3 Results and discussion

3.3.1 Catalyst characterization

Previously, we partly reported the characterization and textual properties of the fresh Pd/La(x)/Al_2O_3 catalysts.[25,26] Briefly, the introduced La was highly dispersed in the Al_2O_3 matrix. The average Pd particle diameters were determined to be 3−4 nm using the CO adsorption measurements. The *in situ* Pd K-edge XAS measurements for Pd/La(15)/Al_2O_3 and Pd/Al_2O_3 were performed under flowing He (100 mL/min) at 200 °C after H_2 reduction at 400 °C for 30 min, as shown in **Figure 1**. The FT-EXAFS spectra of the Pd/Al_2O_3 and Pd/La(15)/Al_2O_3 exhibited a peak at 2.6 Å, which was attributed to the contribution of the Pd–Pd bond. The EXAFS curve-fitting (**Table S1**) demonstrates that the peak in the FT-EXAFS spectra contained only the contribution of the Pd–Pd bond, indicating that the Pd species in Pd/La(15)/Al_2O_3 and Pd/Al_2O_3 are in a metallic state. Meanwhile, the Pd K-edge X-ray absorption near edge structure (XANES) show that the edge position for Pd/La(15)/Al_2O_3 slightly shifted positively compared with that of Pd/Al_2O_3, despite the similar average particle sizes of Pd in Pd/Al_2O_3 and Pd/La(15)/Al_2O_3. These results are consistent with our previous study using *in situ* Pd K-edge XAS measurements in transmission mode.[26]

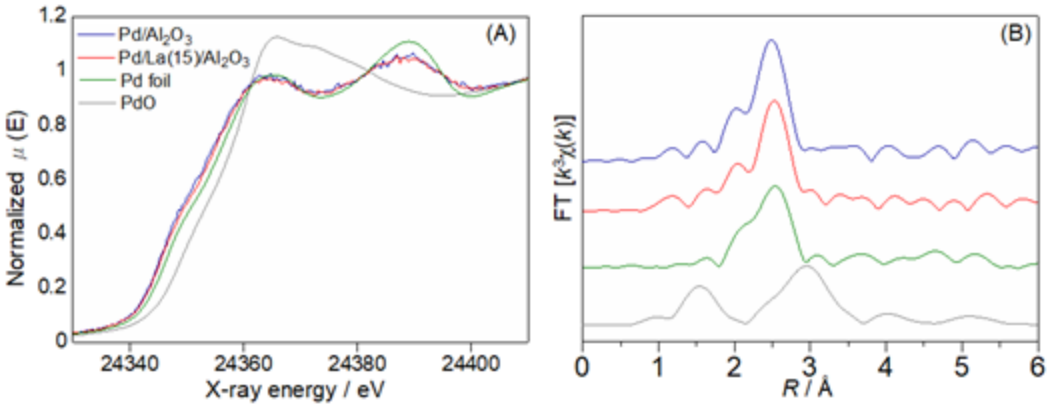

Figure 1. *In situ* Pd K-edge XAS spectra. (A) the XANES spectra and (B) the k^3-weighted FT-EXAFS results of Pd foil, PdO, Pd/Al_2O_3, and Pd/La(15)/Al_2O_3. The spectra of Pd/La(15)/Al_2O_3 and Pd/Al_2O_3 were collected under a flow of He (100 ml/min) at 200 ˚C after H_2 reduction at 500 ˚C for 15 min. The spectra of PdO and Pd were recorded at the room temperature in the air.

Pd L_3-edge XAS measurements were carried out to investigate the electronic states of Pd in Pd/Al_2O_3 and Pd/La(15)/Al_2O_3. For Pd, XAS at the K edge (~24.350 keV), which can probe the 1s to 4p transition, is commonly measured and advantageous for *in situ* and *operando* experiments.[28] The L_3-edge XAS (~3.175 keV), which probes the 2p to 4d transition, can provide information regarding the empty d density of states (DOS), which is crucial for distinguishing

subtle differences in the electronic states of Pd species.[29–31] The Pd L_3-edge XANES spectra, which were recorded without any exposure to air after the H_2 reduction pretreatment, are shown in **Figure 2**. The Pd L_3-edge spectra of Pd/La(15)/Al_2O_3 show an increased intensity in the white line, compared to that of Pd/Al_2O_3, suggesting that the introduction of La led to a change in the electronic structure of Pd, and the Pd loaded on La(15)/Al_2O_3 was more electron-deficient than that on Al_2O_3. Additionally, the characteristic absorption peak at 3,182 eV for Pd hydride[31] was not observed, suggesting that the increased intensity in the white line in the Pd L_3-edge spectra for Pd/La(15)/Al_2O_3 was not due to the impact of palladium hydride.

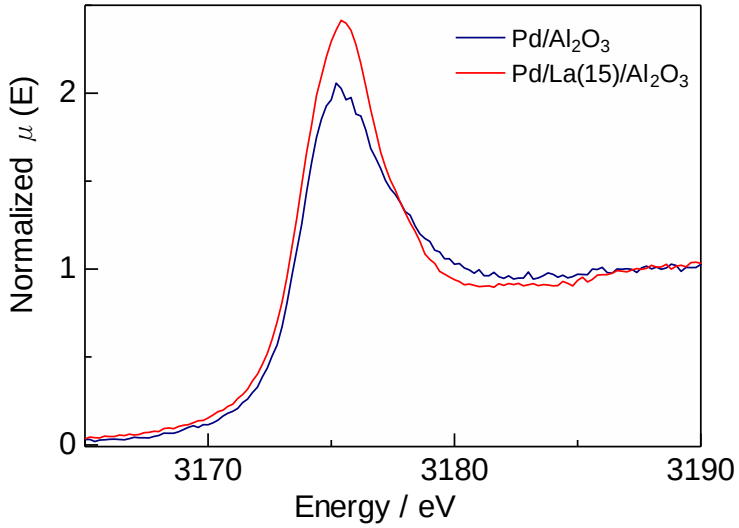

Figure 2. Pd L_3-edge XANES spectra of Pd/Al_2O_3 and Pd/La(15)/Al_2O_3 catalysts. The samples were pretreated under the flow of H_2 at ambient pressure before the spectra were recorded at room temperature under vacuum conditions.

3.3.2 Promotional effect of La on the NO reduction activity

To investigate the effect of La on the catalytic activity of Pd/La(15)/Al_2O_3 and Pd/Al_2O_3 during the NO–CO reaction, we performed *in situ*/*operando* Pd K-edge XAS measurements in fluorescence mode under the flow of 0.5% NO/He, He, and 0.5% CO/He with an SV of ~ 100,000 h^{-1} at 200 °C after H_2 pretreatment at 400 °C. Here, the low contact time or high SV conditions afforded a lower NO conversion level than the previously reported results.[26] **Figure 3** shows the *in situ* Pd K-edge XANES and FT-EXAFS spectra of the Pd/Al_2O_3 and Pd/La(15)/Al_2O_3 catalysts collected under a He flow after H_2 reduction and a flow of NO (0.5% NO/He, 100 mL min^{-1}). Notably, all the spectra were collected at 200 °C. The XANES spectra of Pd/Al_2O_3 and Pd/La(15)/Al_2O_3 show the evolution of the absorption edge to high energy under a flow of 0.5% NO/He. The k^3-weighted FT-EXAFS spectra of Pd/La(15)/Al_2O_3 showed that NO flowing caused a decrease in the peak attributed to

Pd–Pd scattering and an increase in the peak assigned to the Pd–O scattering, suggesting that Pd was oxidized by NO. However, in the k^3-weighted FT-EXAFS spectra of Pd/Al_2O_3 where the contribution of Pd–Pd decreased, the Pd–O contribution did not increase. This lack of evidence for Pd–O bonds was attributed to the generation of oxidized and dispersed Pd species, which do not generate PdO species with well-defined Pd–O bonds, as demonstrated in our previous study.[26] Our previous studies revealed that the dispersion occurs through oxidation of Pd metal by NO, yielding dispersed Pd oxide species with concomitant formation of N_2O.[26,32] Similar phenomena of redispersion have been reported for related materials.[33–35] For further information, we analyzed the XANES data using linear combination fitting (LCF) with the XANES spectra of well-reduced catalysts and PdO powder as references. The results of the LCF analysis revealed that the Pd species were oxidized under the flow of NO **(Figure 3C)**. The fraction of Pd^0 species in $Pd/La(15)/Al_2O_3$ declined faster than that in Pd/Al_2O_3, indicating that the introduction of La favored the effective oxidation of Pd by NO. Oppositely, the Pd oxide species in both Pd/Al_2O_3 and $Pd/La(15)/Al_2O_3$ were reduced to Pd with the subsequent introduction of CO, where the fraction of Pd^0 species obtained by the LCF calculation increased.

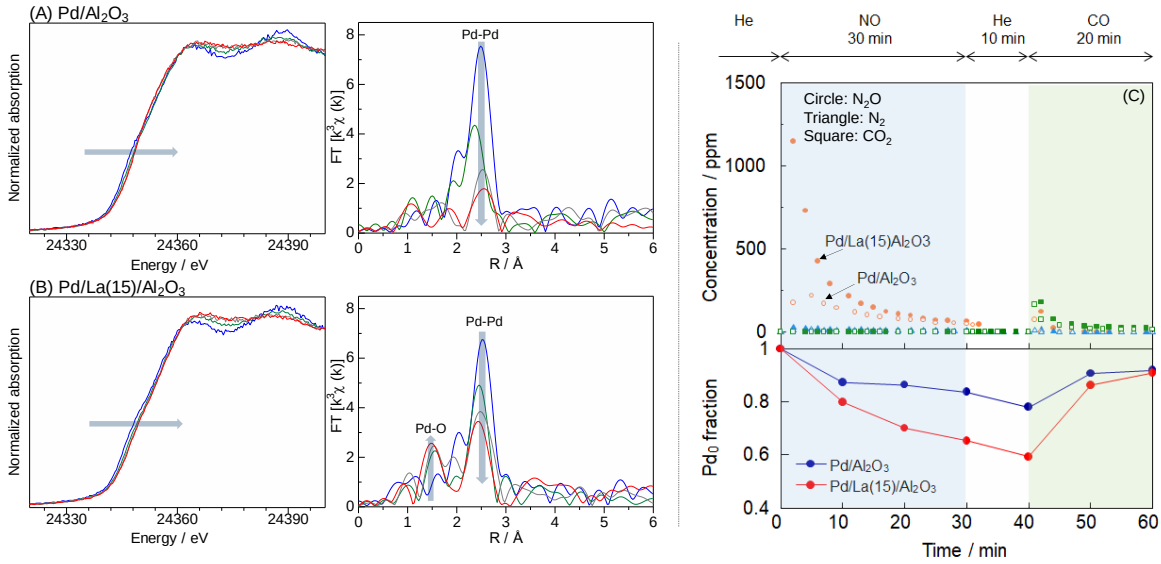

Figure 3. *In situ* Pd K-edge XANES and k^3-weighted FT-EXAFS spectra for (A) Pd/Al_2O_3 and (B) $Pd/La(15)/Al_2O_3$ under the flow of NO (0.5% NO/He, 100 mL min^{-1}) at 200 °C. (C) The variation of product concentration and the fraction of Pd^0 species as a function of time under a flow of NO (0.5% NO/He, 100 mL min^{-1}), He, and CO (0.5% CO/He, 100 mL min^{-1}).

To further explore the origin of the promotional effect of La, *in situ* IR measurements were performed to investigate the reactivity of Pd/Al_2O_3 and $Pd/La(15)/Al_2O_3$ toward NO. The IR spectra were recorded after exposure to NO for 30 min, as shown in **Figure 4A**. Prior to the introduction of NO, the catalyst pellets were pretreated with H_2 at 400 °C for 0.5 h and cooled to 200 °C. The

gas-phase products were simultaneously monitored using a mass spectrometer, which were shown in **Figure 4B**. In the Pd/Al_2O_3 spectra, strong peaks appeared at 1805, 1767, and 1741 cm^{-1} and were attributed to the NO molecules adsorbed on the Pd.[36] The weak peak observed at 1568 cm^{-1} was assigned to the nitrate species adsorbed on the Al oxide sites.[36] For that of $Pd/La(15)/Al_2O_3$, peaks observed within the range of 1100–1600 cm^{-1} were related to the surface NO_x species. More specifically, the peak at 1189 cm^{-1} was attributed to the surface nitrite species, and the broad peaks within the range of 1300–1600 cm^{-1} were assigned to the surface nitrate species with various vibrational modes. [36–38] For $Pd/La(15)/Al_2O_3$ catalyst, with the increase of surface nitrite species, the formation of gaseous N_2O was also observed. These results suggested that the conversion of NO over $Pd/La(15)/Al_2O_3$ at 200 °C involved a disproportionation reaction yielding surface nitrite species and N_2O released to the gas phase. Furthermore, virtually no nitrite species were observed in the IR spectra of Pd/Al_2O_3 and $La(15)/Al_2O_3$, indicating that both Pd and La were critical for the formation of surface nitrite species. Note that although the formation of N_2 was also observed over $Pd/La/Al_2O_3$, the concentration of N_2O was much higher than that of N_2 (**Figure 3C**), indicating that the addition of La promoted the conversion of NO to N_2O more efficiently than to N_2 at low temperature. Combining these results with those obtained in our previous study where the nitrite surface species were observed to exhibit a facile catalytic reactivity after the introduction of CO as a reductant at 200 °C,[25,26] it was considered that the efficient generation of nitrite species and its facile reactivity were crucial to the promotional effect of La in NO reduction.

Figure 5 showed the results of catalytic test for the primary reactions involved in TWC process, such as NO–C_3H_6, NO–H_2, N_2O–H_2, C_3H_6–O_2, and CO–O_2 reactions, over powder catalysts, besides the previously reported NO–CO reaction.[25,26] In a practical TWC process, NO and O_2 function as oxidants that can react with reducing gases such as CO, H_2, and HC. For all the reactions performed, reactant conversions were promoted by the introduction of La, indicating that the presence of La enhanced the catalytic activity in the reactions involved in the TWC process in addition to the promotional effect of La on the NO–CO reaction.[25,26]

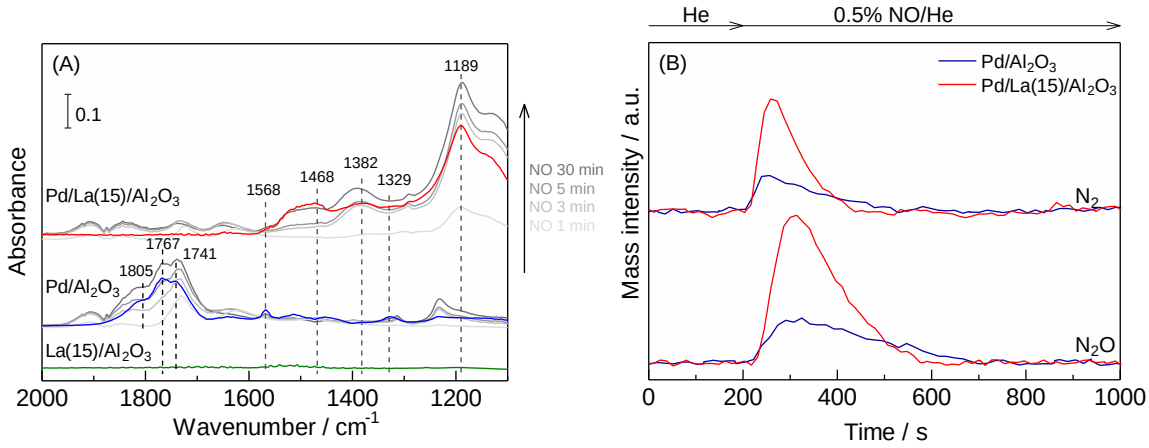

Figure 4. (A) *Operando*/*in situ* IR spectra of species adsorbed on $La(15)/Al_2O_3$, Pd/Al_2O_3, and $Pd/La(15)/Al_2O_3$ at 200 °C. The grey spectra were collected under the flow of 0.5% NO/He. The red, blue, and green spectra were recorded under a He flow after the introduction of 0.5% NO/He. (B) Evolution of N_2 and N_2O upon exposure of the $Pd/La(15)/Al_2O_3$ and Pd/Al_2O_3 to a stream of 0.5% NO/He.

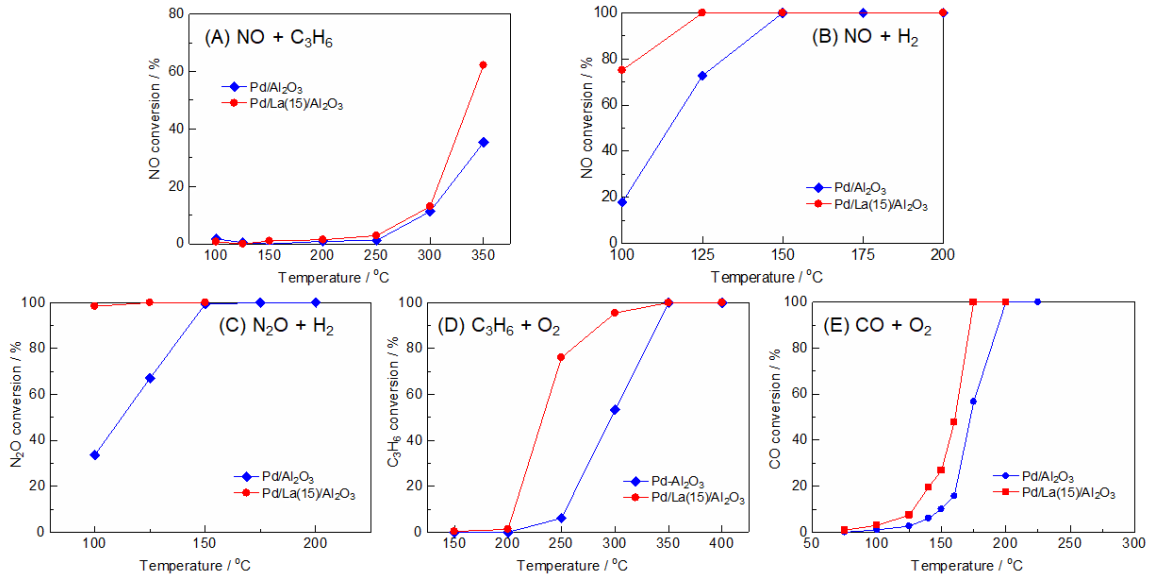

Figure 5. Catalytic conversions toward the basic reactions over Pd/Al_2O_3 and $Pd/La(15)/Al_2O_3$. Conditions: (A) 0.5% NO, 0.1% C_3H_6, He balance. (B) 0.5% NO, 0.5% H_2, He balance. (C) 0.5% N_2O, 0.5% H_2, He balance; (D) 0.5% C_3H_6, 2.25% O_2, He balance. (E) 0.5% CO, 0.5% O_2, He balance; Total flow rate: 100 mL min^{-1}; Weight of catalyst: 15 mg.

3.3.3 The effect of hydrothermal aging

The catalysts aged at 800 °C for 4 h were characterized to clarify the effect of La on the catalytic durability. The BET specific surface areas (S_{BET}) determined from the N_2 adsorption isotherms (**Figure 6**) are summarized in **Table 2** with the Pd particle sizes. Pd/Al_2O_3 showed a higher S_{BET} than $Pd/La(x)/Al_2O_3$ after the aging treatment, and the S_{BET} of the aged $Pd/La(x)/Al_2O_3$ decreased with an increasing loading amount for La. The Pd particle size in fresh Pd/Al_2O_3 and $Pd/La/Al_2O_3$ catalysts were determined to be 3–4 nm by CO adsorption combined with HADDF-STEM, which were taken from our previous report.[39] The particle sizes of Pd in the aged $Pd/La(5)/Al_2O_3$ and $Pd/La(15)/Al_2O_3$ catalysts were smaller than those in Pd/Al_2O_3, although Pd/Al_2O_3 retained a higher specific surface area, indicating that a moderate loading of La (5 and 15 wt%) enhanced the resistance of Pd nanoparticles against aggregation. However, an excessive La loading was inefficient in stabilizing the dispersion of Pd. The HAADF-STEM images of the aged Pd/Al_2O_3 and $Pd/La(15)/Al_2O_3$ (**Figure 7**) show that the Pd species in Pd/Al_2O_3 and $Pd/La(15)/Al_2O_3$ aggregated into larger nanoparticles after aging. The La species appeared atomically dispersed on Al_2O_3.

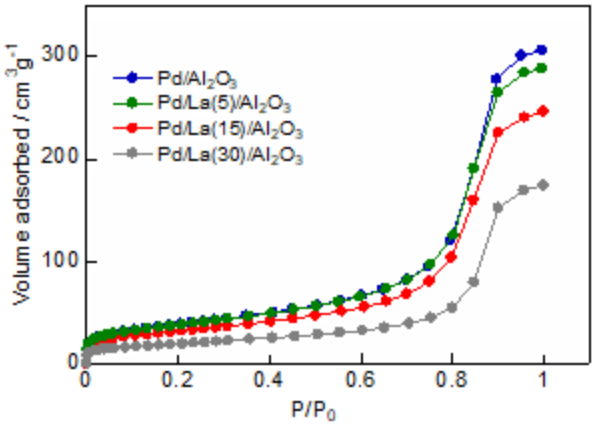

Figure 6. N_2 adsorption isotherm of $Pd/La(x)/Al_2O_3$ (x = 0, 5, 15, and 30 wt%) at 77K. The catalysts were aged under redox hydrothermal conditions at 800 °C for 4 h.

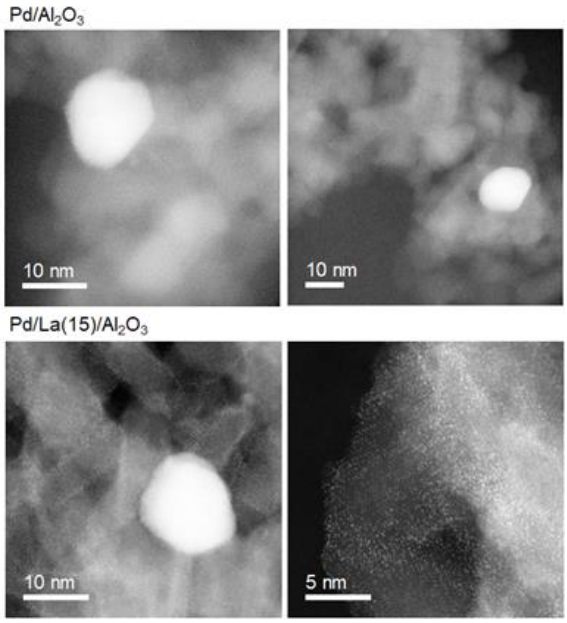

Figure 7. HAADF-STEM images of Pd/Al_2O_3 after aging at 800 ˚C for 4 h.

Figure 8A shows the powder XRD patterns of the aged Pd/Al_2O_3 and $Pd/La(x)/Al_2O_3$. The XRD patterns of the aged Pd/Al_2O_3 and $Pd/La(x)/Al_2O_3$ (x = 5 and 15 wt%) show peaks attributed to the γ-Al_2O_3 phase; no peaks assignable to La_2O_3 or $LaAlO_3$ were observed indicating that the aged Pd/Al_2O_3 and $Pd/La(x)/Al_2O_3$ (x = 5, 15 wt%) mainly comprised γ-Al_2O_3.[40] Noteworthily, the XRD patterns of La_2O_3 and $LaAlO_3$ were obtained from our previous report.[39] In contrast, the XRD pattern for the aged $Pd/La(30)/Al_2O_3$ shows sharp peaks corresponding to the $LaAlO_3$ phase, suggesting that the excessive introduction of La led to the formation of $LaAlO_3$ after aging under hydrothermal redox conditions at 800 °C. In the ^{27}Al MAS NMR spectra of the aged Pd/Al_2O_3 and $Pd/La(x)/Al_2O_3$ (x = 5 and 15 wt%) (**Figure 8B**), two peaks were observed at approximately 13 and 73 ppm, which were assignable to the octahedrally and tetrahedrally coordinated Al^{3+}, respectively.[41] This suggests that Pd/Al_2O_3 and $Pd/La(x)/Al_2O_3$ (x = 5 and 15 wt%) predominantly comprised the γ-Al_2O_3 phase. However, in the NMR spectra of the aged $Pd/La(30)/Al_2O_3$, the intensity of the peak attributed to the tetrahedrally coordinated Al^{3+} decreased, and the peak of the octahedrally coordinated Al^{3+} sharpened, which was similar to the shape of the octahedrally coordinated Al^{3+} in the NMR spectra of $LaAlO_3$. The results of the XAS measurements for the aged $Pd/La(x)/Al_2O_3$ (x = 5, 15, and 30 wt %) are shown in **Figures 8C** and **D**. The La–Al and La–La scatterings in $LaAlO_3$ were observed at approximately 2.9 and 3.5 Å (without phase shift correction), respectively. The La–O scattering in La_2O_3 was observed at approximately 2.0 Å. La–O scattering peaks were observed for all the $Pd/La(x)/Al_2O_3$ catalysts. The results of the curve-fitting analysis are summarized in **Table 3**, which shows that only the La–

O contribution can be observed in the EXAFS spectra of Pd/La(x)/Al_2O_3 (x = 5 and 15 wt%) after aging. These results show the peaks attributed to the La–O contribution, suggesting the high dispersion of La species in Pd/La(5)/Al_2O_3 and Pd/La(15)/Al_2O_3 after aging. However, the FT-EXAFS spectra of Pd/La(30)/Al_2O_3 exhibit peaks corresponding to La–Al and La–La contributions, indicating the formation of $LaAlO_3$ after aging at 800 °C. The results of La K-edge XAS are consistent with the aforementioned XRD and ^{27}Al MAS NMR results.

Table 2. Textural properties of Pd/Al_2O_3 and Pd/La(x)/Al_2O_3 aged at 800 °C.

Catalyst	S_{BET}[a]/ m^2g^{-1}	Pd particle size[b] / nm	Pd particle size[c] / nm
Pd/Al_2O_3	140	12.0	16.9
Pd/La(5)/Al_2O_3	136	8.1	9.8
Pd/La(15)/Al_2O_3	114	6.1	9.7
Pd/La(30)/Al_2O_3	70	21.5	19.8

[a]Determined by N_2 adsorption. [b]Estimated by CO adsorption at −20 °C. [c]Estimated by STEM.

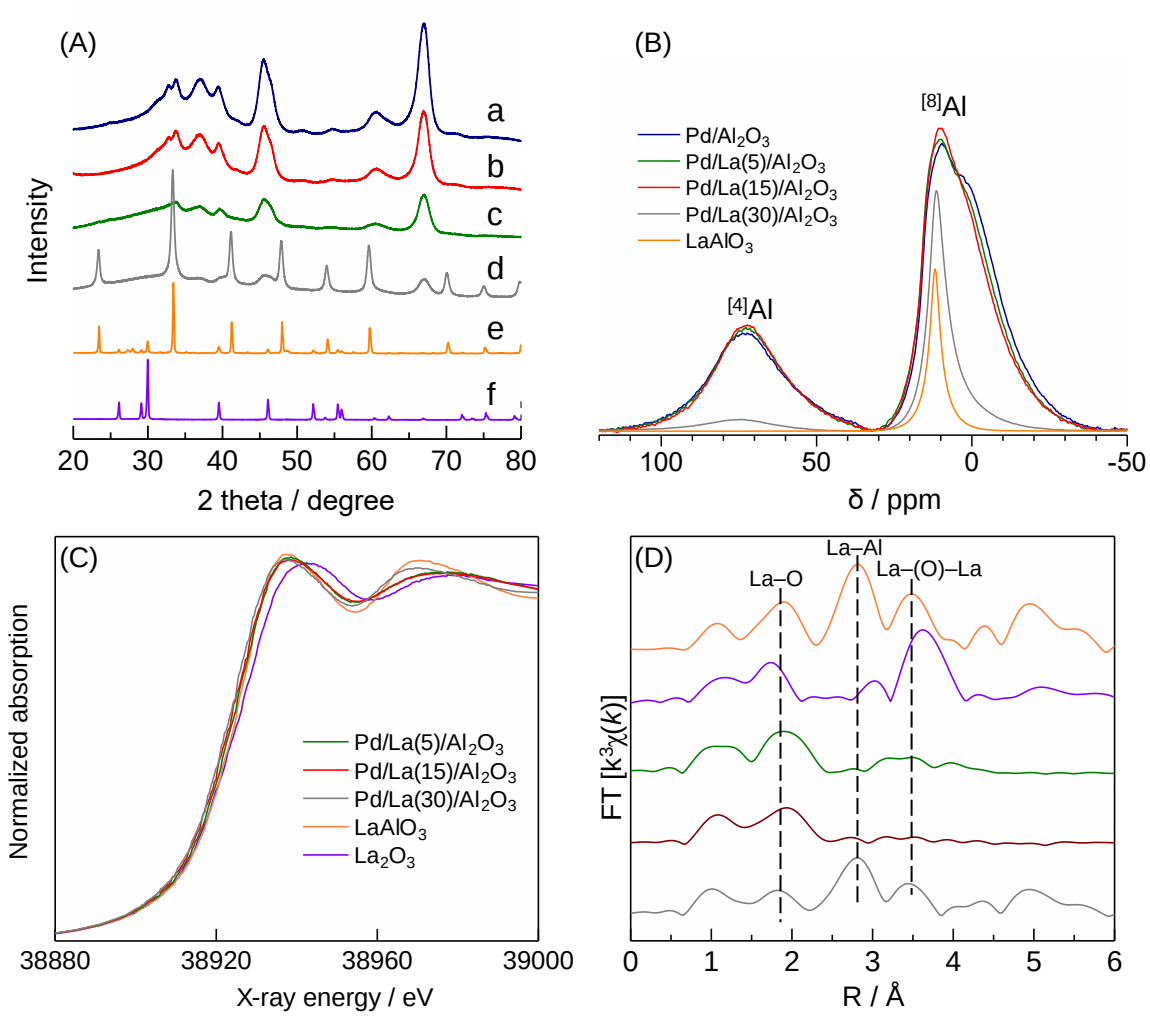

Figure 8. (A) XRD patterns of (a) Pd/Al_2O_3, (b) $Pd/La(5)/Al_2O_3$, (c) $Pd/La(15)/Al_2O_3$, (d) $Pd/La(30)/Al_2O_3$ aged at 800 °C. (e) $LaAlO_3$ and (f) La_2O_3. (B) ^{27}Al MAS NMR of Pd/Al_2O_3 and $Pd/La(x)/Al_2O_3$ (x = 5,15, and 30 wt%) aged at 800 °C. La K-edge (C) XANES and (D) k^3-weighted FT-EXAFS spectra of the aged samples of $Pd/La(x)/Al_2O_3$ (x = 5, 15, and 30 wt%) with the reference compounds La_2O_3 and $LaAlO_3$. The spectra were recorded at room temperature in air.

Table 3. Curve-fitting analysis of La K-edge FT-EXAFS of the aged $Pd/La(x)/Al_2O_3$ (x = 5, 15, and 30 wt%).

Sample	Shell	CN [a]	*R* (Å) [b]	σ (Å) [c]	R_f (%) [d]
$Pd/La(5)/Al_2O_3$	La–O	3.0	2.56	0.10	0.6
$Pd/La(15)/Al_2O_3$	La–O	3.0	2.57	0.10	0.6
$Pd/La(30)/Al_2O_3$	La–O	4.5	2.62	0.09	1.0
	La–Al	2.5	3.33	0.04	

[a] Coordination number. [b] Bond distance. [c] Debye–Waller factor. [d] Residual factor.

We investigated the effect of La on the catalytic durability of the NO–CO reaction in the light-off mode using the monolithic honeycomb Pd/Al_2O_3 and $Pd/La(x)/Al_2O_3$ catalysts after hydrothermal treatment at 800 °C (x = 5 and 15 wt%), as shown in **Figure 9**. The $Pd/La/Al_2O_3$ catalysts exhibited better catalytic performance after the aging treatment, compared to Pd/Al_2O_3.

Although their catalytic performance significantly decreased, compared with that of the fresh catalysts, as reported in our previous study.[39] For clarity, The relationship between the La content and T_{50} behavior was correlated and defined as the temperature at which the conversion reached 50%, demonstrating the effect of La on the catalytic performance, as shown in **Figure 10**. Pd/La(15)/Al_2O_3 showed a higher conversion of NO and CO than Pd/La(5)/Al_2O_3 after aging.

Figure 11 shows the results of the TWC light-off test over the aged honeycomb catalysts. It shows the conversion of NO, CO, and C_3H_6. The catalytic conversions for NO over Pd/La/Al_2O_3 was higher than that over Pd/Al_2O_3, demonstrating the promotional effect of La. In addition, the aged Pd/La(15)/Al_2O_3 catalyst exhibited a higher NO removal efficiency than that of the conventionally used Pd/La(5)/Al_2O_3 catalyst, particularly in the region of low temperatures (< 250 °C). However, Pd/Al_2O_3 showed higher catalytic conversion of CO and C_3H_6 than Pd/La(x)/Al_2O_3 (x = 5 and 15 wt%). This is possibly because that the weakened adsorption strength of CO and C_3H_6 adsorbed on electron-deficient Pd^0 species decreased catalytic activity for the CO and C_3H_6 oxidation reactions especially in the presence of other competitive adsorbates such as NO_x under the TWC conditions.

Considering the fluctuation of the λ values between high (lean) and low (rich) values under real working conditions due to an engine fuel-cut operation which was introduced relatively recently to improve fuel efficiency,[2,42] it is important for the TWC catalysts to efficiently respond to the change in λ conditions and exhibit high performance under the fluctuating conditions of the exhaust gases.[3,41,42] It is crucial to investigate the λ-switching performance of the honeycomb catalysts under real automotive TWC conditions. Thus, a λ-switching test was performed for the honeycomb model catalysts, as shown in **Figure 12**. The experiment was conducted under lean conditions (λ = 1.05), changed to rich conditions and finally switched to lean conditions. Notably, there were detection delays due to the experimental setup (3.2 s for CO and 1.0 s for NO relative to C_3H_6). For the change from lean to rich (from ca. 5 s), the NO conversion over Pd/La(15)/Al_2O_3 occurred at a higher speed than that over the other catalysts. The NO conversion over all the honeycomb catalysts decreased gradually under rich condition, which was possibly the result of CO poisoning as observed during NO–CO reaction in our previous study.[19] It was also observed that high conversion of CO and C_3H_6 was retained for Pd/La(5)/Al_2O_3 during the change from lean to rich. For the subsequent change from rich to lean (from ca. 36 s), a high NO conversion was retained over Pd/La/Al_2O_3, compared to Pd/Al_2O_3, demonstrating the positive effect of the introduction of La. These results indicate that the addition of La enhanced the resistance of Pd/La/Al_2O_3 catalysts towards the fluctuation of exhaust feed composition. Such promotional effect of La plays an important role for the Pd/La/Al_2O_3 catalysts under real working conditions.

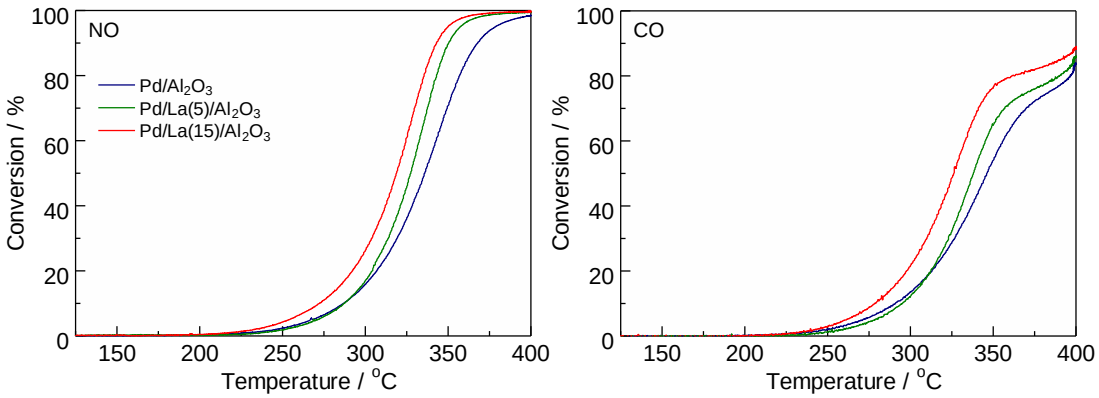

Figure 9. Conversion of (A) NO and (B) CO for NO–CO light-off tests for the aged Pd/La(x)/Al_2O_3 catalysts (x = 0, 5, and 15 wt%) under a gas mixture containing 0.1% NO and 0.1% CO with N_2 balance. SV = 100,000 h^{-1}; heating rate: 25 °C/min.

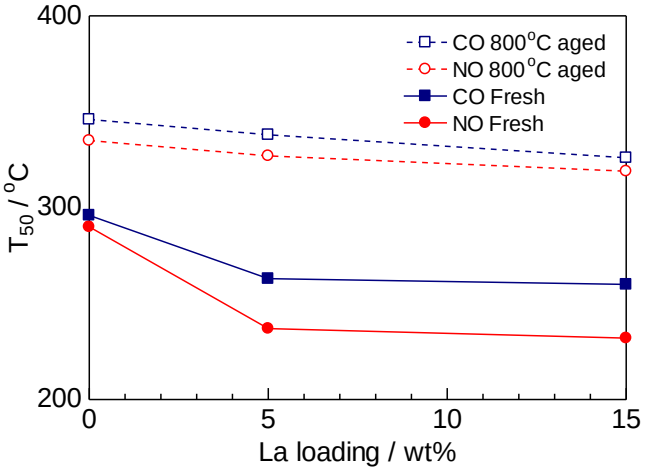

Figure 10. Effect of La content on T_{50} behavior over the aged catalysts for the TWC light-off performance tests.

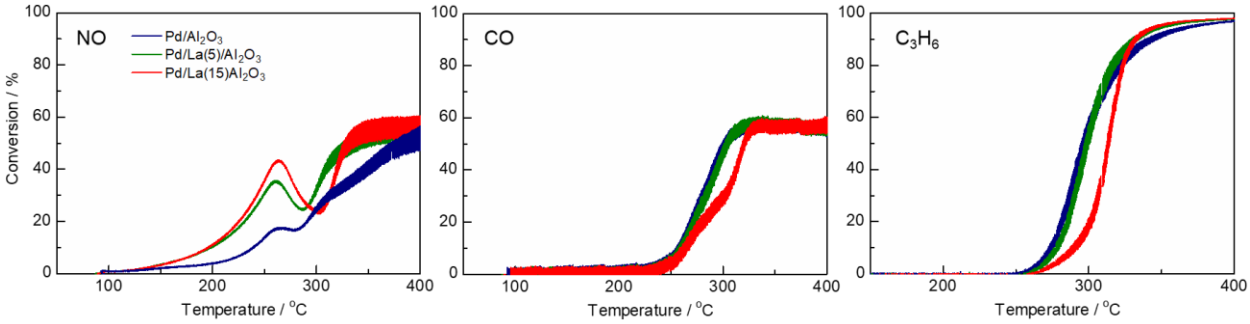

Figure 11. Conversion of NO, CO, and C_3H_6 for TWC light-off tests using Pd/La(x)/Al_2O_3-coated honeycomb catalysts (x = 0, 5, and 15 wt%) aged at 800 °C under 1-Hz perturbed gases between λ = 1.05 and 0.95. Conditions: NO (0.1%), CO (2.4–0.6%), O_2 (0.6–1.65%), C_3H_6 (420 ppm), CO_2 (15%), H_2 (0.8%), H_2O (10%), N_2 balance; SV = 100,000 h^{-1}; heating rate: 25 °C/min.

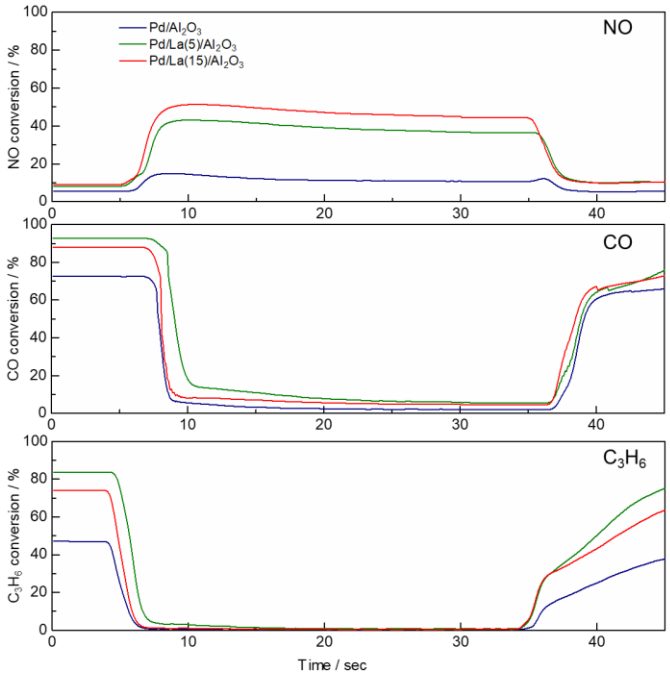

Figure 12. Performance of λ-switching test for NO, CO, and C_3H_6 on the Pd/La(x)/Al_2O_3-coated honeycomb catalysts (x = 0, 5, and 15 wt%) aged at 800 °C upon lambda jumps (λ = 1.05–0.95). The detection delays here are caused by the experimental setup (3.2 s for CO and 1.0 s for NO relative to C_3H_6).

3.4 Conclusion

We investigated the role of La in Pd/La(x)/Al_2O_3 (x = 5, 15, and 30 wt%) during the $DeNO_x$ process. The obtained results show that NO conversion was promoted effectively by Pd/La/Al_2O_3 via a disproportionation reaction to yield surface nitrite species and gas-phase N_2O. Furthermore, we investigated the effect of La on the catalytic durability under hydrothermal redox conditions at high temperatures. It was observed that Pd/La/Al_2O_3 exhibits better catalytic durability than Pd/Al_2O_3. A higher loading amount of La (15 wt%) favored the stable dispersion of Pd nanoparticles against sintering and in turn, retained a higher catalytic activity in Pd/La(15)/Al_2O_3 during the $DeNO_x$ process after the aging treatment.

Reference

(1) Wang, J.; Chen, H.; Hu, Z.; Yao, M.; Li, Y. A Review on the Pd-Based Three-Way Catalyst. *Catal Rev Sci Eng* **2015**, *57*, 79–144.

(2) Farrauto, R. J.; Deeba, M.; Alerasool, S. Gasoline Automobile Catalysis and Its Historical Journey to Cleaner Air. *Nat Catal* **2019**, *2*, 603–613.

(3) Rood, S.; Eslava, S.; Manigrasso, A.; Bannister, C. Recent Advances in Gasoline Three-Way Catalyst Formulation: A Review. *Proceedings of the Institution of Mechanical Engineers, Part D: Journal of Automobile Engineering* **2019**, *234*, 936–949.

(4) Asakura, H.; Hosokawa, S.; Ina, T.; Kato, K.; Nitta, K.; Uera, K.; Uruga, T.; Miura, H.; Shishido, T.; Ohyama, J.; Satsuma, A.; Sato, K.; Yamamoto, A.; Hinokuma, S.; Yoshida, H.; Machida, M.; Yamazoe, S.; Tsukuda, T.; Teramura, K.; Tanaka, T. Dynamic Behavior of Rh Species in Rh/Al_2O_3 Model Catalyst during Three-Way Catalytic Reaction: An Operando X-Ray Absorption Spectroscopy Study. *Journal of the American Chemical Society* **2018**, *140*, 176–184.

(5) Ueda, K.; Tsuji, M.; Ohyama, J.; Satsuma, A. Tandem Base-Metal Oxide Catalyst: Superior NO Reduction Performance to the Rh Catalyst in $NO\text{-}C_3H_6\text{-}CO\text{-}O_2$. *ACS Catalysis* **2019**, *9*, 2866−2869.

(6) Thomas, C. R.; Pihl, J. A.; Lance, M. J.; Toops, T. J.; Parks, J. E.; Lauterbach, J. Effects of Four-Mode Hydrothermal Aging on Three-Way Catalysts for Passive Selective Catalytic Reduction to Control Emissions from Lean-Burn Gasoline Engine. *Applied Catalysis B: Environmental* **2019**, *244* (November 2018), 284–294.

(7) Datye, A. K.; Votsmeier, M. Opportunities and Challenges in the Development of Advanced Materials for Emission Control Catalysts. *Nat Mater* **2020**, *20*, 1049–1059.

(8) Zheng, T.; Lu, B.; Harle, G.; Yang, D.; Wang, C.; Zhao, Y. A Comparative Study of Rh-Only, Pd-Only and Pd/Rh Catalysts. *Applied Catalysis A: General* **2020**, *602*, 117649.

(9) Kusada, K.; Wu, D.; Nanba, Y.; Koyama, M.; Yamamoto, T.; Tran, X. Q.; Toriyama, T.; Matsumura, S.; Ito, A.; Sato, K.; Nagaoka, K.; Seo, O.; Song, C.; Chen, Y.; Palina, N.; Kumara, L. S. R.; Hiroi, S.; Sakata, O.; Kawaguchi, S.; Kubota, Y.; Kitagawa, H. Highly Stable and Active Solid-Solution-Alloy Three-Way Catalyst by Utilizing Configurational-Entropy Effect. *Advanced Materials* **2021**, *33*, 2005206.

(10) Khivantsev, K.; Vargas, C. G.; Tian, J.; Kovarik, L.; Jaegers, N. R.; Szanyi, J.; Wang, Y. Economizing on Precious Metals in Three‐Way Catalysts: Thermally Stable and Highly Active Single‐Atom Rhodium on Ceria for NO Abatement under Dry and Industrially Relevant Conditions. *Angew. Chem. Int. Ed.* **2021**, *133*, 395–402.

(11) Haneda, M.; Nakamura, Y.; Yamada, T.; Minami, S.; Kato, N.; Iwashina, K.; Endo, Y.; Nakahara, Y.; Iwachido, K. Comprehensive Study of the Light-Off Performance and Surface Properties of Engine-Aged Pd-Based Three-Way Catalysts. *Catalysis Science & Technology* **2021**, *11* (3), 912–922.

(12) Getsoian, A. (Bean); Theis, J. R.; Paxton, W. A.; Lance, M. J.; Lambert, C. K. Remarkable Improvement in Low Temperature Performance of Model Three-Way Catalysts through Solution Atomic Layer Deposition. *Nature Catalysis* **2019**, *2* (7), 614–622.

(13) Huang, C.; Shan, W.; Lian, Z.; Zhang, Y.; He, H. Recent Advances in Three-Way Catalysts of Natural Gas Vehicles. *Catalysis Science and Technology* **2020**, *10*, 6407–6419.

(14) Li, L.; Zhang, N.; Wu, R.; Song, L.; Zhang, G.; He, H. Comparative Study of Moisture-Treated $Pd@CeO_2/Al_2O_3$ and $Pd/CeO_2/Al_2O_3$ Catalysts for Automobile Exhaust Emission Reactions: Effect of Core-Shell Interface. *ACS Applied Materials and Interfaces* **2020**, *12*, 10350–10358.

(15) Kang, S. B.; Nam, I. S.; Cho, B. K.; Kim, C. H.; Oh, S. H. Kinetic Model for Modern Double-Layered Pd/Rh TWC as a Function of Metal Loadings and Mileage. *Chemical Engineering Journal* **2015**, *278*, 328–338.

(16) Machida, M.; Fujiwara, A.; Yoshida, H.; Ohyama, J.; Asakura, H.; Hosokawa, S.; Tanaka, T.; Haneda, M.; Tomita, A.; Miki, T.; Iwashina, K.; Endo, Y.; Nakahara, Y.; Minami, S.; Kato, N.; Hayashi, Y.; Goto, H.; Hori, M.; Tsuda, T.; Miura, K.; Kimata, F.; Iwachido, K. Deactivation Mechanism of $Pd/CeO_2\text{-}ZrO_2$ Three-Way Catalysts Analyzed by Chassis-Dynamometer Tests and in Situ Diffuse Reflectance Spectroscopy. *ACS*

Catalysis **2019**, *9* (7), 6415−6424.
(17) Kobayashi, T.; Yamada, T.; Kayano, K. Effect of Basic Metal Additives on NOx Reduction Property of Pd-Based Three-Way Catalyst. *Appl Catal B* **2001**, *30* (3–4), 287–292.
(18) Takayama, A.; Kurokawa, T.; Nakayama, H.; Katoh, T.; Nagata, M. Effect of Ba and La Additives to the Pd Layer of a Pd:Rh TWC. In *SAE Technical Paper*; 2017.
(19) Jing, Y.; Wang, G.; Wei Ting, K.; Maeno, Z.; Oshima, K.; Satokawa, S.; Nagaoka, S.; Shimizu, K.; Toyao, T. Roles of the Basic Metals La, Ba and Sr as Additives in Al_2O_3-Supported Pd-Based Three-Way Catalysts. *Journal of Catalysis* **2021**, *400*, 387–396.
(20) Schaper, H.; Doesburg, E. B. M. M.; Van Reijen, L. L. The Influence of Lanthanum Oxide on the Thermal Stability of Gamma Alumina Catalyst Supports. *Applied Catalysis* **1983**, *7* (2), 211–220.
(21) Yamamoto, T.; Hatsui, T.; Matsuyama, T.; Tanaka, T.; Funabiki, T. Structures and Acid-Base Properties of La/Al_2O_3- Role of La Addition to Enhance Thermal Stability of γ-Al_2O_3. *Chemistry of Materials* **2003**, *15*, 4830–4840.
(22) Muraki, H.; Shinjyoh, H.;Fujitani, Y.; Muraki, H.; Shinjoh, H.; Fujitani, Y. Effect of Lanthanum on the NO Reduction over Palladium Catalysts. *Appl Catal* **1986**, *22*, 325–335.
(23) Valden, M.; Keiski, R. L.; Xiang, N.; Pere, J.; Aaltonen, J.; Pessa, M.; Maunula, T.; Savimäki, A.; Lahti, A.; Härkönen, M. Reactivity of Pd/Al_2O_3, Pd/La_2O_3-Al_2O_3 and $Pd/LaAlO_3$ Catalysts for the Reduction of NO by CO: CO and NO Adsorption. *Journal of Catalysis* **1996**, *161*, 614–625.
(24) Vedyagin, A. A.; Kenzhin, R. M.; Tashlanov, M. Y.; Alikin, E. A.; Stoyanovskii, V. O.; Plyusnin, P. E.; Shubin, Y. V; Mishakov, I. V; Smirnov, M. Y.; Kalinkin, A. V; Bukhtiyarov, V. I. Effect of La Addition on the Performance of Three-Way Catalysts Containing Palladium and Rhodium. *Topics in Catalysis* **2020**, *63*, 152–165.
(25) Toyao, T.; Jing, Y.; Kon, K.; Hayama, T.; Nagaoka, S.; Shimizu, K. ichi. Catalytic NO-CO Reactions over La-Al2O3 Supported Pd: Promotion Effect of La. *Chemistry Letters* **2018**, *47* (8), 1036–1039.
(26) Jing, Y.; Cai, Z.; Liu, C.; Toyao, T.; Maeno, Z.; Asakura, H.; Hiwasa, S.; Nagaoka, S.; Kondoh, H.; Shimizu, K. Promotional Effect of La in the Three-Way Catalysis of La-Loaded Al_2O_3-Supported Pd Catalysts ($Pd/La/Al_2O_3$). *ACS Catalysis* **2020**, *10*, 1010–1023.
(27) Ravel, B.; Newville, M. ATHENA, ARTEMIS, HEPHAESTUS: Data Analysis for X-Ray Absorption Spectroscopy Using IFEFFIT. *Journal of Synchrotron Radiation* **2005**, *12* (4), 537–541.
(28) Marchionni, V.; Nachtegaal, M.; Ferri, D. Influence of CO on Dry CH_4 Oxidation on Pd/Al_2O_3 by Operando Spectroscopy: A Multitechnique Modulated Excitation Study. *ACS Catalysis* **2020**, *10*, 4791–4804.
(29) Tew, M. W.; Miller, J. T.; Van Bokhoven, J. A. Particle Size Effect of Hydride Formation and Surface Hydrogen Adsorption of Nanosized Palladium Catalysts: L_3 Edge vs K Edge X-Ray Absorption Spectroscopy. *Journal of Physical Chemistry C* **2009**, *113*, 15140–15147.
(30) Shimizu, K. I.; Kamiya, Y.; Osaki, K.; Yoshida, H.; Satsuma, A. The Average Pd Oxidation State in Pd/SiO_2 Quantified by L_3-Edge XANES Analysis and Its Effects on Catalytic Activity for CO Oxidation. *Catalysis Science and Technology* **2012**, *2*, 767–772.
(31) Dann, E. K.; Gibson, E. K.; Blackmore, R. H.; Catlow, C. R. A.; Collier, P.; Chutia, A.; Erden, T. E.; Hardacre, C.; Kroner, A.; Nachtegaal, M.; Raj, A.; Rogers, S. M.; Taylor, S. F. R.; Thompson, P.; Tierney, G. F.; Zeinalipour-Yazdi, C. D.; Goguet, A.; Wells, P. P. Structural Selectivity of Supported Pd Nanoparticles for Catalytic NH_3 Oxidation Resolved Using Combined Operando Spectroscopy. *Nature Catalysis* **2019**, *2* (2), 157–163.
(32) Yasumura, S.; Ide, H.; Ueda, T.; Jing, Y.; Liu, C.; Kon, K.; Toyao, T.; Maeno, Z.; Shimizu, K. Transformation of Bulk Pd to Pd Cations in Small-Pore CHA Zeolites Facilitated by NO. *JACS Au* **2021**, *1*, 201–211.
(33) Che, M.; Dutel, J. F.; Gallezot, P.; Primet, M. A Study of the Chemisorption of Nitric Oxide on PdY Zeolite. Evidence for a Room Temperature Oxidative Dissolution of Pd Crystallites. *Journal of Physical Chemistry* **1976**, *80*, 2371–2381.
(34) Aylor, A. W.; Lobree, L. J.; Reimer, J. A.; Bell, A. T. Investigations of the Dispersion of Pd in H-ZSM-5. *Journal of Catalysis* **1997**, *172*, 453–462.
(35) Paredis, K.; Ono, L. K.; Behafarid, F.; Zhang, Z.; Yang, J. C.; Frenkel, A. I.; Cuenya, B. R. Evolution of the

Structure and Chemical State of Pd Nanoparticles during the in Situ Catalytic Reduction of NO with H_2. *Journal of the American Chemical Society* **2011**, *133*, 13455–13464.

(36) Sedlmair, C.; Seshan, K.; Jentys, A.; Lercher, J. A. Elementary Steps of NOx Adsorption and Surface Reaction on a Commercial Storage-Reduction Catalyst. *Journal of Catalysis* **2003**, *214*, 308–316.

(37) Brown, W. A.; King, D. A. NO Chemisorption and Reactions on Metal Surfaces: A New Perspective. *Journal of Physical Chemistry B* **2000**, *104* (12), 2578–2595.

(38) Fanson, P. T.; Horton, M. R.; Delgass, W. N.; Lauterbach, J. FTIR Analysis of Storage Behavior and Sulfur Tolerance in Barium-Based NOx Storage and Reduction (NSR) Catalysts. *Applied Catalysis B: Environmental* **2003**, *46*, 393–413.

(39) Jing, Y.; Cai, Z.; Liu, C.; Toyao, T.; Maeno, Z.; Asakura, H.; Hiwasa, S.; Nagaoka, S.; Kondoh, H.; Shimizu, K. Promotional Effect of La in the Three-Way Catalysis of La-Loaded Al_2O_3-Supported Pd Catalysts (Pd/La/Al_2O_3). *ACS Catalysis* **2020**, *10*, 1010–1023.

(40) Honkanen, M.; Wang, J.; Kärkkäinen, M.; Huuhtanen, M.; Jiang, H.; Kallinen, K.; Keiski, R. L.; Akola, J.; Vippola, M. Regeneration of Sulfur-Poisoned Pd-Based Catalyst for Natural Gas Oxidation. *Journal of Catalysis* **2018**, *358*, 253–265.

(41) Kwak, J. H.; Hu, J.; Lukaski, A.; Kim, D. H.; Szanyi, J.; Peden, C. H. F. Role of Pentacoordinated Al^{3+} Ions in the High Temperature Phase Transformation of γ-Al_2O_3. *Journal of Physical Chemistry C* **2008**, *112*, 9486–9492.

(42) Choi, M.; Song, J.; Lee, E.; Ma, S.; Lee, S.; Seo, J.; Yoo, S.; Lee, J. The Development of a Nox Reduction System during the Fuel Cut Period for Gasoline Vehicles. In *SAE Technical Papers*; SAE International, 2019; Vol. 2019-April.

(43) Machida, M.; Ueno, M.; Omura, T.; Kurusu, S.; Hinokuma, S.; Nanba, T.; Shinozaki, O.; Furutani, H. CeO_2-Grafted Mn-Fe Oxide Composites as Alternative Oxygen-Storage Materials for Three-Way Catalysts: Laboratory and Chassis Dynamometer Tests. *Industrial and Engineering Chemistry Research* **2017**, *56*, 3184−3193.

Chapter 4

Roles of the Basic Metals La, Ba and Sr as Additives in Al_2O_3-supported Pd-based Three-Way Catalysts

4.1 Introduction

Three-way catalysts (TWCs) provide an efficient means of reducing the pollutant emissions from gasoline-powered vehicles, by simultaneously removing compounds such as NO_x, CO and hydrocarbons (HCs) [1–3]. These catalysts are typically made of platinum group metals (PGMs), including Pt, Pd and Rh [4,5], because these elements exhibit superior catalytic performance and durability in comparison to nonprecious metals such as Cu, Ni and Fe [6–9]. As the regulatory requirements to reduce automotive emissions become increasingly strict, the development of effective support materials to improve the catalytic performance of PGMs is of great importance [10–13].

Al_2O_3 is widely used as a support material in TWCs because it has the advantages of possessing suitable mechanical strength, relatively good thermal stability and a high surface area [14,15]. Alkaline and alkaline earth metals as well as lanthanides are frequently combined with Al_2O_3 as structural stabilizers to suppress the transformation of Al_2O_3 from the γ to α phase [16–21]. Certain basic metals, such as La and Ba, are also known to stabilize Pd species during thermal treatment, resulting in improved dispersion of the Pd [22–25]. However, to date, only limited studies have been conducted to investigate the promotional effect of these basic metal additives on the catalytic performances of TWCs [26–30]. As an example, Muraki and coworkers reported that the addition of La promoted the NO_x chemisorption, leading to the selective reduction of NO_x rather than O_2, and also inhibited the HCs adsorption on Pd, resulting in more efficient reduction of NO_x [31–34]. In addition, Sekiba et al confirmed that the introduction of La_2O_3 and BaO into a $Pd/CeO_2/Al_2O_3$ catalyst enhanced the catalytic performance of this material during NO conversion under reducing conditions [35]. Kobayashi and co-workers have also reported that the abilities of Pd-based catalysts to catalytically remove NO_x were improved following the addition of basic elements, including La, Ba and Sr [36]. Prior reports such as these have suggested that the electron densities of Pd species are increased by the addition of these elements. Our own group recently reported work assessing the promotional effect of La in La-loaded Al_2O_3-supported Pd ($Pd/La/Al_2O_3$) catalysts serving as TWCs [37,38]. These prior studies demonstrated that metallic Pd^0 species in $Pd/La/Al_2O_3$ are more electron-deficient than those in Pd/Al_2O_3, which in turn suppresses the poisoning effect of CO and increases the catalytic activity for the removal of NO. Moreover, we reexamined the effective loading amount of La, which has conventionally been in the range of 3–5 wt%, with the aim of optimizing the specific surface area of the La/Al_2O_3 supports, and found that substantially increasing the La loading to 15 wt% provided a more effective TWC that was more reactive with NO, and suppressed the poisoning effect of CO. Although such work greatly contributed to the body of knowledge concerning TWCs, our present understanding of the roles of basic metal

additives in reactions over Pd-based catalysts remains insufficient. It would therefore be highly beneficial to systematically investigate the functions of such additives in TWCs so as to develop efficient support materials that maximize the catalytic activity of Pd, which is the most commonly used active metal in modern commercial TWCs [39–41].

The present study performed a systematic investigation of the promotional effect of the basic metals La, Ba and Sr on the TWC process. A series of $Pd/M/Al_2O_3$ catalysts (M = La, Ba or Sr) was synthesized and these materials were investigated using various spectroscopic methods together with kinetics analyses. The results showed that metallic Pd^0 species loaded on Ba/Al_2O_3 and Sr/Al_2O_3 were more electron-rich than those on Al_2O_3, while the Pd^0 species on La/Al_2O_3 were more electron-deficient. The present data also indicated that $Pd/La/Al_2O_3$ promoted the catalytic reduction of NO most efficiently and that $Pd/Ba/Al_2O_3$ showed higher catalytic activity for the oxidations of C_3H_6 and CO.

4.2 Methods

4.2.1 Preparation of catalysts

Commercially available γ-Al_2O_3 was used as the support, and the introduction of basic metal (La, Ba, or Sr) to Al_2O_3 was carried out as described in previous studies [37,38]. The basic-metal-loaded Al_2O_3 was dried at 120 °C for 2 h, followed by calcination in air at 600 °C for 2 h and were noted as M/Al_2O_3 (M = La, Ba, or Sr). The corresponding supported Pd (3wt % Pd) catalysts were prepared by the impregnation method with an aqueous $Pd(NH_3)_2(NO_2)_2$ as a precursor. The mixture was then stirred for 15 min (200rpm) at room temperature. After stirring, the mixture was evaporated to dryness at 50 °C under reduced pressure, dried at 90 °C for 12 h, and calcined in air at 300, 500 or 600 °C for 3h. Afterward, the calcined samples were pretreated under a flow of H_2 (20ml/min) at 500 °C for 0.5 h in a Pyrex tube. The samples pretreated under the flow of H_2 were used for the characterization experiments unless otherwise stated. Before each catalytic activity test and *in situ/operando* experiments, the samples were reduced again under flowing 10%H_2/He (100 mL/min) at 400 °C for 0.5 h.

The slurry, which was composed of an inorganic binder, the calcined catalyst powders, and water, was coated onto a cordierite honeycomb (25.4 mmφ × 50 mm, 400 cells/in^2; NGK Insulators, Ltd.) to prepare the monolithic honeycomb catalysts. The thus prepared monolithic honeycomb catalysts were dried in air at 120 °C for 1h, followed by calcination at 600 °C for 2 h.

Monolithic honeycomb catalysts were aged at 1000 °C for 4 h under hydrothermal redox conditions. The gas compositions for rich (3% H_2, 3% CO, 10% H_2O, and N_2 balance), lean (3% O_2, 10% H_2O, and N_2 balance), and stoichiometric (10% H_2O and N_2 balance) conditions were applied with intervals of 180 s for rich, 10 s for stoichiometric, 180 s for lean, and 10 s for stoichiometric atmospheres with flow rate = 3 L/min (space velocity (SV) = 7,200 h^{-1}).

4.2.2 Catalyst characterization

X-ray diffraction (XRD) patterns were measured using Cu-Kα radiation using Miniflex (Rigaku). N_2 adsorption measurements were conducted using AUTOSORB 6AG (Yuasa Ionics). High-angle annular dark-field scanning transmission electron microscopy (HAADF-STEM) images were collected using JEM-ARM200F (JEOL). CO-adsorption experiments were performed at -20 °C using BELCAT (MicrotracBEL).

X-ray photoelectron spectroscopy (XPS) was performed on ESCA-3400HSE (Shimadzu), equipped with a modified UHV chamber using Mg Kα radiation. Binding energies were calibrated using the Al2s peak of Al_2O_3 (119.5 eV). The reduced samples were measured after the H_2 reduction using an Ar-filled glove box to avoid exposure of the samples to air.

4.2.3 (*Operando/in situ*) infrared (IR) spectroscopy

Operando IR measurements were carried out at 150 °C using FT/IR-4200 (JASCO) with a Mercury-Cadmium-Telluride (MCT) detector. Samples (40 mg) were pressed to make pellets (ϕ = 20 mm), which were placed in the quartz IR cell having CaF_2 windows. The samples were heated under flowing 10% H_2/He (100 mL min^{-1}) at 400 °C for 0.5 h prior to the measurements. After cooling to 150 °C under flowing He, 0.5% NO/He was introduced for 10 min. After being purged by He for 10 min, 1% CO/He was introduced into the system for 10 min. The composition of the eluent was analyzed by a high-sampling-rate TCD GC (490 Micro GC; Agilent) and IR gas cell (JASCO FT/IR-4100). A reference spectrum, recorded at 150 °C under a flow of pure He, was subtracted from each spectrum.

The *in situ* IR measurements for CO adsorption was carried out at 40 °C by using the same apparatus described above. Prior to the adsorption experiments, the samples were exposed to 10% H_2/He for 30 min at 400 °C, followed by cooling to 40 °C under the flow of He. *In situ* IR spectra were collected after the introduction of CO, followed by purge in the flow of He for 10 min.

4.2.4 (*Operando*) X-ray absorption spectroscopy (XAS)

X-ray absorption spectroscopy (XAS) were performed in transmittance mode at the BL14B2 beamline of SPring-8 with a Si(311) double crystal monochromator. For measurements at the La, Ba and Sr K-edges, samples were sealed in polyethylene cells in air, and the spectra were measured at room temperature. For *operando* Pd K-edge XAS measurements, the high-sampling-rate TCD GC was employed for the analysis of N_2, N_2O, and CO. 150 mg of the samples in pellet form (φ: 10 mm) were added into a quartz cell with Kapton film windows. The catalyst was pretreated under a flow of 5% H_2/He (200 mL min^{-1}) at 400 °C for 0.5 h, followed by cooling to 150 °C. Subsequently, 0.5% NO/He, 0.5% CO/He, and 0.5%NO+0.5%CO/He (1000 mL min^{-1}) were introduced. The SV employed was ~ 30, 000 h^{-1}. The analysis was performed using Athena software ver. 0.9.25 included in the Demeter package [42]. The Fourier transformation of the k^3-weighted extended X-ray absorption fine structure (EXAFS) was carried out over a *k* range of 3–12 $Å^{-1}$.

4.2.5 Catalytic reactions

For the catalytic NO–CO reaction using the powdered catalysts, 15 mg of the catalyst was placed in a reactor using quartz wool in the catalyst bed. After the reduction of the catalyst under 10% H_2/He flow (100 mL min^{-1}) at 400°C for 0.5 h, the catalyst was cooled to 100 °C and the catalytic NO–CO reaction was started by supplying a gas mixture (0.5% CO, 0.5% NO, and He) at 100 mL·min^{-1} (*W*/*F* corresponds to 1.5×10^{-4} g·min·cm^{-3}). Products were analyzed by GC (Shimadzu

GC-8A with a SHINCARBON ST column). The yields were calculated based on the following equation.

$$NO + CO \rightarrow 0.5\ N_2 + CO_2 \quad (1)$$

For the catalytic NO–C_3H_6 reaction using the powdered catalysts, a mixed gas containing 0.45% NO and 0.05% C_3H_6 (He balance) was fed to 15mg catalysts at 100 mL min^{-1} (*W*/*F* corresponds to 1.5×10^{-4} g·min·cm^{-3}) after the reduction under the flow of 10% H_2/He at 400°C for 0.5 h and cooling to 200 °C. The yield was calculated based on the following equation.

$$9NO + C_3H_6 \rightarrow 4.5\ N_2 + 3\ CO_2 + 3H_2O \quad (2)$$

For catalytic reactions on the honeycomb catalysts using MEXA-series (Horiba Ltd.), the catalysts were placed in a tubular-type reactor, and their catalytic performance was investigated by supplying a gas mixture containing NO, CO, C_3H_6, O_2, H_2, CO_2, H_2O, and N_2 balance at SV = 100,000 h^{-1}. Conversions of NO, CO, and C_3H_6, were monitored using a gas analyzer (ABB, AO-2020). Before each catalytic activity test, the honeycomb catalyst was pre-treated under a flow of the reaction gas (1 Hz perturbation between λ = 0.95 and λ = 1.05) at 400 °C for 0.5 h, followed by cooling to 100 °C under N_2. The λ values were calculated according to the following equation (see **Tables 1** for detailed gas compositions).

$$\lambda = \frac{O_2 + 0.5CO + 0.5H_2O + CO_2 + 0.5NO}{0.5H_2 + CO + 1.5C_3H_6 + 0.5H_2O + CO_2} \quad (3)$$

Table 1. Composition of the simulated exhaust gas mixtures for TWC light-off tests.

λ	NO / %	CO / %	C_3H_6 / ppm	O_2 / %	H_2 / %	CO_2 / %	H_2O / %	N_2 / %
0.95	0.1	2.4	420	0.6	0.8	15	10	balance
1.00	0.1	0.6	420	0.6	0.2	15	10	balance
1.05	0.1	0.6	420	1.65	0.2	15	10	balance

4.3 Results and discussion

4.3.1 Catalysts characterization

The conditions used to prepare the $Pd/M/Al_2O_3$ and Pd/Al_2O_3 catalysts as well as the physicochemical properties of these materials are summarized in **Table 2**. We have employed higher Pd loading of 3 wt% in the present research than that used in the previous study (1 wt%) for ease of various measurements. Note that the 3 wt% Pd loading is within the range for the real-world applications. The loading amount of M was adjusted to be the same in the mol% (6.4, 10 and 10 wt% for Sr, Ba and La, respectively) The average Pd particle size in each catalyst was adjusted to approximately 6 nm by controlling the calcination temperature. Pd/Al_2O_3 was found to have a higher Brunauer–Emmett–Teller (BET) surface area compared with the $Pd/M/Al_2O_3$ series of samples in the as-prepared state (fresh). The XRD patterns provided in **Figure 1** demonstrate that each catalyst generated broad diffraction peaks attributable to γ-Al_2O_3. Peaks related to $BaCO_3$ and $SrCO_3$ were also present in the XRD patterns obtained from the $Pd/Ba/Al_2O_3$ and $Pd/Sr/Al_2O_3$ catalysts, respectively, confirming the presence of these carbonate species. These results are consistent with previous reports [37,38].

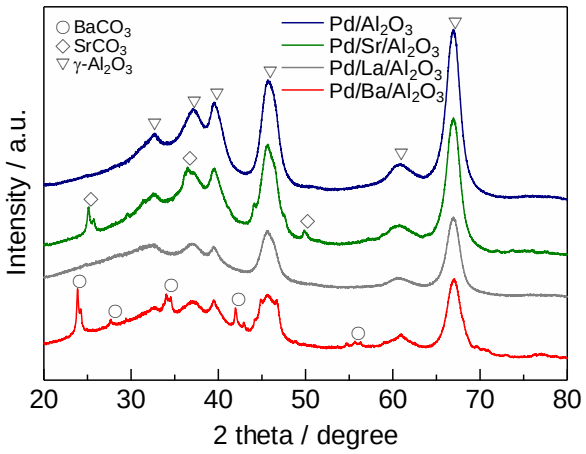

Figure 1. XRD patterns of Pd/Al_2O_3 and $Pd/M/Al_2O_3$ (M = La, Ba, or Sr) catalysts.

Characterization of the M/Al_2O_3 specimens using HAADF-STEM demonstrated that La, Ba and Sr were thoroughly dispersed on the atomic level over the γ-Al_2O_3 support (**Figure 2**). The data acquired from characterizations of the samples and of reference compounds using XAS at the La, Ba and Sr K edges are presented in **Figure 3**. Curve-fitting analyses of the EXAFS results are summarized in **Table 3** and show that the spectrum of each $Pd/M/Al_2O_3$ specimen contained only a single M–O contribution. It is therefore evident that La, Ba and Sr were all atomically dispersed on the γ-Al_2O_3, in agreement with the HAADF-STEM assessments and with reports based on earlier studies of similar materials [37,38,43–45].

Table 2. Preparation conditions and physicochemical characteristics of Pd/Al_2O_3 and $Pd/M/Al_2O_3$.

Catalyst[a]	Loading amount of M	$T_{Calcination}$ / °C	$T_{H2\ reduction}$ / °C	S_{BET} / $m^2\ g^{-1}$	CO adsorbed[b] / $\mu mol\ g^{-1}$	Particle size of Pd[c] / nm
Pd/Al_2O_3	-	600	500	155	52.6	6.0
$Pd/Sr/Al_2O_3$	6.4 wt%	500	500	146	51.9	6.1
$Pd/Ba/Al_2O_3$	10 wt%	300	500	139	47.8	6.5
$Pd/La/Al_2O_3$	10 wt%	500	500	134	55.1	5.7

[a]Pd loading amount = 3 wt%. [b]Measured at at -20 °C. [c]Estimated from the CO adsorption experiments.

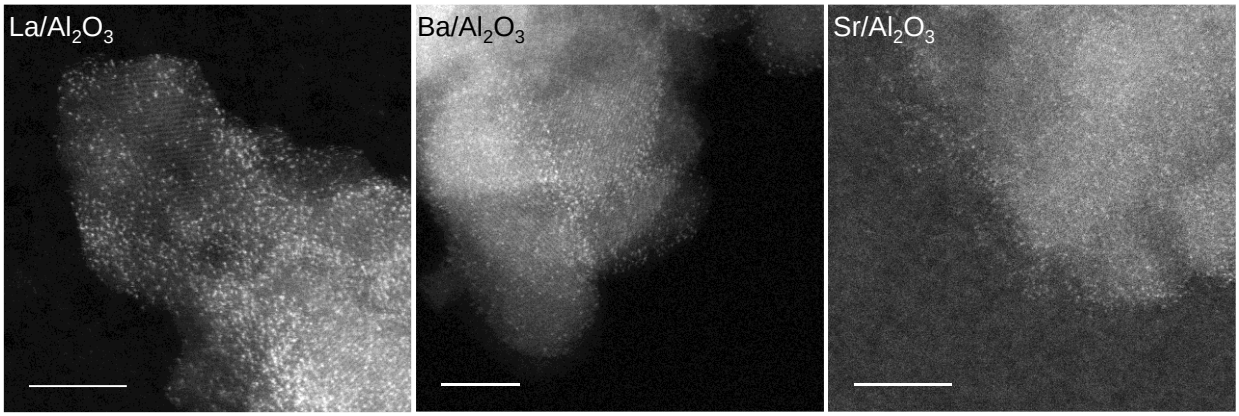

Figure 2. HAADF-STEM images of the M/Al_2O_3 (M = La, Ba or Sr) supports.

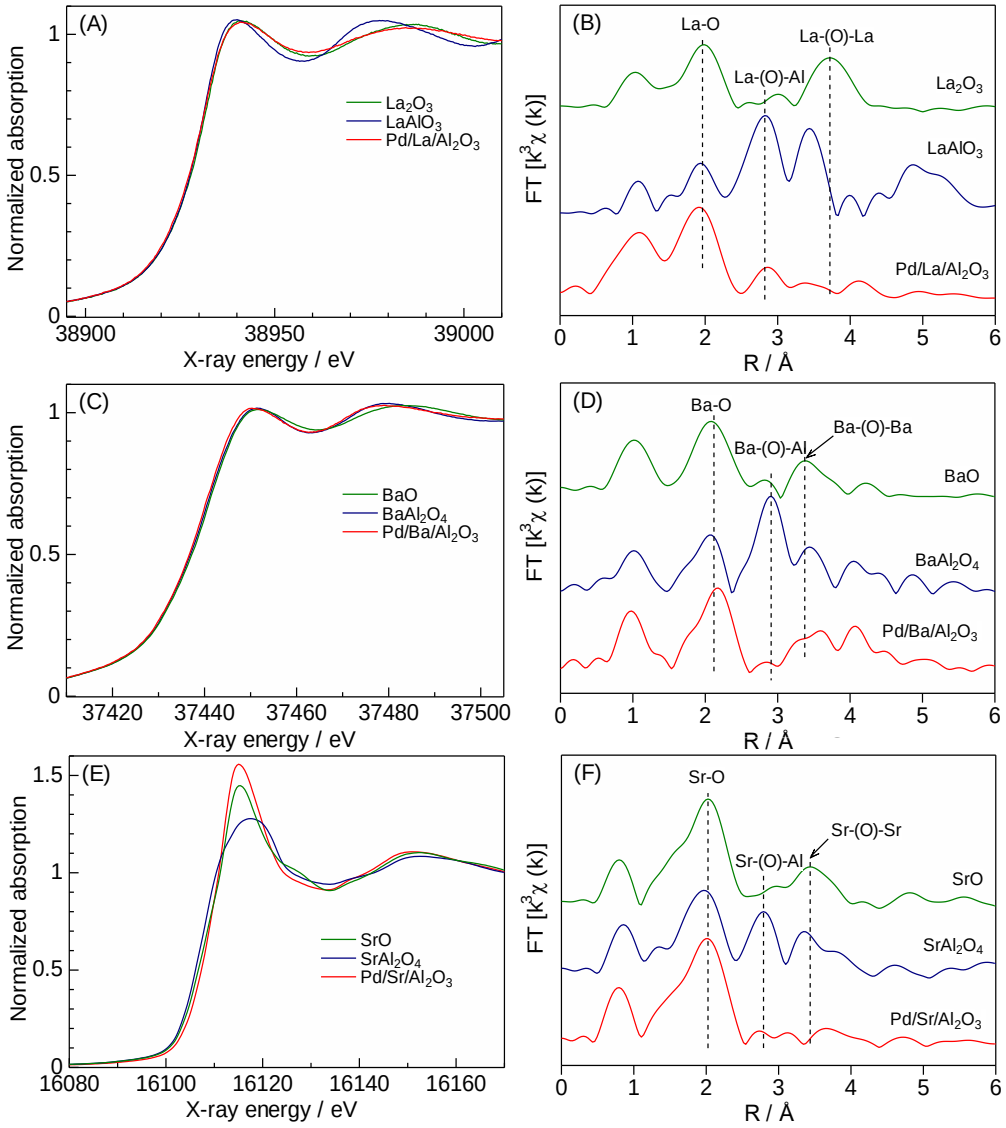

Figure 3. The La, Ba, and Sr K-edge (A, C, E) XANES spectra and (B, D, F) k^3-weighted EXAFS Fourier transforms of Pd/M/Al_2O_3 (M = La, Ba, or Sr) catalysts.

Table 3. Curve-fitting analysis of La, Ba and Sr K-edge EXAFS for Pd/M/Al_2O_3 (M = La, Ba, or Sr).

Sample	Shell	CN [a]	*R* (Å) [b]	σ^2 (Å^2) [c]	R_f (%) [d]
Pd/La/Al_2O_3	La–O	5.2	2.54	0.014	0.60
Pd/Ba/Al_2O_3	Ba–O	4.5	2.76	0.011	0.36
Pd/Sr/Al_2O_3	Sr–O	5.0	2.58	0.012	0.79

[a] Coordination number. [b] Bond distance. [c] Debye-Waller factor. [d] Residual factor.

The electronic structures of the Pd nanoparticles in the Pd/Al_2O_3 and Pd/M/Al_2O_3 catalysts were assessed using IR spectroscopy in conjunction with CO adsorption as well as XPS. **Figure 4A** presents the *in situ* IR spectra acquired from the Pd catalysts following CO adsorption. In these spectra, the peak at approximately 2080 cm^{-1} is attributed to CO molecules bound to the

on-top sites of metallic surfaces [46]. The centers of the peaks generated by the $Pd/Ba/Al_2O_3$ and $Pd/Sr/Al_2O_3$ appeared at lower wavenumbers (2078 and 2080 cm^{-1}, respectively) compared with the peak produced by the Pd/Al_2O_3 (2082 cm^{-1}), whereas the peak in the $Pd/La/Al_2O_3$ spectrum was located at a higher wavenumber (2084 cm^{-1}). It is well known that the adsorption strength of CO on transition metals is mostly determined by the contribution from π back-donation of transition metals to the CO $2\pi^*$ antibonding orbital, which is the lowest unoccupied molecular orbital (LUMO) [47,48]. The stronger the back-donation is, the weaker the C≡O bonds become, resulting in more activation of adsorbed CO molecules [49]. That is, in the present case, $\nu_{C=O}$ is weaker (red-shifted) when CO is adsorbed on negatively charged Pd due to the enhanced back-donation character of Pd to CO $2\pi*$ antibonding orbitals. Therefore, the metallic Pd^0 species supported on Sr/Al_2O_3 and Ba/Al_2O_3 were determined to be more electron-rich compared to those on pristine Al_2O_3, whereas those on La/Al_2O_3 were more electron-deficient.

Figure 4B provides Pd 3d XPS spectra obtained from the Pd/Al_2O_3 and $Pd/M/Al_2O_3$ specimens immediately after H_2 reduction, avoiding any subsequent exposure to air by using a glove box connected to the XPS sample chamber. These spectra include signals from both the $3d_{5/2}$ and $3d_{3/2}$ Pd core levels, and the $3d_{5/2}$ signal in the binding energy range of 335-336 eV can be assigned to metallic Pd [50–52]. Notably, the $3d_{5/2}$ signals generated by the $Pd/Sr/Al_2O_3$ (335.2 eV) and $Pd/Ba/Al_2O_3$ (335.3 eV) appeared at lower energies, while that produced by the $Pd/La/Al_2O_3$ (335.7 eV) was located at a higher energy compared with the result for the Pd/Al_2O_3 (335.5 eV). These data indicate that the Pd^0 species loaded on the Ba/Al_2O_3 and Sr/Al_2O_3 were more electron-rich but those on the La/Al_2O_3 were electron-poor relative to the Pd/Al_2O_3. Thus, the XPS spectra were consistent with the results of the *in situ* IR analyses following CO adsorption.

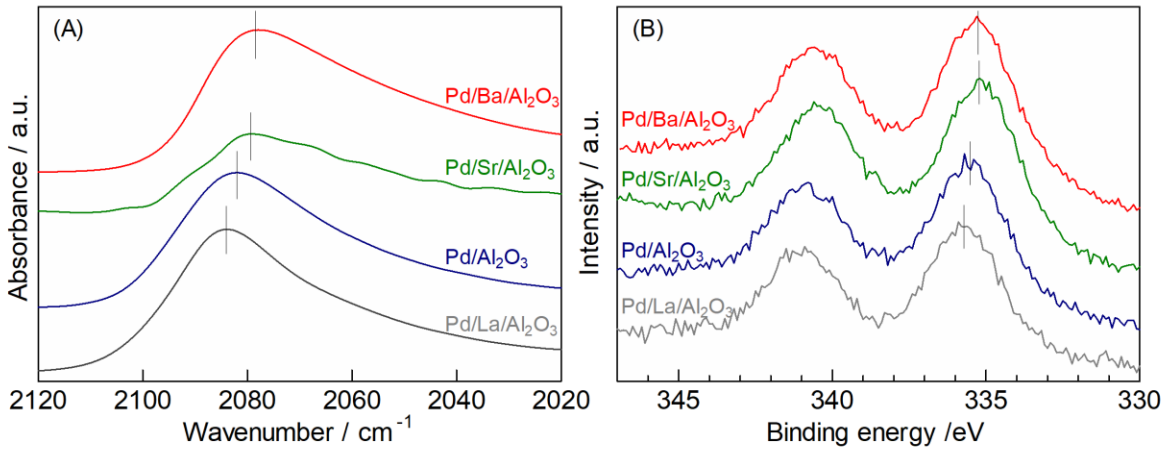

Figure 4. (A) *In situ* IR spectra of CO adsorbed on the Pd/Al_2O_3 and $Pd/M/Al_2O_3$ (M = La, Ba or Sr) catalysts. These spectra were collected under a flow of He following a 30 min exposure to CO. (B) Pd 3d XPS spectra for the Pd/Al_2O_3 and $Pd/M/Al_2O_3$ (M = La, Ba or Sr) catalysts. Spectra were obtained

from the samples immediately after H_2 reduction without any exposure to air using a glove box connected to the XPS chamber.

4.3.2 Promotional effect of the basic metal additives on the NO reduction activity

Figure 5 summarizes the catalytic conversions of NO during the NO–CO reaction, which is a primary $DeNO_x$ reaction [53–56], over the Pd/Al_2O_3 and $Pd/M/Al_2O_3$ catalysts in powder form under steady state conditions. The introduction of La, Ba or Sr evidently enhanced the catalytic conversions of both NO and CO, especially at low temperatures (below 250 °C). It should be noted that N_2O and CO_2 were the main products in this low temperature region, and mass balance was 100% for all the temperature regime. Also, we have performed Weisz-Prater analysis [57] and confirmed that our activity tests were performed in the kinetic regimes. The catalytic activities of these materials, in terms of the conversions of both NO and CO, were found to decrease in the order of $Pd/La/Al_2O_3$ > $Pd/Ba/Al_2O_3$ > $Pd/Sr/Al_2O_3$ > Pd/Al_2O_3. In addition, the NO–C_3H_6 reaction, which is another important primary $DeNO_x$ reaction [58,59], were also carried out to study the effect of basic metal additives on the NO reduction activity (**Figure 6**). $Pd/Ba/Al_2O_3$ showed the highest NO conversion at 300 °C, followed by $Pd/La/Al_2O_3$ and $Pd/Sr/Al_2O_3$. The results indicate that the introductions of La, Ba or Sr are also effective for the NO–C_3H_6 reaction.

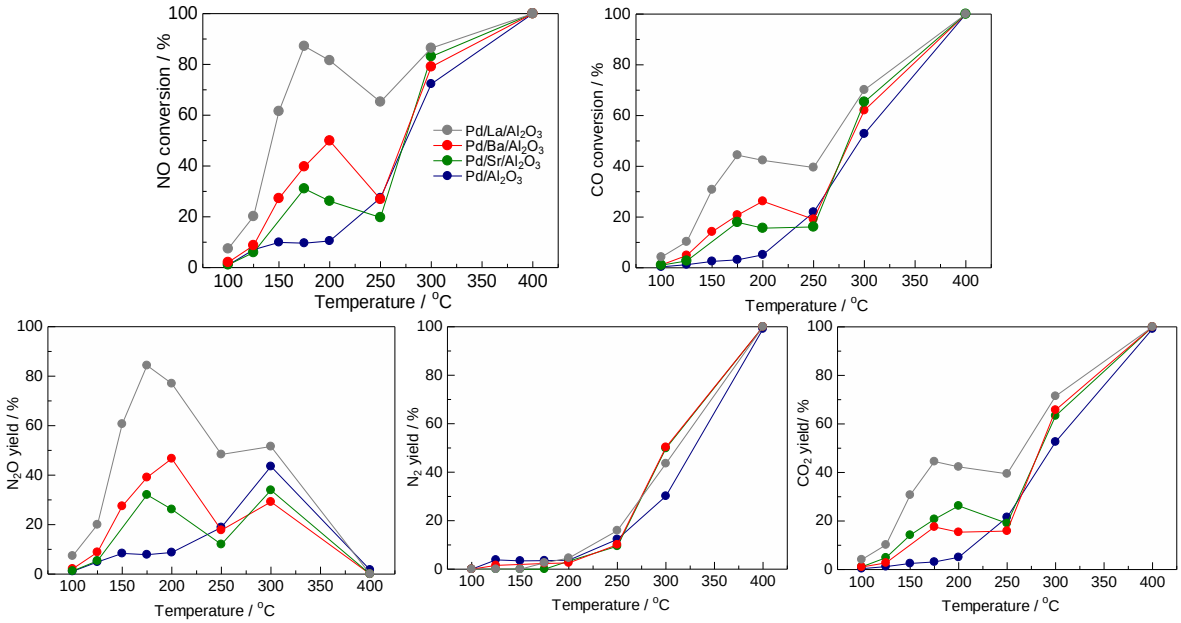

Figure 5. Catalytic NO–CO reaction over a powder sample of Pd/Al_2O_3 and $Pd/M/Al_2O_3$ (M = La, Ba or Sr). Gas condition: 0.5% NO, 0.5% CO and He balance.

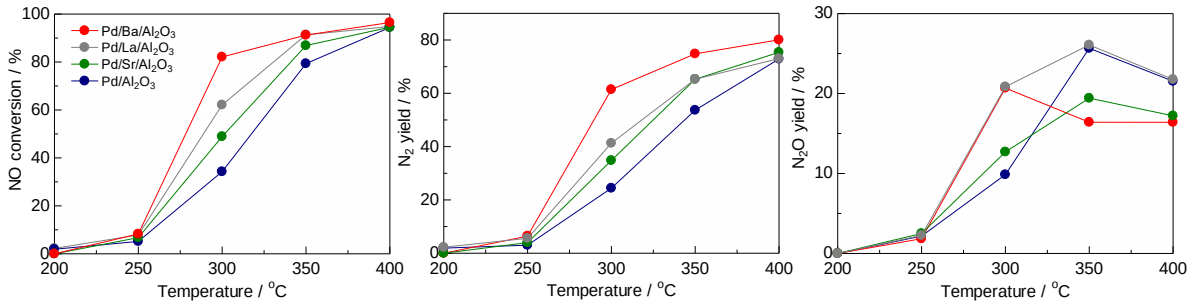

Figure 6. Catalytic NO–C_3H_6 reaction over a powder sample of Pd/Al_2O_3 and $Pd/M/Al_2O_3$ (M = La, Ba or Sr). Condition: 0.45 %NO, 0.05% C_3H_6, He balance.

To further investigate the role of these metals in the NO–CO reaction, the effects of the CO concentration on the reaction rates over Pd/Al_2O_3 and the $Pd/M/Al_2O_3$ specimens were examined, with the results presented in **Figure 7**. It should be noted that turnover frequency (TOF) based on reaction rates and amount of CO adsorbed (**Table 2**) were determined from the reaction data for NO conversions up to 30%. The apparent reaction orders based on these log-log plots with respect to CO were determined to be -0.50, -1.07, -1.00 and -0.94 over the $Pd/La/Al_2O_3$, $Pd/Ba/Al_2O_3$, $Pd/Sr/Al_2O_3$ and Pd/Al_2O_3, respectively. The negative values indicate that CO inhibited the NO–CO reaction over the catalysts used in the present study, in association with the strong adsorption of CO molecules on the surfaces of the supported Pd nanoparticles [60,61]. The apparent reaction order associated with the $Pd/La/Al_2O_3$ was more positive than that over the other catalysts, suggesting that the poisoning effect of CO was weakened following the introduction of La [37]. In contrast, the apparent reaction orders obtained for the $Pd/Ba/Al_2O_3$ and $Pd/Sr/Al_2O_3$ were more negative than that for the pristine Pd/Al_2O_3. The most probable explanation for these results is that electron-deficient Pd^0 species on the La/Al_2O_3 weakened the adsorption of CO molecules on the Pd surface, thus suppressing the poisoning effect of CO, whereas electron-rich Pd^0 species on the Ba/Al_2O_3 and Sr/Al_2O_3 enhanced this adsorption, thus promoting the poisoning effect. It should also be noted that the reduction in the CO poisoning effect obtained following La addition in the present study was less than that observed in previous work using $Pd/La/Al_2O_3$ with La and Pd loadings of 15 and 1 wt%, respectively. This discrepancy can presumably be ascribed to the larger Pd particle size resulting from the higher Pd loading of 3 wt% in the present research, which reduced the support effects to change the electronic properties of the supported Pd species.

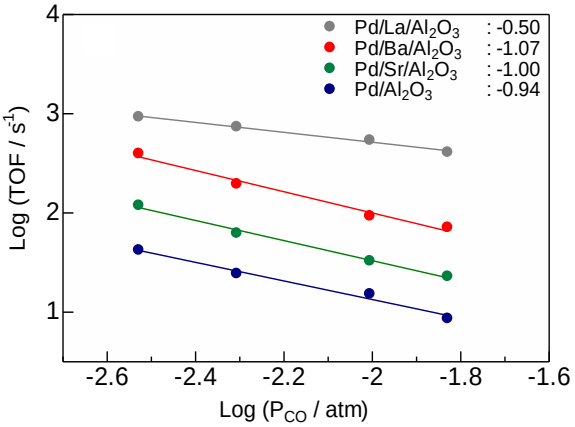

Figure 7. The log of the TOF as a function of the log of the CO concentration during the NO–CO reaction for each material. Conditions: 0.5% NO, 0.3-1.5% CO with He as the balance at 200 °C.

The effects of these metal additives on the chemical states of Pd during the NO–CO reaction were further investigated by performing *operando* Pd K-edge XAS analyses [62,63] under 0.5% NO/He, 0.5% CO/He or 0.5%NO+0.5%CO/He flows at 200 °C. Prior to analysis, each sample was pre-reduced at 500 °C under a flow of 10% H_2/He, and then reduced again in the XAS cell under 10% H_2/He at 400 °C just prior to the experiment. The *operando* Pd K-edge X-ray absorption near-edge structure (XANES) data and the FT of the k^3-weighted EXAFS spectra acquired under a 0.5% NO/He flow are shown in **Figures 8 and 9**. Note that the Pd/La/Al_2O_3 spectra are included in the main text as representative data. In each case, the absorption edge positions gradually shifted to higher energies following exposure to NO, while the intensity of the FT peak corresponding to Pd–Pd bonds (at approximately 2.5 Å) decreased. These results demonstrate that the Pd in these materials was oxidized by the NO. It was also found that no Pd–O contribution was seen in the FT of the k^3-weighted EXAFS spectra of Pd/Al_2O_3, which is in accordance with our previous study [37]. This lack of evidence for Pd–O bonds is attributed to the formation of oxidized and highly dispersed Pd species, which do not generate PdO species with well-defined Pd–O bonds. Similar phenomena have been reported for related materials [64–67]. In contrast, a Pd–O contribution was observed in the Pd/M/Al_2O_3 spectra, especially those of the Pd/La/Al_2O_3 and Pd/Ba/Al_2O_3. This finding reflects the strong anchoring effects of La and Ba, which would be expected to limit the deactivation of Pd species under the harsh TWC reaction conditions [24,25].

During these oxidation trials, N_2O was formed as the gas phase product and was monitored using a gas chromatograph with a thermal conductivity detector operating at a high sampling rate (**Figure 8C**). The Pd^0 fraction (Pd^0/(Pd^0+Pd^{II})) obtained from linear combination fitting of the XANES data indicated that the Pd species were oxidized by the NO introduced into

the system (**Figure 8D**). Thirty minutes after the introduction of NO, the Pd^0 fraction was determined to be 0.71 in the case of the $Pd/La/Al_2O_3$, which exhibited the highest level of oxidation among the four catalysts that were tested. After a He purge to remove residual gaseous NO, CO was introduced such that the partly oxidized Pd species were reduced with the simultaneous formation of N_2O and a small amount of CO_2. The results demonstrated that surface-adsorbed NO_x species that had been generated upon exposure to NO and retained during the He purge served as the source of N_2O. The incorporation of the basic metal additives evidently promoted the oxidation of Pd with decreasing effect in the order of La > Ba > Sr. It is also worth noting that the formation of CO_2 was observed along with the reduction of partially oxidized species. Based on these results, it is apparent that the NO–CO reaction over supported Pd catalysts comprises a redox cycle involving Pd species with NO as an oxidant and CO as a reductant.

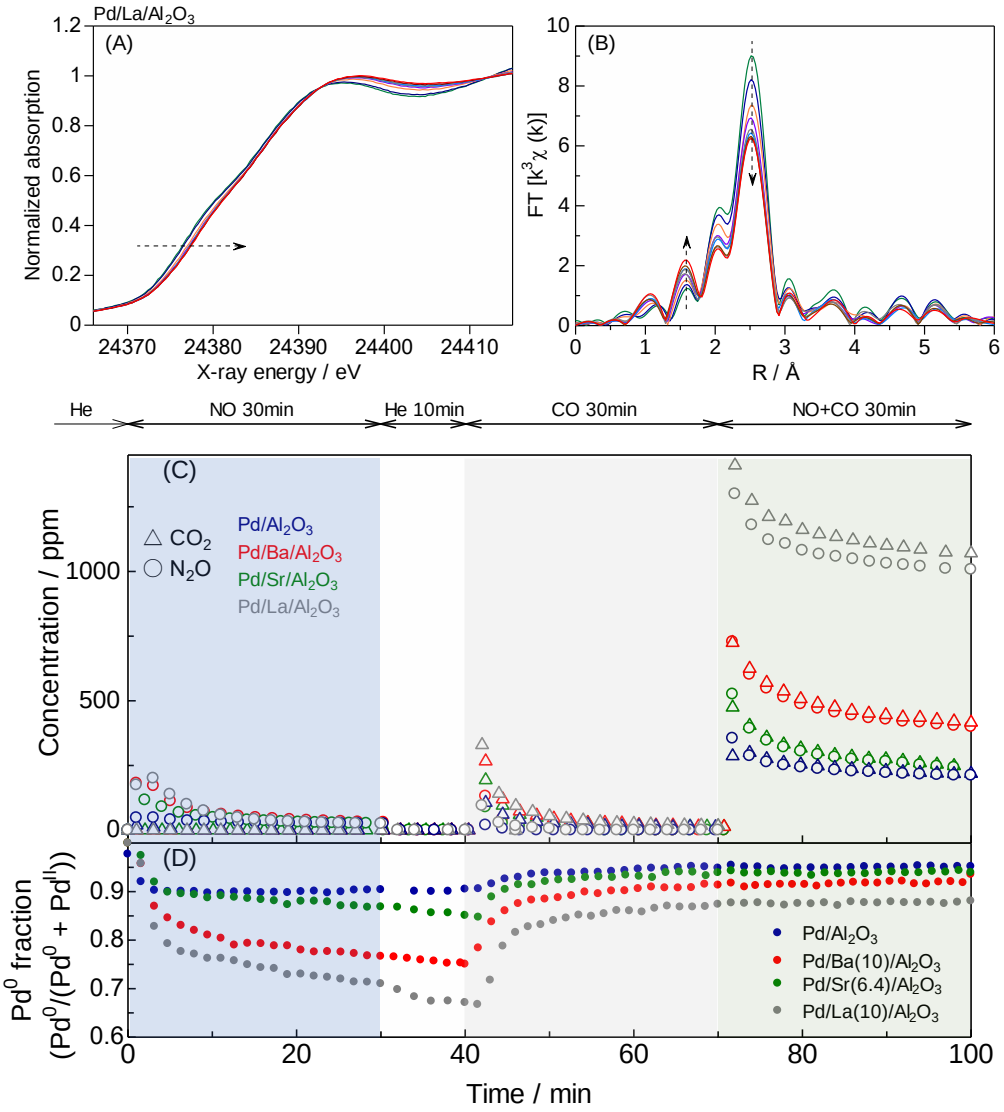

Figure 8. Results of the *operando* Pd K-edge XAS analyses. Pd K-edge (A) XANES spectra and (B) k^3-weighted EXAFS FTs for $Pd/La/Al_2O_3$, acquired under flowing 0.5% NO/He (1000 mL/min) at 150 °C after the pretreatment. Changes in (C) the product concentrations in the gas phase and (D) the fraction of Pd^0 under NO, CO and NO+CO flows at 150 °C.

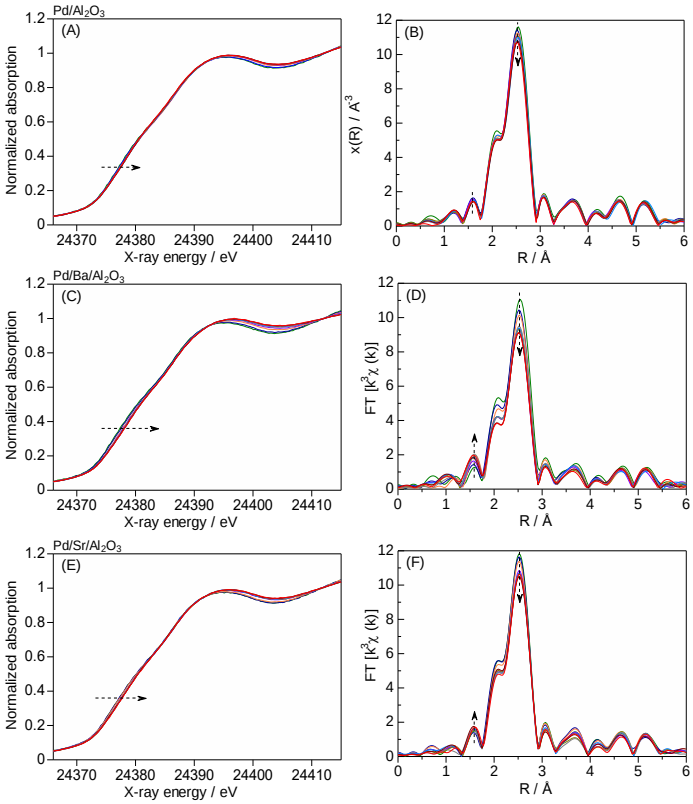

Figure 9. *Operando* Pd K-edge XANES spectra for and k^3-weighted EXAFS Fourier transforms for (A, B) Pd/Al_2O_3, (C, D) $Pd/Ba/Al_2O_3$, and (E, F) $Pd/Sr/Al_2O_3$ catalysts measured under the flow of 0.5% NO/He at 150 °C.

Operando IR data were acquired to assess the roles of La, Ba and Sr in the formation of surface adsorbed species as well as the reactivities of these metals during the NO reduction. The results are provided in **Figure 10**. These spectra were collected under a flow of He after the introduction of 0.5% NO/He for 30 min followed by a flow of 0.5% CO/He. Subsequent to exposure to NO, various NO_x species were produced on the surfaces of the catalysts, as reflected in the peaks that appeared in the 1100–1700 cm^{-1} region [68–70]. Specifically, the peaks at 1191 and 1232 cm^{-1} are attributed to surface nitrite species [38,71,72]. The intensities of these peaks in the spectra of each $Pd/M/Al_2O_3$ specimen were higher than that generated by the Pd/Al_2O_3, indicating that the introduction of La, Ba or Sr promoted the formation of surface nitrite species more efficiently. The absorption bands in the 1250-1650 cm^{-1} region are due to the presence of nitrate species with different adsorption modes [38,73–75]. The band at around 1660 cm^{-1} is assigned to Pd-adsorbed NO species [38,76,77]. Considering that the *operando* XAS data demonstrated that N_2O was formed when solely NO was introduced, it is believed that the disproportionation reaction of NO occurred to produce both gaseous N_2O and surface nitrite species on the $Pd/M/Al_2O_3$. It is also important to note that the peaks obtained from the $Pd/M/Al_2O_3$ samples were essentially absent in the spectra

generated by the M/Al_2O_3 without Pd (shown in seagreen), indicating the importance of combining Pd and M/Al_2O_3 as supports.

During the subsequent exposures of the Pd/Al_2O_3 and $Pd/M/Al_2O_3$ series to a flow of 0.5% CO/He, two strong peaks appeared at approximately 1560 and 1360 cm^{-1} that are attributed to carbonate adsorbed on the catalyst surfaces [78]. After the introduction of CO, the intensities of the peaks related to nitrite species on the $Pd/M/Al_2O_3$ samples decreased. As demonstrated in **Figure 10B**, the intensities of these peaks in the $Pd/La/Al_2O_3$ spectra declined more rapidly than in the $Pd/Ba/Al_2O_3$ and $Pd/Sr/Al_2O_3$ spectra, indicating that nitrites on the $Pd/La/Al_2O_3$ were more reactive with CO. Simultaneous with the decline in surface nitrite species, higher concentrations of N_2O and CO_2 were formed on the $Pd/La/Al_2O_3$ than on the $Pd/Ba/Al_2O_3$ and $Pd/Sr/Al_2O_3$, as shown in **Figure 10C**. This trend is in agreement with the results obtained during the catalytic NO–CO reaction trials described above. These data confirm that the efficient formation of nitrites and the reactivity of these species with CO played important roles in promoting the NO–CO reaction.

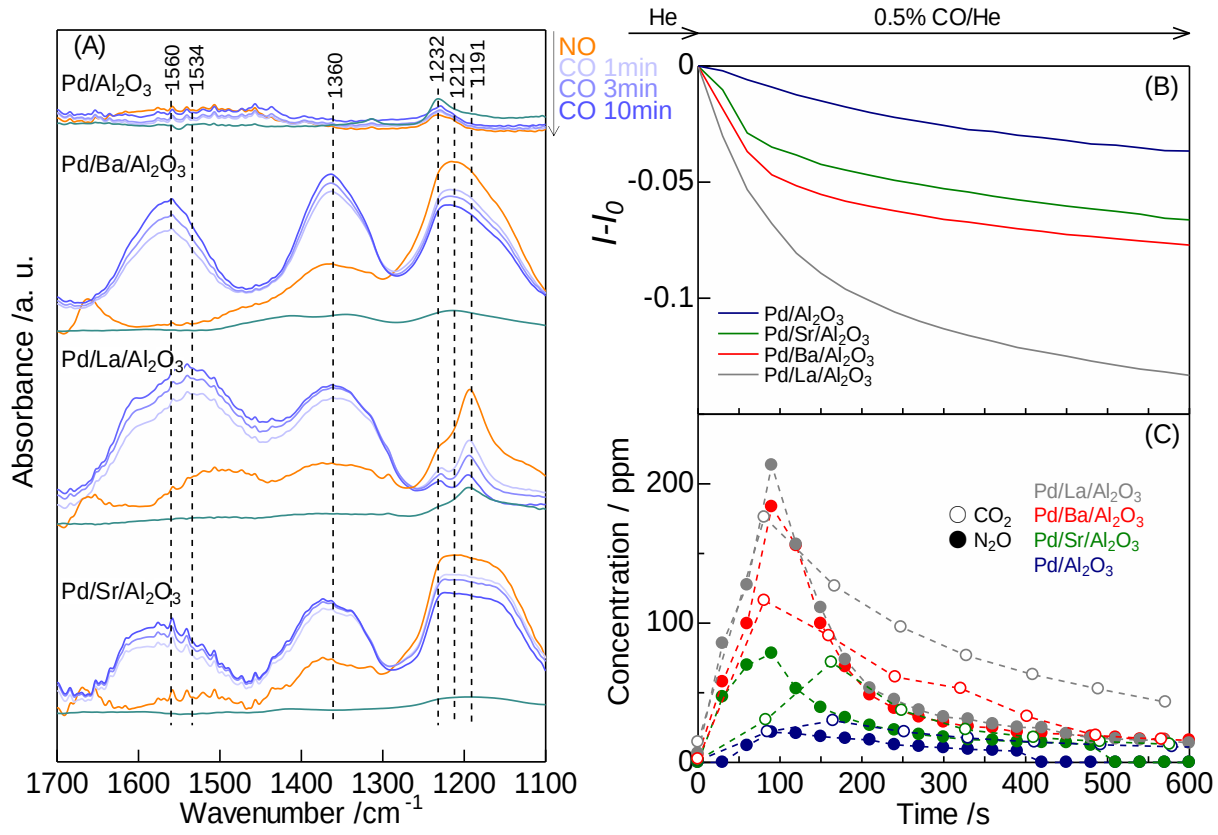

Figure 10. (A) *Operando* IR spectra showing the evolution of surface species adsorbed on the Pd/Al_2O_3 and $Pd/M/Al_2O_3$ (M = La, Ba or Sr) as well as the supports without Pd at 150 °C. The orange (Pd/Al_2O_3 and $Pd/M/Al_2O_3$) and seagreen (Al_2O_3 and M/Al_2O_3) spectra were collected under a flow of He after exposure to NO for 10 min. Subsequently, 0.5% CO/He was introduced into the cell in trials with the Pd/Al_2O_3 and $Pd/M/Al_2O_3$ and spectra were continuously acquired with simultaneous analysis of the gas phase products. Variations in (B) the intensities of peaks related to surface nitrite species and (C) the concentrations of N_2O and CO_2 in the effluent gas upon the introduction of 0.5% CO/He.

4.3.3 Catalytic activity test using honeycomb catalysts under TWC condition.

The results of TWC light-off tests over the honeycomb catalysts are shown in **Figure 11**. The fresh monolithic Pd/M/Al_2O_3 exhibited higher NO conversion than the Pd/Al_2O_3, suggesting that the basic metal additives enhanced the ability of these honeycomb materials to remove NO from automotive emissions under TWC conditions. In addition, the La-loaded catalyst exhibited a higher degree of NO conversion in comparison with the others, in agreement with the NO–CO reaction data and corresponding *operando* XAS and IR results. In contrast, throughout the C_3H_6 and CO oxidation trials, the Ba-loaded sample showed higher CO and C_3H_6 conversions relative to the materials incorporating Sr and La. Ba is known to provide exceptional performance when added to Pd/Al_2O_3 catalysts intended for the oxidation of HCs such as methane, especially in the presence of water vapor [23,79,80]. This promotional effect has been attributed to electron donation from the Ba to the Pd on the support, in agreement with the findings of the present study.

The stability of these honeycomb catalysts was investigated using aged catalysts that were exposed to hydrothermal redox conditions. Information concerning stability is vitally important with regard to real-world applications of these catalysts because they will be exposed to harsh conditions in association with dynamic changes in temperature and ambient atmosphere during use [81–83]. It is also important to note that the hydrothermal aging of such materials, as an aspect of TWC research, must be conducted under varying lean/stoichiometric/rich conditions to simulate the actual operating conditions [84,85]. Although the conversions of NO, CO and C_3H_6 over each of the catalysts decreased after the aging treatment, the aged Pd/M/Al_2O_3 catalysts still exhibited higher catalytic performance than the aged Pd/Al_2O_3. The data also indicated that La was the most effective additive in terms of NO conversion, while Sr and Ba promoted the oxidations of C_3H_6 and CO to the greatest extent. Again, the high oxidation activities observed following the addition of these electron-donating basic metals are in good agreement with previous studies in which the oxidations of HCs were examined using Pd/Al_2O_3 catalysts modified with these elements [79,80].

The aged catalysts were characterized by XRD and N_2 adsorption techniques as shown in **Figure 12**. Note that the powder catalysts were subjected to the hydrothermal aging treatment for these measurements. Sharp peaks related to metallic Pd were observed in each of the XRD patterns, indicating that the Pd nanoparticles had aggregated into large particles that were detectable by XRD during aging. Peaks attributed to $BaAl_2O_4$ and $SrAl_2O_4$ were also observed in the XRD patterns obtained from the aged Pd/Ba/Al_2O_3 and Pd/Sr/Al_2O_3, respectively, whereas the XRD pattern generated by the aged Pd/La/Al_2O_3 showed no peaks assignable to $LaAlO_3$. In addition, α-Al_2O_3 peaks appeared in the pattern of the aged Pd/Al_2O_3, suggesting a phase

transformation from γ-Al_2O_3 to α-Al_2O_3. Conversely, the aged Pd/M/Al_2O_3 materials were comprised mainly of γ-Al_2O_3, with no evidence of α-Al_2O_3 being formed. The Sr, Ba, and La K-edge EXAFS FTs for the aged materials are shown in **Figure 13**. Results of the curve fitting analysis of EXAFS summarized in **Table 4** show that the aged Pd/Sr/Al_2O_3 and Pd/Ba/Al_2O_3 catalysts only contained M–O contribution, and the aged Pd/La/Al_2O_3 catalyst comprises both La–O and slight La–(O)–Al contribution. The S_{BET} values for both the fresh and aged catalysts are given in **Figure 12B**. These data show that the Pd/M/Al_2O_3 specimens retained high surface areas during the aging. Therefore, the addition of basic metals appears to have enhanced the thermal stability of the Al_2O_3 in these materials. These results are in agreement with previous reports of research focused on improving the thermal stability of Al_2O_3 by using basic metal additives as modifiers [86].

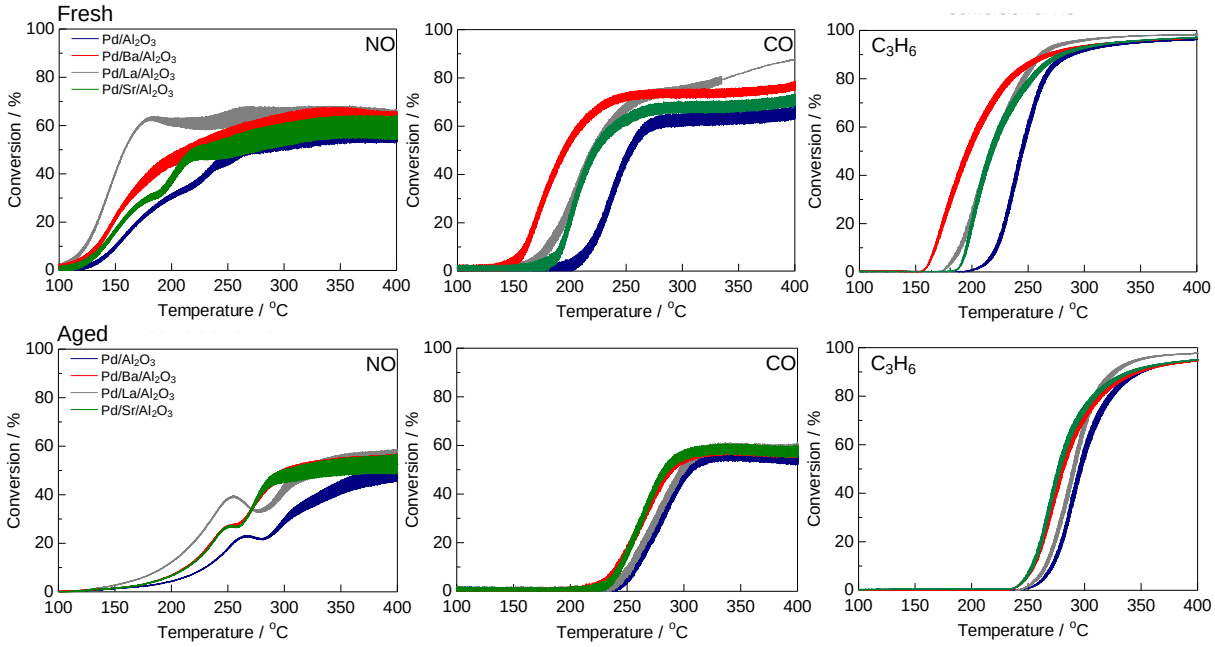

Figure 11. The conversions of NO, CO and C_3H_6 during TWC light-off tests over fresh and aged Pd/Al_2O_3-and Pd/M/Al_2O_3-coated honeycomb catalysts under gases perturbed at 1 Hz between λ = 0.95 and λ = 1.05. Heating rate: 25 °C/min; Gases: NO (0.1%), CO (2.4-0.6%), C_3H_6 (420 ppm), O_2 (0.6-1.65%), H_2 (0.8%), CO_2 (15%), H_2O (10%), N_2 balance; SV = 100,000 h^{-1}.

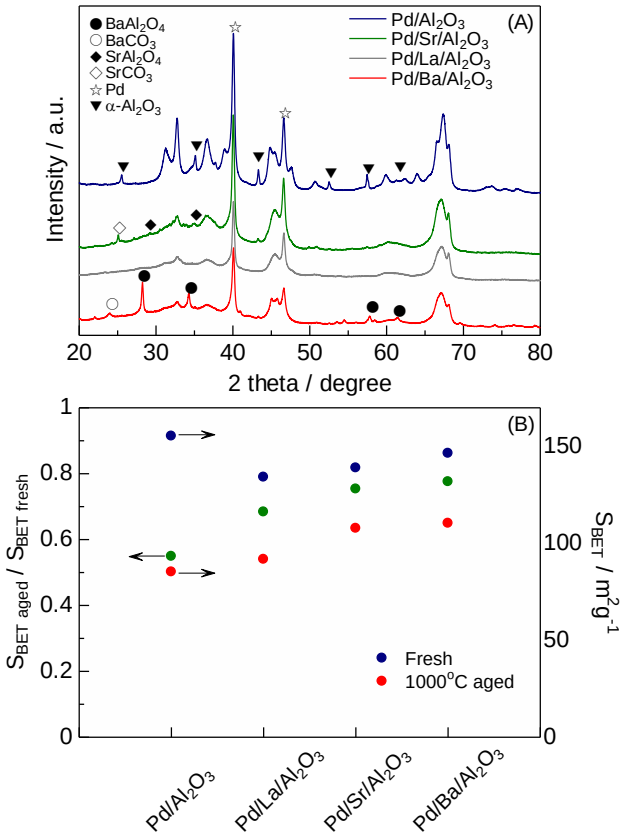

Figure 12. (A) XRD patterns obtained from aged Pd/Al_2O_3 and $Pd/M/Al_2O_3$ (M = La, Ba or Sr). (B) S_{BET} values of fresh ($S_{BET\ fresh}$) and aged ($S_{BET\ aged}$) Pd/Al_2O_3 and $Pd/M/Al_2O_3$ (M = La, Ba or Sr) and the ratios of $S_{BET\ aged}$ to $S_{BET\ fresh}$.

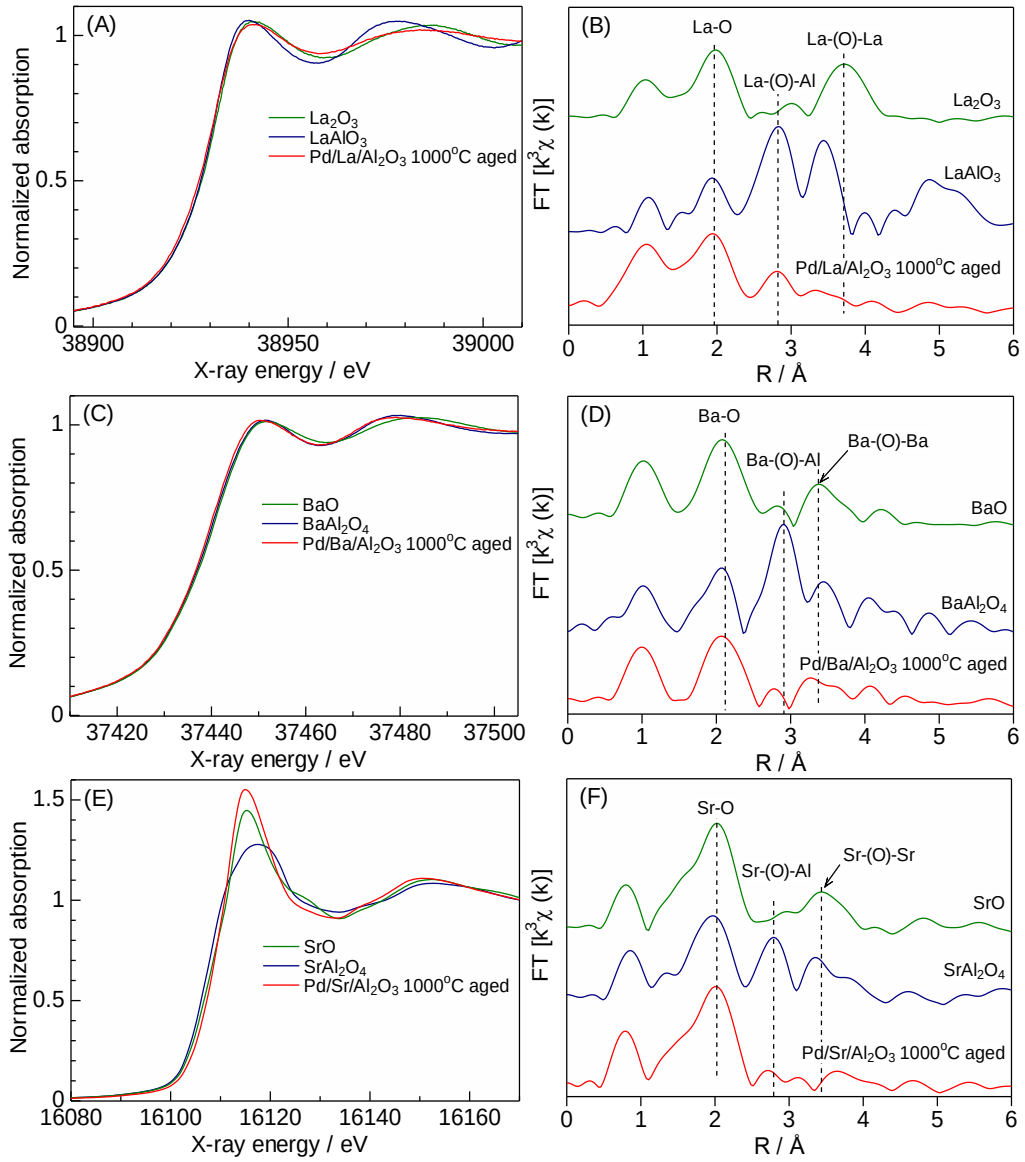

Figure 13. The La, Ba and Sr K-edge (A, C, E) XANES spectra and (B, D, F) k^3-weighted EXAFS Fourier transforms of $Pd/M/Al_2O_3$ (M = La, Ba, or Sr) catalysts after aging at 1000 °C.

Table 4. Curve-fitting analysis of La, Ba and Sr K-edge EXAFS for $Pd/M/Al_2O_3$ (M = La, Ba, or Sr) after aging at 1000 °C.

Sample	Shell	CN [a]	*R* (Å) [b]	σ^2 (Å^2) [c]	R_f (%) [d]
$Pd/La/Al_2O_3$	La–O	4.1	2.58	0.014	0.60
	La–(O)–Al	1.3	3.31	0.003	
$Pd/Ba/Al_2O_3$	Ba–O	4.5	2.76	0.011	0.36
$Pd/Sr/Al_2O_3$	Sr–O	5.0	2.58	0.012	0.79

[a] Coordination number. [b] Bond distance. [c] Debye-Waller factor. [d] Residual factor.

4.4 Conclusions

In this study, we examined the role of basic metal additives in $Pd/M/Al_2O_3$ (M = La, Ba or Sr) during the three-way catalytic process, using spectroscopic and kinetic measurements. Those catalysts loaded with the basic metals (the $Pd/M/Al_2O_3$ series) exhibited enhanced catalytic activity during the conversions of NO and CO. In addition, metallic Pd nanoparticles supported on La/Al_2O_3 were found to have a decreased electron density, such that the CO poisoning effect was suppressed. Conversely, Pd supported on Sr/Al_2O_3 and Ba/Al_2O_3 showed increased electron density. The presence of the atomically dispersed basic metals promoted the efficient formation of surface nitrite species, such that the $DeNO_x$ activity of the powdered catalysts was improved. Honeycomb-type monolithic catalysts were also prepared and their performance was examined under simulated TWC conditions. The results showed that the $Pd/M/Al_2O_3$ catalysts were superior in terms of promoting the reactions of NO, CO and C_3H_6 compared with the Pd/Al_2O_3 catalyst. $Pd/La/Al_2O_3$ was found to enhance NO reduction to a greater extent than the catalysts investigated in this work, while $Pd/Ba/Al_2O_3$ demonstrated superior catalytic performance during the oxidation of CO and C_3H_6.

References

(1) Wang, J.; Chen, H.; Hu, Z.; Yao, M.; Li, Y. A Review on the Pd-Based Three-Way Catalyst. *Catalysis Reviews* **2015**, *57*, 79–144.

(2) Matsumoto, S. Recent Advances in Automobile Exhaust Catalysts. *Catal Today* **2004**, *90*, 183–190.

(3) Shelef, M.; McCabe, R. W. Twenty-Five Years after Introduction of Automotive Catalysts: What Next? *Catal Today* **2000**, *62*, 35–50.

(4) Rood, S.; Eslava, S.; Manigrasso, A.; Bannister, C. Recent Advances in Gasoline Three-Way Catalyst Formulation: A Review. *Proceedings of the Institution of Mechanical Engineers, Part D: Journal of Automobile Engineering* **2020**, *234*, 936–949.

(5) Zheng, T.; Lu, B.; Harle, G.; Yang, D.; Wang, C.; Zhao, Y. A Comparative Study of Rh-Only, Pd-Only and Pd/Rh Catalysts. *Appl Catal A Gen* **2020**, *602*, 117649.

(6) Hosokawa, S.; Matsuki, K.; Tamaru, K.; Oshino, Y.; Aritani, H.; Asakura, H.; Teramura, K.; Tanaka, T. Selective Reduction of NO over Cu/Al_2O_3: Enhanced Catalytic Activity by Infinitesimal Loading of Rh on Cu/Al_2O_3. *Molecular Catalysis* **2017**, *442*, 74–82.

(7) Hirakawa, T.; Shimokawa, Y.; Tokuzumi, W.; Sato, T.; Tsushida, M.; Yoshida, H.; Hinokuma, S.; Ohyama, J.; Machida, M. Multicomponent Spinel Oxide Solid Solutions: A Possible Alternative to Platinum Group Metal Three-Way Catalysts. *ACS Catal* **2019**, *9*, 11763−11773.

(8) Ueda, K.; Tsuji, M.; Ohyama, J.; Satsuma, A. Tandem Base-Metal Oxide Catalyst: Superior NO Reduction Performance to the Rh Catalyst in $NO\text{-}C_3H_6\text{-}CO\text{-}O_2$. *ACS Catal* **2019**, *9*, 2866−2869.

(9) Ohyama, J.; Shibano, J.; Satsuma, A.; Fukuda, R.; Yamamoto, Y.; Arai, S.; Shishido, T.; Asakura, H.; Hosokawa, S.; Tanaka, T. Quantum Chemical Computation-Driven Development of Cu-Shell-Ru-Core Nanoparticle Catalyst for NO Reduction Reaction. *Journal of Physical Chemistry C* **2019**, *123* (33), 20251–20256.

(10) Yoon, D. Y.; Kim, Y. J.; Lim, J. H.; Cho, B. K.; Hong, S. B.; Nam, I. S.; Choung, J. W. Thermal Stability of Pd-Containing $LaAlO_3$ Perovskite as a Modern TWC. *J Catal* **2015**, *330*, 71–83.

(11) Farrauto, R. J.; Deeba, M.; Alerasool, S. Gasoline Automobile Catalysis and Its Historical Journey to Cleaner Air. *Nat Catal* **2019**, *2*, 603–613.

(12) Twigg, M. V. Catalytic Control of Emissions from Cars. *Catal Today* **2011**, *163*, 33–41.

(13) Li, L.; Zhang, N.; Wu, R.; Song, L.; Zhang, G.; He, H. Comparative Study of Moisture-Treated $Pd@CeO_2/Al_2O_3$ and $Pd/CeO_2/Al_2O_3$ Catalysts for Automobile Exhaust Emission Reactions: Effect of Core-Shell Interface. *ACS Appl Mater Interfaces* **2020**, *12*, 10350–10358.

(14) Machida, M.; Uchida, Y.; Ishikawa, Y.; Hinokuma, S.; Yoshida, H.; Ohyama, J.; Nagao, Y.; Endo, Y.; Iwashina, K.; Nakahara, Y. Thermostable Rh Metal Nanoparticles Formed on Al_2O_3 by High-Temperature H_2 Reduction and Its Impact on Three-Way Catalysis. *Journal of Physical Chemistry C* **2019**, *123*, 24584−24591.

(15) Huang, C.; Shan, W.; Lian, Z.; Zhang, Y.; He, H. Recent Advances in Three-Way Catalysts of Natural Gas Vehicles. *Catal Sci Technol* **2020**, *10*, 6407–6419.

(16) Arai, H.; Machida, M. Thermal Stabilization of Catalyst Supports and Their Application to High-Temperature Catalytic Combustion. *Appl Catal A Gen* **1996**, *138*, 161–176.

(17) Kwak, J. H.; Hu, J.; Lukaski, A.; Kim, D. H.; Szanyi, J.; Peden, C. H. F. Role of Pentacoordinated Al^{3+} Ions in the High Temperature Phase Transformation of $\gamma\text{-}Al_2O_3$. *Journal of Physical Chemistry C* **2008**, *112*, 9486–9492.

(18) Di Monte, R.; Fornasiero, P.; Kaspar, J.; Graziani, M.; Gatica, J. M.; Bernal, S.; Gomez-Herrero, A. Stabilisation of Nanostructured $Ce_{0.2}Zr_{0.8}O_2$ Solid Solution by Impregnation on Al_2O_3: A Suitable Method for the Production of Thermally Stable Oxygen Storage/Release Promoters for Three-Way Catalysts. *Chemical Communications* **2000**, No. 21, 2167–2168.

(19) Nishio, Y.; Ozawa, M. Thermal Stability and Microstructural Change of Lanthanum Modified Alumina

Catalytic Support. *Journal of the Ceramic Society of Japan* **2007**, *115*, 633–636.
(20) Vedyagin, A. A.; Kenzhin, R. M.; Tashlanov, M. Y.; Alikin, E. A.; Stoyanovskii, V. O.; Plyusnin, P. E.; Shubin, Y. V.; Mishakov, I. V.; Smirnov, M. Y.; Kalinkin, A. V.; Bukhtiyarov, V. I. Effect of La Addition on the Performance of Three-Way Catalysts Containing Palladium and Rhodium. *Top Catal* **2020**, *63*, 152–165.
(21) Kolli, T.; Lassi, U.; Rahkamaa-Tolonen, K.; Kinnunen, T. J. J.; Keiski, R. L. The Effect of Barium on the Catalytic Behaviour of Fresh and Aged Pd-Ba-OSC/Al_2O_3 Catalysts. *Appl Catal A Gen* **2006**, *298*, 65–72.
(22) Suhonen, S.; Valden, M.; Pessa, M.; Savimäki, A.; Härkönen, M.; Hietikko, M.; Pursiainen, J.; Laitinen, R. Characterization of Alumina Supported Pd Catalysts Modified by Rare Earth Oxides Using X-Ray Photoelectron Spectroscopy and X-Ray Diffraction: Enhanced Thermal Stability of PdO in Nd/Pd Catalysts. *Appl Catal A Gen* **2001**, *207*, 113–120.
(23) Klingstedt, F.; Karhu, H.; Kalantar Neyestanaki, A.; Lindfors, L. E.; Salmi, T.; Väyrynen, J. Barium Promoted Palladium Catalysts for the Emission Control of Natural Gas Driven Vehicles and Biofuel Combustion Systems. *J Catal* **2002**, *206*, 248–262.
(24) Takahashi, M.; Kikuchi, S.; Iwachido, K.; Ikeda, M.; Goto, H. Development of New Three-Way Catalyst Technologies to Improve Purification Performance for Exhaust Emission after Severe Thermal Aging. *Transactions of Society of Automotive Engineers of Japan* **2013**, *44*, 15–20.
(25) Takayama, A.; Kurokawa, T.; Nakayama, H.; Katoh, T.; Nagata, M. Effect of Ba and La Additives to the Pd Layer of a Pd:Rh TWC. *SAE Technical Paper* **2017**, 2017-01–0922.
(26) David Logan, A.; Graham, G. W. NO Chemisorption on Pd(100) with Ultra-Thin Overlayers of Oxidized La and Al. *Surface Science Letters* **1992**, *277*, L47–L51.
(27) Matsuura, S.; Hirai, A.; Arimura, K.; Shinjoh, H. Development of Three-Way Catalyst with Using Only Pd as Activator. *SAE Technical Papers* **1995**, 950257.
(28) Valden, M.; Keiski, R. L.; Xiang, N.; Pere, J.; Aaltonen, J.; Pessa, M.; Maunula, T.; Savimäki, A.; Lahti, A.; Härkönen, M. Reactivity of Pd/Al_2O_3, Pd/La_2O_3-Al_2O_3 and Pd/$LaAlO_3$ Catalysts for the Reduction of NO by CO: CO and NO Adsorption. *J Catal* **1996**, *161*, 614–625.
(29) Skoglundh, M.; Johansson, H.; Löwendahl, L.; Jansson, K.; Dahl, L.; Hirschauer, B. Cobalt-Promoted Palladium as a Three-Way Catalyst. *Appl Catal B* **1996**, *7*, 299–319.
(30) Tanikawa, K.; Egawa, C. Effect of Barium Addition over Palladium Catalyst for CO-NO-O_2 Reaction. *J Mol Catal A Chem* **2011**, *349*, 94–99.
(31) Muraki, H.; Shinjoh, H.; Fujitani, Y. Effect of Lanthanum on the No Reduction over Palladium Catalysts. *Appl Catal* **1986**, *22*, 325–335.
(32) Muraki, H.; Shinjoh, H.; Sobukawa, H.; Yokota, K.; Fujitani, Y. Palladium-Lanthanum Catalysts for Automotive Emission Control. *Industrial and Engineering Chemistry Product Research and Development* **1986**, *25*, 202–208.
(33) Muraki, H.; Yokota, K.; Fujitani, Y. Nitric Oxide Reduction Performance of Automotive Palladium Catalysts. *Appl Catal* **1989**, *48*, 93–105.
(34) Shinjoh, H. Rare Earth Metals for Automotive Exhaust Catalysts. *J Alloys Compd* **2006**, *408–412*, 1061–1064.
(35) Sekiba, T.; Kimura, S.; Yamamoto, H.; Okada, A. Development of Automotive Palladium Three-Way Catalysts. *Catal Today* **1994**, *22*, 113–126.
(36) Kobayashi, T.; Yamada, T.; Kayano, K. Effect of Basic Metal Additives on NO_x Reduction Property of Pd-Based Three-Way Catalyst. *Appl Catal B* **2001**, *30*, 287–292.
(37) Jing, Y.; Cai, Z.; Liu, C.; Toyao, T.; Maeno, Z.; Asakura, H.; Hiwasa, S.; Nagaoka, S.; Kondoh, H.; Shimizu, K. Promotional Effect of La in the Three-Way Catalysis of La-Loaded Al_2O_3-Supported Pd Catalysts (Pd/La/Al_2O_3). *ACS Catal* **2020**, *10*, 1010–1023.
(38) Toyao, T.; Jing, Y.; Kon, K.; Hayama, T.; Nagaoka, S.; Shimizu, K. Catalytic NO–CO Reactions over La-Al_2O_3 Supported Pd: Promotion Effect of La. *Chem Lett* **2018**, *47*, 1036–1039.
(39) Gandhi, H. S.; Graham, G. W.; McCabe, R. W. Automotive Exhaust Catalysis. *J Catal* **2003**, *216*, 433–442.
(40) Kang, S. B.; Nam, I. S.; Cho, B. K.; Kim, C. H.; Oh, S. H. Kinetic Model for Modern Double-Layered Pd/Rh

TWC as a Function of Metal Loadings and Mileage. *Chemical Engineering Journal* **2015**, *278*, 328–338.
(41) Fujiwara, A.; Tsurunari, Y.; Yoshida, H.; Ohyama, J.; Yamada, T.; Haneda, M.; Miki, T.; Machida, M. Thermal Deactivation of Pd/CeO_2-ZrO_2 Three-Way Catalysts during Real Engine Aging: Analysis by a Surface plus Peripheral Site Model. *ACS Omega* **2020**, *5*, 28897−28906.
(42) Ravel, B.; Newville, M. ATHENA, ARTEMIS, HEPHAESTUS: Data Analysis for X-Ray Absorption Spectroscopy Using IFEFFIT. *J Synchrotron Radiat* **2005**, *12*, 537–541.
(43) Yamamoto, T.; Hatsui, T.; Matsuyama, T.; Tanaka, T.; Funabiki, T. Structures and Acid-Base Properties of La/Al_2O_3- Role of La Addition to Enhance Thermal Stability of γ-Al_2O_3. *Chemistry of Materials* **2003**, *15*, 4830–4840.
(44) Smith, S. J.; Huang, B.; Bartholomew, C. H.; Campbell, B. J.; Boerio-Goates, J.; Woodfield, B. F. La-Dopant Location in La-Doped γ-Al_2O_3 Nanoparticles Synthesized Using a Novel One-Pot Process. *Journal of Physical Chemistry C* **2015**, *119*, 25053−25062.
(45) Tamai, K.; Hosokawa, S.; Yamamoto, A.; Asakura, H.; Teramura, K.; Tanaka, T. Identification of Active Ba Species on TiO_2 Photocatalyst for NO_x Trapping. *Chem Lett* **2020**, *49*, 859–862.
(46) Zorn, K.; Giorgio, S.; Halwax, E.; Henry, C. R.; Grönbeck, H.; Rupprechter, G. CO Oxidation on Technological Pd-Al_2O_3 Catalysts: Oxidation State and Activity. *Journal of Physical Chemistry C* **2011**, *115*, 1103–1111.
(47) Gajdoš, M.; Eichler, A.; Hafner, J. CO Adsorption on Close-Packed Transition and Noble Metal Surfaces: Trends from Ab Initio Calculations. *Journal of Physics Condensed Matter* **2004**, *16*, 1141–1164.
(48) Zeinalipour-Yazdi, C. D.; Cooksy, A. L.; Efstathiou, A. M. CO Adsorption on Transition Metal Clusters: Trends from Density Functional Theory. *Surf Sci* **2008**, *602*, 1858–1862.
(49) Gonzalez, S.; Illas, F. CO Adsorption on Monometallic Pd, Rh, Cu and Bimetallic PdCu and RhCu Monolayers Supported on Ru(0001). *Surf Sci* **2005**, *598*, 144–155.
(50) Ketteler, G.; Ogletree, D. F.; Bluhm, H.; Liu, H.; Hebenstreit, E. L. D.; Salmeron, M. In Situ Spectroscopic Study of the Oxidation and Reduction of Pd(111). *J Am Chem Soc* **2005**, *127* (51), 18269–18273.
(51) Kim, Y. N.; Kim, M. Y.; Choi, M. Synergistic Integration of Catalysis and Ion-Exchange for Highly Selective Reduction of Nitrate into N2. *Chemical Engineering Journal* **2016**, *289*, 423–432.
(52) Toyoshima, R.; Amemiya, K.; Mase, K.; Kondoh, H. Orientation-Dependent Hindrance to the Oxidation of Pd-Au Alloy Surfaces. *Journal of Physical Chemistry Letters* **2020**, *11*, 9249–9254.
(53) Zhang, L.; Filot, I. A. W.; Su, Y. Q.; Liu, J. X.; Hensen, E. J. M. Transition Metal Doping of Pd(111) for the NO + CO Reaction. *J Catal* **2018**, *363*, 154–163.
(54) Takagi, N.; Ishimura, K.; Miura, H.; Shishido, T.; Fukuda, R.; Ehara, M.; Sakaki, S. Catalysis of Cu Cluster for NO Reduction by CO: Theoretical Insight into the Reaction Mechanism. *ACS Omega* **2019**, *4*, 2596–2609.
(55) Grünbacher, M.; Tarjomannejad, A.; Nezhad, P. D. K.; Praty, C.; Ploner, K.; Mohammadi, A.; Niaei, A.; Klötzer, B.; Schwarz, S.; Bernardi, J.; Farzi, A.; Gómez, M. J. I.; Rivero, V. T.; Penner, S. Promotion of La(Cu0.7Mn0.3)0.98M0.02O3−δ (M = Pd, Pt, Ru and Rh) Perovskite Catalysts by Noble Metals for the Reduction of NO by CO. *J Catal* **2019**, *379*, 18–32.
(56) Savereide, L.; Gosavi, A.; Hicks, K. E.; Notestein, J. M. Identifying Properties of Low-Loaded CoOx/CeO2 via X-Ray Absorption Spectroscopy for NO Reduction by CO. *J Catal* **2020**, *381*, 355–362.
(57) Oyama, S. T.; Zhang, X.; Lu, J.; Gu, Y.; Fujitani, T. Epoxidation of Propylene with H_2 and O_2 in the Explosive Regime in a Packed-Bed Catalytic Membrane Reactor. *J Catal* **2008**, *257*, 1–4.
(58) Macleod, N.; Isaac, J.; Lambert, R. M. Sodium Promotion of the NO+C_3H_6 Reaction over Rh/γ-Al_2O_3 Catalysts. *J Catal* **2000**, *193*, 115–122.
(59) Konsolakis, M.; Yentekakis, I. V. The Reduction of NO by Propene over Ba-Promoted Pt/γ-Al_2O_3 Catalysts. *J Catal* **2001**, *198*, 142–150.
(60) Berlowitz, P. J.; Peden, C. H. F.; Goodman, D. W. Kinetics of CO Oxidation on Single-Crystal Pd, Pt, and Ir. *Journal of Physical Chemistry* **1988**, *92*, 5213–5221.
(61) Peterson, E. J.; DeLaRiva, A. T.; Lin, S.; Johnson, R. S.; Guo, H.; Miller, J. T.; Kwak, J. H.; Peden, C. H. F.;

Kiefer, B.; Allard, L. F.; Ribeiro, F. H.; Datye, A. K. Low-Temperature Carbon Monoxide Oxidation Catalysed by Regenerable Atomically Dispersed Palladium on Alumina. *Nat Commun* **2014**, *5*, 4885.

(62) Asakura, H.; Hosokawa, S.; Ina, T.; Kato, K.; Nitta, K.; Uera, K.; Uruga, T.; Miura, H.; Shishido, T.; Ohyama, J.; Satsuma, A.; Sato, K.; Yamamoto, A.; Hinokuma, S.; Yoshida, H.; Machida, M.; Yamazoe, S.; Tsukuda, T.; Teramura, K.; Tanaka, T. Dynamic Behavior of Rh Species in Rh/Al_2O_3 Model Catalyst during Three-Way Catalytic Reaction: An Operando X-Ray Absorption Spectroscopy Study. *J Am Chem Soc* **2018**, *140*, 176–184.

(63) Decarolis, D.; Clark, A. H.; Pellegrinelli, T.; Nachtegaal, M.; Lynch, E. W.; Catlow, C. R. A.; Gibson, E. K.; Goguet, A.; Wells, P. P. Spatial Profiling of a Pd/Al_2O_3 Catalyst during Selective Ammonia Oxidation. *ACS Catal* **2021**, *11*, 2141–2149.

(64) Che, M.; Dutel, J. F.; Gallezot, P.; Primet, M. A Study of the Chemisorption of Nitric Oxide on PdY Zeolite. Evidence for a Room Temperature Oxidative Dissolution of Pd Crystallites. *Journal of Physical Chemistry* **1976**, *80*, 2371–2381.

(65) Aylor, A. W.; Lobree, L. J.; Reimer, J. A.; Bell, A. T. Investigations of the Dispersion of Pd in H-ZSM-5. *J Catal* **1997**, *172*, 453–462.

(66) Paredis, K.; Ono, L. K.; Behafarid, F.; Zhang, Z.; Yang, J. C.; Frenkel, A. I.; Cuenya, B. R. Evolution of the Structure and Chemical State of Pd Nanoparticles during the in Situ Catalytic Reduction of NO with H_2. *J Am Chem Soc* **2011**, *133*, 13455–13464.

(67) Yasumura, S.; Ide, H.; Ueda, T.; Jing, Y.; Liu, C.; Kon, K.; Toyao, T.; Maeno, Z.; Shimizu, K. Transformation of Bulk Pd to Pd Cations in Small-Pore CHA Zeolites Facilitated by NO. *JACS Au* **2021**, *1*, 201–211.

(68) Fanson, P. T.; Horton, M. R.; Delgass, W. N.; Lauterbach, J. FTIR Analysis of Storage Behavior and Sulfur Tolerance in Barium-Based NOx Storage and Reduction (NSR) Catalysts. *Appl Catal B* **2003**, *46*, 393–413.

(69) Fujiwara, K.; Pratsinis, S. E. Single Pd Atoms on TiO_2 Dominate Photocatalytic NO_x Removal. *Appl Catal B* **2018**, *226*, 127–134.

(70) Brown, W. A.; King, D. A. NO Chemisorption and Reactions on Metal Surfaces: A New Perspective. *Journal of Physical Chemistry B* **2000**, *104* (12), 2578–2595.

(71) Sedlmair, C.; Seshan, K.; Jentys, A.; Lercher, J. A. Elementary Steps of NOx Adsorption and Surface Reaction on a Commercial Storage-Reduction Catalyst. *J Catal* **2003**, *214*, 308–316.

(72) Nova, I.; Castoldi, L.; Lietti, L.; Tronconi, E.; Forzatti, P.; Prinetto, F.; Ghiotti, G. NOx Adsorption Study over Pt-Ba/Alumina Catalysts: FT-IR and Pulse Experiments. *J Catal* **2004**, *222*, 377–388.

(73) Chi, Y.; Chuang, S. S. C. Infrared and TPD Studies of Nitrates Adsorbed on Tb_4O_7, La_2O_3, BaO, and MgO/y-Al_2O_3. *Journal of Physical Chemistry B* **2000**, *104*, 4673–4683.

(74) Lietti, L.; Daturi, M.; Blasin-Aubé, V.; Ghiotti, G.; Prinetto, F.; Forzatti, P. Relevance of the Nitrite Route in the NOx Adsorption Mechanism over $Pt\text{-}Ba/Al_2O_3$ NO_x Storage Reduction Catalysts Investigated by Using Operando FTIR Spectroscopy. *ChemCatChem* **2012**, *4*, 55–58.

(75) Greenaway, A. G.; Marberger, A.; Thetford, A.; Lezcano-González, I.; Agote-Arán, M.; Nachtegaal, M.; Ferri, D.; Kröcher, O.; Catlow, C. R. A.; Beale, A. M. Detection of Key Transient Cu Intermediates in SSZ-13 during NH3-SCR DeNOx by Modulation Excitation IR Spectroscopy. *Chem Sci* **2020**, *11*, 447–455.

(76) Pieta, I. S.; García-Diéguez, M.; Herrera, C.; Larrubia, M. A.; Alemany, L. J. In Situ DRIFT-TRM Study of Simultaneous NOx and Soot Removal over Pt-Ba and Pt-K NSR Catalysts. *J Catal* **2010**, *270*, 256–267.

(77) Haneda, M.; Kintaichi, Y.; Nakamura, I.; Fujitani, T.; Hamada, H. Effect of Surface Structure of Supported Palladium Catalysts on the Activity for Direct Decomposition of Nitrogen Monoxide. *J Catal* **2003**, *218*, 405–410.

(78) Frola, F.; Manzoli, M.; Prinetto, F.; Ghiotti, G.; Castoldi, L.; Lietti, L. $Pt\text{-}Ba/Al_2O_3$ NSR Catalysts at Different Ba Loading: Characterization of Morphological, Structural, and Surface Properties. *Journal of Physical Chemistry C* **2008**, *112*, 12869–12878.

(79) Shinjoh, H.; Isomura, N.; Sobukawa, H.; Sugiura, M. Effect of Alkaline Addition on Hydrocarbon Oxidation Activities of Palladium Three-Way Catalyst. *Stud Surf Sci Catal* **1998**, *116*, 83–91.

(80) Friberg, I.; Sadokhina, N.; Olsson, L. Complete Methane Oxidation over Ba Modified Pd/Al_2O_3: The Effect

of Water Vapor. *Appl Catal B* **2018**, *231*, 242–250.
(81) Gong, J.; Wang, D.; Li, J.; Currier, N.; Yezerets, A. Dynamic Oxygen Storage Modeling in a Three-Way Catalyst for Natural Gas Engines: A Dual-Site and Shrinking-Core Diffusion Approach. *Appl Catal B* **2017**, *203*, 936–945.
(82) Machida, M.; Fujiwara, A.; Yoshida, H.; Ohyama, J.; Asakura, H.; Hosokawa, S.; Tanaka, T.; Haneda, M.; Tomita, A.; Miki, T.; Iwashina, K.; Endo, Y.; Nakahara, Y.; Minami, S.; Kato, N.; Hayashi, Y.; Goto, H.; Hori, M.; Tsuda, T.; Miura, K.; Kimata, F.; Iwachido, K. Deactivation Mechanism of Pd/CeO_2-ZrO_2 Three-Way Catalysts Analyzed by Chassis-Dynamometer Tests and in Situ Diffuse Reflectance Spectroscopy. *ACS Catal* **2019**, *9*, 6415−6424.
(83) Okajima, T.; Sivakumar, S.; Shingyouchi, H.; Yamaguchi, K.; Kusaka, J.; Nagata, M. Modeling on a Three-Way Catalyst Used in Series Hybrid Electric Vehicles Considering Its Specific Engine Operation Attribute. *Ind Eng Chem Res* **2021**, *60*, 1583−1601.
(84) Datye, A. K.; Votsmeier, M. Opportunities and Challenges in the Development of Advanced Materials for Emission Control Catalysts. *Nat Mater* **2020**.
(85) Haneda, M.; Nakamura, Y.; Yamada, T.; Minami, S.; Kato, N.; Iwashina, K.; Endo, Y.; Nakahara, Y.; Iwachido, K. Comprehensive Study of the Light-off Performance and Surface Properties of Engine-Aged Pd-Based Three-Way Catalysts. *Catal Sci Technol* **2021**, *11*, 912–922.
(86) Di Monte, R.; Fornasiero, P.; Kaspar, J.; Graziani, M.; Gatica, J. M.; Bernal, S.; Gomez-Herrero, A. Stabilisation of Nanostructured $Ce_{0.2}Zr_{0.8}O_2$ Solid Solution by Impregnation on Al_2O_3: A Suitable Method for the Production of Thermally Stable Oxygen Storage/Release Promoters for Three-Way Catalysts. *Chemical Communications* **2000**, No. 21, 2167–2168.

Chapter 5

Role of Ba in an Al_2O_3-Supported Pd-Based Catalyst under Practical Three-way Catalysis Conditions

5.1 Introduction

Three-way catalytic converters are widely used to control automotive emissions generated by gasoline vehicles.[1–5] Air pollutants, such as NO_x, CO, and hydrocarbons (HCs), are reduced using three-way catalysts that typically use platinum group metals (PGMs), such as Rh, Pd, and Pt,[6–14] which are beneficial for catalytic performance and durability compared to other non-precious metals. Although catalysts that contain non-noble metal components, such as Cu, Ni, and Fe, have recently been intensively studied,[15–21] real-world operating systems still need large amounts of PGMs to meet strict regulations that require reductions of more than 99% in tailpipe emissions relative to engine-generated emissions.[22] Therefore, designing effective catalytic supports is very important for maximizing PGM activity.[22,23]

Al_2O_3 is widely used as a support material in three-way catalysts because of extensive advantages that include good thermal stability, mechanical strength, and high surface area.[24] Alkaline earth and lanthanide metals are often introduced into Al_2O_3 as structural stabilizers that suppress the γ-to-α phase transformation.[25–27] Basic metals, such as La and Ba, are also known to stabilize Pd, which is the most commonly used active metal in modern commercial three-way catalysts[28–33] under TWC conditions, resulting in improved Pd dispersion even after catalyst exposure to harsh operating conditions.[34–39] In addition to the stabilizing benefits received by the support metals from basic metal additives and the stabilizing supports themselves, these basic metals have been shown to promote catalytic TWC performance.[40–49] Such promotional effects are the consequence of changes in the electron density of Pd species and the efficient formation of reactive intermediates at perimeter supported-metal and support sites.[50,51] While these results make important contributions to the TWC field, the roles played by basic metal additives in three-way catalytic reactions over Pd-based catalysts remain inadequately understood. In particular, reports under real operating conditions (i.e., catalytic testing using real vehicles driven on a chassis dynamometer) are scarce. While obtaining fundamental insight by investigating simple model reactions is highly important, research that explores complex real TWC processes, where deviations from stoichiometric conditions (i.e., fuel cut and acceleration) are often encountered and many competing reactions involving reactants such as NO_x, CO, HCs, H_2O, CO_2, NH_3, and SO_x, among others, take place, is equally important for developing a detailed mechanistic understanding and for practical implementation purposes.[52]

In this study, we subjected a gasoline-engine-powered vehicle to TWC testing to investigate the role played by Ba in a standard three-way catalyst composed of Pd and Rh, as active PGMs, as well as Al_2O_3-based and Ce-Zr mixed-oxide-based supports. More specifically, two types of honeycomb catalyst were prepared: one containing Ba and the other devoid of Ba,

with the Ba-containing catalyst found to more effectively reduce all monitored emissions (NO_x, CO, and non-methane HCs). The presence of Ba was also found to suppress aggregation of the supported metals. Moreover, model reactions were subjected to *in situ/operando* infrared (IR) spectroscopy to investigate the catalyst surface during TWC processes, which revealed that the efficient generation of surface-reactive nitrate intermediates and their subsequent reactions with CO, C_3H_6, and H_2 also play key roles. This process is akin to the NO_x storage and reduction (NSR)[53–55] mechanism commonly employed to control diesel emissions at low temperatures (< 300 °C); it also avoids the TWC limitations of traditional stoichiometric gasoline-fueled engines by enabling the reaction under non-steady-state conditions.

5.2 Experimental section

5.2.1 Vehicle testing

A commercial vehicle was subjected to practical testing as follows. The catalyst (Pd/Al_2O_3 or $Pd/Ba/Al_2O_3$) was used in a Pd-Rh three-way catalyst with a double-layered structure. The Pd and Rh catalyst wash coats were coated on a 1.0-L ceramic monolith with a cell density of 600 in^{-2}.[56] The bottom layer consisted of Pd supported on a wash coat of Al_2O_3, Ba/Al_2O_3, and Ce-Zr mixed oxide. The bottom layer wash-coat loading was ~100 g/L with a Pd loading of 3 g/L and a Ba loading of 5 g/L that corresponds to 10 wt% loading to the Al_2O_3 support. The top layer consisted of Rh supported on another wash coat of Ce-Zr mixed oxide and La-loaded Al_2O_3. The top layer wash-coat loading was ~100 g/L with a Rh loading of 0.3 g/L. The prepared three-way catalysts were bench-aged using a 1.8-L gasoline engine with a peak temperature of 950 °C for 75 h. The aged catalysts were mounted in a commercial vehicle with a 1.5-L engine, and vehicle emission testing was conducted according to the LA-4 driving cycle (U.S. Federal and Californian city cycle). The concentrations of NO_x (NO + NO_2), CO, and total hydrocarbons (THC), as well as the catalyst-bed temperature and AFR were monitored using a Horiba MEXA series emission measurement system.

5.2.2 CO adsorbed in the postmortem catalysts

The CO uptake of each Pd-Rh three-way catalyst was measured using a metal dispersion analyzer (BEL-METAL-3, MicrotracBEL). The catalyst sample was pretreated under 10% O_2 in He at 400 °C to remove organic contaminants and then reduced using 10% H_2 in He at 400 °C. The active Ba and ceria sites for CO capture in the catalyst sample were quenched by injecting 10% CO_2 in He to form inactive carbonate species. CO was then pulse injected using 10% CO in He and the uptake by the Pd and Rh particles in the sample was measured.

5.2.3 Preparing the powder catalysts

Commercial γ-Al_2O_3 was used as the support material, and Ba was added to the γ-Al_2O_3 using the impregnation method described in our previous study.[5751] An aqueous $Ba(NO_3)_2$ solution was impregnated into γ-Al_2O_3 followed by drying at 120 °C for 2h. The as-prepared material was calcined at 600 °C in air for 2 h to obtain the Ba/Al_2O_3 (Ba = 10 wt%) support material. Pd/Al_2O_3 and $Pd/Ba/Al_2O_3$ (Pd = 1 wt%) were prepared by adding an aqueous solution of $Pd(NH_3)(NO_2)_2$ (Kojima Kagaku) to 2 g of Al_2O_3 or Ba/Al_2O_3 in a 200 mL gas vessel. The mixture was stirred at room temperature for 15 min (200 rpm) before evaporation to dryness at 50 °C. The material was then dried at 90 °C for 2 h and subsequently calcined at 500 °C in air for 3 h. The calcined samples

were then reduced under a flow of H_2 at 500 °C for 30 min to prepare fresh Pd/Al_2O_3 and $Pd/Ba/Al_2O_3$ catalysts.

5.2.4 *In situ*/*operando* infrared (IR) spectroscopy

In situ/*operando* IR spectroscopy was performed at 450 °C using a JASCO FT/IR-4200 spectrometer with a liquid-N_2-cooled mercury-cadmium-telluride (MCT) detector. Powder samples (40 mg) were pressed to prepare self-supporting pellets (ϕ = 20 mm) that were placed in a quartz IR cell with CaF_2 windows connected to a gas flow system. The pellets were reduced under a flow of 10% H_2 in He (100 mL min^{-1}) at 450 °C for 0.5 h following exposure to a flow of 0.5% NO + 2% O_2 in He at 450 °C for 0.5 h to remove surface carbonate species prior spectral acquisition. After purging under a flow of He for 10 min, 0.5% NO in He was introduced for 10 min, followed by 0.5% NO + 2% O_2 in He for 10 min. After purging with He to remove gas-phase NO and O_2, 0.5% CO in He, 0.2%C_3H_6 in He, or 0.5% H_2 in He was introduced into the system for 10 min. The effluent composition was analyzed using a high-sampling-rate gas chromatograph with a TCD detector (490 Micro GC; Agilent Technologies Inc.).

5.3 Results and discussion

3.3.1 Vehicle testing

Practical testing was performed for honeycomb Pd-Rh three-way catalysts, with and without Ba, using a commercial vehicle according to the LA-4 driving cycle (U.S. Federal and Californian city cycle). **Figure 1** shows accumulated NO_x, CO, and non-methane total HC (THC) emissions and transient emissions in the tailpipe, as well as the air-to-fuel ratio (AFR), exhaust volume, catalyst bed temperature, and the corresponding vehicle speed for the entire LA-4 driving-cycle vehicle-testing range. These experiments were highly reproducibility, as confirmed by identical monitored values for the operating conditions, including exhaust volume and catalyst bed temperature, although the AFR values varied slightly between the two catalysts. Note that the vehicle speed is only provided for the experiments involving Ba, for clarity. Three-way catalysts function under highly complex conditions and experience dramatic perturbations in exhaust volume and AFR (**Figure 1A-C**). Less accumulated NO_x, CO, and THC emissions were observed for the Ba-containing honeycomb catalyst compared with the catalyst devoid of Ba, which suggests that the introduction of Ba enhances catalytic efficiency for the reduction of all monitored emissions. Specifically, the Ba additive promoted the removal of NO_x more efficiently than CO and THC.

Figure 2 shows matrices that correlate operating conditions with emissions and clarify the relationships between the amounts of emitted NO_x, CO, and THC, and the conditions of the two types of catalyst. Overall, the honeycomb catalysts with and without the Ba additives show similar correlations; however, some differences are nevertheless observed. Notably, exhaust emissions and exhaust volume are less correlated using the Ba-containing catalyst than that devoid of Ba, which indicates that the former catalyst performs more consistently against exhaust-volume fluctuations. It is also worth mentioning that the two catalysts show a greater difference in NO_x emissions than CO and THC emissions.

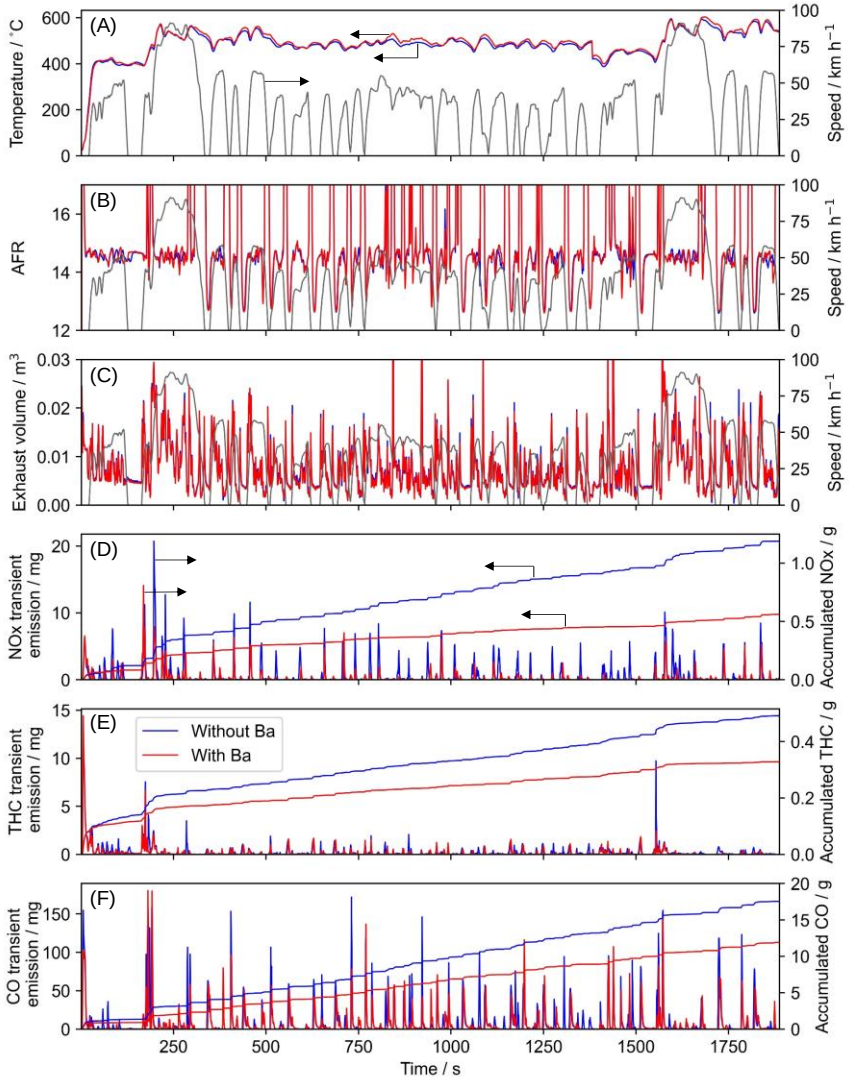

Figure 1. (A) Catalyst bed temperature, (B) AFR, and (C) exhaust volume, and transient and corresponding accumulated (D) NO_x, (E) THC, and (F) CO emissions monitored at the tailpipe during the LA-4 driving cycle (U.S. Federal and Californian city cycle) using a vehicle with a 1.5-L gasoline engine and a Pd-Rh three-way catalyst with Ba (red) and without Ba (blue).

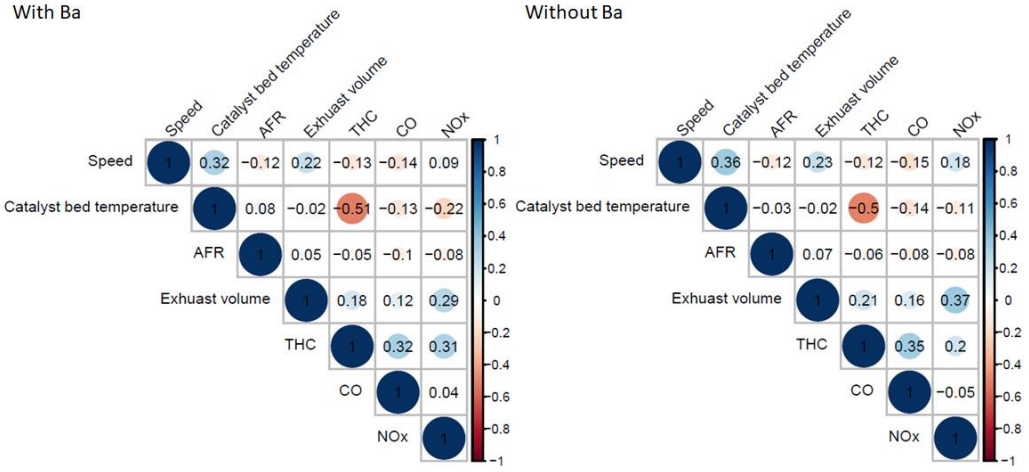

Figure 2. Correlation maps of vehicle speed, catalyst bed temperature, AFR, exhaust volume, and the transient NO_x, CO, and THC emissions for Pd-Rh three-way catalysts with Ba (left) and without Ba (right).

Figures 3 and 4 show vehicle testing results in narrow time ranges (0–200 s and 800–1000 s, respectively). **Figure 3** reveals that significant NO_x, CO, and THC emissions are observed in the cold-start period, where the catalyst bed temperature is below its light-off temperature (t < 25 s; i.e., the period before the catalyst is functional) for both honeycomb catalysts (with and without Ba), owing to the low temperature of the catalyst bed.[58,59] More specifically, emissions over the Ba-containing catalyst are very similar to those over the Ba-free catalyst in the cold start stage (**Figure 3D**), which indicates that Ba does not exhibit a promotional effect toward the removal of exhaust components, including NO_x, at such low temperatures. On the other hand, the Ba-containing honeycomb catalyst emitted less transient NO_x, CO, and THC when heated to a moderate temperature (around 400 °C), as observed in the 25–125 s time range, which suggests that the introduction of Ba enhances catalytic activity toward all monitored exhaust components at such a moderate temperature.

NO_x was emitted predominantly with a higher exhaust volume when the catalyst bed temperature exceeded 400 °C, especially when accelerating and even when the AFR was close to the stoichiometric value. NO_x emissions using the Ba-containing honeycomb catalyst varied less with perturbed exhaust volume compared to the Ba-free catalyst. In contrast, CO and HCs were generally emitted under rich conditions when immediately accelerating after having decelerated, such as at ~965 s (**Figures 4E** and **4F**). Note that the dramatic increase in AFR during deceleration is the result of an engine fuel-cut operation employed to improve fuel efficiency.[60,61] We also found that the introduction of Ba not only improves exhaust gas purification efficiency but also delayed NO_x emission times (e.g., at approximately 860, 890, and 975 s). This delay is ascribable to NO_x being trapped by the introduced Ba species and suggests that a process similar to the NSR mechanism,[55,60,61]which is commonly used to control diesel emissions at low temperatures (< 300 °C), proceeds under the TWC operating conditions, leading to exhaust-emission suppression, although the catalysts and operating conditions are not intended to be used for this purpose. Such NSR processes at high temperatures that are relevant to TWC conditions are discussed below (*vide infra*). Note that some emission delays observed for the two catalysts are possibly due to slight differences in operating conditions, such as the AFR, for example. As a side note, sulfur poisoning effect for TWC applications is negligible unlike the diesel application because the temperature range of TWC is high, resulting in almost no accumulation of sulfur species on the catalyst surface. Also, although NH_3 can form over Ba-

based catalysts during the rich operation, such NH_3 is immediately decomposed by reactive oxygen species of oxygen storage materials such as CeO_2-ZrO_2 that are used as catalyst supports together with Al_2O_3-based supports.

Figure 5 shows CO uptake over postmortem Pd-Rh three-way catalyst powders with and without Ba collected from the front and rear zones of the honeycomb catalysts, which reveals that the Ba-containing catalyst retains higher CO uptake values in both the front and rear zones after gasoline-engine aging, indicating that the introduction of Ba stabilizes precious-metal dispersion, consistent with previous studies.[65,66] The catalyst powder collected from the rear zone showed higher CO uptake than that collected from the front zone for each catalyst because powder in the front zone is usually exposed to higher temperatures that lead to more severe sintering of the supported metals. Some Ba species are thought to form $BaAl_2O_4$ as observed on a $Pd/Ba/Al_2O_3$ catalyst which was subjected to the hydrothermal aging treatment at 1000 °C.[67] Equivalency of the thermal stress toward the catalysts between the engine aging and the hydrothermal aging at 1000 °C was confirmed by similarity of the specific surface areas for the two aged catalysts.

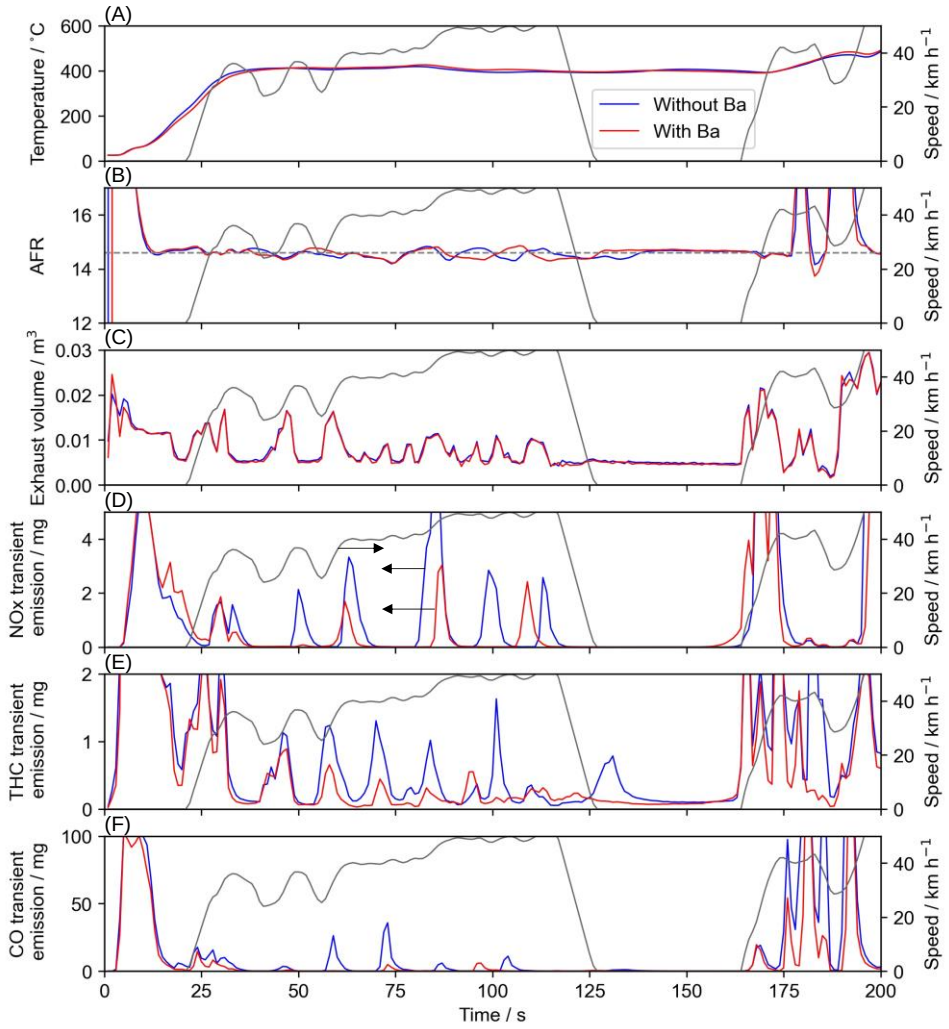

Figure 3. (A) Catalyst bed temperature, (B) AFR, (C) exhaust volume and transient (D) NO_x, (E) THC, and (F) CO emissions monitored at the tailpipe during a LA-4 driving cycle (U.S. Federal and Californian city cycle) using a vehicle with a 1.5-L gasoline engine and a Pd-Rh three-way catalyst with Ba (red) and without Ba (blue) in the narrow 0–200s time range. The stoichiometric AFR value (14.6) is marked by a gray dashed line.

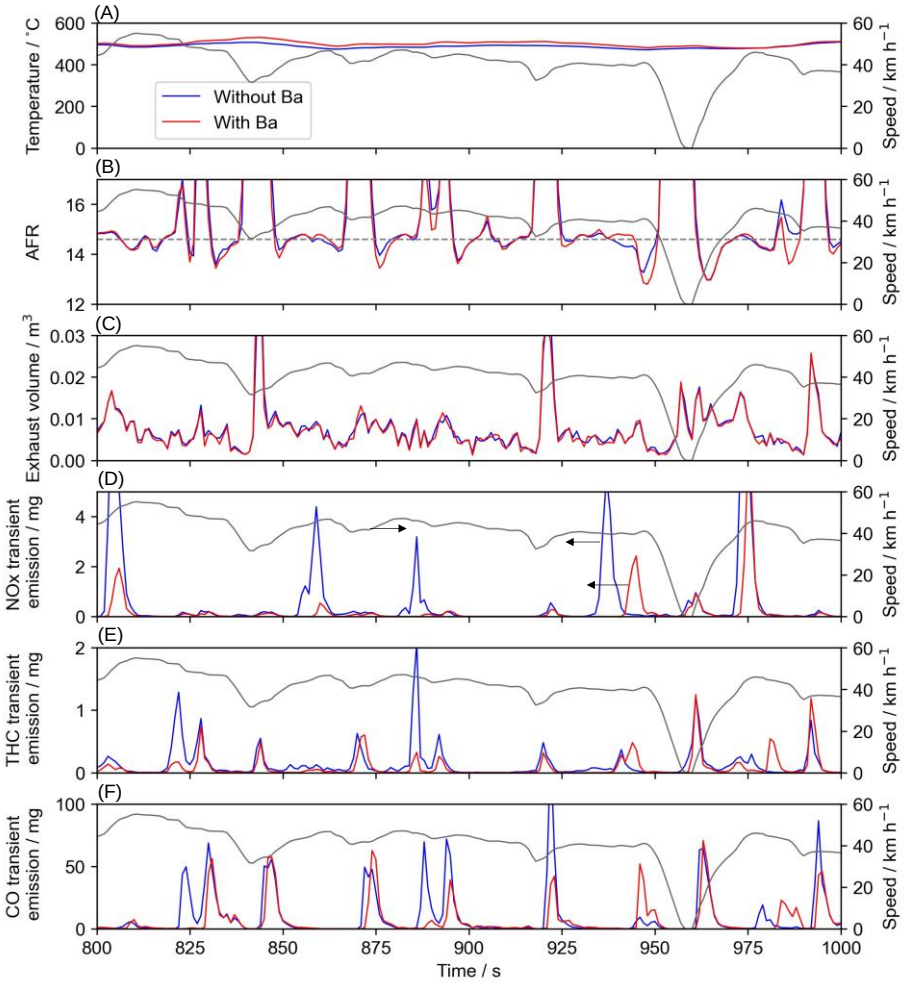

Figure 4. (A) Catalyst bed temperature, (B) AFR, (C) exhaust volume and transient (D) NO_x, (E) THC, and (F) CO emissions monitored at the tailpipe during a LA-4 driving cycle (U.S. Federal and Californian city cycle) using a vehicle with a 1.5-L gasoline engine and a Pd-Rh three-way catalyst with Ba (red) and without Ba (blue) in the narrow 800–1000s time range. The stoichiometric AFR value (14.6) is marked by a gray dashed line.

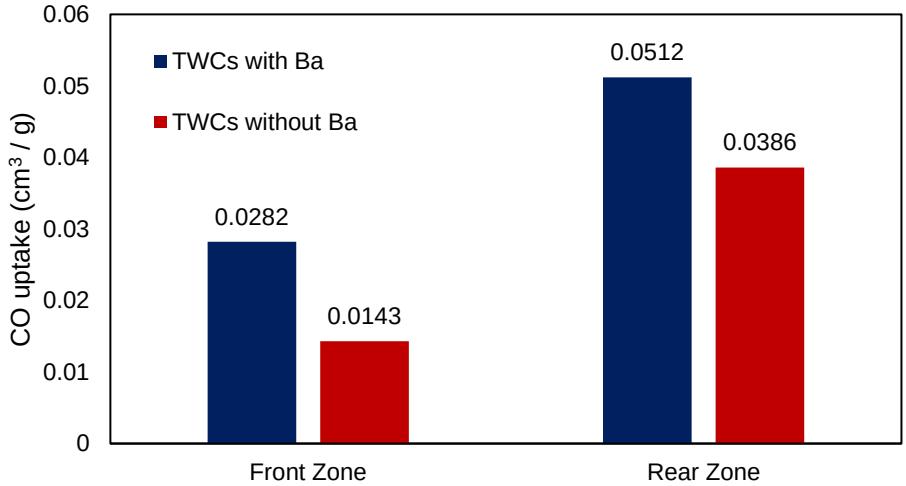

Figure 5. CO uptakes of Pd-Rh three-way catalysts with and without Ba collected from the front and

rear zones of postmortem honeycomb catalysts.

5.3.2 *In situ*/*operando* IR studies using model catalyst powders

In situ/*operando* IR spectroscopy was used to investigate the role played by the Ba additive in the formation of surface-adsorbed species upon the introduction of NO, and their reactivities toward various reductant gases, such as CO, C_3H_6, and H_2 (i.e., the NSR process). For this purpose, we prepared two model Pd/Al_2O_3 and $Pd/Ba/Al_2O_3$ catalysts (Pd = 1 wt.%, Ba = 10 wt.%). These catalysts were pretreated under a flow of 10% H_2 in He at 450 °C for 30 min prior to any experiment. Pd/Al_2O_3 and $Pd/Ba/Al_2O_3$ were subjected to high-angle annular dark-field scanning transmission electron microscopy (HAADF-STEM), with images shown in **Figure 6**. The Ba in $Pd/Ba/Al_2O_3$ is highly dispersed and is spatially uniform as a dopant dispersion, in agreement with reports based on earlier studies of similar materials (see also **Figure 6** for the bare Ba/Al_2O_3 support and Pd/Al_2O_3).[67,68] Moreover, the obtained images show that the Pd nanoparticles in Pd/Al_2O_3 and $Pd/Ba/Al_2O_3$ are 1.8 and 2.4 nm in size, respectively. It is also worth mentioning that we have previously revealed that the Pd^0 species loaded on Ba/Al_2O_3 is more electron-rich than that loaded on pristine Al_2O_3.[67]

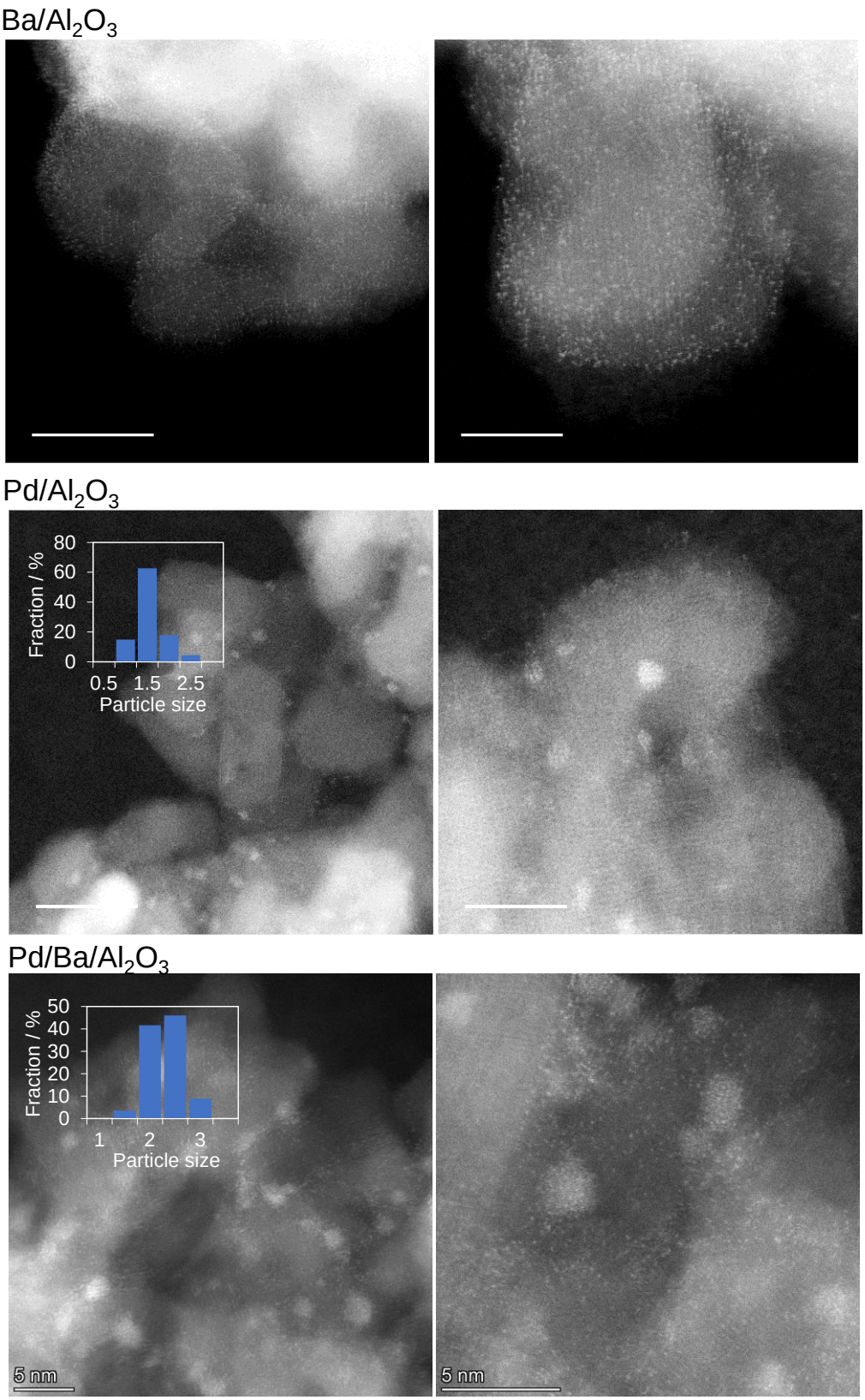

Figure 6. HAADF-STEM images of Ba/Al_2O_3, Pd/Al_2O_3, and $Pd/Ba/Al_2O_3$.

In situ IR spectra recorded during exposure of Pd/Al_2O_3, $Pd/Ba/Al_2O_3$, and Ba/Al_2O_3 to 0.5% NO in He are shown in **Figure 7.** Peaks at 1777, 1844, and 1912 cm^{-1} are observed in the spectrum of exposed Pd/Al_2O_3 (**Figure 7A**), together with a negative peak at 1289 cm^{-1} that corresponds to the decomposition of surface carbonate species.[64,69] The peak at 1777 cm^{-1} is assigned to NO molecules adsorbed on Pd^0 species,[57,64,70] while absorption bands at 1844 and 1912 cm^{-1} are assigned to gas-phase NO molecules. Exposed $Pd/Ba/Al_2O_3$ exhibited weak peaks at 1210 and 1356 cm^{-1} when NO is initially introduced, which are attributable to nitrite species.[64,71] The peak at 1210 cm^{-1} gradually grew and peaks at 1314, 1411, and 1546 cm^{-1} appeared. The weak peak at 1546 cm^{-1} is assigned to nitrate species adsorbed at Al oxide sites, while those at 1314 and 1411 cm^{-1} are attributable to nitrate species adsorbed at Ba sites.[71–73] These results indicate that the introduction of Ba favors the formation of adsorbed surface NO_x species and that NO is adsorbed on $Pd/Ba/Al_2O_3$ in the forms of both nitrite and nitrate species at 450 °C under NO flow.

These samples were also subjected to *in situ* IR spectroscopy during exposure to a mixture of NO and O_2 to investigate the effect of Ba under lean conditions where excess oxygen is present in the automotive emission. Because modern gasoline vehicles employ engine fuel-cut operations for improved fuel efficiency,[60,61] excess air intake occurs during practical TWC processes and, therefore, such investigations under excess-oxygen conditions are very important. Peaks at 1571, 1594, and 1625 cm^{-1} are observed in the spectrum of Pd/Al_2O_3 (**Figure 7A**) after exposure to the NO/O_2 mixture for 10 min. The peak at 1571 cm^{-1} is assigned to nitrate species adsorbed at Al oxide sites,[71] while peaks at around 1625 and 1594 cm^{-1} are assigned to gas-phase NO_2, a product of the reaction of NO and O_2 at 450 °C. $Pd/Ba/Al_2O_3$ exhibited peaks at 1210 and 1356 cm^{-1} (**Figure 7B**) at the commencement of exposure, which are attributable to surface nitrite species.[64,71] Peaks at 1314, 1411, and 1546 cm^{-1} appeared upon further exposure, while that at 1210 cm^{-1} declined gradually and disappeared completely after exposure for 10 min, which implies that nitrate species are formed via nitrite as an intermediate. The peaks in the 1200–1550 cm^{-1} range in the spectrum of $Pd/Ba/Al_2O_3$ after exposure to the NO/O_2 mixture are related to various surface NO_x species, and are much more intense than those observed after exposure to NO, which suggests that more NO is captured and stored in the presence of O_2. These results suggest that Ba promotes the formation of surface-adsorbed NO_x species more efficiently in the presence of O_2 (lean conditions). Although such observations are well-known for the diesel engine exhaust gas purification process,[74] this study clarified the effect of the presence of O_2 in TWC processes that operate at much higher temperatures. Moreover, the effect of H_2O addition on the formation of surface NO_x species over $Pd/Ba/Al_2O_3$ was investigated, as shown in **Figure 8**.[51,67]

The peaks observed in the 1200–1550 cm^{-1} range that are attributed to surface nitrate species with various vibrational mode were observed, and no peaks of H_2O adsorbed were observed under this condition. These observed adsorption species and their intensity are almost identical to those generated on $Pd/Ba/Al_2O_3$ in the absence of H_2O, indicating that the presence of H_2O have no significant impact on the formation of surface NO_x species at temperature employed (450 °C).

Furthermore, the species adsorbed on the Ba/Al_2O_3 surface exposed to NO and the NO/O_2 mixture were also investigated to elucidate the role Pd plays in the formation of adsorbed NO_x species, the results of which are shown in **Figure 7C**. Peaks appeared at 1210 and 1366 cm^{-1} in the spectrum of Ba/Al_2O_3 upon exposure to NO, which are assigned to surface nitrite species.[64,71] Although a weak peak attributable to nitrate is apparent at 1509 cm^{-1}, no significant nitrate species formed on the Ba/Al_2O_3 surface when exposed to NO.[71] However, peaks assigned to nitrite species were observed at 1200 and 1356 cm^{-1} when Ba/Al_2O_3 was initially exposed to the NO/O_2 mixture.[64,71] The peak at 1200 cm^{-1} decreased in intensity upon further exposure to the NO/O_2 mixture, while peaks at 1314 and 1402 cm^{-1} appeared and are attributable to surface nitrate species.[71–73] **Figure 7D** shows the time evolution of surface nitrite and nitrate species adsorbed on Ba/Al_2O_3 and $Pd/Ba/Al_2O_3$ during exposure to the NO/O_2 mixture. Note that the absorbance at 1440 cm^{-1} was solely due to nitrate species and was used to track the evolution of surface nitrate, since nitrite does not absorb at this wavenumber. Only nitrite species were observed for Ba/Al_2O_3 within the first 100 s of exposure to the NO/O_2 mixture. Nitrate species peaks began to appear, and the intensity of the nitrite peak decreased with further exposure, which suggests that surface nitrate species are formed via nitrite as an intermediate. $Pd/Ba/Al_2O_3$ showed a higher surface-nitrate formation rate than Ba/Al_2O_3. Furthermore, nitrite species adsorbed on $Pd/Ba/Al_2O_3$ exhibited shorter lifetimes than those on Ba/Al_2O_3. These results suggest that Pd facilitates the formation of surface nitrate species by promoting the oxidation of nitrite to nitrate. We also found that the surface nitrate species adsorbed on Ba/Al_2O_3 absorb more intensely than those on $Pd/Ba/Al_2O_3$ after exposure to the NO/O_2 mixture for 10 min, which indicates that Ba/Al_2O_3 has a higher total NO_x storage capacity than $Pd/Ba/Al_2O_3$ at this temperature.

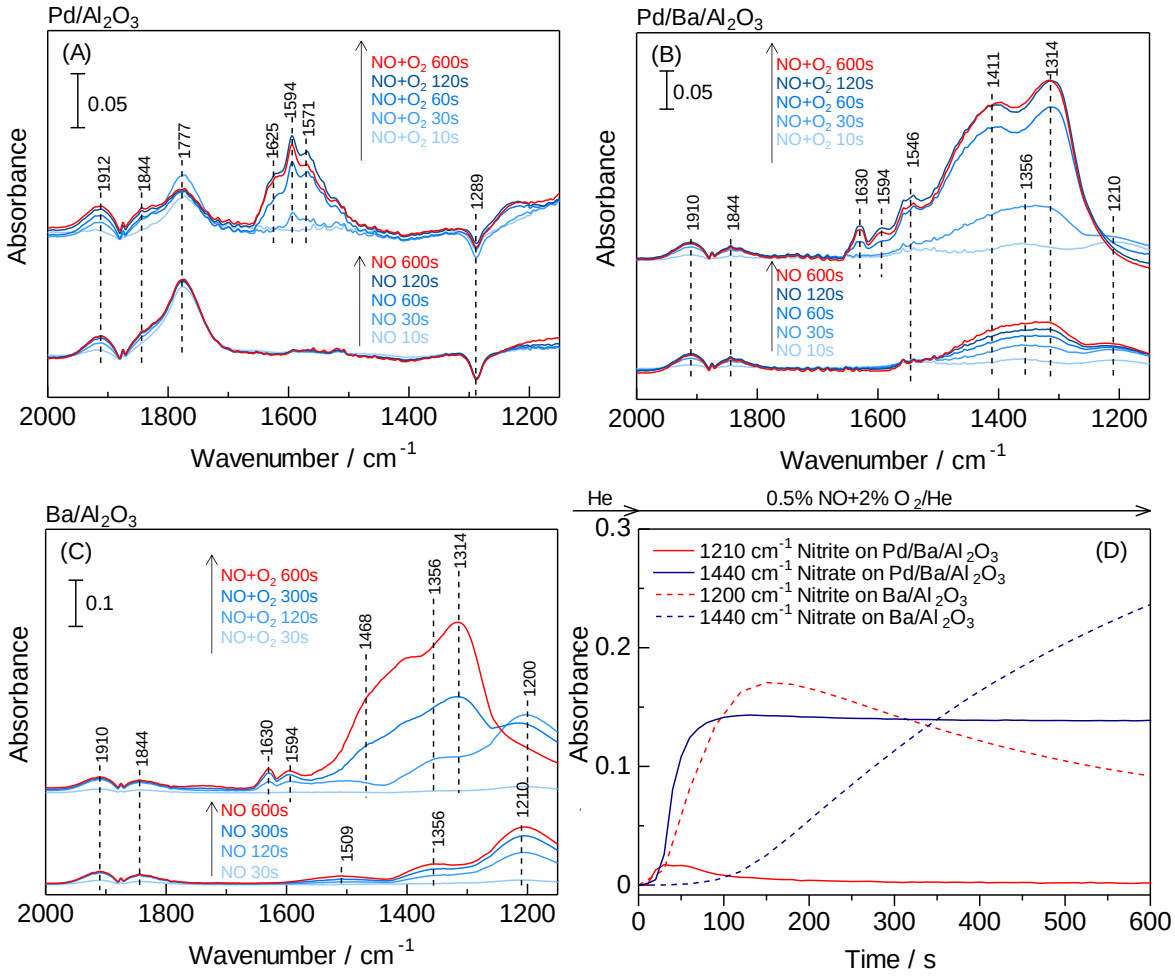

Figure 7. *In situ* IR spectra showing the evolution of surface species adsorbed on (A) Pd/Al_2O_3, (B) $Pd/Ba/Al_2O_3$, and (C) Ba/Al_2O_3 at 450 °C when exposed to NO or a NO/O_2 mixture. (D) Time evolution of the IR absorbance intensities of surface NO_x species.

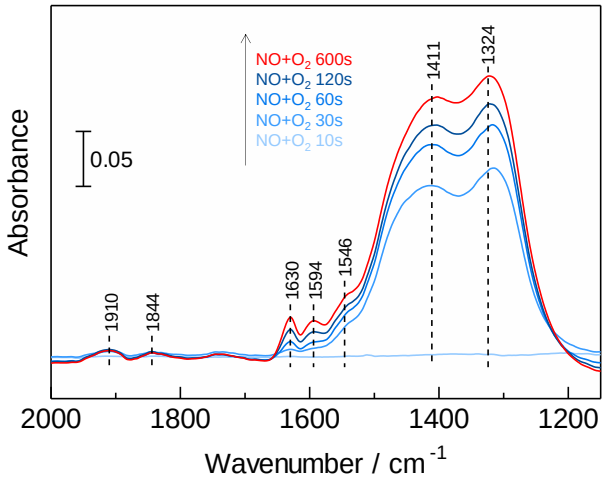

Figure 8. *In situ* IR spectra showing the evolution of surface species adsorbed on $Pd/Ba/Al_2O_3$ at 450 °C when exposed to NO/O_2 mixture in the presence of H_2O. Gas condition: 0.5% NO, 2% O_2, 2% H_2O, He balance; total flow rate: 100 mL min^{-1}.

Operando IR spectroscopy was used to assess the role played by Ba during NO reduction as CO, C_3H_6, or H_2 is introduced as a reductant. As shown in **Figure 8**, bands are observed in the 1200–1600 cm^{-1} range in the IR spectrum of the specimen collected under He flow after exposure to the NO/O_2 mixture for 10 min; these broad bands are assigned to differently adsorbed nitrate species. As depicted in **Figure 8A**, two peaks appeared in the spectrum at 1351 and 1557 cm^{-1} during subsequent exposure of the $Pd/Ba/Al_2O_3$ catalyst to 0.5% CO in He, which are attributable to adsorbed carbonate species.[64,69] The absorbance intensity at ~1351 cm^{-1} increased slightly as CO was initially introduced and then decreased with further exposure to 0.5% CO/He because peaks corresponding to surface nitrate and carbonate species overlap in the 1300–1550 cm^{-1} range. The effluent gas at the outlet was analyzed by gas chromatography (GC) using a thermal conductivity detector (TCD). N_2 and CO_2 were also simultaneously detected over $Pd/Ba/Al_2O_3$ along with the consumption of surface nitrate species after the introduction of 0.5% CO/He, as shown in **Figure 8B**, which indicates that the adsorbed surface nitrate species react with CO to form N_2 and CO_2.

In a similar manner to CO, the reactivity of surface NO_x species toward C_3H_6 was also studied by *operando* IR spectroscopy. As shown in **Figure 8C**, peaks attributable to nitrate species were less intense while that at ~1555 cm^{-1} related to carbonate species was more intense after the introduction of C_3H_6.[64,69] The concentrations of N_2 and CO_2 following the introduction of CO over $Pd/Ba/Al_2O_3$ were higher than those after the introduction of C_3H_6 (**Figure 8D**), which suggests that CO is more reactive toward the reduction of adsorbed NO_x species than C_3H_6. **Figure 8E** shows the evolution of surface NO_x species as H_2 is introduced as the reductant, while **Figure 8F** shows the production of N_2. Note that the negative peak in the spectrum of $Pd/Ba/Al_2O_3$ after the introduction of 0.5% H_2 in He for 10 min is due to the decomposition of carbonate species remaining on the catalyst surface. The evolution of surface NO_x species over Ba/Al_2O_3 upon the introduction of H_2 was also investigated, the results of which are shown in **Figure 9**. Peaks at 1319, 1411, and 1540 cm^{-1} are observed in the Ba/Al_2O_3 spectrum collected under He flow after exposure to the NO/O_2 mixture; those at 1319 and 1411 cm^{-1} are related to nitrate species affiliated with Ba, while that at 1540 cm^{-1} is attributable to nitrate species adsorbed at Al oxide sites.[71–73] The peaks related to nitrate species declined slightly when exposed to H_2, while no peaks corresponding to N_2, N_2O, or NH_3 were detected, which suggests that nitrate species adsorbed on Ba/Al_2O_3 are unreactive toward H_2 in the absence of Pd. The lower nitrate peak intensities may be due to thermal desorption. These results indicate that the efficient formation of reactive surface nitrate species and their subsequent reactions with reductant gases, such as CO, hydrocarbons, and H_2, which are akin to the NO_x storage and reduction (NSR) mechanism, play

important roles in promoting NO_x reduction in the TWC process.

Furthermore, the impact of H_2O on the reactivity of surface NO_x species toward CO, which was chosen as a representative reductant in this study, was also investigated. The *operando* IR spectra shown in **Figure 10** presents the evolution of surface adsorbed species on $Pd/Ba/Al_2O_3$ after successively flowing 0.5% NO + 2% O_2/He, He, and 0.5% CO/He in the presence of 2% H_2O. After the introduction of CO, the peak assignable to carbonate species was observed at 1557 cm^{-1} and the formation of N_2 and CO_2 were observed simultaneously. The formation of CO_2 over $Pd/Ba/Al_2O_3$ in the presence of H_2O was higher than that in the absence of H_2O and the production of H_2 was also detected after the introduction of CO for 2 min. This H_2 production was due to the water gas shift reaction ($CO + H_2O \rightleftarrows CO_2 + H_2$) occurred by the co-feed of CO and H_2O at such a high temperature (450 °C).[35,75,76] Although this result suggests complex nature of TWC, it also indicates that the observed phenomena, i.e. the efficient generation of surface reactive nitrate intermediates and their subsequent reactions with reductants, is highly important even under practical conditions.

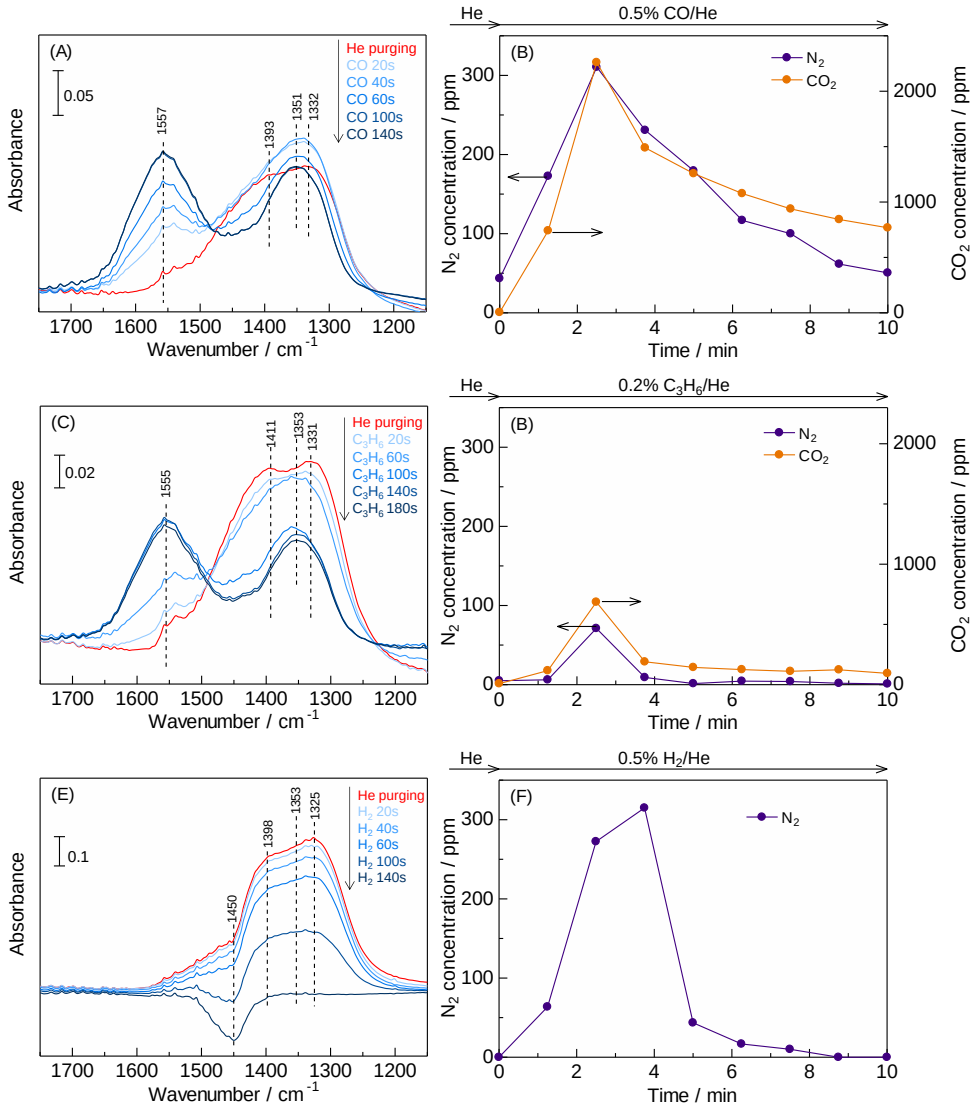

Figure 8. *Operando* IR spectra showing the evolution of surface species adsorbed on Pd/Ba/Al_2O_3 at 450 °C after successively flowing 0.5% NO + 2% O_2/He, He, and (A) 0.5% CO/He, (C) 0.2% C_3H_6/He and (E) 0.5% H_2/He, and (B, D, F) corresponding product concentrations in the effluent gases as functions of time.

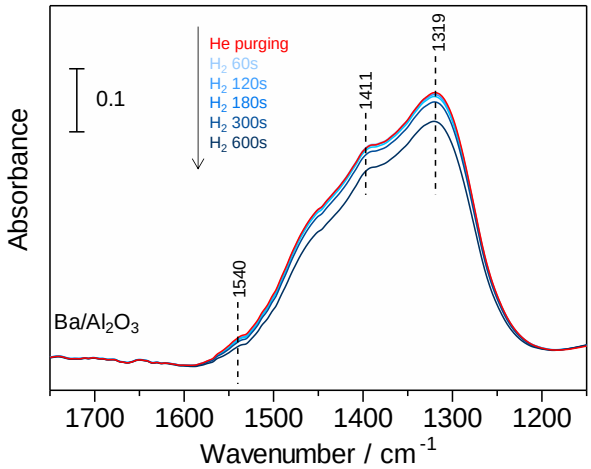

Figure 9. *In situ* IR spectra showing the evolution of surface species adsorbed on the Ba/Al_2O_3 support at 450 °C after successively flowing 0.5% NO + 2% O_2/He, He, and 0.5% H_2/He.

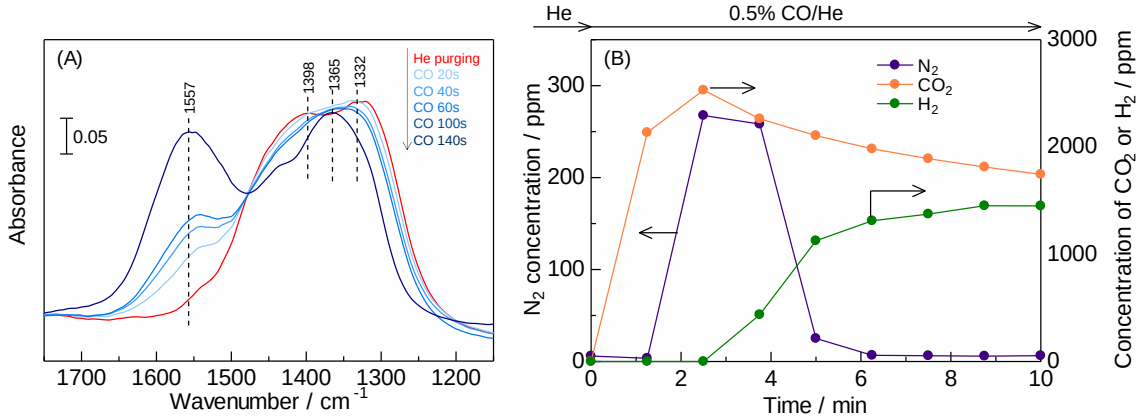

Figure 10. (A) *Operando* IR spectra showing the evolution of surface species adsorbed on $Pd/Ba/Al_2O_3$ at 450 °C in the presence of 2% H_2O after successively flowing 0.5% NO + 2% O_2/He, He, and 0.5% CO/He, and (B) the corresponding product concentrations in the effluent gases as a function of time.

5.4 Conclusions

We investigated the role of Ba in the standard TWC process using a vehicle powered by a gasoline engine. The Ba-containing honeycomb catalyst was found to be more effective in reducing all monitored emissions (NO_x, CO, and non-methane HCs); the presence of Ba was also found to suppress supported-metal aggregation. Moreover, *in situ/operando* IR spectroscopy using Pd/Al_2O_3 and $Pd/Ba/Al_2O_3$ powder catalysts revealed that the efficient generation of surface reactive nitrate intermediates and their subsequent reactions with H_2, CO, and C_3H_6, as reductants, also play key roles. This process is akin to the NO_x storage and reduction (NSR) mechanism commonly used to control diesel emissions, which avoids the TWC limitations associated with traditional gasoline-fueled stoichiometric engines by enabling reactions under non-steady-state conditions.

References

(1) Shelef, M.; McCabe, R. W. Twenty-Five Years after Introduction of Automotive Catalysts: What Next? *Catal Today* **2000**, *62*, 35–50.

(2) Matsumoto, S. Recent Advances in Automobile Exhaust Catalysts. *Catal Today* **2004**, *90* (3–4), 183–190.

(3) Granger, P.; Parvulescu, V. I. Catalytic NOx Abatement Systems for Mobile Sources: From Three-Way to Lean Burn After-Treatment Technologies. *Chem Rev* **2011**, *111*, 3155–3207.

(4) Wang, J.; Chen, H.; Hu, Z.; Yao, M.; Li, Y. A Review on the Pd-Based Three-Way Catalyst. *Catal Rev Sci Eng* **2015**, *57*, 79–144.

(5) Takayama, A.; Kurokawa, T.; Nakayama, H.; Katoh, T.; Nagata, M. Effect of Ba and La Additives to the Pd Layer of a Pd:Rh TWC. In *SAE Technical Paper*; 2017.

(6) Rood, S.; Eslava, S.; Manigrasso, A.; Bannister, C. Recent Advances in Gasoline Three-Way Catalyst Formulation: A Review. *Proceedings of the Institution of Mechanical Engineers, Part D: Journal of Automobile Engineering* **2019**, *234*, 936–949.

(7) Puspito Buwono, H.; Omori, Y.; Shioya, N.; Yoshida, H.; Hinokuma, S.; Nagao, Y.; Iwashina, K.; Endo, Y.; Nakahara, Y.; Machida, M. Enhanced Rh-Anchoring on the Composite Metal Phosphate $Y_{0.33}Zr_2(PO_4)_3$ in Three-Way Catalysis. *Catalysis Science and Technology* **2019**, *9* (19), 5447–5455.

(8) Huang, C.; Shan, W.; Lian, Z.; Zhang, Y.; He, H. Recent Advances in Three-Way Catalysts of Natural Gas Vehicles. *Catal Sci Technol* **2020**, *10*, 6407–6419.

(9) Li, L.; Zhang, N.; Wu, R.; Song, L.; Zhang, G.; He, H. Comparative Study of Moisture-Treated Pd@CeO_2/Al2O3 and Pd/CeO2/Al2O3 Catalysts for Automobile Exhaust Emission Reactions: *ACS Applied Materials and Interfaces* **2020**, *12* (9), 10350–10358.

(10) Haneda, M.; Nakamura, Y.; Yamada, T.; Minami, S.; Kato, N.; Iwashina, K.; Endo, Y.; Nakahara, Y.; Iwachido, K. Comprehensive Study of the Light-off Performance and Surface Properties of Engine-Aged Pd-Based Three-Way Catalysts. *Catalysis Science and Technology* **2021**, *11* (3), 912–922.

(11) Khivantsev, K.; Vargas, C. G.; Tian, J.; Kovarik, L.; Jaegers, N. R.; Szanyi, J.; Wang, Y. Economizing on Precious Metals in Three‐Way Catalysts: Thermally Stable and Highly Active Single‐Atom Rhodium on Ceria for NO Abatement under Dry and Industrially Relevant Conditions. *Angew. Chem. Int. Ed.* **2021**, *133*, 395–402.

(12) Hosokawa, S.; Oshino, Y.; Tanabe, T.; Koga, H.; Beppu, K.; Asakura, H.; Teramura, K.; Motohashi, T.; Okumura, M.; Tanaka, T. Strong Metal–Support Interaction in Pd/$Ca_2AlMnO_{5+\delta}$: Catalytic NO Reduction over Mn-Doped CaO Shell. *ACS Catalysis* **2021**, 7996–8003.

(13) Li, L.; Liu, S.; Jiang, R.; Ji, Y.; Li, H.; Guo, X.; Jia, L.; Zhong, Z.; Su, F. Subnanometric Pt on Cu Nanoparticles Confined in Y-Zeolite: Highly-Efficient Catalysts for Selective Catalytic Reduction of NOx by CO. *ChemCatChem* **2021**, *13* (6), 1568–1577.

(14) Machida, M.; Uchida, Y.; Iwashita, S.; Yoshida, H.; Tsushida, M.; Ohyama, J.; Nagao, Y.; Endo, Y.; Wakabayashi, T. Catalyst Deactivation via Rhodium-Support Interactions under High-Temperature Oxidizing Conditions: A Comparative Study on Hexaaluminates versus Al2O3. *ACS Catalysis* **2021**, *11* (15), 9462–9470.

(15) Ueda, K.; Ohyama, J.; Satsuma, A. Investigation of Reaction Mechanism of NO-C_3H_6-CO-O_2 Reaction over $NiFe_2O_4$ Catalyst. *ACS Omega* **2017**, *2*, 3135−3143.

(16) Koga, H.; Tada, K.; Hayashi, A.; Ato, Y.; Okumura, M. High NOx Reduction Activity of an Ultrathin Zirconia Film Covering a Cu Surface: A DFT Study. *Catalysis Letters* **2017**, *147*, 1827–1833.

(17) Hosokawa, S.; Matsuki, K.; Tamaru, K.; Oshino, Y.; Aritani, H.; Asakura, H.; Teramura, K.; Tanaka, T. Selective Reduction of NO over Cu/Al_2O_3: Enhanced Catalytic Activity by Infinitesimal Loading of Rh on Cu/Al_2O_3. *Molecular Catalysis* **2017**, *442*, 74–82.

(18) Hirakawa, T.; Shimokawa, Y.; Tokuzumi, W.; Sato, T.; Tsushida, M.; Yoshida, H.; Hinokuma, S.; Ohyama, J.; Machida, M. Multicomponent Spinel Oxide Solid Solutions: A Possible Alternative to Platinum Group Metal

Three-Way Catalysts. *ACS Catalysis* **2019**, *9*, 11763−11773.
(19) York, A. P. E.; Cooper, C. S.; Simmance, K.; Wilkinson, S. K. Non-PGM Iron Perovskite Three-Way Gasoline Emissions Control Catalysts: Kinetics, Reaction Mechanism and Catalyst Sizing Study. *Topics in Catalysis* **2020**, *63* (3–4), 256–267.
(20) Alcalde-Santiago, V.; Davó-Quiñonero, A.; Bailón-García, E.; Lozano-Castelló, D.; Bueno-López, A. Copper-Lanthanum Catalysts for NOx and Soot Removal. *ChemCatChem* **2020**, *12* (24), 6375–6384.
(21) Yoshida, H.; Oyama, H.; Shiomori, R.; Hirakawa, T.; Ohyama, J.; Machida, M. Enhanced Catalytic NO Reduction in NO–CO–C_3H_6–O_2 Reaction Using Pseudo-Spinel (NiCu)Al_2O_4 Supported on γ-Al_2O_3. *ACS Catalysis* **2021**, 7302–7309.
(22) Farrauto, R. J.; Deeba, M.; Alerasool, S. Gasoline Automobile Catalysis and Its Historical Journey to Cleaner Air. *Nat Catal* **2019**, *2*, 603–613.
(23) Twigg, M. v. Catalytic Control of Emissions from Cars. *Catal Today* **2011**, *163*, 33–41.
(24) Machida, M.; Uchida, Y.; Ishikawa, Y.; Hinokuma, S.; Yoshida, H.; Ohyama, J.; Nagao, Y.; Endo, Y.; Iwashina, K.; Nakahara, Y. Thermostable Rh Metal Nanoparticles Formed on Al_2O_3 by High-Temperature H_2 Reduction and Its Impact on Three-Way Catalysis. *Journal of Physical Chemistry C* **2019**, *123*, 24584−24591.
(25) Di Monte, R.; Fornasiero, P.; Kaspar, J.; Graziani, M.; Gatica, J. M.; Bernal, S.; Gomez-Herrero, A. Stabilisation of Nanostructured $Ce_{0.2}Zr_{0.8}O_2$ Solid Solution by Impregnation on Al_2O_3: A Suitable Method for the Production of Thermally Stable Oxygen Storage/Release Promoters for Three-Way Catalysts. *Chemical Communications* **2000**, No. 21, 2167–2168.
(26) Nishio, Y.; Ozawa, M. Thermal Stability and Microstructural Change of Lanthanum Modified Alumina Catalytic Support. *Journal of the Ceramic Society of Japan* **2007**, *115*, 633–636.
(27) Kwak, J. H. H.; Hu, J.; Lukaski, A.; Kim, D. H. H.; Szanyi, J.; Peden, C. H. F. H. F. Role of Pentacoordinated Al3+ Ions in the High Temperature Phase Transformation of γ-Al2O3. *Journal of Physical Chemistry C* **2008**, *112* (25), 9486–9492.
(28) Gandhi, H. S.; Graham, G. W.; McCabe, R. W. Automotive Exhaust Catalysis. *Journal of Catalysis* **2003**, *216*, 433–442.
(29) Kang, S. B.; Nam, I. S.; Cho, B. K.; Kim, C. H.; Oh, S. H. Kinetic Model for Modern Double-Layered Pd/Rh TWC as a Function of Metal Loadings and Mileage. *Chemical Engineering Journal* **2015**, *278*, 328–338.
(30) Machida, M.; Ueno, M.; Omura, T.; Kurusu, S.; Hinokuma, S.; Nanba, T.; Shinozaki, O.; Furutani, H. CeO2-Grafted Mn-Fe Oxide Composites as Alternative Oxygen-Storage Materials for Three-Way Catalysts: Laboratory and Chassis Dynamometer Tests. *Ind Eng Chem Res* **2017**, *56* (12), 3184–3193.
(31) Kusatsugu, K.; Nakamura, Y.; Haneda, M. Three-Way Catalytic Performance of Fe-Doped Pd/CeO2-ZrO2 under Lean/Rich Perturbation Conditions. *Applied Catalysis A: General* **2019**, *587* (September), 117268.
(32) Vedyagin, A. A.; Kenzhin, R. M.; Tashlanov, M. Y.; Alikin, E. A.; Stoyanovskii, V. O.; Plyusnin, P. E.; Shubin, Y. V; Mishakov, I. V; Smirnov, M. Y.; Kalinkin, A. V; Bukhtiyarov, V. I. Effect of La Addition on the Performance of Three-Way Catalysts Containing Palladium and Rhodium. *Top Catal* **2020**, *63*, 152–165.
(33) Fujiwara, A.; Yoshida, H.; Ohyama, J.; Machida, M. Change in the Pd Oxidation State during Light-Off of Three-Way Catalysis Analyzed by in Situ Diffuse Reflectance Spectroscopy. *Journal of Physical Chemistry C* **2020**, *124* (23), 12531–12538.
(34) Suhonen, S.; Valden, M.; Pessa, M.; Savimäki, A.; Härkönen, M.; Hietikko, M.; Pursiainen, J.; Laitinen, R. Characterization of Alumina Supported Pd Catalysts Modified by Rare Earth Oxides Using X-Ray Photoelectron Spectroscopy and X-Ray Diffraction: Enhanced Thermal Stability of PdO in Nd/Pd Catalysts. *Appl Catal A Gen* **2001**, *207*, 113–120.
(35) Klingstedt, F.; Karhu, H.; Kalantar Neyestanaki, A.; Lindfors, L. E.; Salmi, T.; Väyrynen, J. Barium Promoted Palladium Catalysts for the Emission Control of Natural Gas Driven Vehicles and Biofuel Combustion Systems. *J Catal* **2002**, *206*, 248–262.
(36) Takahashi, M.; Kikuchi, S.; Iwachido, K.; Ikeda, M.; Goto, H. Development of New Three-Way Catalyst Technologies to Improve Purification Performance for Exhaust Emission after Severe Thermal Aging.

Transactions of Society of Automotive Engineers of Japan **2013**, *44*, 15–20.
(37) Winkler, A.; Eyssler, A.; Mägli, A.; Liati, A.; Dimopoulos Eggenschwiler, P.; Bach, C. Fuel Impact on the Aging of TWC's under Real Driving Conditions. *Fuel* **2013**, *111*, 855–864.
(38) Machida, M.; Fujiwara, A.; Yoshida, H.; Ohyama, J.; Asakura, H.; Hosokawa, S.; Tanaka, T.; Haneda, M.; Tomita, A.; Miki, T.; Iwashina, K.; Endo, Y.; Nakahara, Y.; Minami, S.; Kato, N.; Hayashi, Y.; Goto, H.; Hori, M.; Tsuda, T.; Miura, K.; Kimata, F.; Iwachido, K. Deactivation Mechanism of Pd/CeO_2-ZrO_2 Three-Way Catalysts Analyzed by Chassis-Dynamometer Tests and in Situ Diffuse Reflectance Spectroscopy. *ACS Catal* **2019**, *9* (7), 6415−6424.
(39) Fujiwara, A.; Tsurunari, Y.; Yoshida, H.; Ohyama, J.; Yamada, T.; Haneda, M.; Miki, T.; Machida, M. Thermal Deactivation of Pd/CeO2-ZrO2Three-Way Catalysts during Real Engine Aging: Analysis by a Surface plus Peripheral Site Model. *ACS Omega* **2020**, *5* (44), 28897–28906.
(40) Muraki, H.; Shinjyoh, H.;Fujitani, Y.; Muraki, H.; Shinjoh, H.; Fujitani, Y. Effect of Lanthanum on the NO Reduction over Palladium Catalysts. *Appl Catal* **1986**, *22*, 325–335.
(41) Muraki, H. ; H.; Shinjoh, H. ; H.; Sobukawa, H. ; H.; Yokota, K. K. ;; Fujitani, Y. Palladium-Lanthanum Catalysts for Automotive Emission Control. *Industrial and Engineering Chemistry Product Research and Development* **1986**, *25* (2), 202–208.
(42) Muraki, H.; Yokota, K.; Fujitani, Y. Nitric Oxide Reduction Performance of Automotive Palladium Catalysts. *Appl Catal* **1989**, *48*, 93–105.
(43) Matsuura, S.; Hirai, A.; Arimura, K.; Shinjoh, H. Development of Three-Way Catalyst with Using Only Pd as Activator. *SAE Technical Papers* **1995**, 950257.
(44) Valden, M.; Keiski, R. L.; Xiang, N.; Pere, J.; Aaltonen, J.; Pessa, M.; Maunula, T.; Savimäki, A.; Lahti, A.; Härkönen, M. Reactivity of Pd/Al_2O_3, Pd/La_2O_3-Al_2O_3 and $Pd/LaAlO_3$ Catalysts for the Reduction of NO by CO: CO and NO Adsorption. *J Catal* **1996**, *161*, 614–625.
(45) Skoglundh, M.; Johansson, H.; Löwendahl, L.; Jansson, K.; Dahl, L.; Hirschauer, B. Cobalt-Promoted Palladium as a Three-Way Catalyst. *Applied Catalysis B: Environmental* **1996**, *7*, 299–319.
(46) Tanikawa, K.; Egawa, C. Effect of Barium Addition over Palladium Catalyst for CO-NO-O2 Reaction. *Journal of Molecular Catalysis A: Chemical* **2011**, *349*, 94–99.
(47) Sekiba, T.; Kimura, S.; Yamamoto, H.; Okada, A. Development of Automotive Palladium Three-Way Catalysts. *Catal Today* **1994**, *22*, 113–126.
(48) Kobayashi, T.; Yamada, T.; Kayano, K. Effect of Basic Metal Additives on NOx Reduction Property of Pd-Based Three-Way Catalyst. *Appl Catal B* **2001**, *30* (3–4), 287–292.
(49) Cao, Y.; Ran, R.; Wu, X.; Weng, D. A New Insight into the Effects of Barium Addition on Pd-Only Catalysts: Pd-Support Interface and CO + NO Reaction Pathway. *Applied Catalysis A: General* **2015**, *501* (x), 17–26.
(50) Toyao, T.; Jing, Y.; Kon, K.; Hayama, T.; Nagaoka, S.; Shimizu, K. Catalytic NO–CO Reactions over La-Al_2O_3 Supported Pd: Promotion Effect of La. *Chem Lett* **2018**, *47*, 1036–1039.
(51) Jing, Y.; Cai, Z.; Liu, C.; Toyao, T.; Maeno, Z.; Asakura, H.; Hiwasa, S.; Nagaoka, S.; Kondoh, H.; Shimizu, K. K. Promotional Effect of La in the Three-Way Catalysis of La-Loaded Al_2O_3-Supported Pd Catalysts ($Pd/La/Al_2O_3$). *ACS Catalysis* **2020**, *10* (2), 1010–1023.
(52) Gong, J.; Wang, D.; Li, J.; Currier, N.; Yezerets, A. Dynamic Oxygen Storage Modeling in a Three-Way Catalyst for Natural Gas Engines: A Dual-Site and Shrinking-Core Diffusion Approach. *Applied Catalysis B: Environmental* **2017**, *203*, 936–945.
(53) Takahashi, N.; Shinjoh, H.; Iijima, T.; Suzuki, T.; Yamazaki, K.; Yokota, K.; Suzuki, H.; Miyoshi, N.; Matsumoto, S.; Tanizawa, T.; Tanaka, T.; Tateishi, S.; Kasahara, K. The New Concept 3-Way Catalyst for Automotive Lean-Burn Engine: NO_x Storage and Reduction Catalyst. *Catalysis Today* **1996**, *27*, 63–69.
(54) Liu, G.; Gao, P. X. A Review of NOx Storage/Reduction Catalysts: Mechanism, Materials and Degradation Studies. *Catalysis Science and Technology* **2011**, *1* (4), 552–568.
(55) Lietti, L.; Daturi, M.; Blasin-Aubé, V.; Ghiotti, G.; Prinetto, F.; Forzatti, P. Relevance of the Nitrite Route in the NOx Adsorption Mechanism over $Pt\text{-}Ba/Al_2O_3$ NO_x Storage Reduction Catalysts Investigated by Using Operando FTIR Spectroscopy. *ChemCatChem* **2012**, *4*, 55–58.

(56) Aderhold, D.; Haynes, A. G.; Spencer, M. L. W.; Winterborn, D. J. W. Monolith Coating Apparatus and Method Therefor. *US Patent* **2013**, *US6599570B*.
(57) Toyao, T.; Jing, Y.; Kon, K.; Hayama, T.; Nagaoka, S.; Shimizu, K. ichi. Catalytic NO-CO Reactions over La-Al2O3 Supported Pd: Promotion Effect of La. *Chem Lett* **2018**, *47* (8), 1036–1039.
(58) Westermann, A.; Azambre, B. Impact of the Zeolite Structure and Acidity on the Adsorption of Unburnt Hydrocarbons Relevant to Cold Start Conditions. *Journal of Physical Chemistry C* **2016**, *120* (45), 25903–25914.
(59) Lee, J.; Theis, J. R.; Kyriakidou, E. A. Vehicle Emissions Trapping Materials: Successes, Challenges, and the Path Forward. *Applied Catalysis B: Environmental* **2019**, *243*, 397–414.
(60) Möller, R.; Votsmeier, M.; Onder, C.; Guzzella, L.; Gieshoff, J. Is Oxygen Storage in Three-Way Catalysts an Equilibrium Controlled Process? *Applied Catalysis B: Environmental* **2009**, *91* (1–2), 30–38.
(61) Choi, M.; Song, J.; Lee, E.; Ma, S.; Lee, S.; Seo, J.; Yoo, S.; Lee, J. The Development of a Nox Reduction System during the Fuel Cut Period for Gasoline Vehicles. In *SAE Technical Papers*; SAE International, 2019; Vol. 2019-April.
(62) Lietti, L.; Daturi, M.; Blasin-Aubé, V.; Ghiotti, G.; Prinetto, F.; Forzatti, P. Relevance of the Nitrite Route in the NOx Adsorption Mechanism over Pt-Ba/Al_2O_3 NO_x Storage Reduction Catalysts Investigated by Using Operando FTIR Spectroscopy. *ChemCatChem* **2012**, *4*, 55–58.
(63) Fanson, P. T.; Horton, M. R.; Delgass, W. N.; Lauterbach, J. FTIR Analysis of Storage Behavior and Sulfur Tolerance in Barium-Based NOχ Storage and Reduction (NSR) Catalysts. *Applied Catalysis B: Environmental* **2003**, *46* (2), 393–413.
(64) Pieta, I. S.; García-Diéguez, M.; Herrera, C.; Larrubia, M. A.; Alemany, L. J. In Situ DRIFT-TRM Study of Simultaneous NOx and Soot Removal over Pt-Ba and Pt-K NSR Catalysts. *Journal of Catalysis* **2010**, *270* (2), 256–267.
(65) Kolli, T.; Lassi, U.; Rahkamaa-Tolonen, K.; Kinnunen, T. J. J.; Keiski, R. L. The Effect of Barium on the Catalytic Behaviour of Fresh and Aged Pd-Ba-OSC/Al2O3 Catalysts. *Applied Catalysis A: General* **2006**, *298* (1–2), 65–72.
(66) Zhang, X.; Long, E.; Li, Y.; Zhang, L.; Guo, J.; Gong, M.; Chen, Y. The Effect of CeO2 and BaO on Pd Catalysts Used for Lean-Burn Natural Gas Vehicles. *Journal of Molecular Catalysis A: Chemical* **2009**, *308* (1–2), 73–78.
(67) Jing, Y.; Wang, G.; Wei Ting, K.; Maeno, Z.; Oshima, K.; Satokawa, S.; Nagaoka, S.; Shimizu, K.; Toyao, T. Roles of the Basic Metals La, Ba and Sr as Additives in Al_2O_3-Supported Pd-Based Three-Way Catalysts. *J Catal* **2021**, *400*, 387–396.
(68) Tamai, K.; Hosokawa, S.; Yamamoto, A.; Asakura, H.; Teramura, K.; Tanaka, T. Identification of Active Ba Species on TiO2 Photocatalyst for NOx Trapping. *Chemistry Letters* **2020**, *49* (7), 859–862.
(69) Frola, F.; Manzoli, M.; Prinetto, F.; Ghiotti, G.; Castoldi, L.; Lietti, L. Pt-Ba/Al_2O_3 NSR Catalysts at Different Ba Loading: Characterization of Morphological, Structural, and Surface Properties. *Journal of Physical Chemistry C* **2008**, *112*, 12869–12878.
(70) Hess, C.; Ozensoy, E.; Yi, C. W.; Goodman, D. W. NO Dimer and Dinitrosyl Formation on Pd(111): From Ultra-High-Vacuum to Elevated Pressure Conditions. *Journal of the American Chemical Society* **2006**, *128* (9), 2988–2994.
(71) Sedlmair, C.; Seshan, K.; Jentys, A.; Lercher, J. A. Elementary Steps of NOx Adsorption and Surface Reaction on a Commercial Storage-Reduction Catalyst. *Journal of Catalysis* **2003**, *214* (2), 308–316.
(72) Nova, I.; Castoldi, L.; Lietti, L.; Tronconi, E.; Forzatti, P.; Prinetto, F.; Ghiotti, G. NOx Adsorption Study over Pt-Ba/Alumina Catalysts: FT-IR and Pulse Experiments. *Journal of Catalysis* **2004**, *222* (2), 377–388.
(73) Castoldi, L.; Lietti, L.; Nova, I.; Matarrese, R.; Forzatti, P.; Vindigni, F.; Morandi, S.; Prinetto, F.; Ghiotti, G. Alkaline- and Alkaline-Earth Oxides Based Lean NOx Traps: Effect of the Storage Component on the Catalytic Reactivity. *Chemical Engineering Journal* **2010**, *161* (3), 416–423.
(74) Takahashi, N.; Imagawa, H. Improvement of Catalysts for NOx Storage and Reduction for Gasoline-Fueled Automotive Exhaust. *Journal of the Japan Petroleum Institute* **2009**, *52* (3), 90–101.

(75) Rajasree, R.; Hoebink, J. H. B. J.; Schouten, J. C. Transient Kinetics of Carbon Monoxide Oxidation by Oxygen over Supported Palladium/Ceria/Zirconia Three-Way Catalysts in the Absence and Presence of Water and Carbon Dioxide. *Journal of Catalysis* **2004**, *223* (1), 36–43.
(76) Kwon, H. J.; Baik, J. H.; Kwon, Y. T.; Nam, I. S.; Oh, S. H. Enhancement Effect of Water on Oxidation Reactions over Commercial Three-Way Catalyst. *Chemical Engineering Journal* **2008**, *141* (1–3), 194–203.

Chapter 6

Promoting Effect of Basic Metal Additives on DeNOx Reactions over Pt-Based Three-Way Catalysts

6.1 Introduction

Three-way catalysis is one of the most efficient methods for limiting gasoline engine exhaust emissions by simultaneously reducing NO_x to N_2 and oxidizing CO and hydrocarbons (HCs) to CO_2.[1–7] Most modern commercial three-way catalysts (TWCs) comprise Pd and small amounts of Rh. Despite the excellent catalytic performance of Pd- and Rh-based TWCs,[8–17] their application has been hindered by the recently increasing prices of Pd and Rh. Therefore, Pt has been economically favored, which has increased its use as a replacement for Pd and Rh in TWCs. However, because of its currently high cost, researchers have shifted their attention away from Pt-based TWCs. Consequently, the development of more effective support materials for enhancing the catalytic efficiency of Pt-based TWCs is critical for meeting increasingly stringent environmental regulations.[18–21]

γ-Al_2O_3 is widely used as a support material for TWCs because of its large surface area, remarkable mechanical strength, and excellent thermal stability.[22,23] Alkaline and rare earth metals are often loaded onto Al_2O_3 to enhance the structural and thermal stability of γ-Al_2O_3 by increasing the γ-to-α phase transition temperature.[23–28] Commonly used basic metals, such as Ba, La, and Sr, are also known to efficiently anchor Pt species, promoting Pt dispersion.[29–31] However, only a few studies have examined the effect of basic metal additives on the performance of TWCs. For example, Burch and Watling investigated the effect of such additives, such as La and Ba, on the reduction of NO by C_3H_6 under lean conditions over Pt-based TWCs and demonstrated that they enhanced the performance of the TWCs but did not considerably affect their N_2/N_2O selectivity.[32] Shinjoh et al. confirmed that adding Ba enhanced the catalytic performance of Pt-based catalysts for NO and C_3H_6 conversion under simulated three-way catalytic conditions. [33] Moreover, they showed that Ba weakened hydrocarbon chemisorption, thereby allowing the catalytic reaction to proceed smoothly. Konsolakis and Yentekakis performed a kinetic study using a Ba-loaded Pt/Al_2O_3 catalyst and demonstrated that Ba increased the adsorption strength of NO molecules on the Pt surface and weakened the N–O bonds, thereby promoting NO dissociation.[34] Although these studies are critical in the three-way catalysis field, our understanding of the role played by basic metal additives, such as Ba, La, and Sr, is still insufficient.

We recently examined the role of Ba, La, and Sr in Pd-based TWCs.[35–37] Our results indicated that adding these basic metals modified the electronic state of Pd nanoparticles. The Pd^0 species loaded on La/Al_2O_3 were more electron-deficient than those loaded on Al_2O_3, leading to suppression of the CO poisoning effect and enhancing the catalytic performance for NO reduction, especially to N_2O. Conversely, the Pd^0 species loaded on Sr/Al_2O_3 and Ba/Al_2O_3 were more electron-rich than those loaded on pristine Al_2O_3. Consequently, the $Pd/Ba/Al_2O_3$ and

$Pd/Sr/Al_2O_3$ catalysts outperformed the Pd/Al_2O_3 catalyst for CO and C_3H_6 oxidation. In addition, we investigated the effects of oxygen storage materials (OSMs), including CeO_2 and CeO_2–ZrO_2, as Pt catalyst supports.[38] Our findings showed that the CeO_2 content of CeO_2–ZrO_2 significantly affected the catalytic performance of Pt/OSMs catalysts in three-way catalytic reactions. The Pt^0 species loaded on the OSMs with higher CeO_2 contents were more electron-deficient, improving the effective resistance of the Pt/OSM catalysts against CO poisoning and consequently enhancing their catalytic performance for NO reduction.

In this study, we examined the effect of basic metal additives on the performance of Pt-based TWCs. The $Pt/M/Al_2O_3$ (M = Ba, La, or Sr) catalysts outperformed the Pt/Al_2O_3 catalyst for NO reduction and CO and C_3H_6 oxidation under three-way catalysis conditions. Moreover, Ba enhanced the catalytic activity of the Pt-based catalysts more efficiently than La and Sr. $Pt/Ba/Al_2O_3$, which was selected as the representative basic-metal-loaded catalyst, was subjected to kinetic analysis and *in situ/operando* spectroscopy experiments, namely, X-ray absorption spectroscopy (XAS), infrared (IR) spectroscopy, and ambient-pressure X-ray photoelectron spectroscopy (AP-XPS), to investigate the role of Ba during NO_x reduction. The Pt^0 species loaded on Ba/Al_2O_3 were more electron-rich than those loaded on Al_2O_3, promoting the dissociation of NO molecules into N and O atoms, as observed using AP-XPS studies. Moreover, the *operando* IR spectroscopy results indicated that the efficient formation of intermediate surface NO_x species and their reactivity toward reductant gases, such as H_2 or CO, was important for the promotional effect of Ba during NO_x reduction. Lastly, the activity and limitations of the $Pt/M/Al_2O_3$ catalysts were compared with those of $Pd/M/Al_2O_3$ and Pt/OSM catalysts.

6.2. Experimental methods

6.2.1 Preparation of materials and catalysts

Commercially available γ-Al_2O_3 was used as the Al_2O_3 support, and basic metals (Sr, Ba, and La) were added to the Al_2O_3 support using an impregnation method, as described in our previous study. [35–37] The corresponding supported Pt (3 wt% Pt) catalysts were prepared by the impregnation method with an aqueous $Pt(NH_3)_2(NO_2)_2$, which was dissolved in HNO_3 (Pt content = 4.6 wt%; Furuya Metal Co., Ltd.) as a precursor. A $Pt(NH_3)_2(NO_2)_2$ solution containing 0.062 g of Pt was added into a glass vessel along with 2 g of unmodified γ-Al_2O_3 or basic-metal-loaded Al_2O_3 (M/Al_2O_3), and the mixture was stirred (200 rpm) at room temperature for 15 min. The mixture was then evaporated to dryness at 50 °C under decreased pressure. Next, the samples were dried at 90 °C for 12 h and subsequently calcined in air at 500 °C for 3 h. Afterward, the calcined samples were pretreated under flowing H_2 (20 mL min^{-1}) at 500 °C for 30 min in a Pyrex

tube. The as-prepared H_2-pretreated samples were used for the characterization experiments unless otherwise stated. Before each catalytic activity test and *in situ*/*operando* spectroscopic experiment, the samples were reduced again under flowing 10%H_2/He (100 mL min^{-1}) gas at 400 °C for 30 min.

The honeycomb catalysts were prepared by coating the catalyst powders (Pt = 3 wt%), a slurry composed of an inactive alumina-based binder, and water onto a cordierite honeycomb (∅25.4 mm × 50 mm, 400 cells/in^2; NGK Insulators, Ltd.). After drying at 120 °C for 1 h, they were calcined at 600 °C for 2 h. The as-prepared honeycomb catalyst contained approximately 60 g/L of coated powder catalyst, equal to a total Pt loading of 0.18 g/L.

The hydrothermal treatment of monolithic honeycomb catalysts was performed at 1000 °C for 4 h under varying redox conditions, i.e., stoichiometric, lean (oxidizing), and rich (reducing) atmospheres. The gas compositions for lean (3% O_2, 10% H_2O, and N_2 balance), stoichiometric (10% H_2O and N_2 balance), and rich (3% CO, 3% H_2, 10% H_2O, and N_2 balance) atmospheres were applied with programmed intervals of 180 s for lean, 10 s for stoichiometric, 180 s for rich, and 10 s for stoichiometric conditions. The flow rate was set to 3 L min^{-1}, which corresponds to a space velocity (SV) = 7,200 h^{-1}.

6.2.2 Catalyst characterization

X-ray diffraction (XRD) patterns were recorded on a Rigaku Miniflex software using Cu-Kα radiation. N_2 adsorption was measured using an AUTOSORB 6AG (Yuasa Ionics Co.). High-angle annular dark-field STEM (HAADF-STEM) characterizations were carried out using a JEM-ARM200F microscope (JEOL) with an accelerating voltage of 300 kV, convergence semi-angle of 17.9 mrad, and screen current of 173 pA. Temperature-programmed reduction (H_2-TPR) measurements were carried out using BELCAT (MicrotracBEL); specifically, unreduced catalysts (0.06 g) were placed in a quartz tube and exposed to 10% H_2/He for 30 min at 500 °C and then to O_2 for 30 min at the same temperature to remove the surface carbonate species. After cooling the samples to -100 °C, the temperature was increased to 800 °C with a heating rate of 10°C/min under flowing 5% H_2/Ar (20 mL/min). The consumption of H_2 was detected using a TCD detector.

6.2.3 *In situ/operando* infrared (IR) spectroscopy

In situ/operando IR spectra were recorded at 200 °C using a JASCO FT/IR-4200 equipped with a liquid-nitrogen-cooled mercury–cadmium–telluride (MCT) detector in transmission mode. For each measurement, a 40 mg sample of each powder was pressed to prepare a self-supporting pellet (∅20 mm), which was placed in a quartz IR cell with CaF_2 windows. The cell was connected to a gas flow system. The pellets were reduced under flowing 10% H_2/He (100 mL min^{-1}) at 400 °C

for 0.5 h prior to measurement. The pellet was then cooled to 200 °C under flowing He, and 0.5% NO/He was introduced for 10 min. After being purged by He for 10 min, 0.5% NO + 2% O_2 (He balance) was flowed into the system, followed by another 10 min of purging with He. Finally, 0.5% H_2/He was supplied to the IR system.

The *in situ* IR spectra for CO chemisorption were recorded at liquid nitrogen temperature. Prior to the adsorption experiments, the samples were exposed to 10% H_2/He at 400 °C for 30 min. The spectra were collected after evacuation for 30 min following 30 min of exposure to 0.5% CO/He.

6.2.4 (*In situ*) X-ray Absorption Spectroscopy (XAS)

The XAS spectra were collected at the BL14B2 beamline of SPring-8. Pt/M/Al_2O_3 (M = Ba, La, or Sr), which was sealed in polyethylene cells in air, was examined at the K-edges of Ba, Sr, and La in transmission mode using a Si(311) double crystal monochromator. The XAS results were analyzed using Athena software ver. 0.9.25 included in the Demeter package.[39]

In situ Pt L_3-edge XAS spectra were recorded in transmittance mode at the BL14B2 beam line of SPring-8 with a Si(311) double crystal monochromator (proposal 2020A1695). For each sample, 45 mg pressed into a pellet (∅ 7 mm) was placed into a quartz cell with Kapton film windows. The catalyst was pretreated under flowing 10% H_2/He (300 mL min^{-1}) at 400 °C for 30 min, followed by cooling to 200 °C. Subsequently, 0.5% NO/He (300 mL min^{-1}) was supplied to the cell for 10 min. The fractions of Pt^0 and Pt^{4+} were estimated with a linear composition fitting (LCF) analysis using the spectra of the corresponding sample before the introduction of NO and PtO_2 as references for Pt^0 and Pt^{4+}, respectively. The SV for the *in situ* Pt L_3-edge XAS measurements was ~ 30,000 h^{-1}.

6.2.5 Ambient-pressure X-Ray photoelectron spectroscopy (AP-XPS)

Ambient pressure X-ray photoelectron spectroscopy (AP-XPS) was performed at beamline 13B of the Photon Factory (PF) at the High Energy Accelerator Research Organization (KEK). Pt/Al_2O_3 and Pt/Ba/Al_2O_3 powders, each with a Pt loading of 10 wt%, were utilized for the AP-XPS experiments to enhance the XPS signal intensity. The promotional effect of Ba was confirmed for these high-Pt-loading powders by *operando* IR experiments. The powder catalysts, reduced under a flow of 10% H_2/He, were coated on a Si substrate using a drop-and-dry method with deionized water as the dispersant. The sample temperature was measured by a thermocouple directly attached to the sample holder in the analysis chamber. The gases were introduced into the chamber using variable leak valves. The samples were pretreated by exposure to H_2 at 350 °C for 30 min followed by cooling to 200 °C under evacuation conditions. Gases were then introduced

into the analysis chamber, and all XPS spectra were collected at 200 °C. Al 2p and N 1s measurements were performed with a photon energy of 630 eV. For Pt/Al_2O_3 and $Pt/Ba/Al_2O_3$, 0.1 Torr NO was introduced for 1 h. For $Pt/Ba/Al_2O_3$, after the subsequent introduction of 0.1 Torr NO and 0.1 Torr O_2 for 1 h followed by evacuation for 10 min, 0.1 Torr H_2 or CO was injected into the chamber to investigate the reactivity of surface species. The binding energy was calibrated using the Al 2p level (Al_2O_3; 74.5 eV). The N 1s XPS spectra were analyzed with the convolution of Gaussian and Lorentzian functions and a Shirley background in the range of 386–408 eV. The obtained peak areas of various surface species were normalized using the intensity of the Al 2p signal to exclude the attenuation caused by the introduced gases.

6.2.6 Catalytic reactions

Catalytic reactions over the catalysts in powder form were carried out using a flow reactor. Specifically, 15 mg of the catalyst was placed in the reactor using quartz wool to support the catalyst bed. After pretreating the catalyst under 10% H_2/He flow (100 mL min^{-1}) at 400 °C for 30 min, the catalyst was cooled to 300 °C, and the catalytic NO–CO reaction was initiated by supplying a gas mixture containing CO (0.5%), NO (0.5%), and He balance at 100 mL min^{-1} (*W*/*F* corresponds to 1.5×10^{-4} g·min·cm^{-3}). The catalysts were exposed to the reaction gas mixture for 5 h at each temperature to reach a steady state. The conversions and yields of the gasses were determined using gas chromatographic (GC) analysis (Shimadzu GC-8A with a SHINCARBON ST column). The yields of N_2 and CO_2 were calculated based on the following equation.

$$NO + CO \rightarrow 0.5\ N_2 + CO_2 \quad (1)$$

Catalytic reactions over the honeycomb catalysts were performed in a flow reactor using MEXA-series (Horiba Ltd.). The catalysts were placed in a tubular-type reactor, and their catalytic performance was measured by supplying a gas mixture typically containing 0.1% NO, 0.6% CO, 420 ppm C_3H_6, 0.6% O_2, 0.2% H_2, 15% CO_2, 10% H_2O, and N_2 balance (λ = 1) at SV = 100,000 h^{-1}. Light-off tests were conducted under the aforementioned gas composition (1 Hz perturbation between $\lambda = 0.95$ and $\lambda = 1.05$, see the detailed gas composition in **Table 1**) at a ramping rate of 25 °C/min. The conversions of CO, NO, and C_3H_6 were monitored using an exhaust gas analyzer (ABB, AO-2020). Prior to each catalytic activity test, the honeycomb catalyst was pre-treated by flowing the reaction gas at 400 °C for 30 min. The λ values were calculated using the following equation (see **Table 1** for further details on the gas compositions).

$$\lambda = \frac{O_2 + 0.5CO + 0.5H_2O + CO_2 + 0.5NO}{0.5H_2 + CO + 1.5C_3H_6 + 0.5H_2O + CO_2} \quad (2)$$

Table 1. Composition of the simulated exhaust gas mixtures for TWC light-off tests.

λ	NO / %	CO / %	C_3H_6 / ppm	O_2 / %	H_2 / %	CO_2 / %	H_2O / %	N_2 / %
0.95	0.1	2.4	420	0.6	0.8	15	10	balance

1.00	0.1	0.6	420	0.6	0.2	15	10	balance
1.05	0.1	0.6	420	1.65	0.2	15	10	balance

6.3. Results and discussion

6.3.1 Catalysts characterization

Table 2 summarizes the preparation conditions and physicochemical characteristics of the Pt/Al_2O_3 and $Pt/M/Al_2O_3$ (M = Ba, La, Sr) catalysts. The loading amounts of Ba, La, and Sr were 10, 10, and 6.4 wt%, respectively. The loading amounts of basic metals were adjusted to fabricate catalysts with the same mole percentage of these metals. The Brunauer–Emmett–Teller specific surface area (S_{BET}) of the fresh as-prepared Pt/Al_2O_3 catalyst was higher than those of the $Pt/M/Al_2O_3$ catalysts. The broad peaks in the XRD patterns of all the catalysts were attributed to γ-Al_2O_3 (**Figure 1)**. However, no characteristic Pt peaks were present in the XRD patterns, suggesting that Pt was well dispersed on Al_2O_3 and M/Al_2O_3 (M = Ba, La, Sr). The characteristic peaks of $SrCO_3$ and $BaCO_3$ emerged in the XRD patterns of $Pt/Sr/Al_2O_3$ and $Pt/Ba/Al_2O_3$, respectively. The results of XRD indicate the presence of crystalline carbonate species of basic metal additive in $Pt/Ba/Al_2O_3$ and $Pt/Sr/Al_2O_3$.[36,37,40,41]

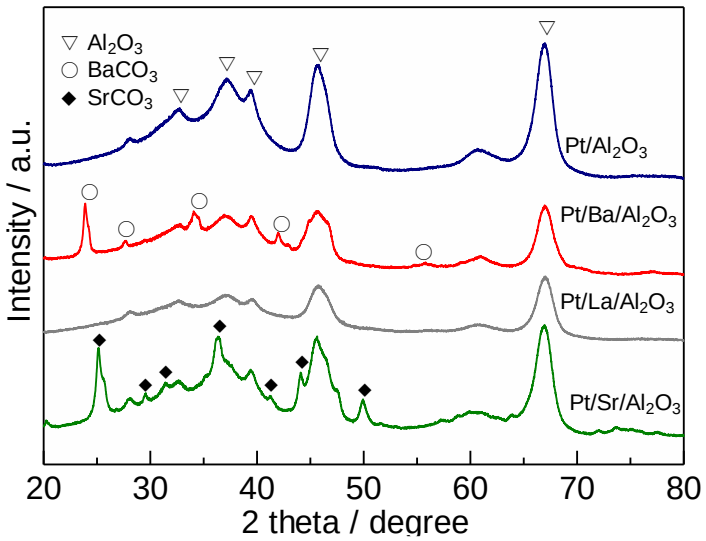

Figure 1. XRD patterns of the fresh Pt/Al_2O_3 and $Pt/M/Al_2O_3$ (M = Ba, La, or Sr) catalysts.

The basic metal additives were observed as bright dots in the HAADF–STEM images of M/Al_2O_3, as shown in **Figure 2**. The HAADF-STEM images of Pt/Al_2O_3 and $Pt/M/Al_2O_3$, as shown in **Figure 3** revealed that the average size of Pt particles ranged between approximately 2 and 3 nm (**Table 2**). More than 1,000 Pt particles in the HAADF-STEM images were manually counted to obtain the average particle size and size distribution using GATAN software. Note that the metal dispersion was not determined by CO chemisorption in this study owing to the interference from

the basic metal additives.[37] Notably, no peaks for adsorbed CO were observed at ca. 2100 cm^{-1} in the IR spectra of Pt/Al_2O_3 and $Pt/M/Al_2O_3$, as shown in **Figure 10** indicating the absence of atomically dispersed Pt species.[40]

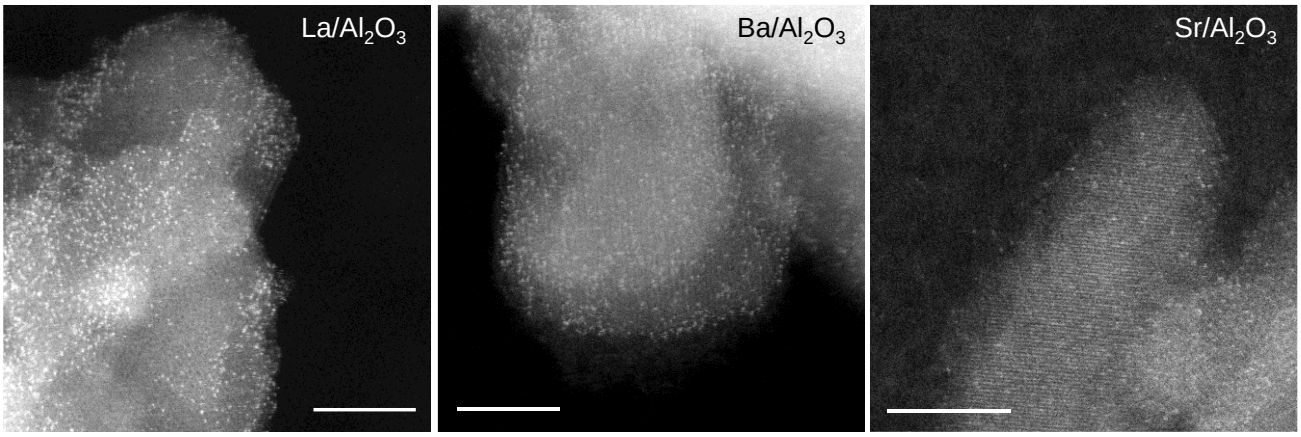

Figure 2. HADDF-STEM images of the M/Al_2O_3 (M = Ba, La, or Sr) supports.

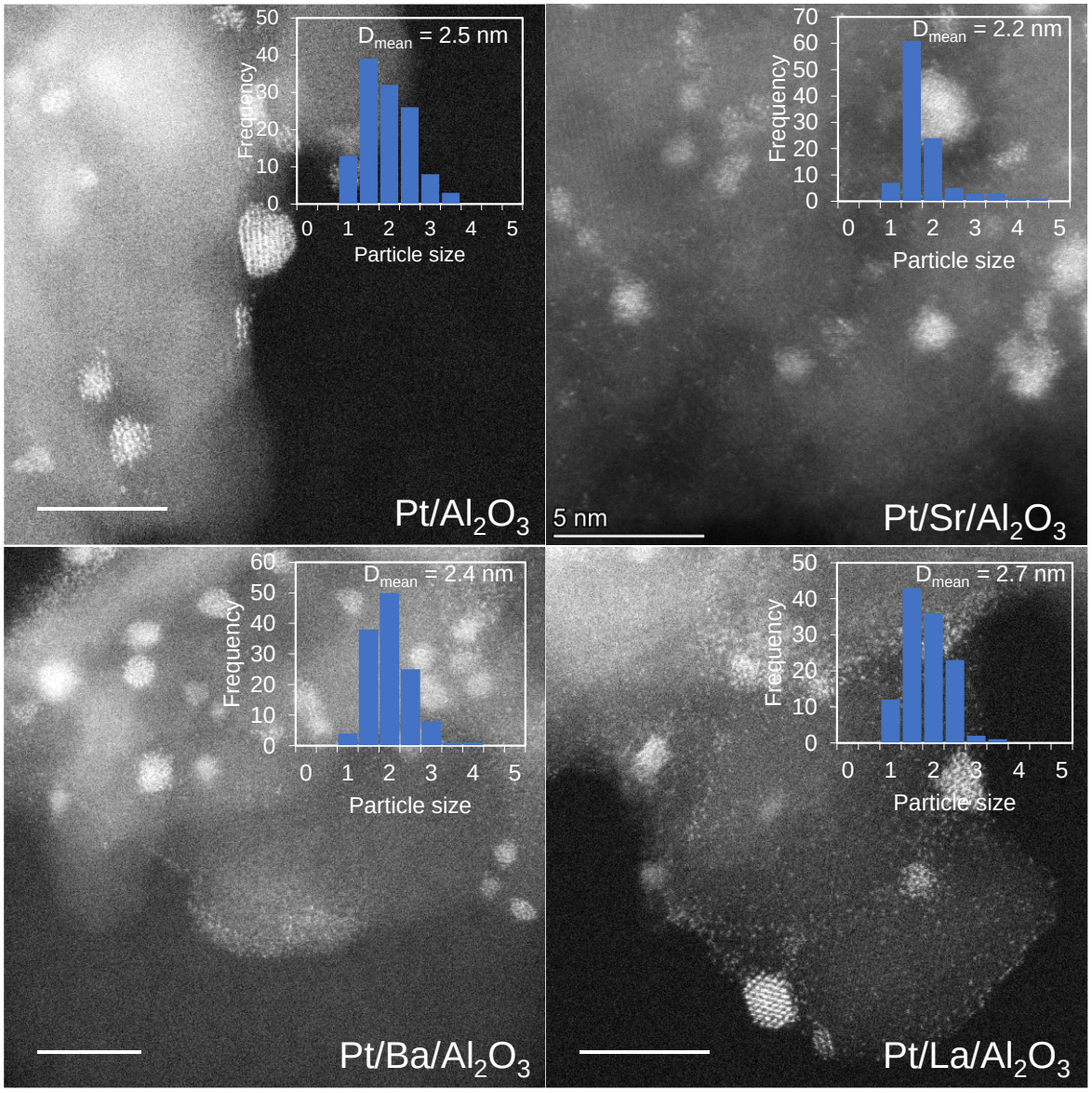

Figure 3. Representative HAADF–STEM images of the Pt/Al_2O_3 and $Pt/M/Al_2O_3$ (M = Ba, La, Sr) catalysts.

Table 2. Preparation conditions and physicochemical characteristics of the fresh Pt/Al_2O_3 and $Pt/M/Al_2O_3$ catalysts

Catalyst[a]	Loading amount of M / wt%	S_{BET} / m^2 g^{-1}	Average size of Pt particles[b] / nm
Pt/Al_2O_3	-	152	2.5
$Pt/Sr/Al_2O_3$	6.4	130	2.2
$Pt/Ba/Al_2O_3$	10	128	2.4
$Pt/La/Al_2O_3$	10	138	2.7

[a]Pt loading: 3 wt%
[b]Obtained using HAADF-STEM data

The XAS profiles of $Pt/M/Al_2O_3$ at the Ba, La, and Sr K-edges are presented in **Figure 4**.

The Fourier transforms (FTs) of the k^3-weighted extended X-ray absorption fine structure (EXAFS) spectra (**Table 3**) were fitted, revealing that the FT-EXAFS spectra of Pt/M/Al_2O_3 (M = Ba, La, Sr) were primarily composed of single M–O contributions. In addition, the H_2-TPR profiles of Pt/Al_2O_3 and Pt/Ba/Al_2O_3 (**Figure 5**) revealed that the Pt oxide can be reduced below 150 °C.

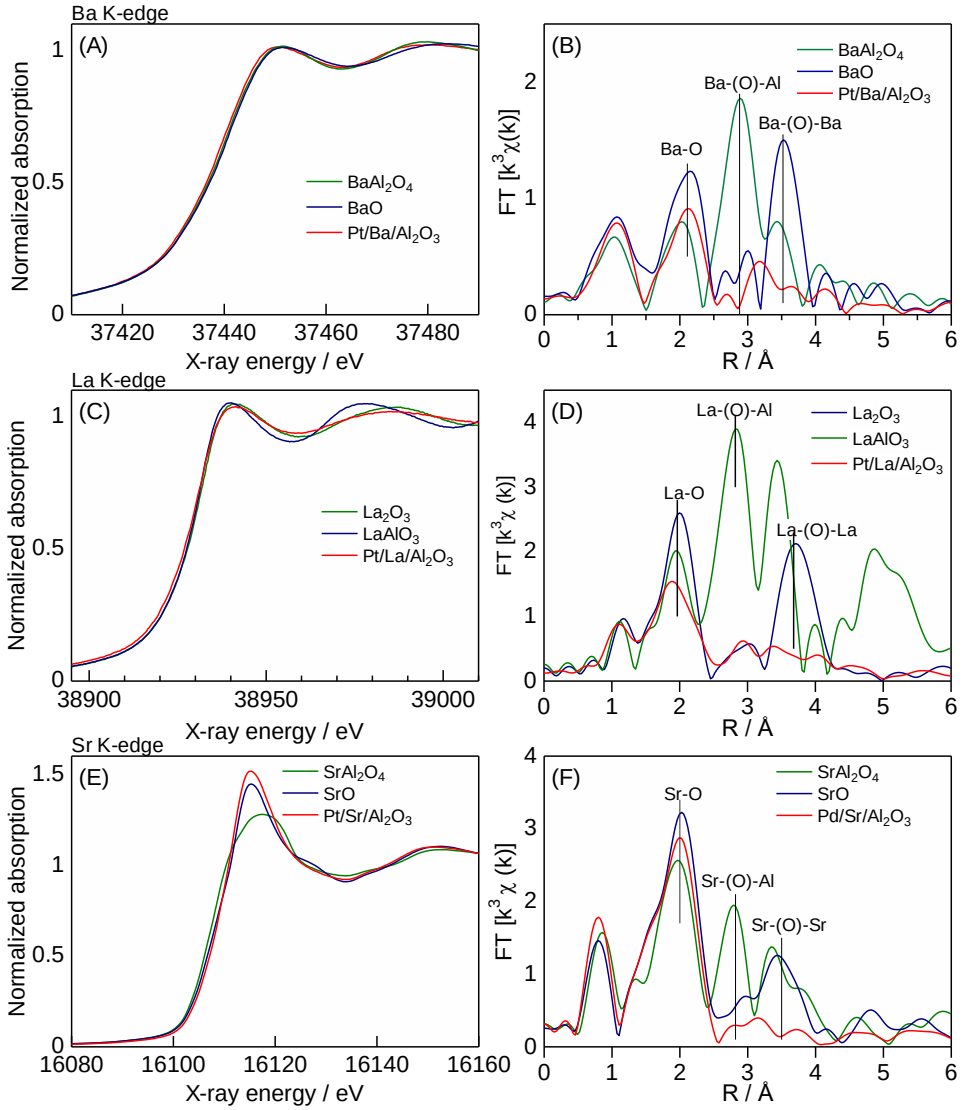

Figure 4. The La, Ba, and Sr K-edge (A, C, E) XANES spectra and (B, D, F) k^3-weighted EXAFS Fourier transforms of Pt/M/Al_2O_3 (M = Ba, La, or Sr) catalysts.

Table 3. Curve-fitting analysis of La, Ba and Sr K-edge EXAFS for Pt/M/Al_2O_3 (M = La, Ba, or Sr).

Sample	Shell	CN [a]	*R* (Å) [b]	σ^2 (Å^2) [c]	R_f (%) [d]
Pt/La/Al_2O_3	La–O	6.7	2.55	0.018	0.90
	La–(O)–Al	1.1	3.30	0.006	
Pt/Ba/Al_2O_3	Ba–O	3.7	2.74	0.014	1.35
Pt/Sr/Al_2O_3	Sr–O	5.7	2.57	0.014	0.74

[a] Coordination number. [b] Bond distance. [c] Debye-Waller factor. [d] Residual factor.

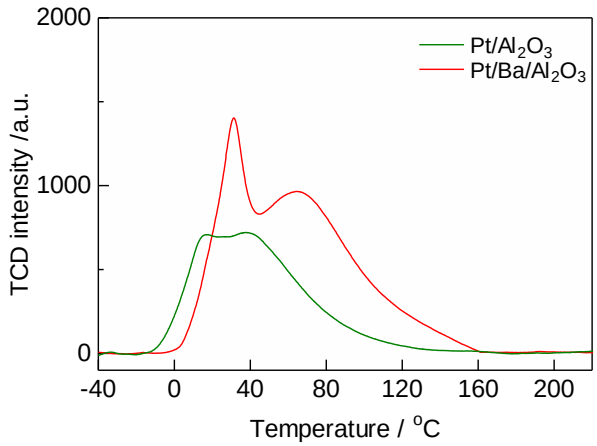

Figure 5. H_2-TPR profile of Pt/Al_2O_3 and $Pt/Ba/Al_2O_3$. Catalyst weight: 60 mg, heating rate: 10 °C/min, gas composition: 5% H_2/Ar, flow rate: 30 mL/min.

6.3.2 Catalytic NO–CO reaction and three-way catalytic reactions using fresh catalysts

The results of a three-way catalytic light-off test using the honeycomb catalysts prepared by coating the powder catalysts onto honeycomb substrates are presented in **Figure 6**. The NO, CO, and C_3H_6 conversions of the $Pt/M/Al_2O_3$ (M = Ba, La, Sr) catalysts were higher than those of Pt/Al_2O_3, indicating that the introduction of basic metal additives enhanced the removal efficiencies of the monitored pollutants. Among these additives, Ba presented the highest efficiency for enhancing the activity of the analyzed TWCs, especially at low temperatures (< 250 °C).

The activities of the Pt/Al_2O_3 and $Pt/M/Al_2O_3$ (M = Ba, La, Sr) powder catalysts for the NO–CO reaction, which was the primary NO reduction reaction of the three-way catalysis process, were examined, as illustrated in **Figure 7**. The results indicated that the basic metals enhanced the activities of the catalysts for the NO and CO reactions. In particular, N_2O was the primary NO reduction product over Pt/Al_2O_3 and $Pt/M/Al_2O_3$ (M = La, Sr) at temperatures below 400 °C. Moreover, the amount of N_2O formed over the $Pt/Ba/Al_2O_3$ catalyst was negligible over the entire temperature range. The N_2O–CO reaction was performed over $Pt/Ba/Al_2O_3$ and Pt/Al_2O_3 to investigate the effect of Ba on the reduction of N_2O by CO, and the results are presented in **Figure 8**. The introduction of Ba caused only a small enhancement in the efficiency of $Pt/Ba/Al_2O_3$ for the N_2O–CO reaction. These results indicated that Ba additives enhanced the catalytic conversion of NO and the selectivity of the direct NO-to-N_2 conversion. The catalytic conversions of NO and CO decreased as follows: $Pt/Ba/Al_2O_3$ > $Pt/La/Al_2O_3$ > $Pt/Sr/Al_2O_3$ > Pt/Al_2O_3, and this trend was consistent with the results obtained under three-way catalytic conditions. Therefore, we selected Ba as the optimal and representative basic metal additive and investigated its role in the three-way catalysis process.

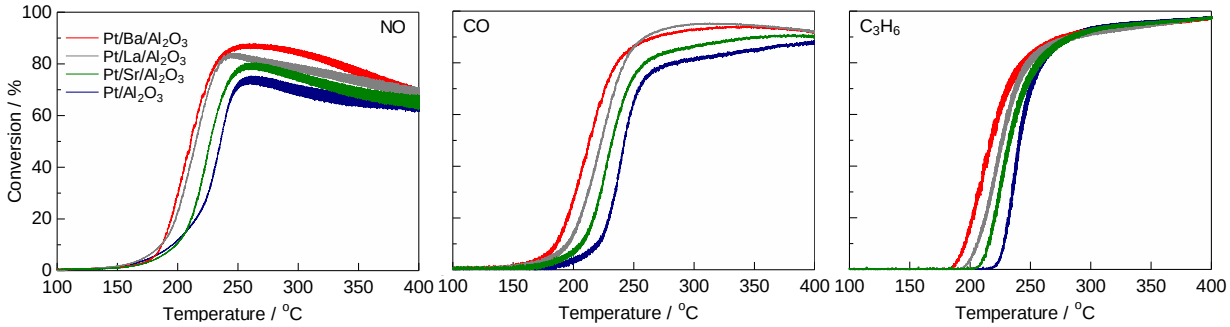

Figure 6. Conversions of NO, CO, and C_3H_6 during the light-off tests over the Pt/Al_2O_3 and Pt/M/Al_2O_3 (M = Ba, La, Sr) catalysts coated on honeycomb monoliths under 1 Hz perturbated gases between λ = 0.95 and λ = 1.05. Heating rate: 25 °C/min; gas composition: NO (0.1%), C_3H_6 (420 ppm), CO (2.4–0.6%), O_2 (0.6–1.65%), H_2 (0.8%), H_2O (10%), CO_2 (15%), N_2 balance; SV = 100,000 h^{-1}.

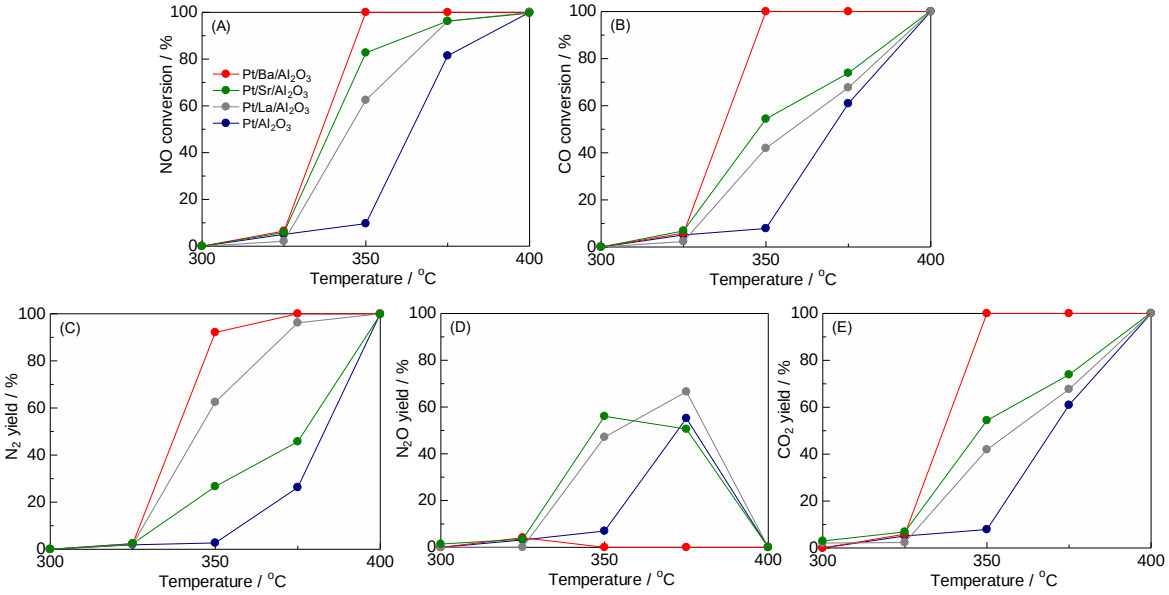

Figure 7. Results of the catalytic activity test during NO–CO reaction over the powder form of Pt/Al_2O_3 and Pt/M/Al_2O_3 (M = Ba, La, or Sr) catalysts. Catalyst weight: 15mg, Gas conditions: 0.5% NO, 0.5% CO, He balance; SV: ~30,000 h^{-1}.

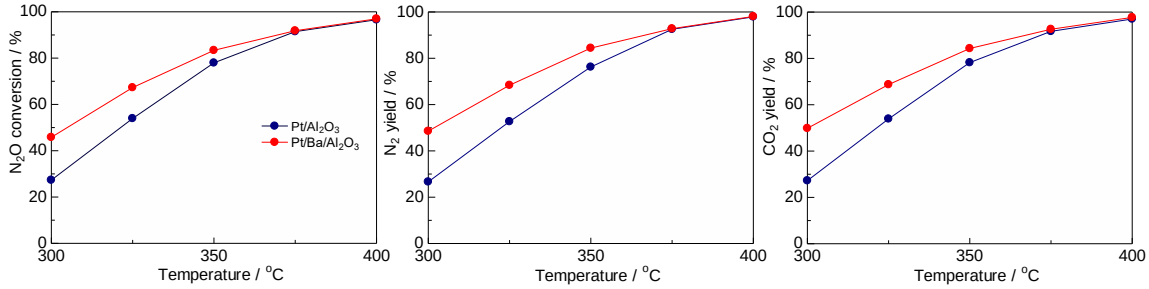

Figure 8. Results of the catalytic activity test during the N_2O–CO reaction over the powder form of Pt/Al_2O_3 and Pt/Ba/Al_2O_3 catalysts. Catalyst weight: 15 mg; Gas conditions: 0.5%N_2O, 0.5% CO, He balance; SV: ~30,000 h^{-1}.

Under real three-way catalytic working conditions, the λ value of the feed composition fluctuates significantly between low (rich, reducing atmosphere) and high (lean, oxidizing atmosphere) values because of an engine fuel-cut operation that was introduced relatively recently to improve fuel efficiency.[37] The response efficiency to fluctuations in the feed composition is critical for the TWCs used to remove exhaust gases under real operating conditions. Therefore, we evaluated the λ-switching performance for NO, CO, and C_3H_6 removal over the honeycomb Pt/Al_2O_3 and $Pt/M/Al_2O_3$ (M = Ba, La, Sr) catalysts (**Figure 9**). Prior to the λ-switching test, the honeycomb catalysts were exposed to lean gas at 300 °C for 5 min. The detection delays between the monitored components (1.0 s for NO and 3.2 s for CO relative to C_3H_6) were ascribed to the experimental setup. After changing the feed gas from rich to lean, the NO conversions of the catalysts decreased; in particular, the NO conversions over $Pt/M/Al_2O_3$, especially $Pt/Ba/Al_2O_3$ and $Pt/La/Al_2O_3$, decreased slower than that over Pt/Al_2O_3. These results indicated that the $Pt/M/Al_2O_3$ (M = Ba, La, Sr) catalysts retained higher NO conversions than the Pt/Al_2O_3 catalyst. The $Pt/M/Al_2O_3$ catalysts were also effective for CO and C_3H_6 conversion. Upon changing the feed gas from lean to rich, higher NO and CO conversions were achieved over $Pt/La/Al_2O_3$, followed by $Pt/Ba/Al_2O_3$. By contrast, Pt/Al_2O_3 outperformed the $Pt/M/Al_2O_3$ catalysts for the C_3H_6 conversion reaction, indicating that basic metal additives were inefficient for C_3H_6 abatement upon changing the reaction conditions from lean to rich feed gas. Overall, $Pt/Ba/Al_2O_3$ was the best catalyst, especially for NO abatement.

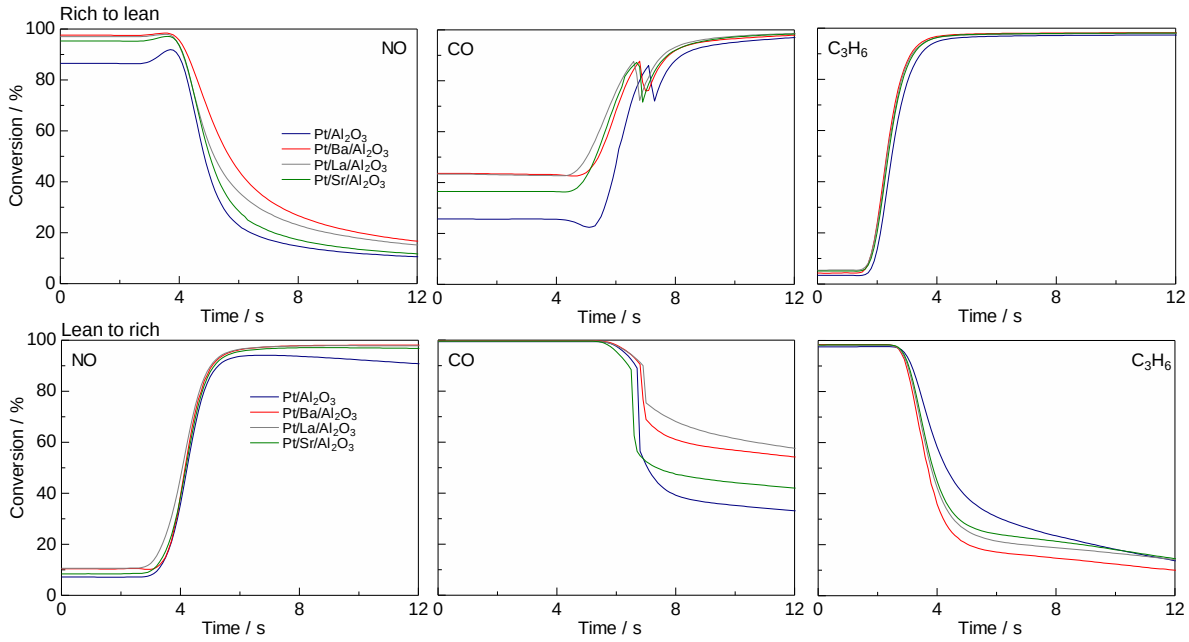

Figure 9. Lambda-switching test over the Pt/Al_2O_3 and $Pt/M/Al_2O_3$ (M = Ba, La, Sr) catalysts coated on honeycomb monoliths during lambda jumps (λ = 1.05–0.95) at 300 °C. The detection delays were ascribed to the experimental setup (3.2 s for CO and 1.0 s for NO relative to C_3H_6).

6.3.3 Mechanistic studies using kinetic and *in situ*/*operando* spectroscopy experiments

The origin of the promotional effect of Ba addition was investigated using kinetic and *in situ*/*operando* spectroscopy methods. First, the electronic states of the Pt nanoparticles supported on Ba/Al_2O_3, La/Al_2O_3, and Al_2O_3 as reference supports were investigated using *in situ* IR spectroscopy. The *in situ* IR spectra of CO adsorbed on Pt/Al_2O_3, $Pt/Ba/Al_2O_3$, and $Pt/La/Al_2O_3$ obtained after evacuation for 10 min following the introduction of 0.5% CO/He for 30 min are presented in **Figure 10**. The spectra were obtained at liquid nitrogen temperature to prevent the formation of surface carbonate species. The peak at approximately 2060–2080 cm^{-1} was attributed to the CO molecules bound to the top sites of the metal surfaces.[41] The characteristic peak of $Pt/Ba/Al_2O_3$ was centered at a lower wavenumber (2065 cm^{-1}) than that of Pt/Al_2O_3 (2077 cm^{-1}), whereas that of $Pt/La/Al_2O_3$ emerged at a higher wavenumber (2079 cm^{-1}). These results revealed that Pt interacted with the basic metal additives. Back-donation from transition metals to the antibonding $2\pi^*$ orbitals of CO molecules contribute primarily to the formation of M–CO bonds. This lowers the binding order of C–O bonds and causes the C–O vibration frequency to downshift.[42–44] The more electrons are transferred from the d orbitals of Pt to the antibonding orbitals of the CO molecules, the weaker the C–O bonds become; this promotes activation and increases the adsorption strength of CO molecules.[45] Specifically, in this study, the vibration frequency of the CO molecules adsorbed on $Pt/Ba/Al_2O_3$ downshifted compared with that of the CO molecules adsorbed on Pt/Al_2O_3, indicating that the Pt^0 species of $Pt/Ba/Al_2O_3$ were more electron-rich than those of Pt/Al_2O_3. In contrast, the Pt^0 species on La/Al_2O_3 were more electron-deficient than those on pristine Al_2O_3 as the CO vibration frequency was higher (blue-shifted) when CO was adsorbed on $Pt/La/Al_2O_3$ than on Al_2O_3. These results were in agreement with the data previously reported for supported Pd-particle-based catalysts.[37]

To further explore the role of Ba, kinetic studies were performed using Pt/Al_2O_3 and $Pt/Ba/Al_2O_3$ powder catalysts. **Figure 11** presents the effect of the CO concentration on the rates of the NO–CO reaction over Pt/Al_2O_3 and $Pt/Ba/Al_2O_3$ catalysts. The TOF was determined using the reaction rate and Pt dispersion, which was obtained using CO adsorption experiments. The apparent CO reaction orders for the NO–CO reactions over the Pt/Al_2O_3 and $Pt/Ba/Al_2O_3$ catalysts were -1.7 and -2.0, respectively. The negative values revealed that the NO–CO reaction over the Pt/Al_2O_3 and $Pt/Ba/Al_2O_3$ catalysts was inhibited by CO, which was in agreement with the adsorption strength of CO molecules on the Pt surface.[46,47] Furthermore, the CO reaction order over $Pt/Ba/Al_2O_3$ was more negative than that over Pt/Al_2O_3, indicating that the introduction of Ba strengthened the poisoning effect of CO. These results were ascribed to the abundant electron-rich Pt^0 species loaded on Ba/Al_2O_3 strengthening CO adsorption, thereby intensifying the

poisoning effect.

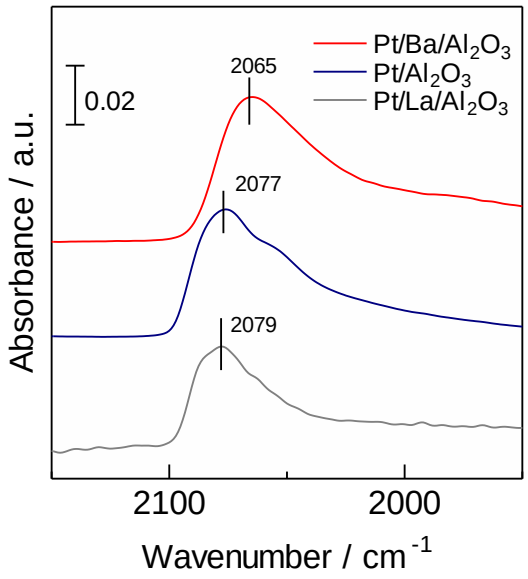

Figure 10. *In situ* IR spectra of CO adsorbed on the Pt/Al_2O_3 and $Pt/M/Al_2O_3$ (M = Ba, La) catalysts. The spectra were recorded after evacuation for 10 min following the introduction of CO for 30 min at liquid N_2 temperature.

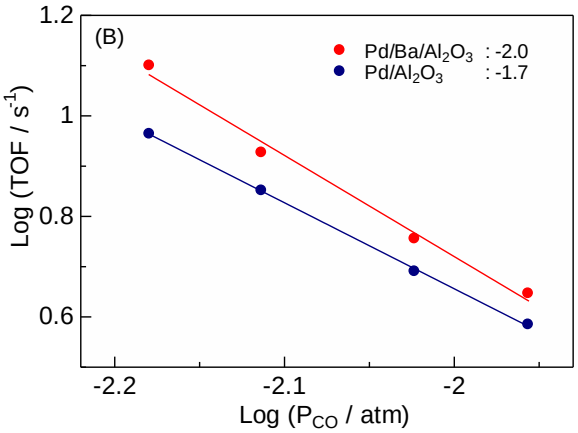

Figure 11. Log of the turnover frequency (TOF) as a function of the log of the CO partial pressure in the NO–CO reaction for Pt/Al_2O_3 and $Pt/Ba/Al_2O_3$. Conditions: 0.5% NO, 0.6–1.1% CO, He balance, and 330 °C. The TOFs were obtained under kinetically controlled conditions with a NO conversion of less than 30% by adjusting the weight of the catalysts.

The as-prepared samples subjected to *in situ* XAS experiments were reduced under a 10% H_2/He flow at 400 °C immediately before analysis. The shapes and white line intensities of the Pt/Al_2O_3 and $Pt/Ba/Al_2O_3$ catalysts were comparable. The *in situ* Pt L_3-edge XANES spectra were recorded under a 0.5% NO/He flow at 200 °C, and the results are presented in **Figure 12**. After NO introduction, the intensities of the white lines of Pt/Al_2O_3 and $Pt/Ba/Al_2O_3$ increased, suggesting that Pt was oxidized by NO. Moreover, the intensity of the white line of $Pt/Ba/Al_2O_3$

was higher than that of Pt/Al_2O_3 after exposure to 0.5% NO/He for 10 min. The results obtained after LCF of the XANES data using the XANES spectra of the reduced samples and PtO_2 as references revealed that the fractions of Pt^0 species of Pt/Al_2O_3 and $Pt/Ba/Al_2O_3$ decreased under the NO/He flow, and the Pt^0 fraction of $Pt/Ba/Al_2O_3$ was lower than that of Pt/Al_2O_3 (**Figure 12B**). The XANES spectra and LCF results suggested that the Ba additive promoted Pt oxidation under flowing NO.

The same process was evaluated using *operando* IR spectroscopy to investigate the evolution of surface-adsorbed species (**Figure 12C**). The simultaneous formation of N_2 and N_2O gases was analyzed, and the results are presented in **Figure 12D**. The peak at 1768 cm^{-1}, which was assigned to the NO adsorbed at the metallic Pt sites,[48,49] bands at 1570 and 1233 cm^{-1}, which were related to the nitrite species adsorbed at the Al oxide sites,[50] and peaks at 1910 and 1844 cm^{-1}, which were attributed to the NO gas molecules, were observed in the IR spectrum of Pt/Al_2O_3. The peaks in the range of 1100–1650 cm^{-1}, which were related to the formation of surface NO_x species with various vibrational modes, were observed in the IR spectrum of $Pt/Ba/Al_2O_3$.[50,51] More specifically, the peaks at 1211 and 1366 cm^{-1} were assigned to the surface nitrite species adsorbed at the Ba sites,[50,52] and the peak at 1534 cm^{-1} was attributed to the surface nitrite species adsorbed at the Al sites.[50] These results indicated that Ba promoted the formation of surface NO_x species. Furthermore, the formation of N_2 and N_2O was observed for Pt/Al_2O_3 and $Pt/Ba/Al_2O_3$. At the beginning of NO introduction, the formation rate of N_2 over $Pt/Ba/Al_2O_3$ was higher than that over Pt/Al_2O_3, indicating that Ba promoted the conversion of NO to N_2 with respect to that over a clean metallic Pt surface.

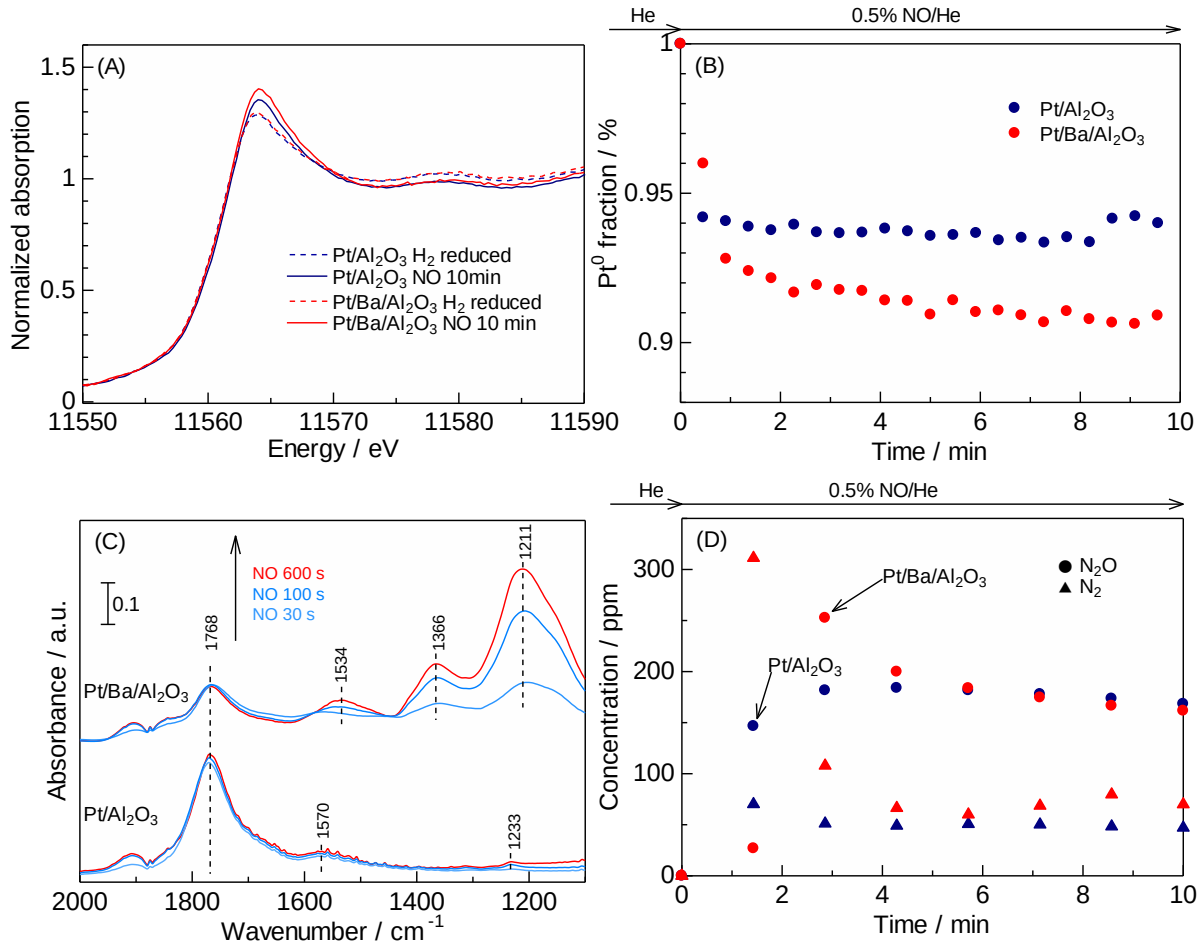

Figure 12. (A, B) *In situ* Pt L_3-edge XAS and (C, D) *operando* IR results under 0.5% NO/He flow at 200 °C. (A) *In situ* Pt L_3-edge XANES spectra and (B) fraction of Pt^0 obtained via LCF analysis. Experimental conditions: 0.5% NO/He flow rate: 300 mL min^{-1}, catalyst mass: 45 mg. (C) *Operando* IR spectra presenting the evolution of the surface species adsorbed on the Pt/Al_2O_3 and $Pt/Ba/Al_2O_3$ catalysts. (D) Concentrations of N_2 and N_2O in the effluent gas of the IR cell. Experimental conditions: 0.5% NO/He flow rate: 100 mL min^{-1}, catalyst mass: 40 mg.

TWCs are often exposed to lean conditions, particularly during the acceleration and fuel-cut steps, which entail air intake. Therefore, evaluating the mechanism and performance of TWCs under excess O_2 conditions is critical. Pt/Al_2O_3 and $Pt/Ba/Al_2O_3$ catalysts were subjected to *in situ* IR spectroscopy to investigate the effect of Ba on the formation of surface-adsorbed species during exposure to a NO/O_2 mixture as shown in **Figure 13**. Upon initial exposure to the NO/O_2 mixture, peaks at 1230, 1298, 1557, 1582, 1613, and 1775 cm^{-1} emerged in the spectrum of Pt/Al_2O_3,[50,53,54] in addition to a negative absorbance peak at 1278 cm^{-1}, which was related to the decomposition of surface carbonate species.[55,56] The peak at 1775 cm^{-1} was attributed to the NO molecules adsorbed on metallic Pt species. The absorbance bands at 1613, 1582, 1557, and 1298 cm^{-1} were assigned to the surface nitrate species with various vibration modes adsorbed at

the Al_2O_3 sites, and the peak at 1230 cm^{-1} corresponded to the surface nitrite species. The intensities of the peaks at 1775 and 1230 cm^{-1} gradually decreased upon further exposure to the NO/O_2 mixture. The peak at 1216 cm^{-1} in the IR spectrum of $Pt/Ba/Al_2O_3$ exposed to NO/O_2 corresponded to the surface nitrite species adsorbed at the Ba sites. The intensity of the peak ascribed to the nitrite species increased and then decreased gradually, such that only the peaks at 1329, 1418, and 1554 cm^{-1} were observed in the spectra of $Pt/Ba/Al_2O_3$ after 10 min of exposure to the NO/O_2 mixture. The peaks at 1329 and 1418 cm^{-1} were assigned to the nitrate species adsorbed at the Ba sites, whereas the peak at 1554 cm^{-1} was related to the nitrate species at the Al_2O_3 sites.[50] These results and the isosbestic point at 1255 cm^{-1} (**Figure 13B**) demonstrated that in the presence of O_2, the formation of nitrate species over $Pt/Ba/Al_2O_3$ proceeded via nitrite species as intermediates.

Operando IR experiments were performed to investigate the role of Ba during the $deNO_x$ reaction upon the introduction of H_2 as a reductant. The effluent gas in the IR cell was monitored using a gas chromatograph equipped with a TCD detector. The peaks at 1329 and 1418 and 1554 cm^{-1}, which emerged in the spectra of Pt/Al_2O_3 after exposure to a NO/O_2 mixture for 10 min followed by purging with He for 10 min, were attributed to the surface nitrate species at the Al_2O_3 sites (**Figure 13C**).[50] The peaks at 1329 and 1418 cm^{-1} in the IR spectrum of $Pt/Ba/Al_2O_3$ were assigned to the nitrate species adsorbed at the Ba sites, whereas the peak at 1554 cm^{-1} was related to the nitrate species at the Al_2O_3 sites.[50] The intensities of the peaks associated with the nitrate species adsorbed on $Pt/Ba/Al_2O_3$ after He purging were much higher than those of the nitrate species adsorbed on Pt/Al_2O_3, indicating that adding Ba efficiently enhanced the formation of surface nitrate species in the presence of O_2. Moreover, the intensities of the nitrate peaks in the IR spectrum of $Pt/Ba/Al_2O_3$ in the presence of NO and O_2 were higher than those in the spectrum of $Pt/Ba/Al_2O_3$ collected under flowing NO, indicating that $Pt/Ba/Al_2O_3$ stored NO_x more efficiently in the presence of O_2. After supplying 0.5% H_2/He, the intensities of the peaks attributed to the surface nitrate species adsorbed on Pt/Al_2O_3 and $Pt/Ba/Al_2O_3$ decreased and the production of N_2 and N_2O increased (**Figure 13D**). N_2 was the primary product of the reactions performed over Pt/Al_2O_3 and $Pt/Ba/Al_2O_3$, and only a limited amount of N_2O formed. The amount of N_2 formed over $Pt/Ba/Al_2O_3$ was higher than that formed over Pt/Al_2O_3. These results suggested that the efficient formation of surface nitrates and their subsequent reactivity with reductant gases played a critical role during NO_x reduction over $Pt/Ba/Al_2O_3$.

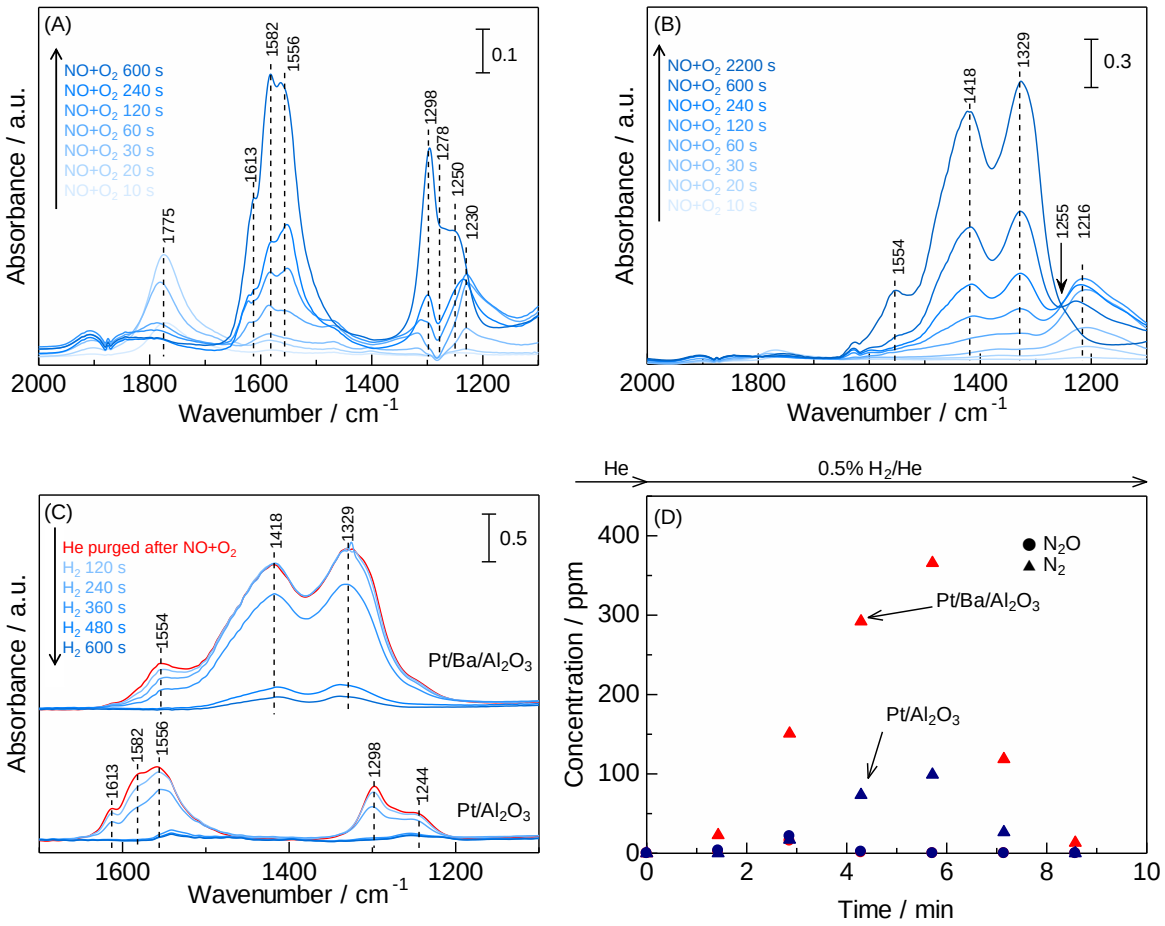

Figure 13. *Operando* IR spectra presenting the evolution of the surface species adsorbed on (A) Pt/Al_2O_3 and (B) $Pt/Ba/Al_2O_3$ after successive flows of 0.5% NO + 2% O_2 and He, and (C) 0.5 %H_2/He at 200 °C. (D) Corresponding product concentrations in the effluent gases over time. Total flow rate: 100 mL min^{-1}, catalyst mass: 40 mg.

Figure 14 presents the N1s AP-XPS spectra of Pt/Al_2O_3 and $Pt/Ba/Al_2O_3$ under various gas conditions at 200 °C. Details on the experimental procedure are included in the Supporting Information. AP-XPS measurements were performed using Pt/Al_2O_3 and $Pt/Ba/Al_2O_3$ catalysts with high Pt loadings (10 wt%) to enhance the signal intensity. The promotional effect of Ba on NO reduction and formation of surface NO_x species for the high-Pt-loading catalysts was confirmed using *operando* IR spectroscopy (**Figure 15**). The obtained AP-XPS spectra were calibrated by setting the binding energy of Al2p in Al_2O_3 to 74.5 eV.[57]

The peaks at 393.0, 398.3, and 400.9 eV in the N1s AP-XPS profile of Pt/Al_2O_3 under exposure to 0.1 Torr NO were assigned to the NO molecules adsorbed on the Si substrate, adsorbed atomic N (N_{ad}), and adsorbed molecular NO (NO_{ad}), respectively (**Figure 14B**).[58–60] Note that the Si wafer was used as a substrate for these measurements (See the Supporting

Information for a more detailed experimental protocol). The presence of the N_{ad} peak indicated that NO dissociation occurred at the catalyst surface. The corresponding peaks in the N1s AP-XPS profile of $Pt/Ba/Al_2O_3$ after exposure to 0.1 Torr NO were observed at 391.3, 398.3, and 400.9 eV, respectively (**Figure 14A**). In addition, the new peak at 403.9 eV in the N1s AP-XPS profile of $Pt/Ba/Al_2O_3$, which was attributed to the surface nitrite species,[60] implied that Ba additives enhanced the formation of surface nitrite species. This was consistent with the *operando* IR spectra recorded under a 0.5% NO/He flow (**Figure 15A**). The areas of peaks related to various adsorbed surface species, which were normalized by the baseline intensity and corrected by the peak area of Al2p to eliminate the attenuation effect caused by the introduced gases,[59] are presented in **Table 4**. The concentrations of the surface species adsorbed on Pt/Al_2O_3 and $Pt/Ba/Al_2O_3$ were obtained by using the normalized peak areas of the adsorbed surface species, and the results are summarized in **Table 4.** The peak area of N_{ad} in the profile of $Pt/Ba/Al_2O_3$ exposed to 0.1 Torr NO was larger than that in the profile of Pt/Al_2O_3, indicating that the Ba additives promoted the dissociation of NO molecules into surface-adsorbed N and O atoms. The total peak area of the NO-derived species adsorbed on $Pt/Ba/Al_2O_3$ was larger than that of the NO-derived species adsorbed on Pt/Al_2O_3 under exposure to 0.1 Torr NO, demonstrating that Ba introduction favored the generation of surface N_{ad} and NO_x species. The interaction between Pt and the NO adsorbed on Pt was predominantly determined by the extent of back-donation from the d orbitals of Pt to the antibonding $2\pi^*$ orbitals of NO, which was similar to the aforementioned interaction between Pt and the CO adsorbed on Pt.[61–64] Therefore, the electron-rich Pt^0 species loaded on Ba/Al_2O_3 enhanced the back-donation from the d orbitals of Pt to the $2\pi^*$ orbitals of N–O, which consequently decreased the N–O bond order and promoted the dissociation of the adsorbed NO molecules more efficiently.

The peaks at 391.0, 397.6, 400.9, and 403.9 eV and a new peak, which emerged at 407.2 eV, were observed in the N1s AP-XPS spectra of $Pt/Ba/Al_2O_3$ exposed to 0.1 Torr NO + 0.1 Torr O_2 for 30 min (**Figure 14A**). The peak at 407.2 eV, which was assigned to the surface nitrate species,[60] revealed that O_2 introduction enhanced the formation of surface-oxidized NO_x species, such as NO_2^- and NO_3^-. This was consistent with the *operando* IR spectra collected under a NO + O_2 flow (**Figure 16**).

The reactivities of the adsorbed N-containing species upon introduction of reductants, including H_2 and CO, were investigated next. After treatment with NO + O_2 (step (b), **Figure 14C**), H_2 was introduced into the XPS chamber after 10 min of evacuation. Upon exposure to 0.1 Torr H_2, the intensities of the peaks ascribed to the N-containing species decreased, and the peaks of surface nitrite and nitrate species disappeared, indicating that the surface-adsorbed N-containing

species reacted with H_2. Subsequently, $Pt/Ba/Al_2O_3$ was treated with NO + O_2 again (step (b*), **Figure 14C**) and was further exposed to 0.1 Torr CO. The peaks attributed to the surface nitrate and nitrite species also disappeared under these reaction conditions. However, the amount of residual N_{ad} on the catalyst surface was higher after CO introduction, implying that the reactivity of H_2 toward the adsorbed N-containing species was higher than that of CO. These results further corroborated the important promotional role of Ba in three-way catalytic processes and highlighted the ability of Ba to enhance the efficient formation of surface N-containing species, which were subsequently reduced during reactions with reductant gases.

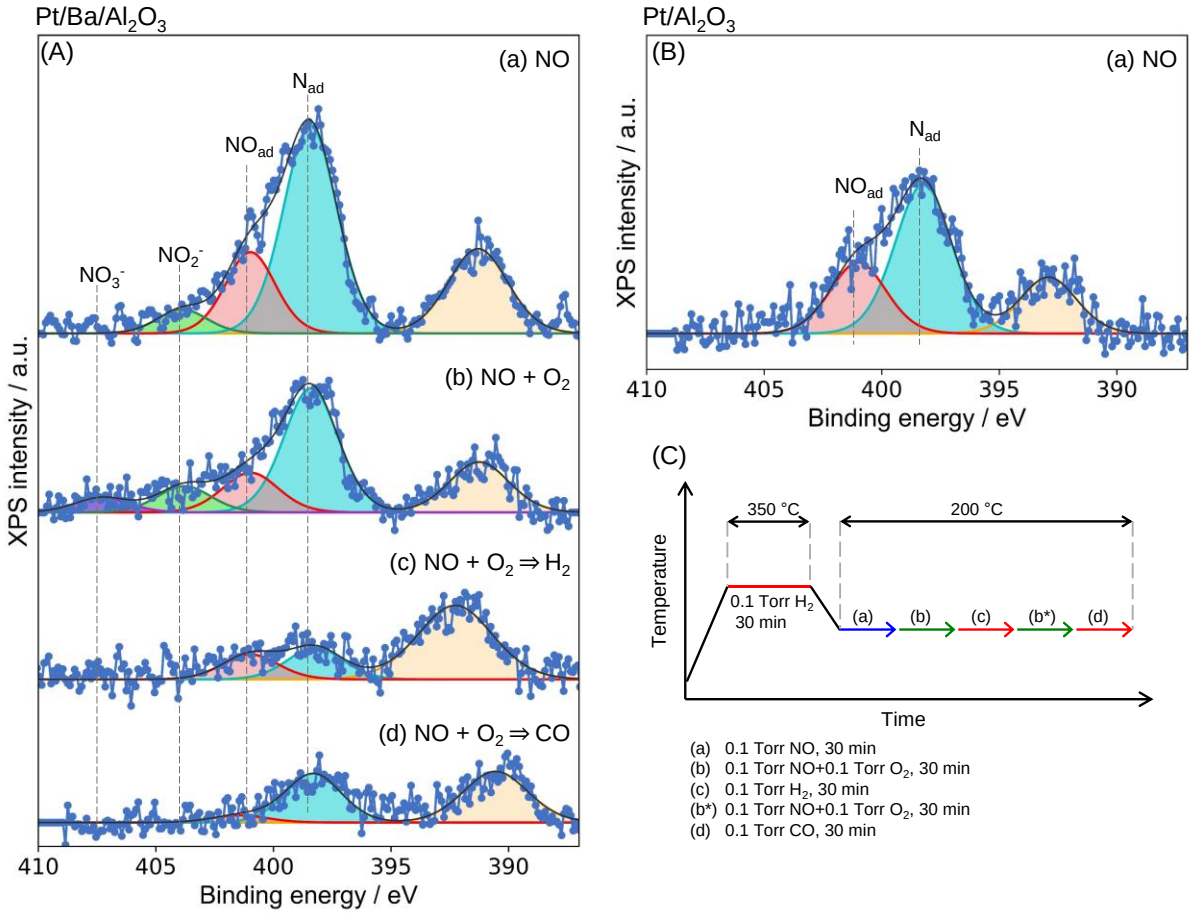

Figure 14. N1s AP-XPS spectra of (A) $Pt/Ba/Al_2O_3$ and (B) Pt/Al_2O_3 (Pt loading: 10 wt%) under exposure to (a) NO, (b) NO + O_2, (c) H_2 after NO + O_2, and (d) CO after NO + O_2 at 200 °C. Blue dots: raw spectrum; black line: sum; yellow: NO species adsorbed on the Si substrate; light blue: adsorbed atomic nitrogen (N_{ad}); red: adsorbed molecular NO (NO_{ad}); green: surface-adsorbed nitrite species; purple: surface-adsorbed nitrate species (NO_3^-). (C) Experimental conditions during the AP-XPS study.

Table 4. Peak concentrations in the N1s AP-XPS spectra of the Pt/Al_2O_3 and $Pt/Ba/Al_2O_3$ catalysts at 200 °C under various gas conditions (Figure 7).

Catalyst	Gas conditions	Peak concentration / % (Peak area)[a]			
		NO_3^-	NO_2^-	NO_{ad}	N_{ad}

Pt/Al_2O_3	(a) 0.1 Torr NO	0 (0)	0 (0)	34 (29)	66 (56)
$Pt/Ba/Al_2O_3$	(a) 0.1 Torr NO	0 (0)	7(8)	25 (28)	68 (78)
$Pt/Ba/Al_2O_3$	(b) 0.1 Torr NO + 0.1 Torr O_2	7 (6)	13 (11)	20 (17)	60 (52)
$Pt/Ba/Al_2O_3$	(c) 0.1 H_2	0 (0)	0 (0)	42 (5)	58 (7)
$Pt/Ba/Al_2O_3$	(d) 0.1 CO	0 (0)	0 (0)	14 (3)	86 (19)

[a]Peak areas were normalized by baseline intensity and corrected by the peak area of Al2p.

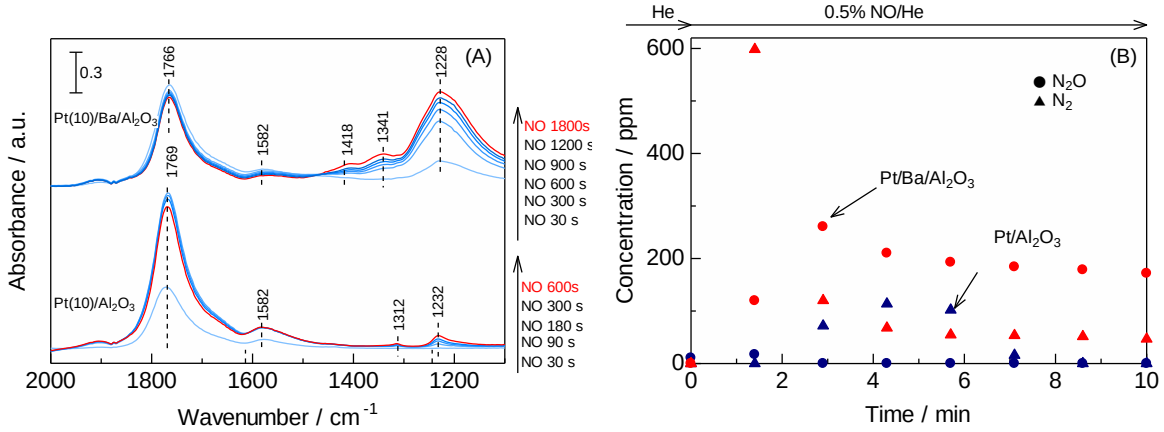

Figure 15. (A) *Operando* IR spectra presenting the evolution of surface species adsorbed on Pt/Al_2O_3 and $Pt/Ba/Al_2O_3$ with Pt loading amount of 10wt% under the flow of 0.5% NO/He at 200 °C as well as (B) the concentration of N_2 and N_2O in the effluent gas of IR cell.

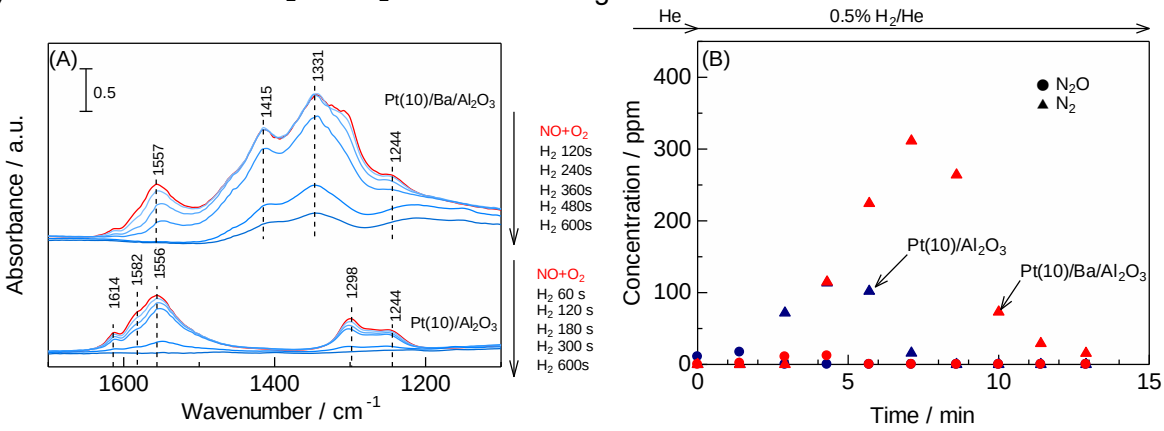

Figure 16. (A) *Operando* IR spectra of the evolution of the surface species adsorbed on $Pt(10)/Al_2O_3$ and $Pt(10)/Ba/Al_2O_3$ at 200 after successive flows of 0.5% NO + 2% O_2/He, He, and 0.5% H_2/He. (B) the concentration of products in the effluent gas upon the introduction of 0.5% H_2/He.

6.3.4 Three-way catalysis using aged catalysts

The catalytic durability of the honeycomb catalysts was studied using catalysts aged by subjecting them to a perturbation cycle of rich, stoichiometric, lean, stoichiometric gas compositions at 1000 °C for 4 h, simulating the practical working conditions of TWCs. The effect of such aging treatment is approximately equivalent to that of 10,000 km of motor vehicle travel under real working conditions. The equivalency of the thermal stress toward the catalysts between the lab-redox and engine aging was confirmed by the similarity of the specific surface areas for the two

aged catalysts. The NO, CO, and C_3H_6 conversions over the hydrothermally treated catalysts decreased, and the NO, CO, and C_3H_6 removal efficiencies of $Pt/M/Al_2O_3$ were higher than that of Pt/Al_2O_3 (**Figure 17**). The aged catalysts were also subjected to a λ-switching test to investigate the effect of the basic metal additives, and the results are illustrated in **Figure 18**. Our results indicated that the NO, CO, and C_3H_6 conversions over the hydrothermally aged $Pt/Ba/Al_2O_3$ catalyst were higher than those of the aged Pt/Al_2O_3 catalyst under three-way catalytic conditions after changing from lean to rich and from rich to lean.

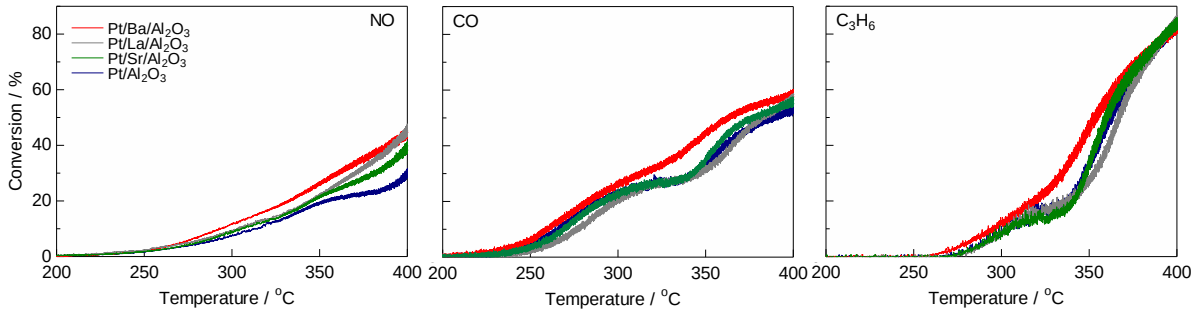

Figure 17. Conversion of NO, CO, and C_3H_6 during the TWC light-off test over the aged Pt/Al_2O_3 and $Pt/M/Al_2O_3$ (M = Ba, La, Sr) catalysts coated on honeycomb monoliths.

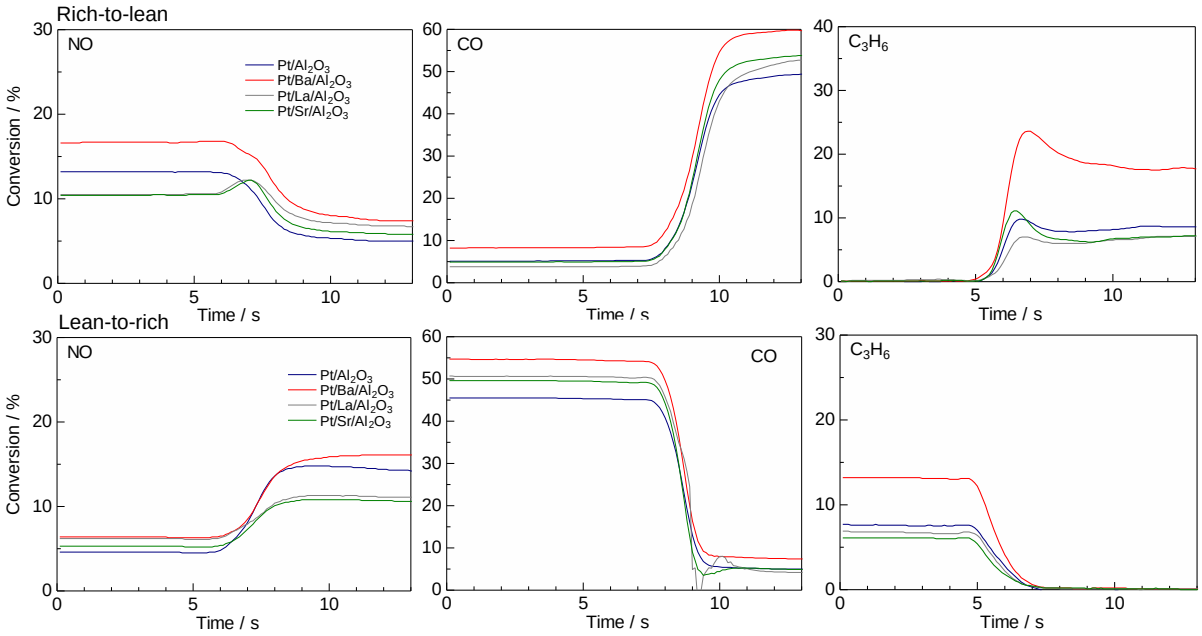

Figure 18. Lambda-switching test over the aged Pt/Al_2O_3 and $Pt/M/Al_2O_3$ (M = Ba, La, Sr) catalysts coated on honeycomb monoliths during lambda jumps (λ = 1.05–0.95) at 300 °C. The time evolution of the conversion rate was recorded at a data collection rate of 10 Hz. The detection delays were attributed to the experimental setup (3.2 s for CO and 1.0 s for NO relative to C_3H_6).

The catalysts hydrothermally aged at 1000 °C for 4 h were characterized using N_2 adsorption and XRD measurements, and the results are presented in **Figure 19**. The sharp peaks

in the XRD patterns of the aged honeycomb catalysts indicated that Pt nanoparticles aggregated into large particles after aging treatment. The characteristic peaks of θ-Al_2O_3 and α-Al_2O_3 in the XRD pattern of the aged Pt/Al_2O_3 indicated that γ-Al_2O_3 was converted into these two phases during hydrothermal aging. However, the characteristic peaks of α-Al_2O_3 were not observed in that of the aged Pt/M/Al_2O_3 (M = Ba, La, Sr) catalysts, indicating that the additives suppressed the formation of α-Al_2O_3. In addition, the characteristic peaks of $SrAl_2O_4$ and $BaAl_2O_4$ were observed in the XRD patterns of the aged Pt/Sr/Al_2O_3 and Pt/Ba/Al_2O_3 catalysts, respectively, whereas the characteristic peaks of to $LaAlO_3$ were not observed in the XRD pattern of aged Pt/La/Al_2O_3. The Ba, La, and Sr K-edge XAS spectra of the aged catalysts are presented in **Figure 20**, and the corresponding curve-fitting data of the EXAFS spectra, are summarized in **Table 5.** According to the fitting data, only the M–O contribution was observed in the EXAFS spectra of the aged Pt/Ba/Al_2O_3 and Pt/Sr/Al_2O_3 catalysts, whereas the La–O and La–(O)–Al contributions appeared in the EXAFS spectra of the aged Pt/La/Al_2O_3 catalyst. The S_{BET} values of the aged catalysts were obtained using N_2 adsorption–desorption experiments, and the results demonstrated that the decrease in the S_{BET} value of the Pt/M/Al_2O_3 catalyst after aging was smaller than that of Pt/Al_2O_3 (**Figure 19B**). These results suggested that basic metal additives enhanced the thermal stability of Al_2O_3. The S_{BET} value of the Pt/Ba/Al_2O_3 catalyst subjected to hydrothermal treatment at 1000 °C was higher than those of Pt/Sr/Al_2O_3 and Pt/La/Al_2O_3, indicating that among the basic metals in this study, Ba most efficiently inhibited the phase transformation of Al_2O_3. Among the basic metals in this study, Ba was more efficient at retaining the S_{BET} value of Al_2O_3. The average Pt particle sizes of the aged Pt/Al_2O_3 and Pt/M/Al_2O_3 (M = Ba, La, Sr) catalysts were determined using HAADF–STEM (**Figures 21**), and the results are summarized in **Figure 19C**. The average Pt particle size of the aged catalysts decreased as follows: Pt/Sr/Al_2O_3 > Pt/Al_2O_3 > Pt/Ba/Al_2O_3 > Pt/La/Al_2O_3, implying that Ba and La suppressed Pt nanoparticle sintering, and La more efficiently stabilized the Pt dispersion than Ba.

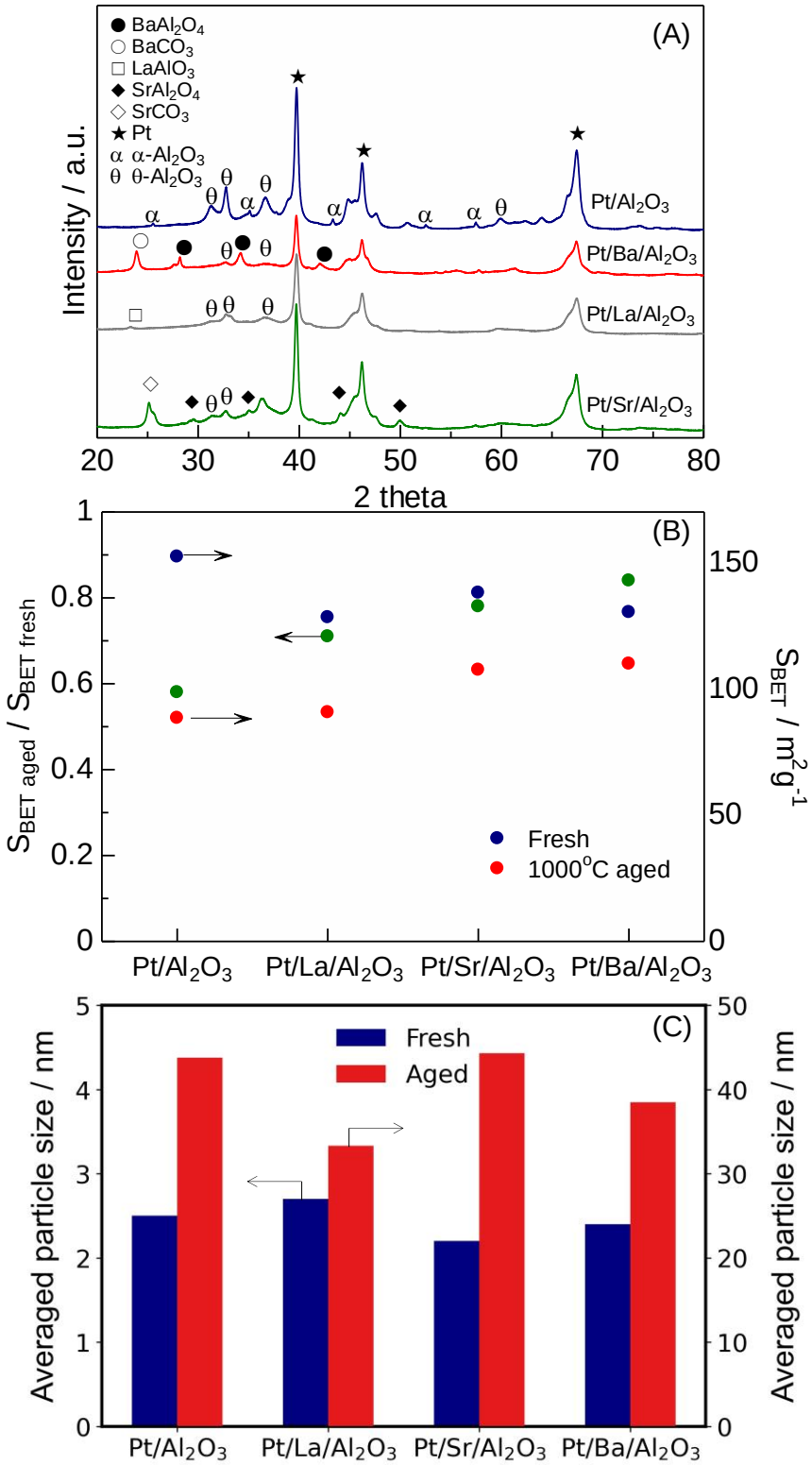

Figure 19. (A) XRD pattern of the aged Pt/Al_2O_3 and $Pt/M/Al_2O_3$ (M = Ba, La, or Sr). (B) Surface area and (C) average Pt particle size in fresh and aged Pt/Al_2O_3 and $Pt/M/Al_2O_3$ catalysts. The characterization data of fresh catalysts were taken from **Table 2**.

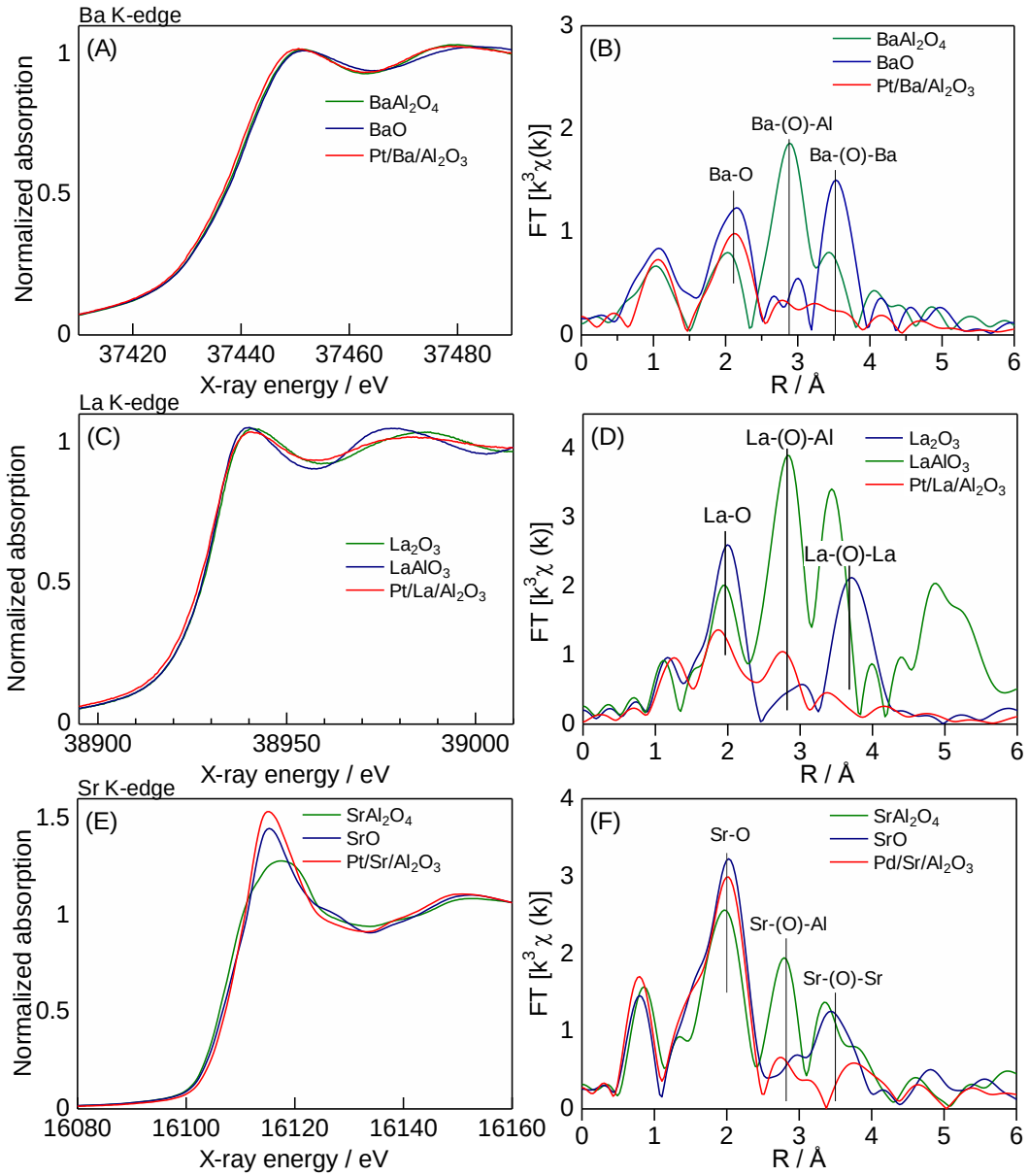

Figure 20. The Ba, La, and Sr K-edge (A, C, E) XANES spectra and (B, D, F) k^3-weighted EXAFS Fourier transforms of Pt/M/Al_2O_3 (M = Ba, La, or Sr) catalysts after aging at 1000 °C.

Table 5. Curve-fitting analysis of La, Ba and Sr K-edge EXAFS for Pt/M/Al_2O_3 (M = Ba, La, or Sr) after aging at 1000 °C.

Sample	Shell	CN [a]	*R* (Å) [b]	σ^2 (Å^2) [c]	R_f (%) [d]
Pt/La/Al_2O_3	La–O	6.4	2.55	0.018	0.90
	La–(O)–Al	1.8	3.30	0.006	
Pt/Ba/Al_2O_3	Ba–O	3.5	2.74	0.011	2.90
Pt/Sr/Al_2O_3	Sr–O	5.7	2.58	0.013	1.80

[a] Coordination number. [b] Bond distance. [c] Debye-Waller factor. [d] Residual factor.

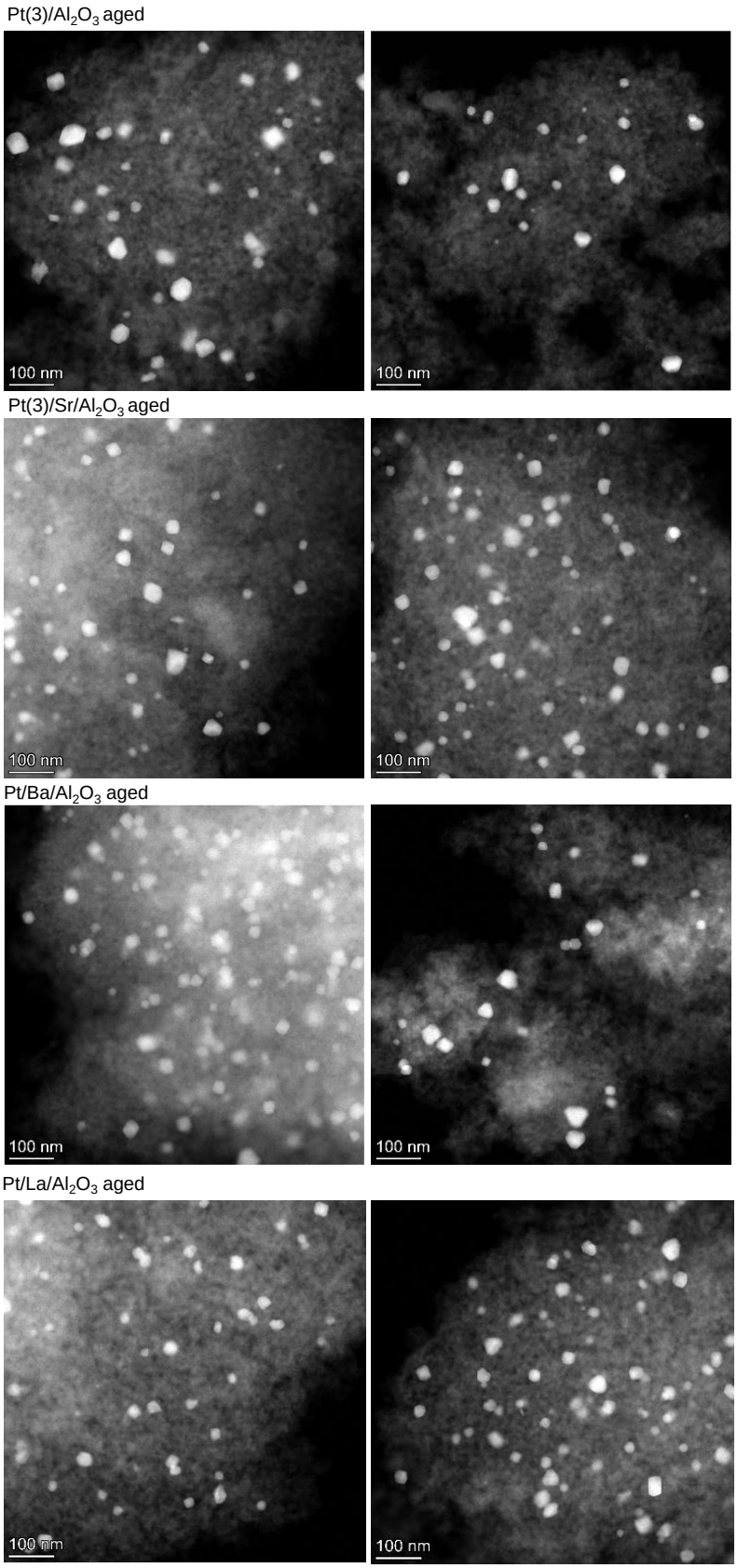

Figure 21. HAADF-STEM images of aged Pt/Al_2O_3 and $Pt/M/Al_2O_3$ (M = Ba, La, or Sr)

6.3.5 Comparison of the Pt/M/Al_2O_3, Pd/M/Al_2O_3, and Pt/OSM catalysts

In addition to the basic-metal-loaded Al_2O_3 catalysts investigated in this study, OSM-supported catalysts, such as CeO_2- and CeO_2–ZrO_2-supported catalysts, have been widely used as TWCs.[65–72] Therefore, in this study, we comprehensively compared the catalytic efficiencies of Pt/M/Al_2O_3 (M = Ba, La, Sr), Pd/M/Al_2O_3 (M = Ba, La, Sr), and Pt/OSM (CeO_2 and CeO_2–ZrO_2) catalysts operated under simulated three-way catalytic conditions. Moreover, we used the 20% conversion temperatures (T_{20}) of NO, CO, and C_3H_6 during a light-off test to evaluate catalyst performance (**Figure 22**). The data for the Pd/M/Al_2O_3 and Pt/OSM catalysts were retrieved from our previous article.[37,38] The Pt and Pd loadings of the catalysts were 3 wt% in both studies.

The T_{20} values of NO over the fresh honeycomb Pt/M/Al_2O_3 catalysts were lower than those of CO and C_3H_6, whereas the T_{20} values of NO over the fresh honeycomb Pt/OSM catalysts were higher than those of CO and C_3H_6. Moreover, the T_{20} values of CO and C_3H_6 over the fresh honeycomb Pt/OSM catalysts were lower than those over the fresh honeycomb Pt/M/Al_2O_3 catalysts. These results indicated that OSM support materials enhanced the catalytic efficiency of Pt in promoting CO and C_3H_6 oxidation more efficiently than the Al_2O_3-based support. Furthermore, the T_{20} values of NO over the Pt-based catalysts were higher than those over the Pd/M/Al_2O_3 catalysts, indicating that the Pt-based catalysts were less efficient than the Pd-based catalysts for NO removal. Moreover, the CO and C_3H_6 oxidation activities of the Pt/OSM catalysts were higher than those of the Pd/M/Al_2O_3 catalysts.

After hydrothermal aging at 1000 °C for 4 h, the S_{BET} values of the catalysts decreased and the supported Pt and Pd nanoparticles aggregated into larger particles, as illustrated in **Figure 23**. The particle sizes of all the hydrothermally aged powdered catalysts were determined using STEM experiments. The Pt particles of the Pt/M/Al_2O_3 catalysts were significantly larger than those of the Pt/OSM catalysts, indicating that OSMs (CeO_2 and CeO_2–ZrO_2) more efficiently stabilized Pt species dispersion than the Al_2O_3 supports. However, despite the difference in Pt particle size, the T_{20} values of NO, CO, and C_3H_6 over the aged Pt/M/Al_2O_3 and Pt/OSM catalysts were similar. This was attributed to the sharp decrease in the S_{BET} values of the Pt/OSM catalysts, which lowered the redox ability of Ce as a critical factor for efficient reaction progression. The T_{20} values of the Pd/M/Al_2O_3 catalysts were lower than those of the Pt/M/Al_2O_3 and Pt/OSM catalysts for all the reactants monitored, especially the NO reduction reaction, even though the Pd particles were larger than the Pt particles. These results indicated that the aged Pd-based catalysts were more efficient TWCs than the aged Pt-based catalysts. Overall, these findings suggest that significant efforts should be dedicated to developing efficient support materials that can enhance

the catalytic performance of Pt and promote the replacement of Pd-based catalysts with Pt-based catalysts in three-way catalytic processes.

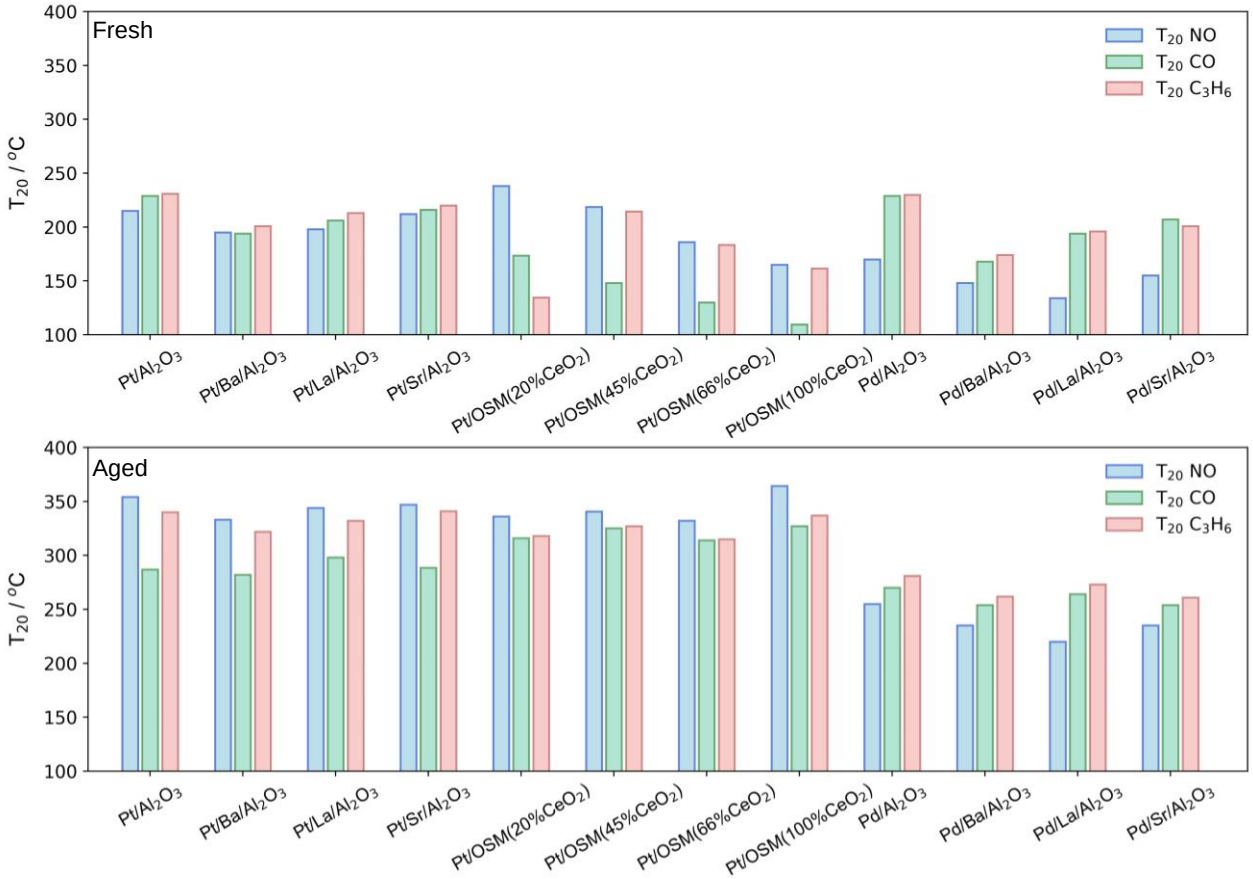

Figure 22. Temperature of 20% conversion for NO, CO, and C_3H_6 in the TWC light-off test over several Pd- and Pt-based catalysts.

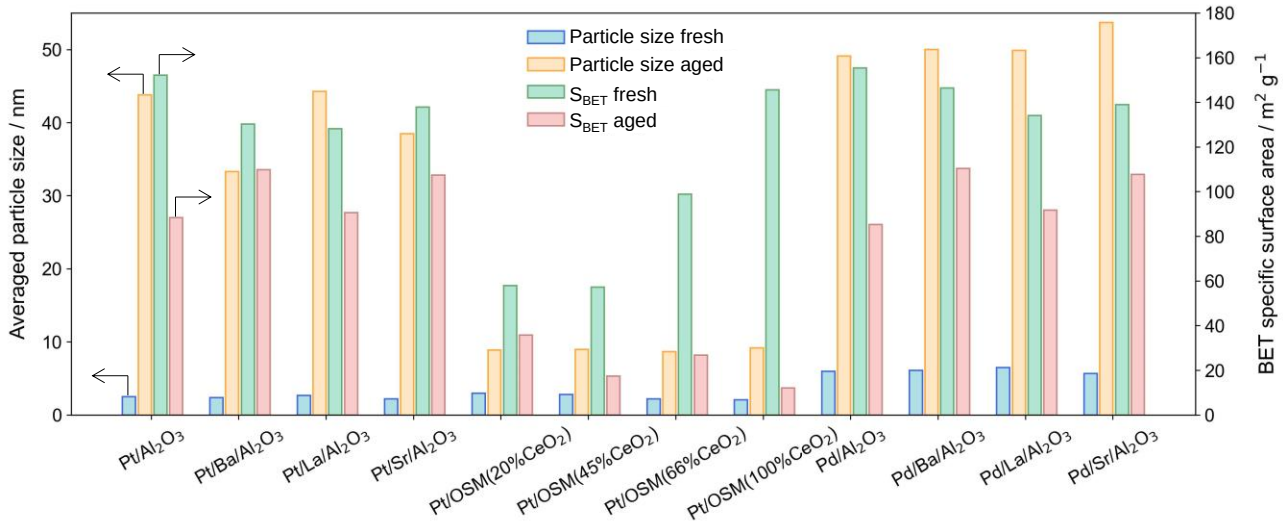

Figure 23. Pt and Pd particle sizes and S_{BET} values of several fresh and aged Pt- and Pd-based catalysts.

6.4 Conclusions

In this study, we examined the promotional effect of basic metal additives in $Pt/M/Al_2O_3$ (M = Ba, La, or Sr) on catalytic efficiency under three-way catalytic conditions. The catalytic activity of $Pt/M/Al_2O_3$ for NO, CO, and C_3H_6 under three-way catalytic conditions was superior to that of Pt/Al_2O_3, and Ba enhanced the catalytic activity of the Pt-based catalysts more efficiently than La and Sr. The role of Ba in $Pt/Ba/Al_2O_3$ was investigated using kinetic studies and various spectroscopy experiments. The Pt^0 species loaded on Ba/Al_2O_3 were more electron-rich than those loaded on Al_2O_3; therefore, the reactivity of $Pt/Ba/Al_2O_3$ toward NO was higher than that of Pt/Al_2O_3. Moreover, the efficient formation of surface N-containing species and their subsequent reaction with reductant gases promoted the effect of Ba in three-way catalytic processes. Although $Pt/M/Al_2O_3$ outperformed Pt/Al_2O_3, the catalytic activities of $Pt/M/Al_2O_3$ and Pt/Al_2O_3 were still lower than that of $Pd/M/Al_2O_3$. Researchers should thus focus on further enhancing the activity of Pt-based catalysts.

References

(1) Shelef, M.; McCabe, R. W. Twenty-Five Years after Introduction of Automotive Catalysts: What Next? *Catal Today* **2000**, *62*, 35–50.

(2) Twigg, M. v. Progress and Future Challenges in Controlling Automotive Exhaust Gas Emissions. *Appl Catal B* **2007**, *70*, 2–15.

(3) Roy, S.; Baiker, A. NOx Storage-Reduction Catalysis: From Mechanism and Materials Properties to Storage-Reduction Performance. *Chem Rev* **2009**, *109*, 4054–4091.

(4) Granger, P.; Parvulescu, V. I. Catalytic NOx Abatement Systems for Mobile Sources: From Three-Way to Lean Burn After-Treatment Technologies. *Chem Rev* **2011**, *111*, 3155–3207.

(5) Wang, J.; Chen, H.; Hu, Z.; Yao, M.; Li, Y. A Review on the Pd-Based Three-Way Catalyst. *Catal Rev Sci Eng* **2015**, *57*, 79–144.

(6) Jeong, H.; Kwon, O.; Kim, B. S.; Bae, J.; Shin, S.; Kim, H. E.; Kim, J.; Lee, H. Highly Durable Metal Ensemble Catalysts with Full Dispersion for Automotive Applications beyond Single-Atom Catalysts. *Nat Catal* **2020**, *3*, 368–375.

(7) Kusada, K.; Wu, D.; Nanba, Y.; Koyama, M.; Yamamoto, T.; Tran, X. Q.; Toriyama, T.; Matsumura, S.; Ito, A.; Sato, K.; Nagaoka, K.; Seo, O.; Song, C.; Chen, Y.; Palina, N.; Kumara, L. S. R.; Hiroi, S.; Sakata, O.; Kawaguchi, S.; Kubota, Y.; Kitagawa, H. Highly Stable and Active Solid-Solution-Alloy Three-Way Catalyst by Utilizing Configurational-Entropy Effect. *Advanced Materials* **2021**, *33*, 2005206.

(8) Rood, S.; Eslava, S.; Manigrasso, A.; Bannister, C. Recent Advances in Gasoline Three-Way Catalyst Formulation: A Review. *Proceedings of the Institution of Mechanical Engineers, Part D: Journal of Automobile Engineering* **2019**, *234*, 936–949.

(9) Puspito Buwono, H.; Omori, Y.; Shioya, N.; Yoshida, H.; Hinokuma, S.; Nagao, Y.; Iwashina, K.; Endo, Y.; Nakahara, Y.; Machida, M. Enhanced Rh-Anchoring on the Composite Metal Phosphate $Y_{0.33}Zr_2(PO_4)_3$ in Three-Way Catalysis. *Catal Sci Technol* **2019**, *9* (19), 5447–5455.

(10) Grünbacher, M.; Tarjomannejad, A.; Nezhad, P. D. K.; Praty, C.; Ploner, K.; Mohammadi, A.; Niaei, A.; Klötzer, B.; Schwarz, S.; Bernardi, J.; Farzi, A.; Gómez, M. J. I.; Rivero, V. T.; Penner, S. Promotion of $La(Cu_{0.7}Mn_{x0.3})_{0.98}M_{0.02}O_{3-\delta}$ (M = Pd, Pt, Ru and Rh) Perovskite Catalysts by Noble Metals for the Reduction of NO by CO. *J Catal* **2019**, *379*, 18–32.

(11) Huang, C.; Shan, W.; Lian, Z.; Zhang, Y.; He, H. Recent Advances in Three-Way Catalysts of Natural Gas Vehicles. *Catal Sci Technol* **2020**, *10*, 6407–6419.

(12) Li, L.; Zhang, N.; Wu, R.; Song, L.; Zhang, G.; He, H. Comparative Study of Moisture-Treated $Pd@CeO_2/Al_2O_3$ and $Pd/CeO_2/Al_2O_3$ Catalysts for Automobile Exhaust Emission Reactions: Effect of Core-Shell Interface. *ACS Appl Mater Interfaces* **2020**, *12*, 10350–10358.

(13) Haneda, M.; Nakamura, Y.; Yamada, T.; Minami, S.; Kato, N.; Iwashina, K.; Endo, Y.; Nakahara, Y.; Iwachido, K. Comprehensive Study of the Light-off Performance and Surface Properties of Engine-Aged Pd-Based Three-Way Catalysts. *Catal Sci Technol* **2021**, *11* (3), 912–922.

(14) Khivantsev, K.; Vargas, C. G.; Tian, J.; Kovarik, L.; Jaegers, N. R.; Szanyi, J.; Wang, Y. Economizing on Precious Metals in Three‐Way Catalysts: Thermally Stable and Highly Active Single‐Atom Rhodium on Ceria for NO Abatement under Dry and Industrially Relevant Conditions. *Angew. Chem. Int. Ed.* **2021**, *133*, 395–402.

(15) Hosokawa, S.; Oshino, Y.; Tanabe, T.; Koga, H.; Beppu, K.; Asakura, H.; Teramura, K.; Motohashi, T.; Okumura, M.; Tanaka, T. Strong Metal–Support Interaction in $Pd/Ca_2AlMnO_{5+\delta}$: Catalytic NO Reduction over Mn-Doped CaO Shell. *ACS Catal* **2021**, 7996–8003.

(16) Yoshida, H.; Oyama, H.; Shiomori, R.; Hirakawa, T.; Ohyama, J.; Machida, M. Enhanced Catalytic NO Reduction in $NO–CO–C_3H_6–O_2$ Reaction Using Pseudo-Spinel $(NiCu)Al_2O_4$ Supported on γ-Al_2O_3. *ACS Catal* **2021**, 7302–7309.

(17) Machida, M.; Uchida, Y.; Iwashita, S.; Yoshida, H.; Tsushida, M.; Ohyama, J.; Nagao, Y.; Endo, Y.; Wakabayashi, T. Catalyst Deactivation via Rhodium-Support Interactions under High-Temperature

Oxidizing Conditions: A Comparative Study on Hexaaluminates versus Al2O3. *ACS Catal* **2021**, *11* (15), 9462–9470.
(18) Twigg, M. v. Catalytic Control of Emissions from Cars. *Catal Today* **2011**, *163*, 33–41.
(19) Farrauto, R. J.; Deeba, M.; Alerasool, S. Gasoline Automobile Catalysis and Its Historical Journey to Cleaner Air. *Nat Catal* **2019**, *2*, 603–613.
(20) Yentekakis, I. V.; Vernoux, P.; Goula, G.; Caravaca, A. Electropositive Promotion by Alkalis or Alkaline Earths of Pt-Group Metals in Emissions Control Catalysis: A Status Report. *Catalysts* **2019**, *9*, 1–72.
(21) Datye, A. K.; Votsmeier, M. Opportunities and Challenges in the Development of Advanced Materials for Emission Control Catalysts. *Nat Mater* **2020**, *20*, 1049–1059.
(22) Yoshida, H.; Hirakawa, T.; Oyama, H.; Nakashima, R.; Hinokuma, S.; Machida, M. Effect of Thermal Aging on Local Structure and Three-Way Catalysis of Cu/Al_2O_3. *Journal of Physical Chemistry C* **2019**, *123*, 10469–10476.
(23) Smith, S. J.; Huang, B.; Bartholomew, C. H.; Campbell, B. J.; Boerio-Goates, J.; Woodfield, B. F. La-Dopant Location in La-Doped γ-Al_2O_3 Nanoparticles Synthesized Using a Novel One-Pot Process. *Journal of Physical Chemistry C* **2015**, *119*, 25053–25062.
(24) Di Monte, R.; Fornasiero, P.; Kaspar, J.; Graziani, M.; Gatica, J. M.; Bernal, S.; Gomez-Herrero, A. Stabilisation of Nanostructured $Ce_{0.2}Zr_{0.8}O_2$ Solid Solution by Impregnation on Al_2O_3: A Suitable Method for the Production of Thermally Stable Oxygen Storage/Release Promoters for Three-Way Catalysts. *Chemical Communications* **2000**, No. 21, 2167–2168.
(25) Nishio, Y.; Ozawa, M. Thermal Stability and Microstructural Change of Lanthanum Modified Alumina Catalytic Support. *Journal of the Ceramic Society of Japan* **2007**, *115*, 633–636.
(26) Lan, L.; Chen, S.; Cao, Y.; Wang, S.; Wu, Q.; Zhou, Y.; Huang, M.; Gong, M.; Chen, Y. Promotion of CeO_2-ZrO_2-Al_2O_3 Composite by Selective Doping with Barium and Its Supported Pd-Only Three-Way Catalyst. *J Mol Catal A Chem* **2015**, *410*, 100–109.
(27) Wakabayashi, R.; Tomita, A.; Kimura, T. A Robust Mesoporous Al_2O_3-Based Nanocomposite Catalyst for Abundant NOx Storage with Rational Design of Pt and Ba Species. *Chemistry – A European Journal* **2021**, *27*, 6706–6712.
(28) Zhang, N.; Yan, H.; Li, L.; Wu, R.; Song, L.; Zhang, G.; Liang, W.; He, H. Use of Rare Earth Elements in Single-Atom Site Catalysis: A Critical Review — Commemorating the 100th Anniversary of the Birth of Academician Guangxian Xu. *Journal of Rare Earths* **2021**, *39* (3), 233–242.
(29) Matsouka, V.; Konsolakis, M.; Yentekakis, I. V.; Papavasiliou, A.; Tsetsekou, A.; Boukos, N. Thermal Aging Behavior of Pt-Only TWC Converters under Simulated Exhaust Conditions: Effect of Rare Earths (CeO_2, La_2O_3) and Alkali (Na) Modifiers. *Top Catal* **2011**, *54*, 1124–1134.
(30) Guo, J.; Shi, Z.; Wu, D.; Yin, H.; Gong, M.; Chen, Y. Study of Pt-Rh/CeO_2-ZrO_2-MxOy (M = Y, La)/Al_2O_3 Three-Way Catalysts. *Appl Surf Sci* **2013**, *273*, 527–535.
(31) Wang, H.; Dong, J.; Allard, L. F.; Lee, S.; Oh, S.; Wang, J.; Li, W.; Shen, M.; Yang, M. Single-Site Pt/La-Al_2O_3 Stabilized by Barium as an Active and Stable Catalyst in Purifying CO and C_3H_6 Emissions. *Appl Catal B* **2019**, *244*, 327–339.
(32) Burch, R.; Watling, T. C. The Effect of Promoters on Pt/Al_2O_3 Catalysts for the Reduction of NO by C_3H_6 under Lean-Burn Conditions. *Appl Catal B* **1997**, *11*, 207–216.
(33) Shinjoh, H.; Tanabe, T.; Sobukawa, H.; Sugiura, M. Effect of Ba Addition on Catalytic Activity of Pt and Rh Catalysts Loaded on γ-Alumina. *Top Catal* **2001**, *16*, 95–99.
(34) Konsolakis, M.; Yentekakis, I. V. The Reduction of NO by Propene over Ba-Promoted Pt/γ-Al_2O_3 Catalysts. *J Catal* **2001**, *198* (1), 142–150.
(35) Toyao, T.; Jing, Y.; Kon, K.; Hayama, T.; Nagaoka, S.; Shimizu, K. ichi. Catalytic NO-CO Reactions over La-Al2O3 Supported Pd: Promotion Effect of La. *Chem Lett* **2018**, *47* (8), 1036–1039.
(36) Jing, Y.; Cai, Z.; Liu, C.; Toyao, T.; Maeno, Z.; Asakura, H.; Hiwasa, S.; Nagaoka, S.; Kondoh, H.; Shimizu, K. Promotional Effect of La in the Three-Way Catalysis of La-Loaded Al_2O_3-Supported Pd Catalysts

(Pd/La/Al_2O_3). *ACS Catal* **2020**, *10*, 1010–1023.
(37) Jing, Y.; Wang, G.; Wei Ting, K.; Maeno, Z.; Oshima, K.; Satokawa, S.; Nagaoka, S.; Shimizu, K.; Toyao, T. Roles of the Basic Metals La, Ba and Sr as Additives in Al_2O_3-Supported Pd-Based Three-Way Catalysts. *J Catal* **2021**, *400*, 387–396.
(38) Wang, G.; Jing, Y.; Ting, K. W.; Maeno, Z.; Zhang, X.; Nagaoka, S.; Shimizu, K.; Toyao, T. Effect of Oxygen Storage Materials on the Performance of Pt-Based Three-Way Catalysts. *Catal Sci Technol* **2022**.
(39) Ravel, B.; Newville, M. ATHENA, ARTEMIS, HEPHAESTUS: Data Analysis for X-Ray Absorption Spectroscopy Using IFEFFIT. *J Synchrotron Radiat* **2005**, *12* (4), 537–541.
(40) DeRita, L.; Resasco, J.; Dai, S.; Boubnov, A.; Thang, H. V.; Hoffman, A. S.; Ro, I.; Graham, G. W.; Bare, S. R.; Pacchioni, G.; Pan, X.; Christopher, P. Structural Evolution of Atomically Dispersed Pt Catalysts Dictates Reactivity. *Nature Materials 2019 18:7* **2019**, *18* (7), 746–751.
(41) Ding, K.; Gulec, A.; Johnson, A. M.; Schweitzer, N. M.; Stucky, G. D.; Marks, L. D.; Stair, P. C. Identification of Active Sites in CO Oxidation and Water-Gas Shift over Supported Pt Catalysts. *Science (1979)* **2015**, *350* (6257), 189–192.
(42) Goclon, J.; Grybos, R.; Witko, M.; Hafner, J. Oxygen Vacancy Formation on Clean and Hydroxylated Low-Index V_2O_5 Surfaces: A Density Functional Investigation. *Phys Rev B* **2009**, *79* (7), 75439.
(43) Zeinalipour-Yazdi, C. D.; Cooksy, A. L.; Efstathiou, A. M. CO Adsorption on Transition Metal Clusters: Trends from Density Functional Theory. *Surf Sci* **2008**, *602*, 1858–1862.
(44) Frenking, G.; Fernández, I.; Holzmann, N.; Pan, S.; Krossing, I.; Zhou, M. Metal–CO Bonding in Mononuclear Transition Metal Carbonyl Complexes. *JACS Au* **2021**, *1* (5), 623–645.
(45) Gonzalez, S.; Illas, F. CO Adsorption on Monometallic Pd, Rh, Cu and Bimetallic PdCu and RhCu Monolayers Supported on Ru(0 0 0 1). *Surf Sci* **2005**, *598* (1–3), 144–155.
(46) Bourane, A.; Dulaurent, O.; Salasc, S.; Sarda, C.; Bouly, C.; Bianchi, D. Heats of Adsorption of Linear NO Species on a Pt/Al_2O_3 Catalyst Using in Situ Infrared Spectroscopy under Adsorption Equilibrium. *J Catal* **2001**, *204* (1), 77–88.
(47) Allian, A. D.; Takanabe, K.; Fujdala, K. L.; Hao, X.; Truex, T. J.; Cai, J.; Buda, C.; Neurock, M.; Iglesia, E. Correction to Chemisorption of CO and Mechanism of CO Oxidation on Supported Platinum Nanoclusters. *J Am Chem Soc* **2011**, *134* (1), 743.
(48) Fujiwara, K.; Pratsinis, S. E. Single Pd Atoms on TiO_2 Dominate Photocatalytic NO_x Removal. *Appl Catal B* **2018**, *226*, 127–134.
(49) Ivanova, E.; Mihaylov, M.; Thibault-Starzyk, F.; Daturi, M.; Hadjiivanov, K. FTIR Spectroscopy Study of CO and NO Adsorption and Co-Adsorption on Pt/TiO_2. *J Mol Catal A Chem* **2007**, *274* (1–2), 179–184.
(50) Sedlmair, C.; Seshan, K.; Jentys, A.; Lercher, J. A. Elementary Steps of NOx Adsorption and Surface Reaction on a Commercial Storage-Reduction Catalyst. *J Catal* **2003**, *214* (2), 308–316.
(51) Pieta, I. S.; Cortes-Reyes, M.; Larrubia, M. A.; Alemany, L. J.; Epling, W. S. Mechanistic Aspect of N_2O Formation Over Pt–Ba/γ-Al_2O_3 Catalysts. *Top Catal* **2019**, *62* (1–4), 117–128.
(52) Lietti, L.; Daturi, M.; Blasin-Aubé, V.; Ghiotti, G.; Prinetto, F.; Forzatti, P. Relevance of the Nitrite Route in the NOx Adsorption Mechanism over Pt-Ba/Al_2O_3 NO_x Storage Reduction Catalysts Investigated by Using Operando FTIR Spectroscopy. *ChemCatChem* **2012**, *4*, 55–58.
(53) Nova, I.; Castoldi, L.; Lietti, L.; Tronconi, E.; Forzatti, P.; Prinetto, F.; Ghiotti, G. NOx Adsorption Study over Pt-Ba/Alumina Catalysts: FT-IR and Pulse Experiments. *J Catal* **2004**, *222* (2), 377–388.
(54) Castoldi, L.; Lietti, L.; Nova, I.; Matarrese, R.; Forzatti, P.; Vindigni, F.; Morandi, S.; Prinetto, F.; Ghiotti, G. Alkaline- and Alkaline-Earth Oxides Based Lean NOx Traps: Effect of the Storage Component on the Catalytic Reactivity. *Chemical Engineering Journal* **2010**, *161* (3), 416–423.
(55) Pieta, I. S.; García-Diéguez, M.; Herrera, C.; Larrubia, M. A.; Alemany, L. J. In Situ DRIFT-TRM Study of Simultaneous NOx and Soot Removal over Pt-Ba and Pt-K NSR Catalysts. *J Catal* **2010**, *270* (2), 256–267.
(56) Frola, F.; Manzoli, M.; Prinetto, F.; Ghiotti, G.; Castoldi, L.; Lietti, L. Pt-Ba/Al_2O_3 NSR Catalysts at Different Ba Loading: Characterization of Morphological, Structural, and Surface Properties. *Journal of Physical Chemistry C* **2008**, *112*, 12869–12878.

(57) Bergman, S. L.; Granestrand, J.; Tang, Y.; París, R. S.; Nilsson, M.; Tao, F. F.; Tang, C.; Pennycook, S. J.; Pettersson, L. J.; Bernasek, S. L. In-Situ Characterization by Near-Ambient Pressure XPS of the Catalytically Active Phase of Pt/Al_2O_3 during NO and CO Oxidation. *Appl Catal B* **2018**, *220*, 506–511.

(58) Shimada, T.; Mun, B. S.; Nakai, I. F.; Banno, A.; Abe, H.; Iwasawa, Y.; Ohta, T.; Kondoh, H. Irreversible Change in the NO Adsorption State on Pt(111) under High Pressure Studied by AP-XPS, NEXAFS, and STM. *Journal of Physical Chemistry C* **2010**, *114* (40), 17030–17035.

(59) Ueda, K.; Isegawa, K.; Amemiya, K.; Mase, K.; Kondoh, H. Operando NAP-XPS Observation and Kinetics Analysis of NO Reduction over Rh(111) Surface: Characterization of Active Surface and Reactive Species. *ACS Catal* **2018**, *8* (12), 11663−11670.

(60) Hwang, J.; Rao, R. R.; Giordano, L.; Akkiraju, K.; Wang, X. R.; Crumlin, E. J.; Bluhm, H.; Shao-Horn, Y. Regulating Oxygen Activity of Perovskites to Promote NOx Oxidation and Reduction Kinetics. *Nat Catal* **2021**, *4* (8), 663–673.

(61) Koper, M. T. M.; Van Santen, R. A. Electric Field Effects on CO and NO Adsorption at the Pt(111) Surface. *Journal of Electroanalytical Chemistry* **1999**, *476* (1), 64–70.

(62) Koper, M. T. M.; Van Santen, R. A.; Wasileski, S. A.; Weaver, M. J. Field-Dependent Chemisorption of Carbon Monoxide and Nitric Oxide on Platinum-Group (111) Surfaces: Quantum Chemical Calculations Compared with Infrared Spectroscopy at Electrochemical and Vacuum-Based Interfaces. *Journal of Chemical Physics* **2000**, *113* (10), 4392–4407.

(63) Zeng, Z. H.; Da Silva, J. L. F.; Li, W. X. Theory of Nitride Oxide Adsorption on Transition Metal (111) Surfaces: A First-Principles Investigation. *Physical Chemistry Chemical Physics* **2010**, *12* (10), 2459–2470.

(64) Shiotari, A.; Hatta, S.; Okuyama, H.; Aruga, T. Role of Hydrogen Bonding in the Catalytic Reduction of Nitric Oxide. *Chem Sci* **2014**, *5* (3), 922–926.

(65) He, H.; Dai, H. X.; Ng, L. H.; Wong, K. W.; Au, C. T. Pd-, Pt-, and Rh-Loaded $Ce_{0.6}Zr_{0.35}Y_{0.05}O_2$ Three-Way Catalysts: An Investigation on Performance and Redox Properties. *J Catal* **2002**, *206* (1), 1–13.

(66) Ozawa, M.; Okouchi, T.; Haneda, M. Three Way Catalytic Activity of Thermally Degenerated Pt/Al_2O_3 and Pt/CeO_2-ZrO_2 Modified Al_2O_3 Model Catalysts. *Catal Today* **2015**, *242*, 329–337.

(67) Andonova, S.; Ok, Z. A.; Drenchev, N.; Ozensoy, E.; Hadjiivanov, K. $Pt/CeO_x/ZrO_x/\gamma$-Al_2O_3 Ternary Mixed Oxide $DeNO_x$ Catalyst: Surface Chemistry and NO_x Interactions. *The Journal of Physical Chemistry C* **2018**, *122* (24), 12850–12863.

(68) Zhou, Z.; Harold, M. P.; Luss, D. Comparison of Pt-BaO/Al_2O_3 and Pt-CeO_2/Al_2O_3 for NOx Storage and Reduction: Impact of Cycling Frequency. *Appl Catal B* **2019**, *255*, 117742.

(69) Dong, F.; Tanabe, T.; Takahashi, N.; Shinjoh, H. Investigation of the Effective Oxygen Storage and Release Performances on the Pt/CeO_2-ZrO_2 Catalysts by Breakthrough Method. *Catal Today* **2019**, *332*, 259–266.

(70) Wu, J.; O'Neill, A. E.; Li, C. H.; Jinschek, J. R.; Cavataio, G. Superior TWC Activity of Rh Supported on Pyrochlore-Phase Ceria Zirconia. *Appl Catal B* **2021**, *280*, 119450.

(71) Kopelent, R.; Tereshchenko, A.; Guda, A.; Smolentsev, G.; Artiglia, L.; Sushkevich, V. L.; Bugaev, A.; Sadykov, I. I.; Baidya, T.; Bodnarchuk, M.; Van Bokhoven, J. A.; Nachtegaal, M.; Safonova, O. V. Enhanced Reducibility of the Ceria-Tin Oxide Solid Solution Modifies the CO Oxidation Mechanism at the Platinum-Oxide Interface. *ACS Catal* **2021**, *11* (15), 9435–9449.

(72) Asakura, H.; Hosokawa, S.; Beppu, K.; Tamai, K.; Ohyama, J.; Shishido, T.; Kato, K.; Teramura, K.; Tanaka, T. Real-Time Observation of the Effect of Oxygen Storage Materials on Pd-Based Three-Way Catalysts under Ideal Automobile Exhaust Conditions: An Operando Study. *Catal Sci Technol* **2021**, *11* (18), 6182–6190.

Chapter 7

Effect of Oxygen Storage Materials on the Performance of Pt-based Three-Way Catalysts

7.1 Introduction

Regulations on vehicular emissions of hydrocarbons (HCs), carbon monoxide (CO), and nitrogen oxides (NO_x) are becoming increasingly stringent worldwide. Significant efforts have been devoted to the development of three-way catalysis (TWC), which is considered as one of the effective technologies for the abatement of exhaust gases.[1–7] In the past few decades, a variety of metal-based catalytic materials have been designed and explored, including platinum group metals (PGMs) and non-noble metals (so-called base metal catalysts) such as Ni, Cu, and Fe. Base metal catalysts have largely been explored to evade the issues arising from the high cost and low availability of noble metals.[8–11] Although base metals catalysts have excellent potential, they lack the intrinsic reactivity and durability required for automotive applications. Consequently, a practical system requires large amounts of PGMs to satisfy strict regulations [12–21].

Contemporary commercial TWCs are generally composed of Pd and a relatively small amount of Rh [22–25]. Although Pd- and Rh-based TWCs deliver excellent catalytic performance, their application has been hindered in the recent years by the increasing price of Pd and Rh. Pt is currently less expensive than Pd and Rh, which incentivizes the use of Pt in place of Pd and Rh. However, Pt-based TWCs have attracted less attention than Pd- and Rh-based TWCs [26–30]. Therefore, the design and development of effective catalytic supports is urgently required to improve the activity and stability of Pt-based TWCs to replace Pd- and Rh-based TWCs or reduce their use.

Compared to Al_2O_3-based commercial TWC supports [31–35] and other promising metal oxide supports [36,37], oxygen storage materials (OSMs) such as CeO_2 and CeO_2-ZrO_2 solid-solutions are effective for control of air-fuel ratios (AFRs) that deviate from the stoichiometric conditions ($\lambda = 1$) in real-world applications; that is because OSMs possess excellent oxygen storage capacity (OSC) due to the rapid redox reaction of Ce, between its 4+ and 3+ oxidation states [38–47]. Introducing the Zr^{4+} cation into the lattice of CeO_2 increases the concentration of structural defects, improves the oxygen mobility, and enhances the Ce^{3+}/Ce ratio on the surface of PGM-based catalysts, producing more oxygen vacancies and Ce in the Ce^{3+} state [48–51]. Note that such structural defects should only be local perturbation and the overall structure should be homogeneous on average as the dynamic oxygen mobility in Pt/CeO_2-ZrO_2 catalysts was proportional to the structural homogeneity arising from the introduction of Zr into the CeO_2 framework [52]. Metal-support interactions (MSIs) and the adsorption and activation of TWC reactants occurring on OSM surfaces also influence the performance of OSMs [53–57]. Wakita and co-workers concluded that the structural disorder in cubic $Ce_{0.5}Zr_{0.5}O_2$, which provides bulk diffusion paths for oxygen ions, was a possible factor contributing to its higher catalytic activity than that of CeO_2 [58]. Fan and co-workers discovered that the strong metal-support interaction (SMSI), which could be modulated under the oxidative/reductive atmosphere, influenced the structure and performance of Pt/$Ce_{0.67}Zr_{0.33}O_2$, and samples with a weaker SMSI exhibited higher conversion of NO

and CO[59]. Nagai and co-workers reported that the Pt–O–Ce bond formed by the Pt–oxide-support interaction acted as an anchor and inhibited the agglomeration of Pt particles under oxidizing conditions at high temperatures[60]. Nunan and co-workers discovered that the degree of Pt/Ce interaction and the resulting activity could be controlled by varying the CeO_2 crystallite size. Reducing the CeO_2 crystallite size increased the Pt/Ce interaction, thereby increasing the activity of fresh and aged catalysts [61]. These are seminal findings in this area of research. However, the fundamental understanding of the properties of OSMs and their effects on the performance of Pt-based TWCs remains insufficient, particularly under conditions relevant to modern three-way catalysis operations, where deviations from stoichiometric conditions (i.e., fuel cut and acceleration) are often encountered. Comprehensive studies are required to further understand the behavior of Pt catalysts loaded on OSM supports during three-way catalysis.

In this study, we further investigated the effect of OSMs on the catalytic performance of Pt-based TWCs. In catalytic evaluations of powdered and monolithic honeycomb catalysts, fresh Pt/OSM(100%CeO_2) and aged Pt/OSM(66%CeO_2) delivered the highest performance among the corresponding sample series. The results of various kinetic and spectroscopic studies, including *in situ* (*operando*) Fourier transform infrared (FT-IR) spectroscopy, X-ray absorption spectroscopy (XAS), and X-ray photoelectron spectroscopy (XPS), proved that the presence of electron-deficient Pt^0 in combination with the excellent redox properties of the Pt and Ce species present in the Pt/OSM catalyst increased the conversion of NO and effectively inhibited poisoning by CO.

7.2 Experimental section

7.2.1 Preparation of catalysts

He (purity >99.995%), H_2 (purity >99.99%), O_2 (purity >99.5%), N_2 (purity >99.99%), Ar (purity >99.99%), NO (purity >99.5%), CO (purity >99.95%), CO_2 (purity >99.99%), C_3H_6 (purity >99.95%) gasses were obtained from Air Water Inc. and were used for catalyst preparations, catalytic reactions using powdered catalysts, and *in situ/operando* experiments. For catalysts ageing under hydrothermal redox conditions and catalytic reactions using honeycomb catalysts, purities of gasses used were as follows; >99.9999% for H_2, >99.5% for O_2, >99.0% for NO, >99.9% for CO, >99.5% for CO_2, and 99.9999% for C_3H_6. Pt-based TWCs (Pt/OSMs; 3 wt% Pt) were prepared using commercially available CeO_2 or CeO_2-ZrO_2 mixed oxide powders according to the following impregnation procedure. An OSM powder (5 g) and an aqueous solution (100 mL) containing 0.247 g (0.769 mmol) of $Pt(NH_3)_2(NO_2)_2$ which dissolved in HNO_3 (Pt content = 4.6 wt.%; Furuya Metal Co., Ltd.) were charged in a 500 mL glass vessel. The mixed solution was stirred for 15 min at room temperature prior to rotary evaporation at 50 °C and drying at 90 °C in an oven for 12 h. Subsequently, the as-obtained solids were calcined in a furnace at 500 °C in a static air atmosphere for 3 h. Prior to catalytic evaluation and *operando*/*in situ* spectroscopic experiments, the catalyst samples were reduced in a flow of 10% H_2/He (100 mL/min) at 400 °C for 30 min.

Monolithic honeycomb catalysts were fabricated by coating a slurry, prepared from calcined catalyst powders, an inactive alumina-based inorganic binder, and water, onto a cordierite honeycomb (25.4 mm × 50 mm, 400 cells/in^2; NGK Insulators, Ltd.), followed by drying at 120 °C in air for 1 h and calcination at 600 °C for 2 h. The as-obtained honeycomb catalysts contained approximately 60 g/L Pt/OSM solids, amounting to a total Pt loading of 0.18 g/L.

The ageing of monolithic honeycomb catalysts was conducted at 1000 °C for 4 h under hydrothermal redox conditions under a perturbation cycle of 180 s (3% CO, 3% H_2, 10% H_2O, and 84% N_2), 10 s (10% H_2O and 90% N_2), 180 s (3% O_2, 10% H_2O, and 87% N_2), and 10 s (10% H_2O and 90% N_2), simulating rich, stoichiometric, lean, and stoichiometric atmospheres, respectively. The total flow rate of the feed gas was 3 L/min, which corresponds to a space velocity of 7200 h^{-1}. The aged powder catalysts used for characterization were obtained through exposing the powder catalysts to the hydrothermal redox conditions. Equivalency of the thermal stress toward the catalysts between the lab-redox and engine ageing was confirmed by similarity of the specific surface areas for the two aged catalysts.

7.2.2 Catalyst characterization

Physical N_2 adsorption measurements were conducted using AUTOSORB 6AG (Yuasa Ionics Co., Ltd., Japan). X-ray diffraction (XRD) patterns were recorded using Cu-Kα radiation on a Miniflex benchtop X-ray diffractometer (Rigaku Corp., Japan) under ambient conditions. High-angle annular

dark-field scanning transmission electron microscopy (HAADF-STEM) and energy dispersive X-ray spectroscopy (EDX) were performed using an FEI Titan G2 80-300 electron microscope. CO adsorption experiments were performed at -70 °C and -185 °C using a BELCAT II apparatus (MicrotracBEL Corp., Japan). Temperature-programmed reduction by H_2 (H_2-TPR) was also performed using the BELCAT I equipment (MicrotracBEL Corp., Japan). Samples (20 mg) were placed in a U-type quartz cell and heated to 850 °C at a rate of 15 °C/min in a flow of 5% H_2/Ar (100 mL/min). The residual H_2 in the outlet gas was quantified using a thermal conductivity detector (TCD) following the removal of water by passing the outlet gas through a 4 Å molecular sieve. XPS characterization of the reduced catalyst specimens was performed on a ESCA-3400HSE spectrometer (Shimadzu, Japan) using Mg-Kα (1253.6 eV) radiation. The samples were prepared in a glove box prior to being connected to the XPS chamber to avoid exposure to air. The binding energies were calibrated with respect to C_{1s} at 285.0 eV. CO adsorption IR experiments for fresh catalysts were conducted at -185 °C after reduction in a flow of 10% H_2/He (20 mL/min) at 400 °C for 30 min. The stream of 1% CO/He (10 mL) was introduced to the catalyst pellet (ϕ = 13 mm) until the intensity of CO adsorption peak was unchanged, followed by evacuation to remove the physically adsorbed CO on the catalyst. The IR spectra were then recorded.

7.2.3 *Operando* infrared (IR) spectroscopy

Operando IR spectroscopic measurements during NO–CO reactions on fresh and aged Pt/OSMs having varying ceria contents were conducted at 200 °C on an FT/IR-4200 spectrometer (JASCO, Japan) equipped with a mercury-cadmium-telluride (MCT) detector. Typically, catalyst pellets (ϕ = 13 mm) pressed using 40 mg samples were charged in a quartz IR cell equipped with CaF_2 windows and a gas line system, and thereafter reduced in a flow of 10% H_2/He (100 mL/min) at 400 °C for 30 min prior to testing. Following the cooling of each pellet to 200 °C in a flow of He, 0.5% NO/He (80 mL/min) was introduced into the cell for 10 min prior to reverting to He flow to purge the residual NO inside the cell. Thereafter, 0.5% CO/He (80 mL/min) was flown into the cell for 10 min. The gas composition at the outlet was identified and quantitatively analyzed using an FT-IR gas cell (JASCO FT/IR-4100) and a 490 Micro gas chromatograph (GC, Agilent Technologies Inc., USA) equipped with MS5A (10 m) and PoraPLOT Q (10 m) columns and a high-sampling-rate TCD. The background of the IR spectrum was subtracted from the reference recorded at 200 °C in a flow of He.

7.2.4 (*In situ*) X-ray absorption spectroscopy (XAS)

All the XAS spectra were recorded in the transmittance mode at the BL14B2 beamline of SPring-8 (proposals 2020A1695 and 2021A1615). A Si (311) double crystal monochromator was used for the Pt L_3-edge, Zr K-edge, and Ce K-edge measurements, whereas a Si (111) double crystal monochromator was used for the Ce L_3-edge measurements. Data analysis was conducted using Athena software ver. 0.9.25, which was included in the Demeter package.

For *ex situ* studies, including measurements of reference compounds, samples in pellet form (ϕ = 10 mm) were sealed in a polyethylene cell in air, and their spectra were recorded at ambient temperature. For *in situ* studies, samples in pellet form (ϕ = 7 mm; mixed with boron nitride (BN) if necessary) were placed in a quartz cell equipped with Kapton film windows and gas lines. For H_2-TPR, upon the introduction of 10% H_2/He (1000 mL/min), the cell was heated to 850 °C at a ramp rate of 15 °C/min. For the NO–CO reactions, the catalyst was reduced in a 10% H_2/He (100 mL/min) flow at 400 °C for 30 min and thereafter cooled to 200 °C. Subsequently, 0.5% NO/He, 0.5% CO/He, or 0.5%NO + 0.5%CO/He were introduced into the cell. The spectra of standard CeO_2 and $Ce(NO_3)_3$, and PtO_2 and Pt foil were used as references for the quantification of the corresponding species (Ce^{4+} and Ce^{3+}, Pt^{4+} and Pt^0) using the linear combination fitting (LCF) method. Note that the LCF analysis provides information about only relative changes because the reference spectra do not exactly match spectra of the main samples even if the formal oxidation states are the same.

7.2.5 Catalytic reactions

Catalytic NO–CO reactions on fresh and aged Pt/OSMs having different ceria contents were performed in a fixed-bed flow reactor. Briefly, 20 mg of catalyst powder was charged in a tubular reactor using quartz wool to fix the layer, followed by reduction in a flow of 10% H_2/He (100 mL/min) at 400 °C for 30 min prior to commencing the reaction. Upon reaching the required temperature, a flowing gas mixture containing 0.5% NO and 0.5% CO in He was supplied at 80 mL/min (*F*/*W* corresponds to 4000 $mL/g_{Cat}/min$). The gas composition in the outlet was quantitatively analyzed by a GC equipped with a SHINCARBON ST column (Shimadzu GC-8A) to determine the conversions and yields according to the following chemical equations:

$$2NO + 2CO \rightarrow N_2 + 2CO_2 \quad (1)$$

$$2NO + CO \rightarrow N_2O + CO_2 \quad (2)$$

Kinetic studies of fresh and aged Pt/OSMs having different ceria contents were carried out under controlled conditions when the conversion was below 10%. The apparent reaction order with respect to NO (CO) was determined from the steady-state reaction rates measured in a stream having different partial pressures of NO (CO) while maintaining a constant CO (NO) content. The activation barrier was determined from the steady-state reaction rates measured at different temperatures. The elimination of mass transfer limitation was confirmed using the Mears criterion for external diffusion and the Weisz-Prater criterion for internal diffusion, which are expressed in equations (3) and (4) [62].

$$\frac{-r_A' \rho_b R n}{k_c C_A} < 0.15 \quad (3)$$

where $-r_A'$, ρ_b, R, n, k_c, and C_A are the reaction rate, bulk density of the catalyst bed, catalyst particle radius, reaction order, mass transfer coefficient, and reactant concentration, respectively. If the value of the term on the left-hand side is lower than 0.15, the external mass transfer effects can

be neglected.

$$C_{WP}=\frac{-r_A^{'}\rho_c R^2}{D_e C_A}<1 \quad (4)$$

where $-r_A^{'}$, ρ_c, R, D_e, and C_A are the reaction rate, catalyst density, catalyst particle radius, effective gas-phase diffusivity, and concentration of reactant A at the catalyst surface, respectively. If the value of C_{WP} is lower than 1, the internal mass transfer effects can be ignored.

Catalytic reactions on the honeycomb catalysts were conducted using a MEXA-series emission measurement system (Horiba Ltd., Japan). The catalysts were charged in a tubular reactor, and their catalytic performance was evaluated by feeding a gas mixture consisting of CO, C_3H_6, H_2, NO, O_2, CO_2, and H_2O (with the remainder being N_2) at different values of lambda at a space velocity (SV) of 100,000 h^{-1}. The value of lambda was calculated according to equation (5) (see **Tables S1-S3** for further details on the gas compositions for the corresponding experiments). Prior to each catalytic activity test, the honeycomb catalyst was pre-treated in a flow of the reaction gas (1 Hz perturbation between λ = 0.95 and λ = 1.05) at 400 °C for 30 min, followed by cooling to 100 °C in a flow of N_2. Conversions of NO, CO, and C_3H_6 were monitored using an exhaust gas analyzer (ABB, AO-2020).

$$\lambda = \frac{O_2 + 0.5CO + 0.5H_2O + CO_2 + 0.5NO}{0.5H_2+CO+1.5C_3H_6 + 0.5H_2O + CO_2}<1 \quad (5)$$

7.3. Results and discussion

7.3.1 Catalyst characterization

BET surface areas (S_{BET}) were determined for fresh and aged Pt/OSMs having different ceria contents based on the results of N_2 adsorption experiments (**Figure 1**). **Figure 2** shows that the S_{BET} of the fresh catalyst increased as the ceria content increased; however, the S_{BET} of the corresponding samples following ageing exhibited an inverse trend. In addition, the ratio between the S_{BET} of the aged specimen and that of the fresh specimen decreased significantly with an increase in the ceria content, particularly for Pt/OSM(100%CeO_2), indicating the sintering of the support during hydrothermal ageing and the low thermal stability of CeO_2. **Figure 3** depicts the morphology and elemental distribution obtained from the EDS mapping of fresh and aged Pt/OSMs having different ceria contents. The zirconium introduced was dispersed uniformly with Ce in the fresh and aged catalysts having 20%, 45%, and 66% ceria. These results indicated the structure of ZrO_2-CeO_2 solid-solution is not destroyed, because no segregation of ZrO_2 from CeO_2 was observed after ageing, which was also confirmed by the XRD characterization. Furthermore, the support did not appear to be compacted, and the Pt particles were uniformly dispersed throughout the fresh catalyst samples. The textual properties calculated from CO-adsorption and STEM measurements, including S_{BET} and the average Pt particle size of fresh and aged Pt/OSMs having different ceria contents are summarized in **Table 4**. Please note that negligible amounts of CO were adsorbed on the aged samples. The aggregation of Pt particles (~9.0 nm) accompanied by the sintering of support was reflected by the change in the average Pt particle size and S_{BET} following hydrothermal ageing, compared with the fresh samples. Therefore, it can be obtained that the hydrothermal aging treatment will lead to the sintering of CeO_2, which can be alleviated by the introduction of ZrO_2, and aggregation of Pt particles.

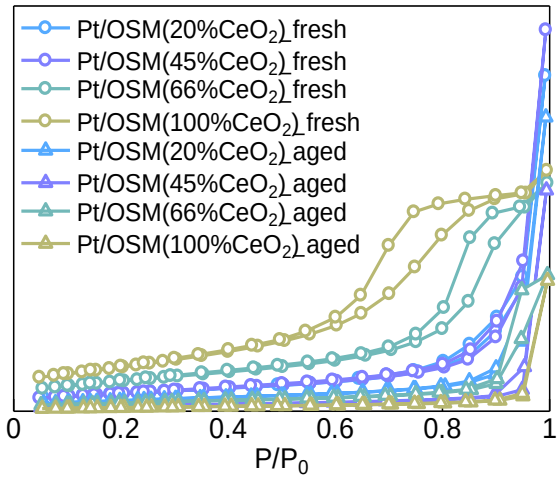

Figure 1. Isothermal N_2 adsorption and desorption curves of fresh and aged Pt/OSMs having different ceria content.

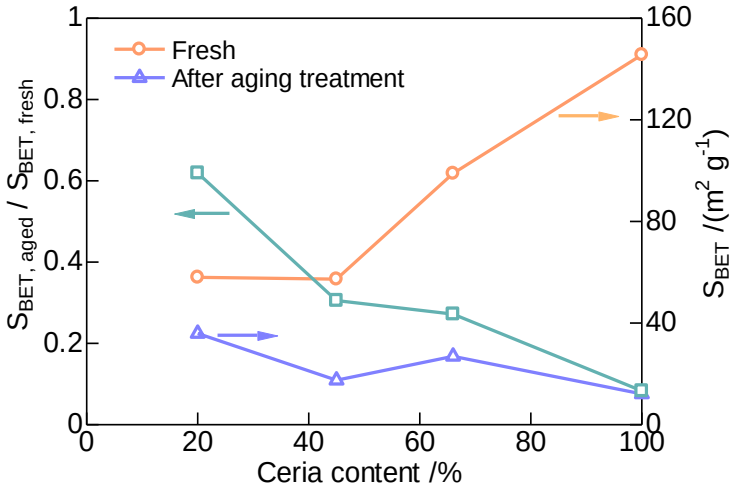

Figure 2. S_{BET} of fresh ($S_{BET, fresh}$) and aged ($S_{BET, aged}$) Pt/OSMs having different ceria content and the ratios of $S_{BET, aged}$ to $S_{BET, fresh}$.

Figure 4A and **4B** show the XRD patterns of fresh and aged Pt/OSMs having different ceria contents, respectively. The patterns exhibited by the fresh and aged samples correspond to cubic fluorite-type CeO_2 and CeO_2-ZrO_2 solid-solutions having different Ce/Zr ratios. The XRD peaks shifted to higher 2θ values with increasing zirconia content, revealing the contraction of the CeO_2 crystal lattice [63]. The absence of peaks attributed to the ZrO_2 and CeO_2 phases and of asymmetric reflections appearing in the fresh and aged samples with increasing zirconia content indicates a homogeneous solid-solution. No peaks attributable to Pt species were observed in the fresh specimens, owing to the small crystallite size and uniform dispersion of Pt on the support. Following hydrothermal ageing, peaks attributable to Pt species were observed in the XRD patterns of all samples, indicating the agglomeration of Pt crystallites at high temperatures. In addition, all reflections from the aged samples became sharper and narrower with increasing ceria content, indicating enhanced lattice contraction and powder sintering, which is consistent with the changes in the S_{BET} and the HAADF-STEM characterization results. In particular, the peak splitting appearing at 2θ = 69.6°, 76.9° and 79.3° in the diffraction pattern of aged Pt/OSM(100%CeO_2) (**Figure 5**) revealed the ceria has grown in size leading to very narrow line widths [64,65]. However, this phenomenon was not observed in the other aged samples, indicating that the introduced zirconia suppresses the sintering of ceria, which has been extensively investigated previously [66]. In addition, the solid-solution structure of ZrO_2-CeO_2 in aged samples can be still maintained even after hydrothermal treatment at 1000 °C.

Pt/OSM(20%CeO_2)

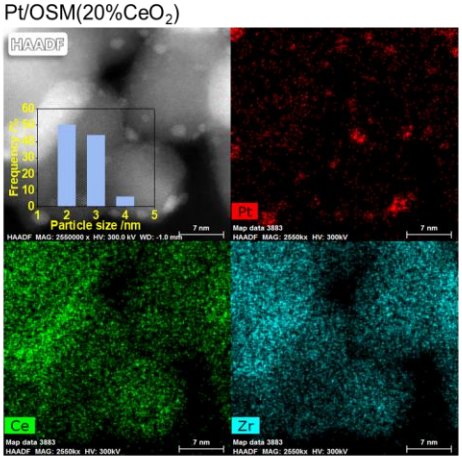

Pt/OSM(45%CeO_2)

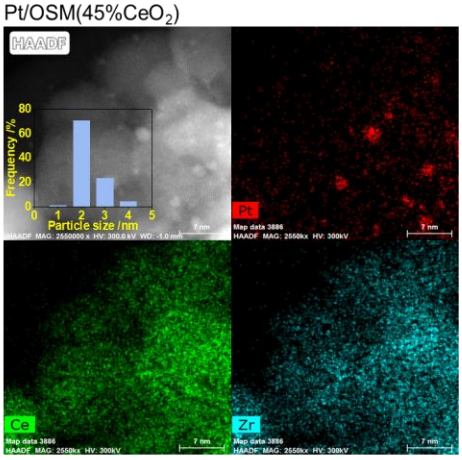

Pt/OSM(66%CeO_2)

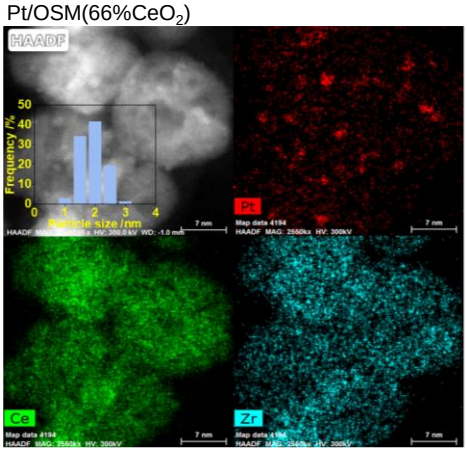

Pt/OSM(100%CeO_2)

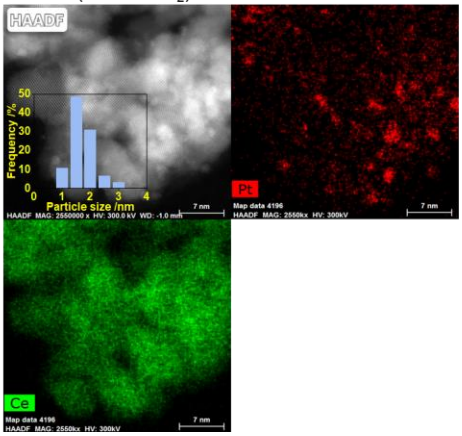

Pt/OSM(20%CeO_2)

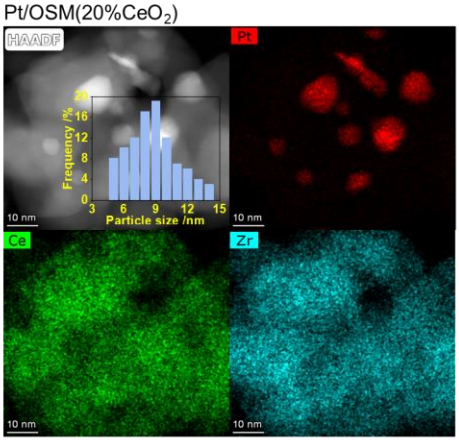

Pt/OSM(45%CeO_2)

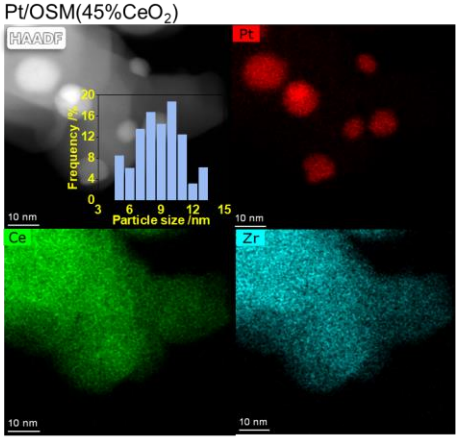

Pt/OSM(66%CeO_2)

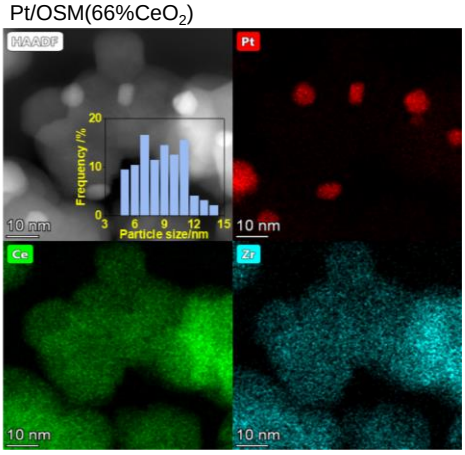

Pt/OSM(100%CeO_2)

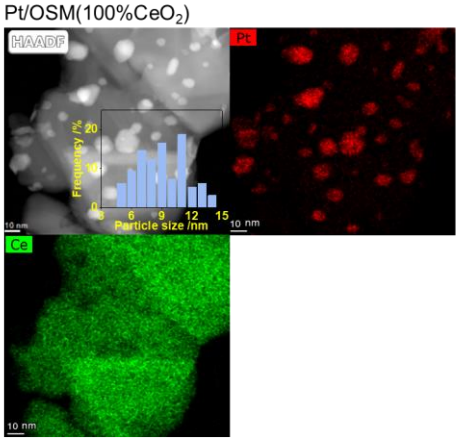

Figure 3. HAADF-STEM images and EDS elemental maps of (A) fresh and (B) aged Pt/OSMs(66%CeO_2).

Table 4. Textual properties of Pt/OSMs having different ceria content.

Catalyst	S_{BET}[a] /m^2 g^{-1}	Pt particle size[b] /nm	Pt particle size[c] /nm
Pt/OSM(20%CeO_2)_fresh	58	4.0	3.0
Pt/OSM(45%CeO_2)_fresh	57	3.9	2.8
Pt/OSM(66%CeO_2)_fresh	99	3.2	2.2
Pt/OSM(100%CeO_2)_fresh	146	2.3	2.1
Pt/OSM(20%CeO_2)_aged	36	-	8.9
Pt/OSM(45%CeO_2)_aged	18	-	9.0
Pt/OSM(66%CeO_2)_aged	27	-	8.7
Pt/OSM(100%CeO_2)_aged	12	-	9.2

[a] Determined by N_2 adsorption, [b] Estimated by CO adsorption at -70 °C, [c] Estimated by HAADF-STEM

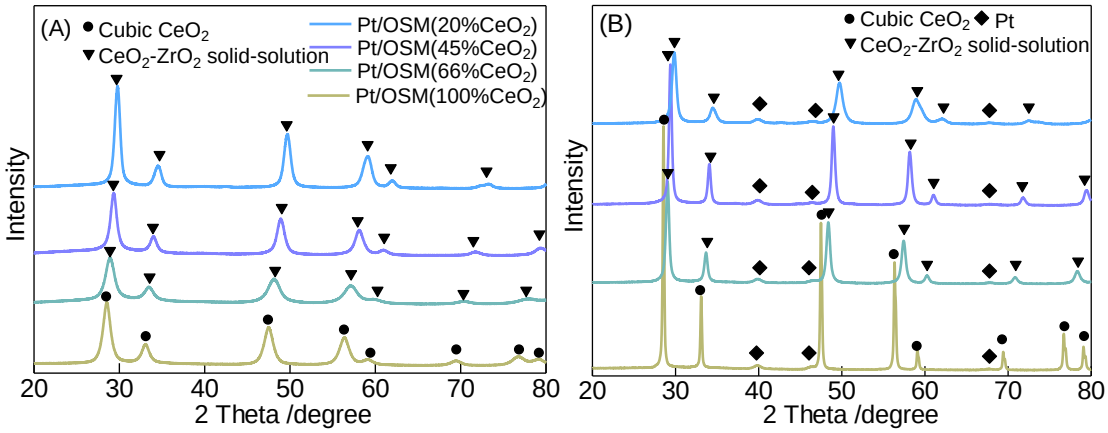

Figure 4. XRD patterns of (A) fresh and (B) aged Pt/OSMs having different ceria content.

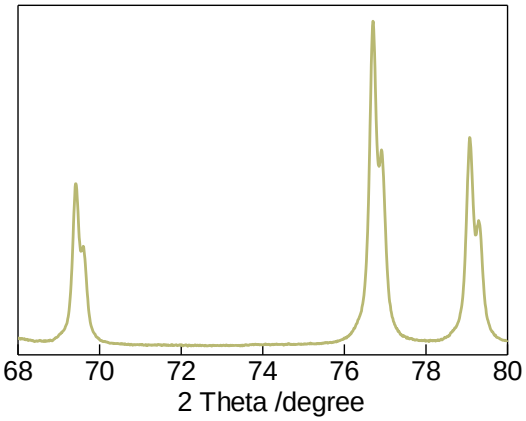

Figure 5. Close-up of XRD pattern of aged Pt/OSM(100%CeO_2) for the peak splitting.

The Zr K-edge X-ray absorption near-edge structure (XANES) spectra of the fresh and aged Pt/OSMs and their reference compounds, including ZrO_2 and Zr foil, are shown in **Figure 6**. The edge position of the XANES of the Pt/OSM samples corresponds closely to that of ZrO_2 used as a reference, indicating that zirconium species in Pt/OSMs exist as Zr^{4+}. **Figure 7** depicts the Ce K-edge XANES spectra of the fresh and aged Pt/OSMs as well as their reference materials, CeO_2 and $Ce(NO_3)_3$. No

difference was evident between the fresh and aged samples and the edge position corresponds well to that of a reference CeO_2 sample, suggesting the local structure of Ce in these specimens was similar to that in CeO_2. **Figure 8 and 9** show the Ce L_3-edge XANES spectra and the evolution of Ce species during the H_2-TPR of OSM(66%CeO_2) and OSM(100%CeO_2) supports. The reduction of Ce^{4+} to Ce^{3+}, indicated by the gradual disappearance of the characteristic double-peak feature at ~5730 and ~5737 eV and the appearance of a sharp peak at ~5725 eV, can be identified from the XANES spectra [67–69]. The well-known two-step reduction profile can be observed in these two samples, which assists in distinguishing between surface and bulk reduction [70,71], and the Ce^{4+} was completely reduced to Ce^{3+} at 800 °C. With the introduction of zirconia into the OSMs (**Figure 10A**), the bulk reduction peak shifted to a lower temperature (~560 °C) compared to that of CeO_2 (~710 °C). This is attributed to the ability of zirconia to introduce sublattice oxygen into the CeO_2-ZrO_2 solid-solution, generating defective structures and highly mobile oxygen atoms in the lattice that could be released at moderate temperatures [72,73]. In particular, a single reduction peak can be noticed in the samples having lower ceria contents, OSM(25%CeO_2), and OSM(45%CeO_2), similar experimental phenomenon was also observed by Kašpar on the $Ce_{0.5}Zr_{0.5}O_2$ and $Ce_{0.4}Zr_{0.6}O_2$ samples during H_2-TPR [74]. Following the loading of Pt species, an intense peak appeared at ~95 °C, which is attributed to the reduction of Pt oxide species, as shown in **Figure 8B** and **9B**. The peak at ~337 °C would be with respect to the concomitant reduction of PtO_x and Ce^{4+}, with the main contribution coming from the Ce component. A broad peak appearing in the vicinity of 700 °C was attributed to the reduction of bulk ceria in PtO_2/OSM(66%CeO_2) and PtO_2/OSM(100%CeO_2). Compared to the pristine support, the reduction of surface Ce^{4+} commences at a lower temperature and a higher rate following the loading of Pt oxide species, resulting from the Pt^0-induced hydrogen spillover effect [75,76]. In the spectra of the PtO_2/OSM(20%CeO_2) and PtO_2/OSM(45%CeO_2) samples (**Figure 10B**), a single peak linked to the reduction of Ce^{4+} was observed, which corresponds to the reduction of their OSM supports. A similar reduction phenomenon was also observed for Rh_2O_3/OSMs and PdO/OSMs having different ceria contents [77,78]. However, no significant gradual changes were observed in the Zr K-edge XANES spectra except for slight fluctuations caused by the reduction of ceria (**Figure 11**), suggesting that the oxidation state of all Zr species in the OSM supports and the PtO_2/OSM samples during H_2 reduction remains constant at a formal valency of 4+. Thus, it can be concluded that the Ce^{4+} in ZrO_2-CeO_2 solid-solution can be reduced to Ce^{3+} accompanied with the reduction of Pt^{4+} to Pt^0, however, the Zr^{4+} keeps unchanged.

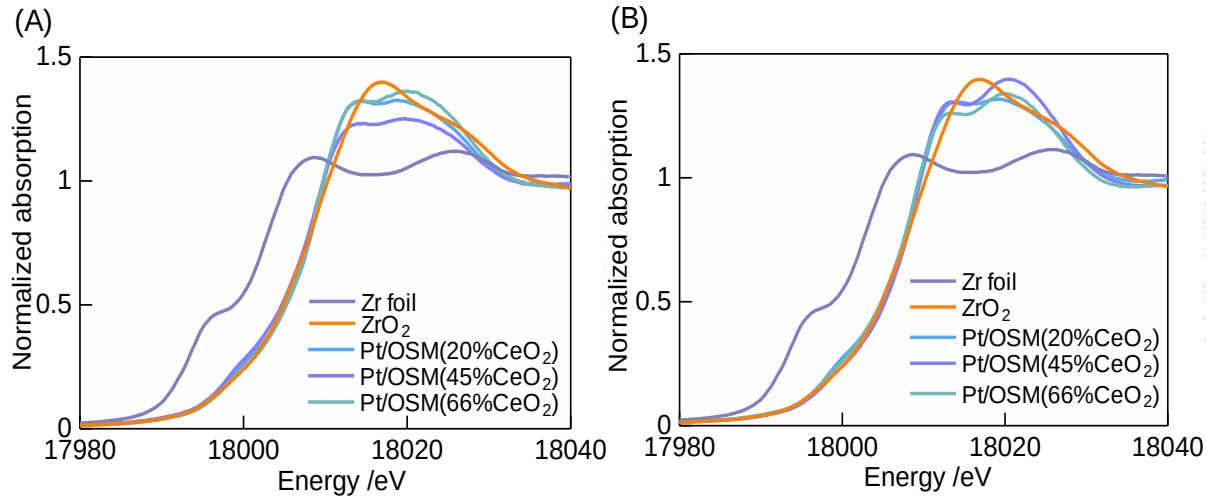

Figure 6. Zr K-edge XANES spectra of (A) fresh and (B) aged Pt/OSMs (27.1 mg for Pt/OSM(20%CeO_2), 44.7 mg for Pt/OSM(45%CeO_2), and 82.0 mg for Pt/OSM(66%CeO_2)) having different ceria content.

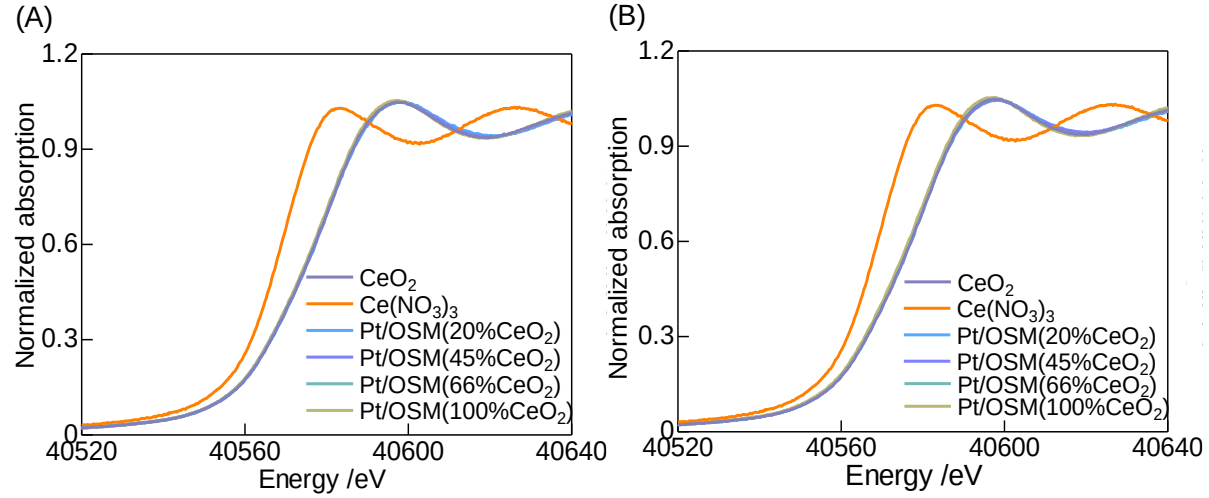

Figure 7. Ce K-edge XANES spectra of (A) fresh and (B) aged Pt/OSMs (110 mg for Pt/OSM(20%CeO_2), 47.0 mg for Pt/OSM(45%CeO_2), 33.0 mg for Pt/OSM(66%CeO_2), and 22.0 mg for Pt/OSM(100%CeO_2) having different ceria content.

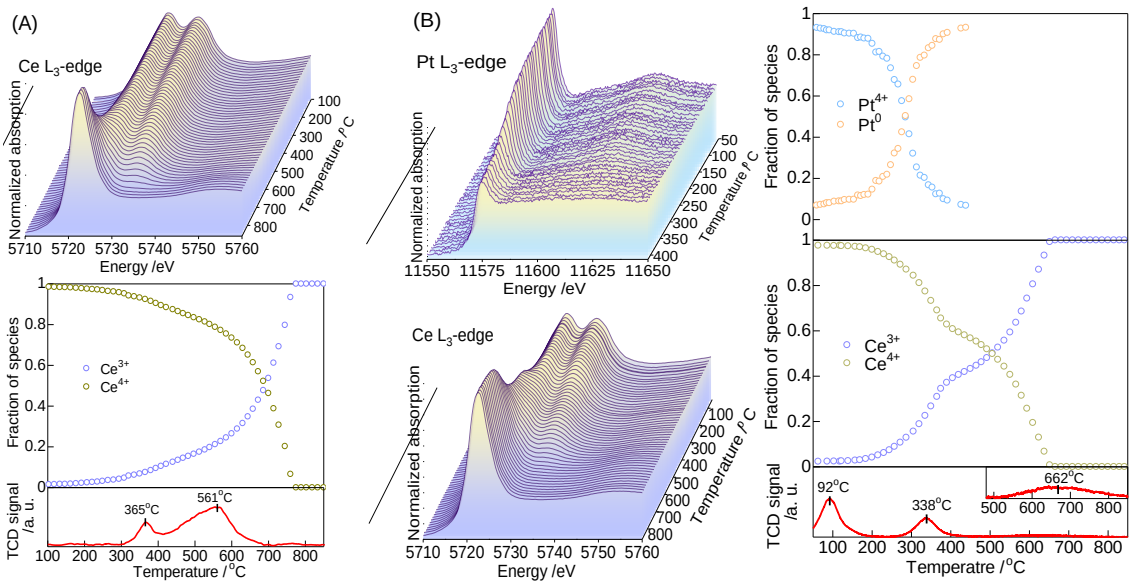

Figure 8. *In situ* Ce and Pt L_3-edge XAS during H_2-TPR of (A) OSM(66%CeO_2) (Sample amount = 1.9 mg with 20.4 mg of BN) and (B) PtO_2/OSM(66%CeO_2) (Sample amount = 2.0 mg with 20.4 mg of BN for Ce L_3-edge, and 21.8 mg with 12.8 mg BN for Pt L_3-edge measurements) conducted in H_2 flow (1000 mL/min) at the heating rate of 15 °C/min using CeO_2 and $Ce(NO_3)_3$, and Pt foil and PtO_2 as references for linear combination fitting analysis.

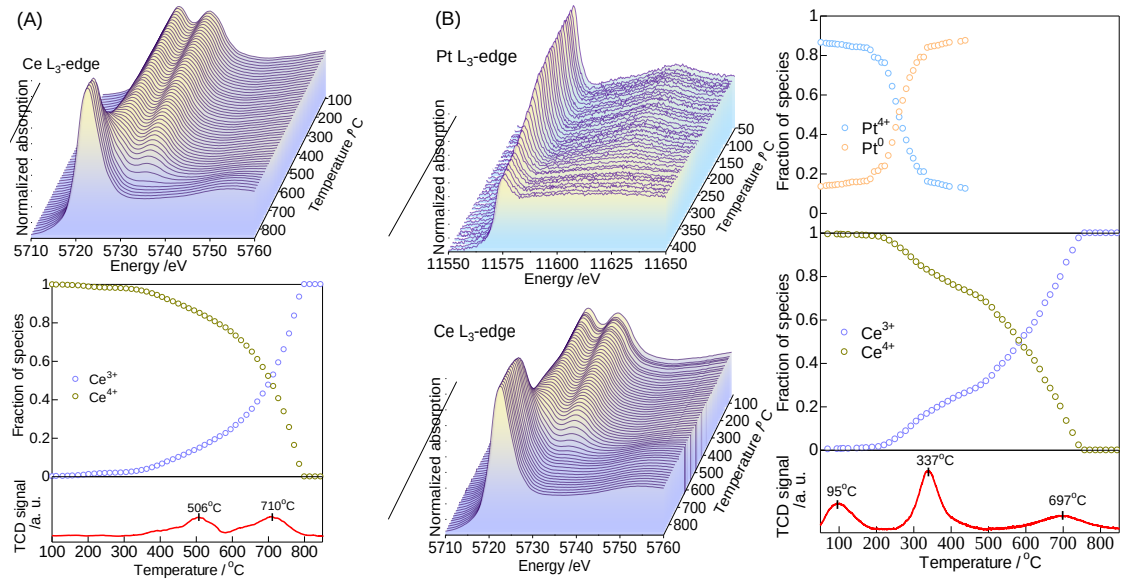

Figure 9. *In situ* Ce and Pt L_3-edge XAS during H_2-TPR of (A) OSM(100%CeO_2) (1.3 mg sample mixed with 20.4 mg BN) and (B) PtO_2/OSM(100%CeO_2) (Sample weight = 1.3 mg with 20.4 mg of BN for Ce L_3-edge and 17.3 mg with 12.8 mg of BN for Pt L_3-edge examination) conducted under H_2 flow (1000 mL/min) at the heating rate of 15 °C/min using CeO_2 and $Ce(NO_3)_3$, and Pt foil and PtO_2 as references for linear combination fitting analysis.

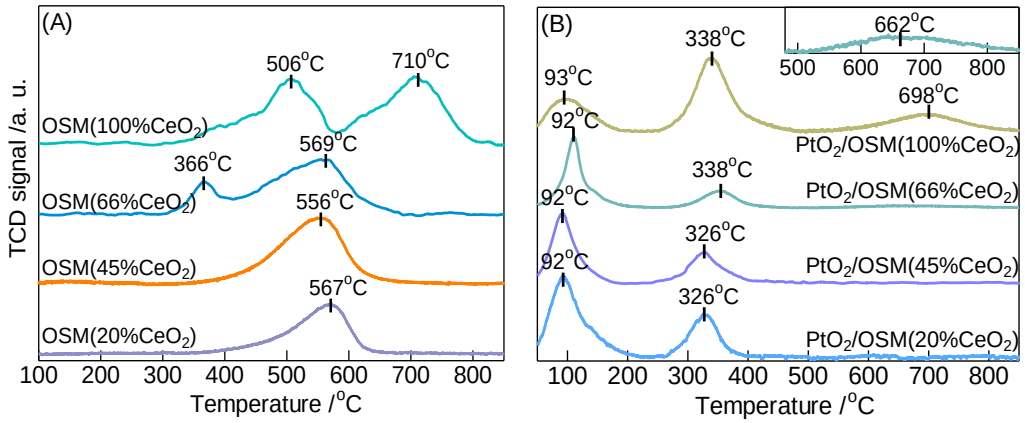

Figure 10. H_2-TPR profiles of (A) OSM supports and (B) PtO_2/OSMs having different ceria content.

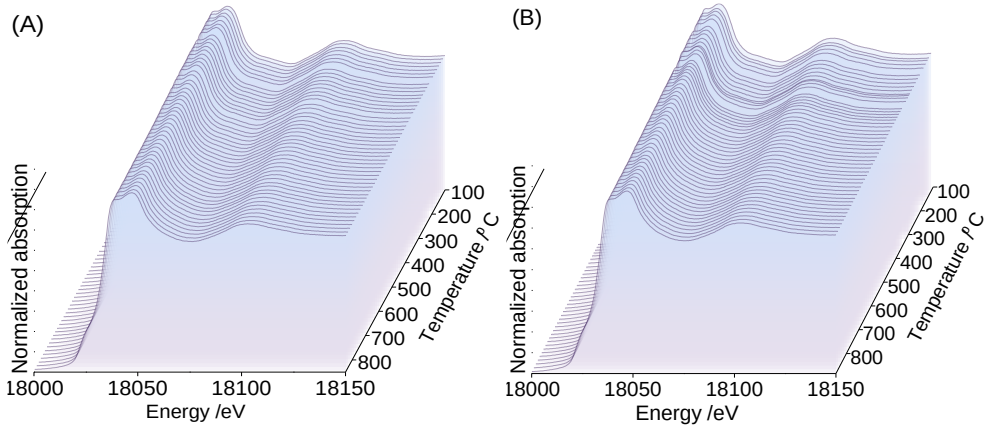

Figure 11. *In situ* Zr K-edge XANES spectra recorded during H_2-TPR of (A) OSM(66%CeO_2) (Sample weight = 18.7 mg with 12.8 mg of BN) and (B) PtO_2/OSM(66%CeO_2) (Sample weight = 19.3 mg sample with 12.8 mg of BN) conducted under H_2 flow (1000 mL/min) using Zr foil and ZrO_2 as reference.

XPS characterization and IR spectroscopy in conjunction with CO-adsorption experiments were carried out to assess the electronic properties of Pt particles in fresh and aged Pt/OSMs with different ceria contents. **Figures 12A and 12B** show the Pt 4f XPS spectra of fresh and aged Pt/OSM specimens, respectively, following reduction using H_2 without exposure to air. Two signals at binding energies of ca. 71 and 74 eV attributed to metallic Pt were observed in these spectra [75]. For the fresh samples, the signals shifted to lower binding energies as the ceria content decreased, suggesting that the Pt^0 species were more electron-rich in Pt/OSMs having a lower ceria content. Following the ageing treatment, the Pt^0 species in Pt/OSM(66%CeO_2) became the most electron-deficient, followed by those in Pt/OSM(45%CeO_2), Pt/OSM(20%CeO_2), and Pt/OSM(100%CeO_2). **Figure 12C** presents the *in situ* IR spectra recorded during the adsorption of CO onto fresh Pt/OSMs. The peak appearing at approximately 2070 cm^{-1} in all these spectra was assigned to CO bound to the on-top sites of the metallic surfaces [79]. The center of the peak gradually shifted to a higher wavenumber as the ceria content increased. And no peaks related to the CO adsorption on Zr^{4+}/Ce^{4+} (~2150 cm^{-1}) and Ce^{3+}

(2130-2120 cm^{-1}) sites were observed. The π back-donation from the transition metal surface to the $2\pi^*$ antibonding orbital of the adsorbate (CO) is the principal contributor to the strength of adsorption [80,81]. This contribution is weakened when Pt is positively charged, leading to a weaker adsorption of CO on the surface and less activation of adsorbed CO, resulting in a blue-shift of the peak center [82]. Therefore, it can be believed that the increasing ceria content in support favors the formation of more electron-deficient metallic Pt^0 species in fresh Pt/OSM samples. This effect of the support on the electron structure of the loaded metal was also observed in $Pd/M/Al_2O_3$ (M = La, Ba, or Sr) TWCs in our previous studies [83,84].

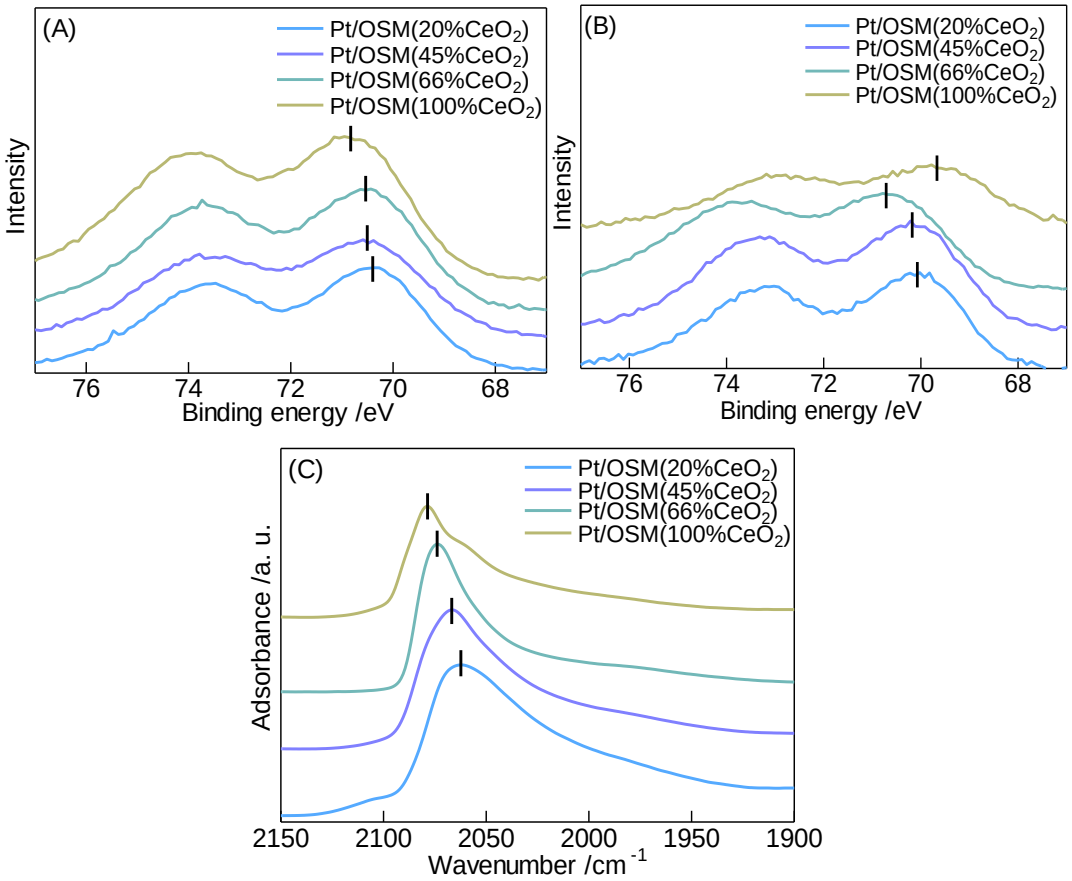

Figure 12. Pt 4f XPS spectra of (A) fresh and (B) aged Pt/OSMs. (C) *In situ* CO adsorption IR spectra of fresh Pt/OSMs following the reduction using H_2 without exposure to air.

7.3.2 Effect of OSMs on catalytic NO–CO reactions

NO–CO reactions were performed on fresh and aged powdered Pt/OSMs having different ceria contents, as shown in **Figure 13**. The catalytic activity was enhanced with the increase in the ceria content among the freshly tested catalysts, and Pt/OSM(100%CeO_2) delivered the highest performance. However, the catalytic performance followed the order Pt/OSM(66%CeO_2) > Pt/OSM(45%CeO_2) > Pt/OSM(20%CeO_2) > Pt/OSM(100%CeO_2) after ageing treatment, due to the thermal stability enhanced by the introduction of zirconia and the promotional effect of ceria in catalytic

activity. These results verify that the ceria content of the OSM support significantly influences the catalytic performance of the as-prepared Pt/OSM in NO–CO reactions. In addition, the catalytic activity of Pt/OSMs decreased dramatically following the ageing treatment due to the aggregation of Pt particles and structural changes in the support. It should be noted that the main products are N_2O and CO_2 with mass balance of 100% in the relatively low temperature region (below 450 °C). Further, to investigate the effect of OSM support on the catalytic properties of Pt/OSM, the apparent reaction orders with respect to NO and CO, as well as the activation barrier, were determined for fresh and aged catalysts from the turnover frequencies (TOFs) in streams having different partial pressures of NO and CO (**Figure 13** and **Table 5**). The TOFs were determined using the steady-state reaction rates measured at NO conversions lower than 10% and CO adsorption amounts at -20 °C. Reactions involving CO are usually of a negative order with respect to the CO concentration on Pt-based catalysts [85,86]; that is because the strong binding of CO to the surface of PGMs inhibits the catalyst, that is, CO serves as a catalyst poison. This phenomenon was also observed for both fresh and aged Pt/OSMs, for which the reaction order with respect to CO was negative, revealing that the strong adsorption of CO onto Pt particles suppressed the NO–CO reactions. By combining the calculated reaction order of CO and the IR and XPS characterization results recorded during the adsorption of CO, the extent to which CO inhibits the reaction can be attributed to the electronic properties of the supported Pt^0 species; increased electron-deficiency reduces the inhibition caused by CO. Therefore, increasing the ceria content of the catalyst reduces poisoning by CO; however, this promoting effect is decreased by the sintering of ceria, as indicated by the fact that Pt/OSM(66%CeO_2) exhibits the strongest poisoning-resistance among all the aged catalysts. The Arrhenius plots indicate that the NO–CO reactions on fresh catalysts having higher ceria contents exhibit lower activation energies, and the corresponding samples exhibit higher activation energies following the ageing treatment, which supports the catalytic evaluation results.

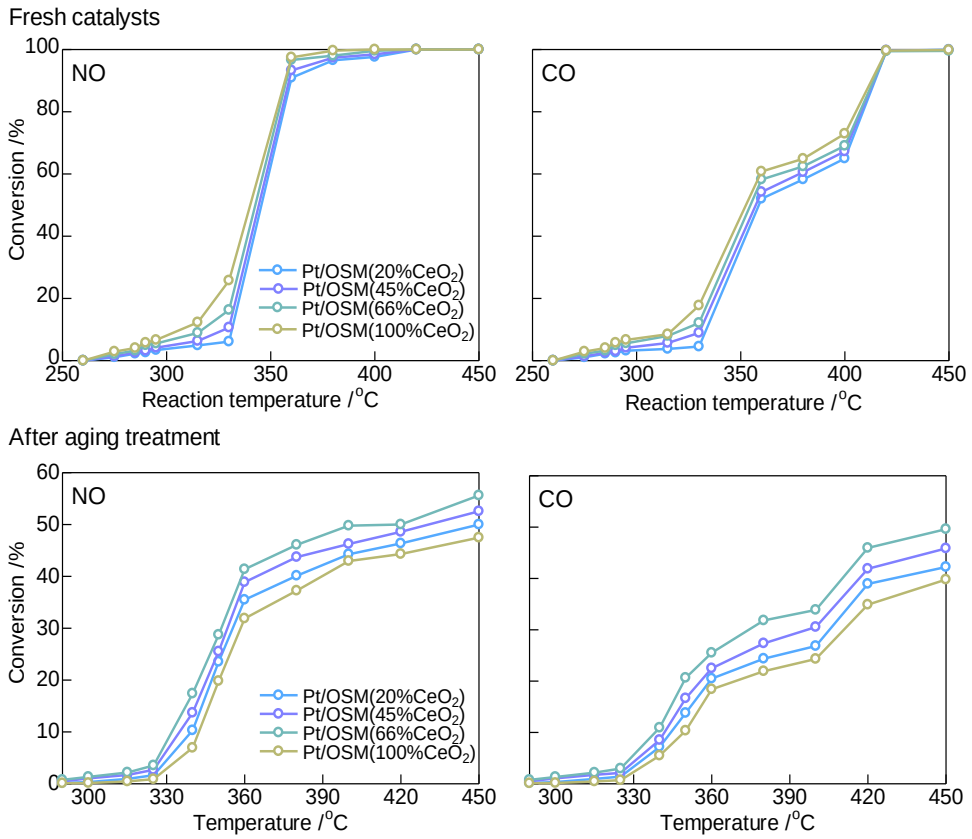

Figure 13. Effect of OSMs having different ceria contents on catalytic NO–CO reactions over powdered fresh and aged Pt/OSMs (20 mg) in a flow of 0.5% NO, 0.5% CO, and 99% He (80 mL/min).

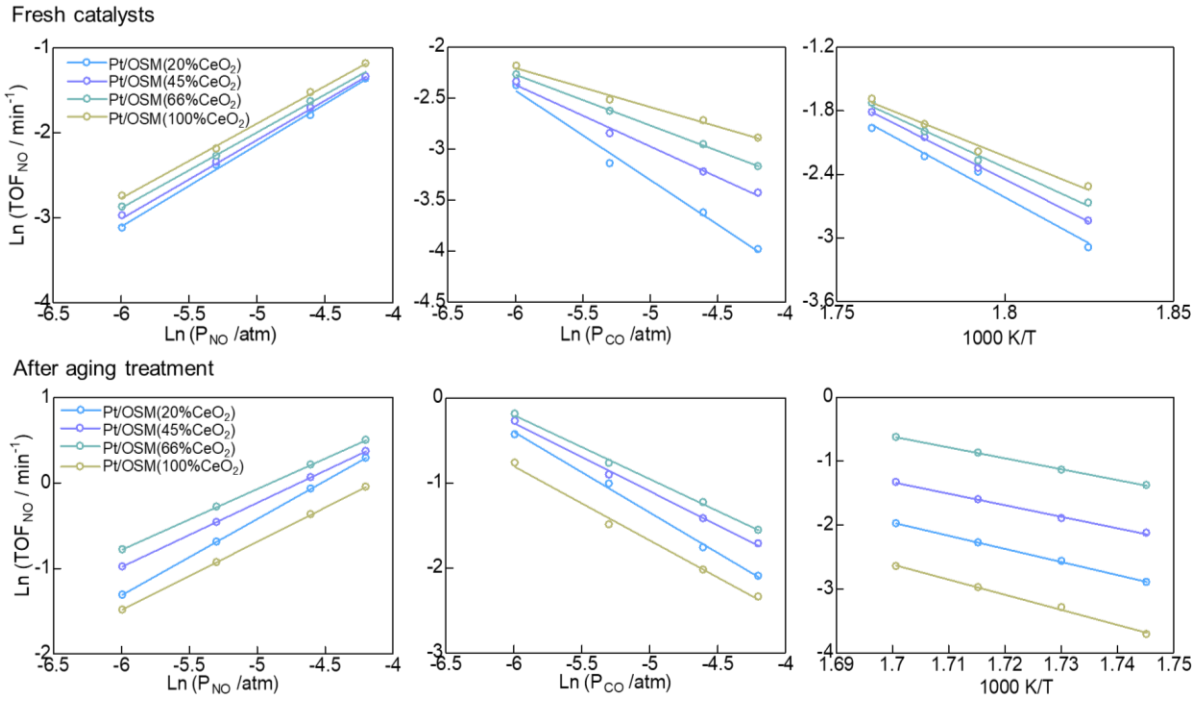

Figure 14. Apparent kinetic studies on NO–CO reactions over fresh and aged powdered Pt/OSMs (20 mg) having different ceria content at the reaction condition of 0.25-1.5% NO (0.5% for Arrhenius plot test), 0.5-2.0% CO (0.5% for Arrhenius plot test) in He flow (80 mL/min), 285 °C and 320 °C for reaction

order measurement on fresh and aged catalysts, while 275-295 °C and 300-315 °C for Arrhenius plot examination on corresponding samples.

Table 5. Kinetic informatics of reaction order and activation barrier.

Catalyst	Reaction order of NO	Reaction order of CO	Activation barrier (kJ mol^{-1})
Pt/OSM(20%CeO_2)_fresh	0.96	-1.15	144
Pt/OSM(45%CeO_2)_fresh	0.91	-0.75	133
Pt/OSM(66%CeO_2)_fresh	0.89	-0.65	121
Pt/OSM(100%CeO_2)_fresh	0.87	-0.50	106
Pt/OSM(20%CeO_2)_aged	1.37	-1.88	170
Pt/OSM(45%CeO_2)_aged	1.15	-1.60	150
Pt/OSM(66%CeO_2)_aged	1.07	-1.50	141
Pt/OSM(100%CeO_2)_aged	1.21	-1.70	193

To gain clearer insights into the effect of OSMs on the formation and evolution of surface species and their reactivity during NO–CO reactions on fresh and aged Pt/OSMs having different ceria contents, *operando* IR spectroscopic experiments were performed and the results are presented in **Figure 15**. Following exposure to NO, various NO_x species were formed on the catalyst surface as evidenced by the peaks appearing in the 1100-1700 cm^{-1} region [87,88]. Specifically, the peak at approximately 1170 cm^{-1} was ascribed to the surface nitrite species [89,90]. The intensity of this peak is higher in the fresh Pt/OSMs having a higher ceria content, indicating that ceria can efficiently promote the production of surface nitrite species. However, nearly no nitrite formation was observed on aged Pt/OSM(100%CeO_2), largely due to the heavy agglomeration of CeO_2 and sintering of Pt particles, as confirmed by N_2 adsorption, HAADF-STEM, and XRD characterizations. Besides, the hydrothermal aging treatment at 1000 °C can cause the strong metal-support interaction (SMSI) in aged catalysts and therefore the Pt particles can be wrapped or covered by Ce species [56, 91], leading to the difficult contact between Pt sites and reactant molecules and the consequential decrease in the intensity of IR absorption peaks of the aged samples. The broad bands in the region of 1250-1650 cm^{-1} were attributed to the characteristic absorption of nitrate species in different modes [91]. The peak at approximately 1781 cm^{-1} is ascribed to the NO species absorbed on Pt particles, which can transform into N_2O and nitrite species through a disproportion reaction [92]. The bands emerging in the region of 1293-1606 cm^{-1} were assigned to carbonate species adsorbed on the catalyst surface, and, upon exposure to CO in a flow of 0.5% CO/He, gradually increased in intensity [93]. However, the intensity of the peak attributed to nitrite species declined during the introduction of CO. As shown in the plots on the right-hand side of **Figure 15**, the rate of consumption of nitrite species, which reflects their reactivity, is enhanced by increases in the ceria content of fresh Pt/OSMs. However, the aged catalysts follow the order Pt/OSM(66%CeO_2) > Pt/OSM(45%CeO_2) > Pt/OSM(20%CeO_2) > Pt/OSM(100%CeO_2) with respect to the reactivity of nitrite species. Furthermore, the as-detected concentrations of N_2O and CO_2 changed in agreement with the reactivity trend. These results reveal that the efficient formation of nitrite species and their reactivity toward CO are crucial to NO–CO reactions on fresh and aged Pt/OSMs, and the increased ceria content in fresh samples can promoted this process.

To understand the redox behaviors of Ce, Pt, and Zr species in fresh and aged catalysts during NO–CO reactions and their effects on catalytic performance, *in situ* Ce and Pt L_3-edge and Zr K-edge XAS measurements were conducted under consecutive flows of 0.5% NO/He and 0.5% CO/He, or a combined flow of 0.5%NO + 0.5%CO/He for the fresh and aged Pt/OSM(66%CeO_2) samples. The corresponding *in situ* Ce and Pt L_3-edge XANES spectra and the LCF analysis results are shown in **Figure 16**. The Ce^{3+} and Pt^0 species in the fresh Pt/OSM(66%CeO_2) sample were oxidized upon the introduction of NO, as evidenced by the change in the intensity of the corresponding peak in the XANES spectra. The Pt species oxidized by NO could be completely reduced by exposure to CO flow; however, the Ce^{4+} species was only partially reduced to Ce^{3+}, which could be re-oxidized by the subsequent NO flow. When the composition of the flowing gas was altered to 0.5%NO + 0.5%CO/He, the fractions of the Ce^{3+}, Ce^{4+}, and Pt^0 species remained nearly unchanged. In contrast, the redox abilities of Ce and Pt species in the aged Pt/OSM(66%CeO_2) specimen were much lower than those in the fresh sample under identical conditions, and the oxidation of Ce^{3+} was easier than the reduction of Ce^{4+}. This is because the hydrothermal ageing treatment causes the aggregation of Pt particles, lattice contraction of CeO_2 and progressive cubic crystallization of ZrO_2, as confirmed by the HAADF-STEM, XRD, and XAS characterizations. The redox behavior of Pt can be correlated to the particle size; the larger particles are more difficult to oxidize [94,95]. The lattice contraction of CeO_2 and the gradual cubic crystallization of ZrO_2 restrict the mobility of oxygen in the CeO_2-ZrO_2 solid-solution, thereby suppressing the redox transition of Ce [74,78]. Unlike Pt and Ce, no prominent redox transition was exhibited by zirconium in the fresh and aged samples, in which it remained in the formal oxidation state of Zr^{4+} (**Figure 17**). These results demonstrate that the Ce and Pt are both involved in NO–CO reactions through their redox cycles and abilities, which are affected by the structural properties and particle size changed by hydrothermal aging treatment, and are crucial to the catalytic activity in NO-CO reactions.

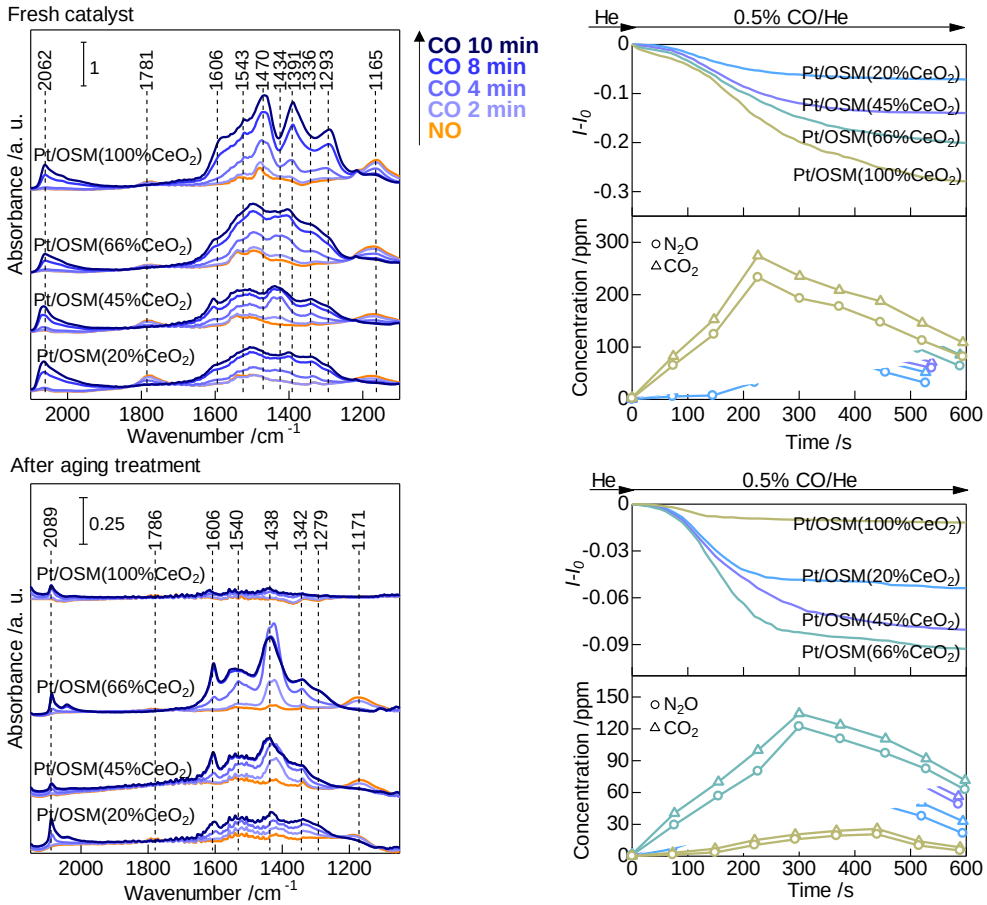

Figure 15. Results of *Operando* IR spectroscopic experiments performed to identify the formation of surface species and their reactivity toward CO on reduced fresh and aged Pt/OSMs recorded continuously following the introduction of 0.5% CO/He (seablue) after exposure to 0.5% NO/He for 10 min followed by He flow (orange) for 10 min at 200 °C; and variations in the intensities of peaks attributed to surface nitrite species and the as-detected concentrations of N_2O and CO_2 (products) during the reactions.

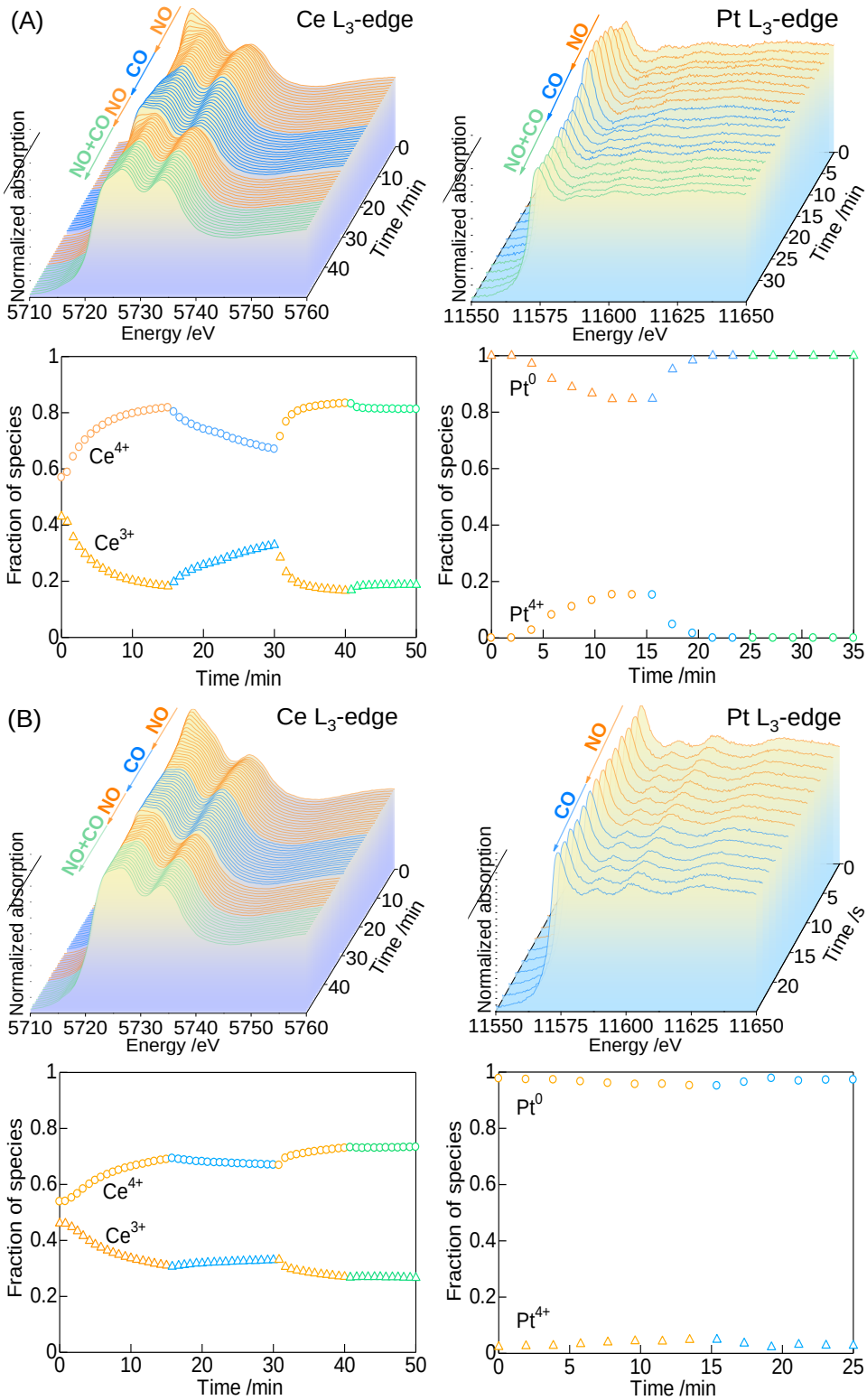

Figure 16. *In situ* Ce and Pt L_3-edge XAS measurements during NO–CO reactions on (A) fresh and (B) aged Pt/OSM(66%CeO_2) (Sample amount = 2.0 mg with 20.4 mg of BN for Ce L_3-edge and 21.8 mg with 12.8 mg of BN for Pt L_3-edge measurements) in a switched flow of 0.5% NO/He, 0.5% CO/He or 0.5%NO+0.5%CO/He (1000 mL/min) at 200 °C following reduction using H_2 at 400 °C, using CeO_2 and $Ce(NO_3)_3$, and Pt foil and PtO_2 as references for linear combination fitting analysis.

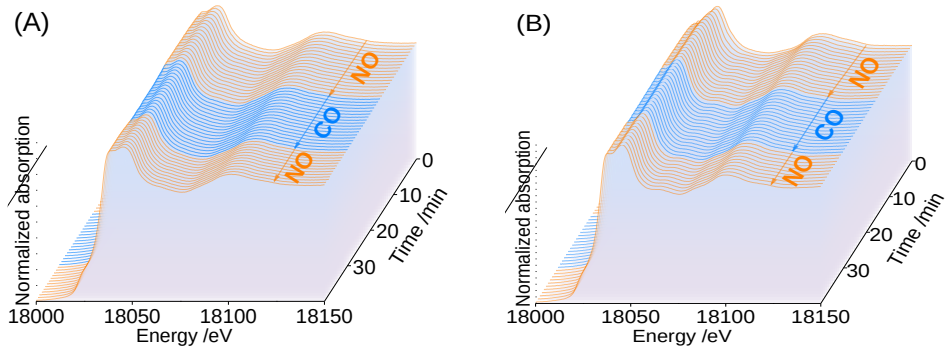

Figure 17. *In situ* Zr K-edge XAS measurements during NO–CO reactions on (A) fresh and (B) aged Pt/OSM(66%CeO_2) (Sample weight = 19.3 mg with 12.8 mg of BN) in a switched flow of 0.5% NO/He and 0.5% CO/He (1000 mL/min) at 200 °C after H_2 reduction at 400 °C, using Zr foil and ZrO_2 as references.

7.3.3 Catalytic evaluation of monolithic honeycomb catalysts under TWC conditions

The effect of OSMs on TWC light-off performance over monolithic honeycombs of fresh and aged Pt/OSMs was investigated in the light-off mode in a switched gas flow with a lambda perturbation of 1 Hz between 0.95 (rich) and 1.05 (lean) at SV = 100,000 h^{-1}, as shown in **Figure 18**. The honeycomb catalyst was pretreated in a flow of gas having an identical composition to that used in the evaluation at 400 °C for 30 min prior to each test. The continuously monitored performance of the fresh Pt/OSMs in the removal of NO, CO, and C_3H_6 increased with the increase in the ceria content in the OSM support, attributing to the promotion of ceria in the formation of nitrite species and their reactivity toward CO and C_3H_6. However, the conversion of NO, CO, and C_3H_6 on aged Pt/OSMs followed the order Pt/OSM(66%CeO_2) > Pt/OSM(45%CeO_2) > Pt/OSM(20%CeO_2) > Pt/OSM(100%CeO_2) considering the promoting effect of ceria, the decreased redox abilities of Pt and Ce species, and the sintering of the OSM supports during the ageing treatment ensured by *in situ* / *operando* XAS and IR as well as N_2 adsorption and XRD characterizations. Although the three-way catalysis activity of Pt/OSMs decreased dramatically following the ageing treatment, it is a vital investigation for practical applications, as catalysts are exposed to extremely harsh conditions that they must withstand for extended periods [96,97]. In addition, we correlated the ceria content with the T_{20} behavior, which was defined as the temperature at which the conversion was 20%, to further demonstrate the effect of OSMs on three-way catalysis performance, as presented in **Figure 19**. In fresh catalysts, T_{20} decreases with increasing ceria content, indicating that the ceria in OSM facilitates the conversion of NO, CO, and C_3H_6 on supported Pt TWCs at lower temperatures. In contrast, Pt/OSM(66%CeO_2) exhibited the lowest T_{20} among the aged catalysts, because of its good thermal stability improved by the introduction of zirconia and relatively high catalytic activity promoted by the ceria.

Figure 20 shows the effect of OSMs on the lambda-sweep performance over monolithic honeycomb Pt/OSM catalysts in the range of 0.95 (rich) to 1.05 (lean) at increments of 0.01 at 300 °C, during which the conversions of NO, CO and C_3H_6 were recorded after maintaining each lambda step for 60 s to examine the steady-state activity. The conversion of NO occurs efficiently in the rich region ($0.95 \leq \lambda < 1$), wherein excess reducing gas components are present. The NO removal efficiency increased with the increase in the ceria content for fresh Pt/OSMs; however, Pt/OSM(66%CeO_2) exhibited the highest efficiency among the aged catalysts, which is in agreement with the results of the light-off performance test. The conversion of CO and C_3H_6 is sufficient in the lean region ($1 < \lambda \leq 1.05$), where oxidation processes are preferred in the presence of abundant O_2. All of the fresh Pt/OSMs exhibited identical maximum removal efficiencies for CO and C_3H_6; however, only Pt/OSM(66%CeO_2) retained high activity among the aged catalysts. The removal efficiencies of CO and C_3H_6 on fresh Pt/OSMs also increased with increasing ceria content in the rich region. These results are in agreement with the aforementioned investigations and demonstrate that the high ceria

content together with the excellent redox properties of Pt and Ce species, which are suppressed following the ageing treatment of Pt/OSM catalysts, promote three-way catalysis. In addition, interesting behaviors are exhibited by the aged catalysts: the NO conversion is lower under rich conditions compared to that under lean conditions, particularly for aged Pt/OSM(20%CeO_2). This is directly opposite to the normal reactivity of NO, as it is an oxidant that reacts with a reductant under reducing conditions. This can be explained by the poisoning effect of CO. Under rich conditions, CO poisoning drastically reduces the NO conversion, while under lean conditions, the CO poisoning is weaker, and consequently the activity is higher. This is also consistent with the fact that the aged Pt/OSM(20%CeO_2) catalyst exhibited the lowest apparent reaction order with respect to CO in the NO–CO reaction. This phenomenon originating from strong CO poisoning is peculiar to Pt and is not seen in Rh and Pd, and it is essential to account for it during the development of Pt-based TWCs. When the reaction temperature was increased to 400 °C (**Figure 21**) and thereafter to 500 °C (**Figure 22**), the conversion of NO, CO, and C_3H_6 on fresh and aged Pt/OSMs was remarkably enhanced, and the differences between the catalytic performances of these catalysts decreased gradually.

The lambda value significantly fluctuates from low (rich) to high (lean) during the modern practical TWC process due to an engine fuel-cut operation which was introduced relatively recently to improve fuel efficiency [99,100], so it is important that the TWC catalysts possess a broad working window and efficiently remove exhaust gases under such turbulent conditions [83,101]. Therefore, the effect of OSMs on TWC lambda-switching performance over Pt/OSM-coated honeycomb catalysts was investigated, and the continuously recorded conversions of NO, CO, and C_3H_6 are shown in **Figure 23**. The catalyst was pretreated under lean conditions (λ = 1.05) at 300 °C for 5 min prior to the commencement of the test under rich conditions (λ = 0.95), followed by switching to lean conditions and then to rich conditions again. There are detection delays for NO and CO relative to C_3H_6 due to the experimental setup (1.0 s for NO and 3.2 s for CO relative to C_3H_6). For the fresh Pt/OSMs, a high NO conversion was retained for the longest duration over Pt/OSM(100%CeO_2), whereas the NO conversion declined faster than for the other catalysts that had lower ceria contents. The NO conversion occurred nearly identically over the catalysts studied for the subsequent change from lean to rich, followed by a gradual decrease in the conversion for Pt/OSM(20%CeO_2) and Pt/OSM(45%CeO_2). A similar gradual decrease in the conversions under rich conditions was also observed for CO and C_3H_6. This was probably caused by CO, which acts as a poison for Pt, as observed during the NO–CO reactions. The reactivities of the aged Pt/OSMs were much lower for all the reactants than that of the fresh Pt/OSMs. The increase in the conversion of NO under lean conditions was also observed here, particularly for aged Pt/OSM(20%CeO_2). This phenomenon can also be explained by the strong poisoning effect of CO under rich conditions, causing the extremely low NO conversion.

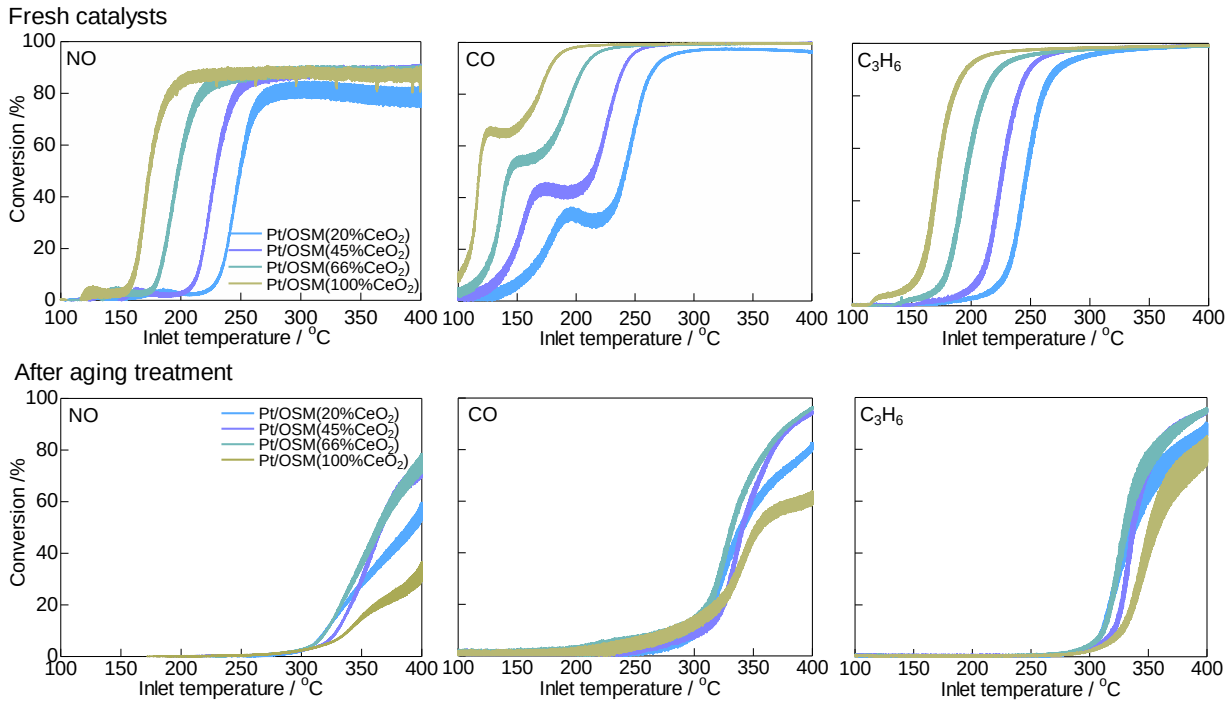

Figure 18. Effect of OSMs on TWC light-off performance over fresh and aged Pt/OSM-coated honeycomb catalysts under a switched flow of CO (2.4-0.6%), C_3H_6 (420 ppm), H_2 (0.8-0.2%), NO (1000 ppm), O_2 (0.6-1.65%), CO_2 (15%) and H_2O (10%) (with the balance being composed of N_2) with lambda perturbation of 1 Hz between 0.95 (rich) and 1.05 (lean) at a heating rate of 25 °C/min and SV = 100,000 h^{-1}.

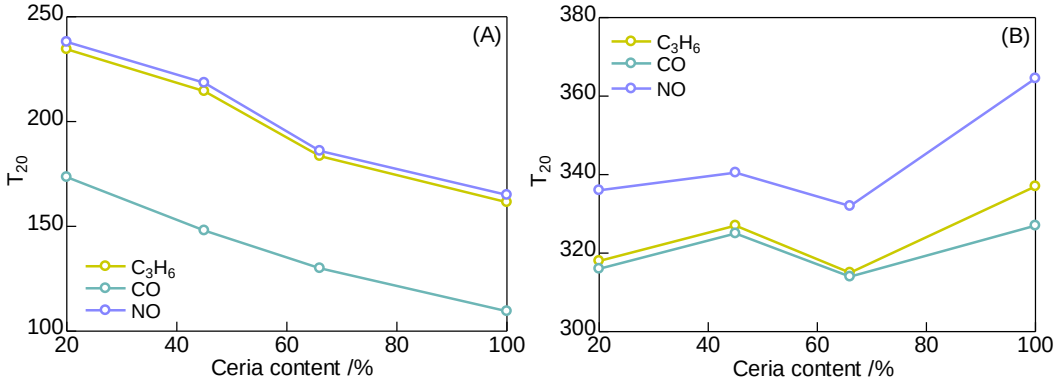

Figure 19. Effect of ceria content on T_{20} behavior over (A) fresh and (B) aged Pt/OSMs having different ceria content for the TWC light-off performance tests over fresh and aged Pt/OSM-coated honeycomb catalysts (Figure 9) under a switched flow of CO (2.4-0.6%), C_3H_6 (420 ppm), H_2 (0.8-0.2%), NO (1000 ppm), O_2 (0.6-1.65%), CO_2 (15%), and H_2O (10%) (with the balance being composed of N_2) with the lambda perturbation set at 1 Hz changing from 0.95 (rich) to 1.05 (lean) at a heating rate of 25 °C/min and SV = 100,000 h^{-1}.

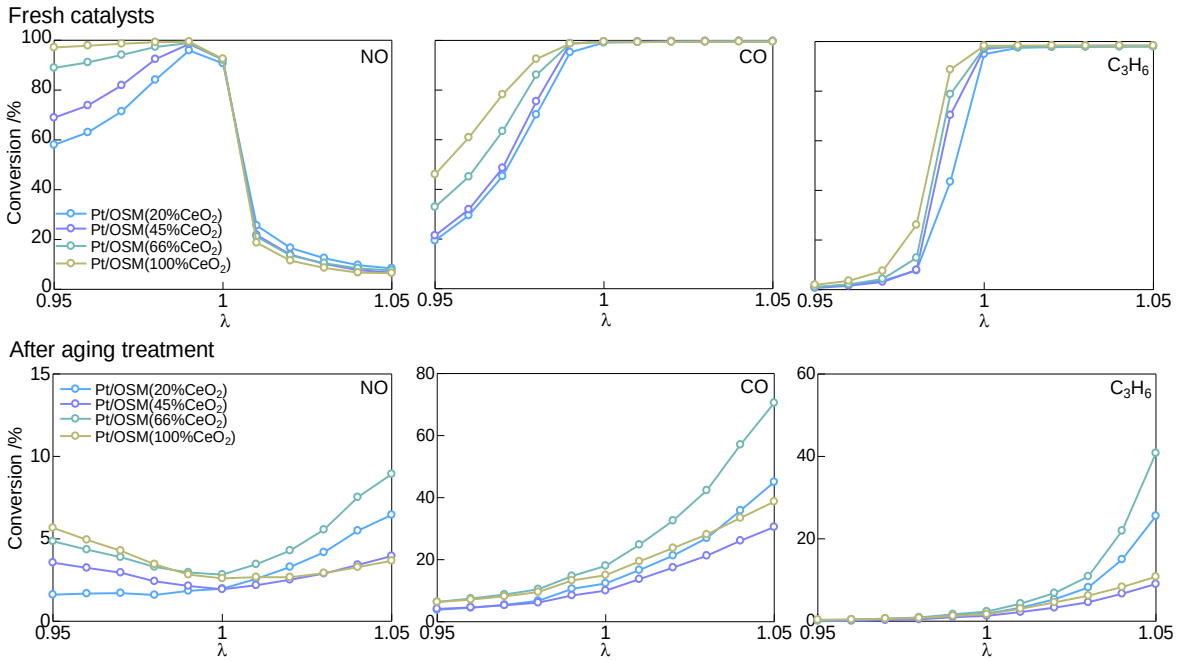

Figure 20. Effect of OSMs on TWC lambda-sweep performance over fresh and aged Pt/OSM-coated honeycomb catalysts under a switched flow of CO (2.4-0.6%), C_3H_6 (420 ppm), H_2 (0.8-0.2%), NO (1000 ppm), O_2 (0.6-1.65%), CO_2 (15%), and H_2O (10%) (with the balance being composed of N_2) with the lambda perturbation interval set at 60 s and changing from 0.95 (rich) to 1.05 (lean) through steps of 0.01 at 300 °C and SV = 100,000 h^{-1}.

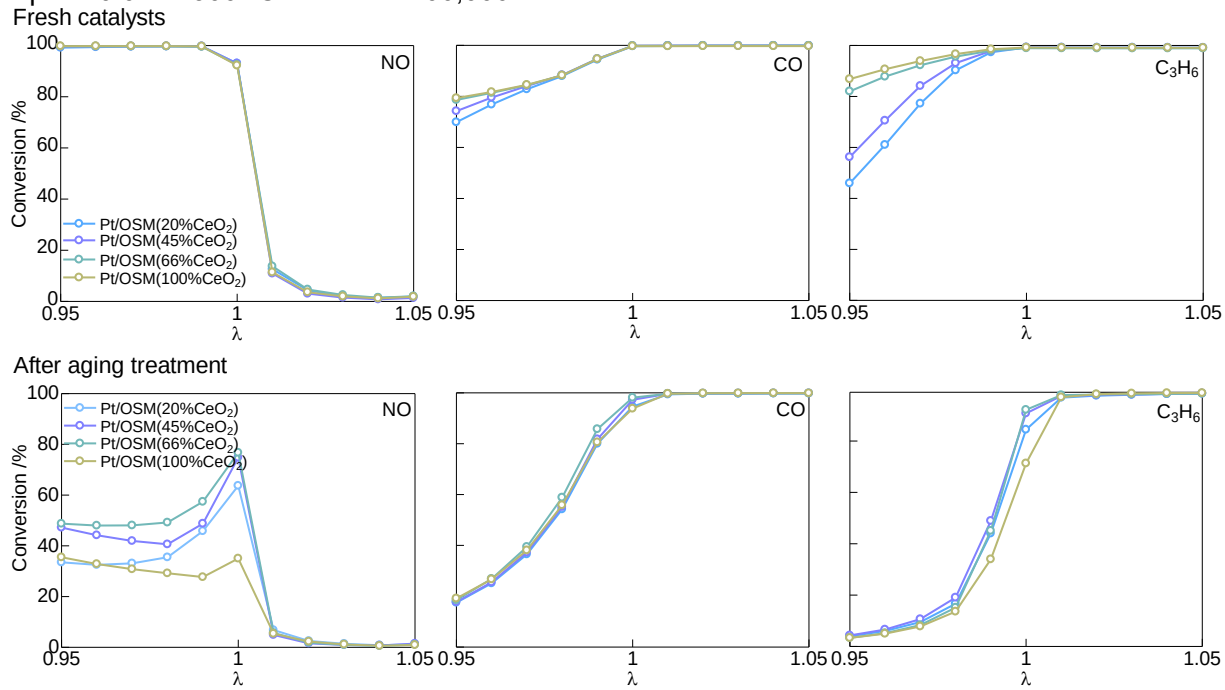

Figure 21. Effect of OSMs on TWC lambda-sweep performance over fresh and aged Pt/OSM-coated honeycomb catalysts under a switched flow of CO (2.4-0.6%), C_3H_6 (420 ppm), H_2 (0.8-0.2%), NO (1000 ppm), O_2 (0.6-1.65%), CO_2 (15%), and H_2O (10%) (with the balance being composed of N_2) with the lambda perturbation interval set at 60 s and changing from 0.95 (rich) to 1.05 (lean) through steps of 0.01 at 400 °C and SV = 100,000 h^{-1}.

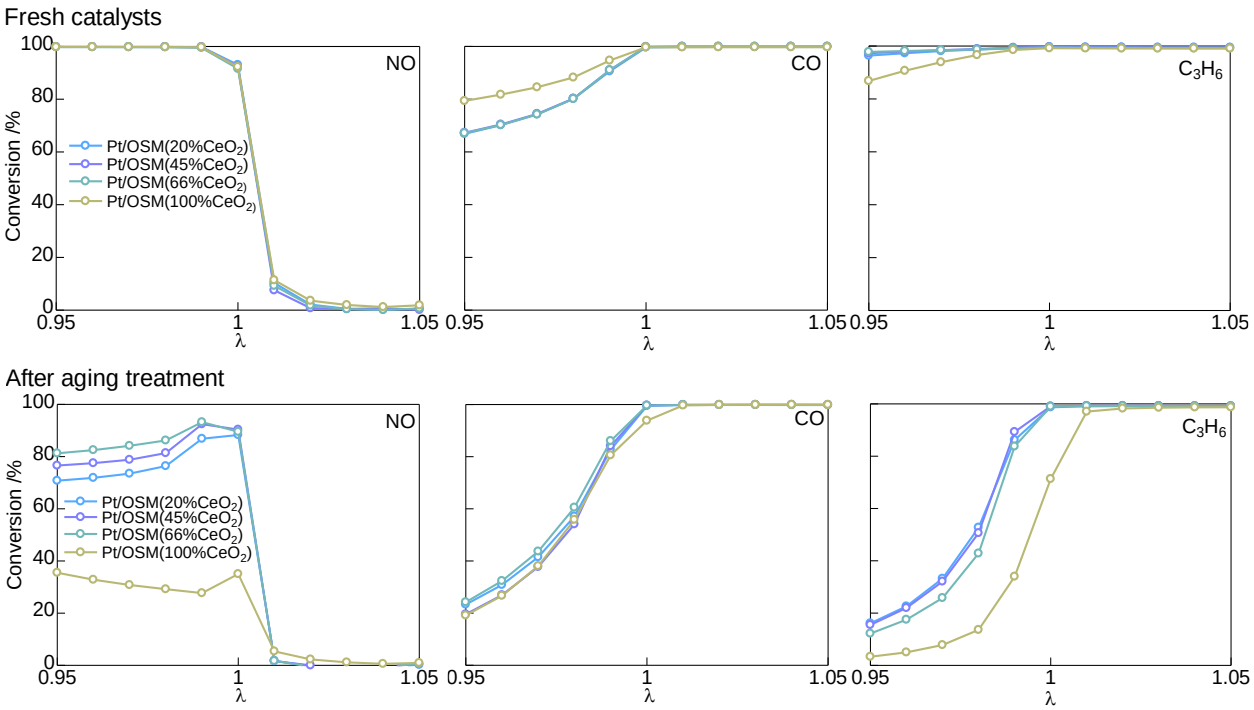

Figure 22. Effect of OSMs on TWC lambda-sweep performance over fresh and aged Pt/OSM-coated honeycomb catalysts under a switched flow of CO (2.4-0.6%), C_3H_6 (420 ppm), H_2 (0.8-0.2%), NO (1000 ppm), O_2 (0.6-1.65%), CO_2 (15%), and H_2O (10%) (with the balance being composed of N_2) with the lambda perturbation interval set at 60 s and changing from 0.95 (rich) to 1.05 (lean) through steps of 0.01 at 500 °C and SV = 100,000 h^{-1}.

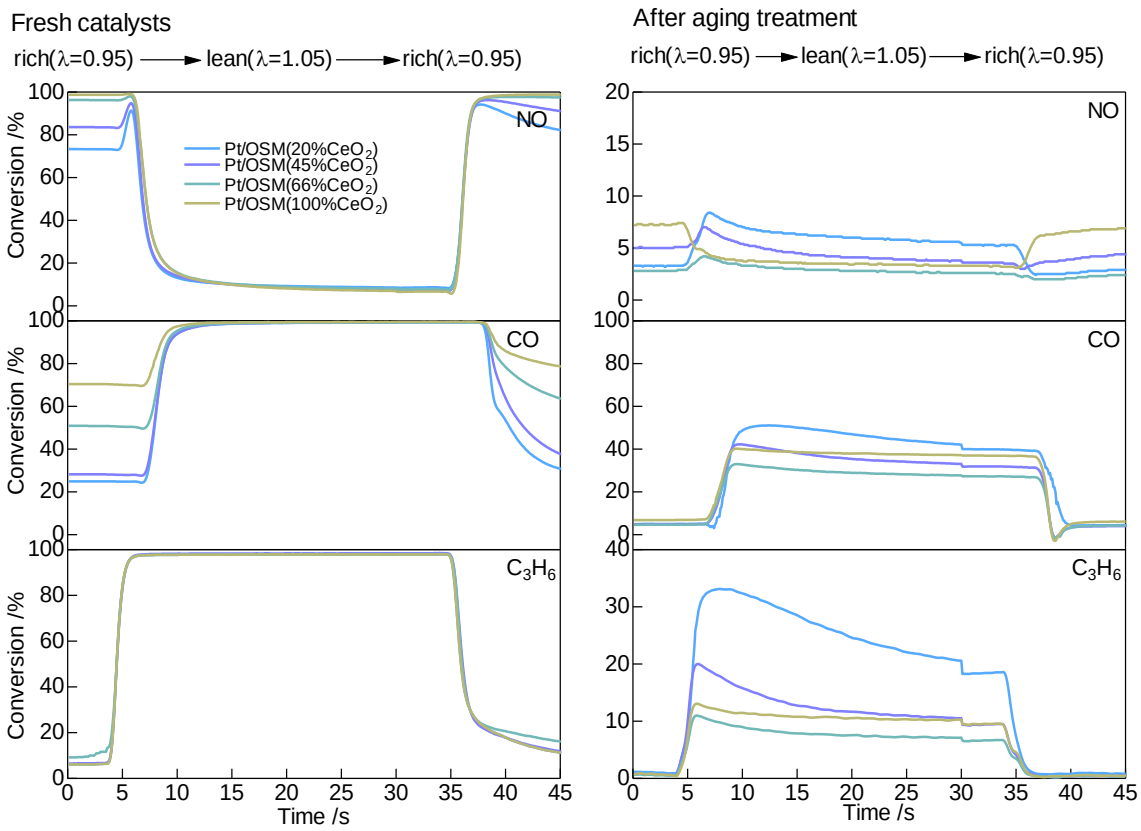

Figure 23. Effect of OSMs on TWC lambda-switching performance over fresh and aged Pt/OSMs-coated honeycomb catalysts under a switched flow of CO (2.4-0.6%), C_3H_6 (420 ppm), H_2 (0.8-0.2%), NO (1000 ppm), O_2 (0.6-1.65%), CO_2 (15%), and H_2O (10%) (with the balance being composed of N_2) with the lambda perturbation interval set at 30 s and changing between 0.95 (rich) and 1.05 (lean) at 300 °C and SV = 100,000 h^{-1}. Note that there are detection delays due to the experimental setup (1.0 s for NO and 3.2 s for CO relative to C_3H_6).

7.4 Conclusions

In this study, we investigated the effect of OSMs on the performance of Pt-based TWCs using a combination of spectroscopic and kinetic measurements. The catalytic evaluations of powdered as well as monolithic honeycomb catalysts showed that Pt/OSM(100%CeO_2) and Pt/OSM(66%CeO_2) exhibited the highest NO conversion among their corresponding fresh and aged sample series. *Operando* and *in situ* CO adsorption IR spectroscopic experiments as well as XPS characterizations revealed that increasing the ceria content of the OSM support promoted not only the production of nitrite species and their reactivity toward CO reactant but also the formation of more electron-deficient Pt^0 species, which results in high performance in the three-way catalysis process and effective resistance to CO poisoning over fresh Pt/OSM catalysts. *In situ* XAS measurements confirmed that both Pt and Ce species in the Pt/OSM catalyst were involved in the TWC reactions through their redox cycles. However, the hydrothermal ageing treatment caused the sintering of the Pt particles and the lattice contraction of CeO_2 in Pt/OSMs. This severely retarded the redox behavior of Pt and Ce species

and reduced the promoting effect of ceria, thereby reducing the catalytic activity of the aged catalysts at relatively low temperatures compared to their fresh counterparts. In addition, the strong poisoning of the Pt catalysts, particularly after hydrothermal ageing during the rich operation, which was more significant than that for Rh and Pd catalysts, should be considered when developing Pt-based TWCs.

Reference

(1) Zhu, X.; Li, K.; Neal, L.; Li, F. Perovskites as Geo-Inspired Oxygen Storage Materials for Chemical Looping and Three-Way Catalysis: A Perspective. *ACS Catalysis* **2018**, *8* (9), 8213–8236.

(2) Huang, C.; Shan, W.; Lian, Z.; Zhang, Y.; He, H. Recent Advances in Three-Way Catalysts of Natural Gas Vehicles. *Catalysis Science and Technology* **2020**, *10* (19), 6407–6419.

(3) Lee, J.; Theis, J. R.; Kyriakidou, E. A. Vehicle Emissions Trapping Materials: Successes, Challenges, and the Path Forward. *Applied Catalysis B: Environmental*. Elsevier B.V. April 1, 2019, pp 397–414.

(4) Wang, J.; Chen, H.; Hu, Z.; Yao, M.; Li, Y. A Review on the Pd-Based Three-Way Catalyst. *Catalysis Reviews* **2015**, *57* (1), 79–144.

(5) Jeong, H.; Kwon, O.; Kim, B. S.; Bae, J.; Shin, S.; Kim, H. E.; Kim, J.; Lee, H. Highly Durable Metal Ensemble Catalysts with Full Dispersion for Automotive Applications beyond Single-Atom Catalysts. *Nature Catalysis* **2020**, *3* (4), 368–375.

(6) Datye, A. K.; Votsmeier, M. Opportunities and Challenges in the Development of Advanced Materials for Emission Control Catalysts. *Nature Materials* **2020**.

(7) Machida, M.; Uchida, Y.; Iwashita, S.; Yoshida, H.; Tsushida, M.; Ohyama, J.; Nagao, Y.; Endo, Y.; Wakabayashi, T. Catalyst Deactivation via Rhodium–Support Interactions under High-Temperature Oxidizing Conditions: A Comparative Study on Hexaaluminates versus Al2O3. *ACS Catalysis* **2021**, *11* (15), 9462–9470.

(8) Ueda, K.; Ohyama, J.; Satsuma, A. Investigation of Reaction Mechanism of NO–C3H6–CO–O2 Reaction over NiFe2O4 Catalyst. *ACS Omega* **2017**, *2* (7), 3135–3143.

(9) Machida, M.; Uchida, Y.; Iwashita, S.; Yoshida, H.; Tsushida, M.; Ohyama, J.; Nagao, Y.; Endo, Y.; Wakabayashi, T. Catalyst Deactivation via Rhodium–Support Interactions under High-Temperature Oxidizing Conditions: A Comparative Study on Hexaaluminates versus Al_2O_3. *ACS Catalysis* **2021**, 9462–9470.

(10) Asakura, H.; Kirihara, M.; Fujita, K.; Hosokawa, S.; Kikkawa, S.; Teramura, K.; Tanaka, T. Fe-Modified CuNi Alloy Catalyst as a Nonprecious Metal Catalyst for Three-Way Catalysis. *Industrial & Engineering Chemistry Research* **2020**, *59* (45), 19907–19917.

(11) Savereide, L.; Gosavi, A.; Hicks, K. E.; Notestein, J. M. Identifying Properties of Low-Loaded CoOX/CeO2 via X-Ray Absorption Spectroscopy for NO Reduction by CO. *Journal of Catalysis* **2020**, *381*, 355–362.

(12) Renème, Y.; Dhainaut, F.; Trentesaux, M.; Ravanbakhsh, B.; Granger, P.; Dujardin, C.; Gengembre, L.; De Cola, P. L. XPS Investigation of Surface Changes during Thermal Aging of Natural Gas Vehicle Catalysts: Influence of Rh Addition to Pd. *Surface and Interface Analysis* **2010**, *42* (6–7), 530–535.

(13) Renème, Y.; Dhainaut, F.; Granger, P. Kinetics of the NO/H 2/O 2 Reactions on Natural Gas Vehicle Catalysts-Influence of Rh Addition to Pd. *Applied Catalysis B: Environmental* **2012**, *111–112*, 424–432.

(14) Renème, Y.; Dhainaut, F.; Schuurman, Y.; Mirodatos, C.; Granger, P. Comparative Surface Analysis and TAP Measurements to Probe the NO Adsorptive Properties of Natural Gas Vehicle Pd-Rh/Al2O3 Catalyst. *Applied Catalysis B: Environmental* **2014**, *160–161* (1), 390–399.

(15) Machida, M.; Fujiwara, A.; Yoshida, H.; Ohyama, J.; Asakura, H.; Hosokawa, S.; Tanaka, T.; Haneda, M.; Tomita, A.; Miki, T.; Iwashina, K.; Endo, Y.; Nakahara, Y.; Minami, S.; Kato, N.; Hayashi, Y.; Goto, H.; Hori, M.; Tsuda, T.; Miura, K.; Kimata, F.; Iwachido, K. Deactivation Mechanism of Pd/CeO2–ZrO2 Three-Way Catalysts Analyzed by Chassis-Dynamometer Tests and in Situ Diffuse Reflectance Spectroscopy. *ACS Catalysis* **2019**, *9* (7), 6415–6424.

(16) Li, L.; Zhang, N.; Huang, X.; Liu, Y.; Li, Y.; Zhang, G.; Song, L.; He, H. Hydrothermal Stability of Core–Shell Pd@Ce0.5Zr0.5O2/Al2O3 Catalyst for Automobile Three-Way Reaction. *ACS Catalysis* **2018**, *8* (4), 3222–3231.

(17) Gong, J.; Wang, D.; Li, J.; Currier, N.; Yezerets, A. Dynamic Oxygen Storage Modeling in a Three-Way Catalyst for Natural Gas Engines: A Dual-Site and Shrinking-Core Diffusion Approach. *Applied Catalysis B: Environmental* **2017**, *203*, 936–945.

(18) Salaev, M. A.; Salaeva, A. A.; Kharlamova, T. S.; Mamontov, G. V. Pt–CeO2-Based Composites in Environmental Catalysis: A Review. *Applied Catalysis B: Environmental* **2021**, *295*, 120286.
(19) Asakura, H.; Hosokawa, S.; Beppu, K.; Tamai, K.; Ohyama, J.; Shishido, T.; Kato, K.; Teramura, K.; Tanaka, T. Real-Time Observation of the Effect of Oxygen Storage Materials on Pd-Based Three-Way Catalysts under Ideal Automobile Exhaust Conditions: An Operando Study . *Catalysis Science & Technology* **2021**, No. x.
(20) Zhang, L.; Filot, I. A. W.; Su, Y. Q.; Liu, J. X.; Hensen, E. J. M. Transition Metal Doping of Pd(1 1 1) for the NO + CO Reaction. *Journal of Catalysis* **2018**, *363*, 154–163.
(21) Grünbacher, M.; Tarjomannejad, A.; Nezhad, P. D. K.; Praty, C.; Ploner, K.; Mohammadi, A.; Niaei, A.; Klötzer, B.; Schwarz, S.; Bernardi, J.; Farzi, A.; Gómez, M. J. I.; Rivero, V. T.; Penner, S. Promotion of La(Cu0.7Mn0.3)0.98M0.02O3−δ (M = Pd, Pt, Ru and Rh) Perovskite Catalysts by Noble Metals for the Reduction of NO by CO. *Journal of Catalysis* **2019**, *379*, 18–32.
(22) Salaün, M.; Kouakou, A.; Da Costa, S.; Da Costa, P. Synthetic Gas Bench Study of a Natural Gas Vehicle Commercial Catalyst in Monolithic Form: On the Effect of Gas Composition. *Applied Catalysis B: Environmental* **2009**, *88* (3–4), 386–397.
(23) Kang, S. B.; Nam, I. S.; Cho, B. K.; Kim, C. H.; Oh, S. H. Kinetic Model for Modern Double-Layered Pd/Rh TWC as a Function of Metal Loadings and Mileage. *Chemical Engineering Journal* **2015**, *278*, 328–338.
(24) Gandhi, H. S.; Graham, G. W.; McCabe, R. W. Automotive Exhaust Catalysis. In *Journal of Catalysis*; Academic Press Inc., 2003; Vol. 216, pp 433–442.
(25) Coney, C.; Hardacre, C.; Morgan, K.; Artioli, N.; York, A. P. E.; Millington, P.; Kolpin, A.; Goguet, A. Investigation of the Oxygen Storage Capacity Behaviour of Three Way Catalysts Using Spatio-Temporal Analysis. *Applied Catalysis B: Environmental* **2019**, *258* (July), 117918.
(26) Meeyoo, V.; Trimm, D. L.; Cant, N. W. The Effect of Sulphur Containing Pollutants on the Oxidation Activity of Precious Metals Used in Vehicle Exhaust Catalysts. *Applied Catalysis B: Environmental* **1998**, *16* (2), L101–L104.
(27) Hatanaka, M.; Takahashi, N.; Tanabe, T.; Nagai, Y.; Dohmae, K.; Aoki, Y.; Yoshida, T.; Shinjoh, H. Ideal Pt Loading for a Pt/CeO2-Based Catalyst Stabilized by a Pt–O–Ce Bond. *Applied Catalysis B: Environmental* **2010**, *99* (1–2), 336–342.
(28) Andonova, S.; Aybegüm Ok, Z.; Drenchev, N.; Ozensoy, E.; Hadjiivanov, K. Pt/CeOx/ZrOx/γ-Al2O3 Ternary Mixed Oxide DeNOx Catalyst: Surface Chemistry and NOx Interactions. *The Journal of Physical Chemistry C* **2018**, *122* (24), 12850–12863.
(29) Ausgabe, D.; Hirose, M.; Ishiguro, N.; Shimomura, K.; Burdet, N.; Matsui, H.; Tada, M.; Takahashi, Y. Oxygen Storage Visualization of Heterogeneous Oxygen Storage Behavior in Platinum-Supported Cerium-Zirconium Oxide Three-Way Catalyst Particles by Hard X-Ray Spectro-Ptychography. *Angewandte Chemie - International Edition* **2018**, *130*, 1490–1495.
(30) Ozawa, M.; Misaki, M.; Iwakawa, M.; Hattori, M.; Kobayashi, K.; Higuchi, K.; Arai, S. Low Content Pt-Doped CeO2 and Core-Shell Type CeO2/ZrO2 Model Catalysts; Microstructure, TPR and Three Way Catalytic Activities. *Catalysis Today* **2019**, *332* (September 2018), 251–258.
(31) Muto, K. I.; Katada, N.; Niwa, M. Complete Oxidation of Methane on Supported Palladium Catalyst: Support Effect. *Applied Catalysis A: General* **1996**, *134* (2), 203–215.
(32) Toyao, T.; Jing, Y.; Kon, K.; Hayama, T.; Nagaoka, S.; Shimizu, K. Catalytic NO–CO Reactions over La-Al $_2$ O $_3$ Supported Pd: Promotion Effect of La. *Chemistry Letters* **2018**, *47* (8), 1036–1039.
(33) Vedyagin, A. A.; Kenzhin, R. M.; Mikhail, ·; Tashlanov, Y.; Alikin, E. A.; Stoyanovskii, V. O.; Plyusnin, P. E.; Shubin, Y. V; Mishakov, I. V; Smirnov, M. Y.; Alexander, ·; Kalinkin, V.; Valerii, ·; Bukhtiyarov, I. Effect of La Addition on the Performance of Three-Way Catalysts Containing Palladium and Rhodium. *Topics in Catalysis* **1234**, *63*, 152–165.
(34) Asakura, H.; Hosokawa, S.; Ina, T.; Kato, K.; Nitta, K.; Uera, K.; Uruga, T.; Miura, H.; Shishido, T.; Ohyama, J.; Satsuma, A.; Sato, K.; Yamamoto, A.; Hinokuma, S.; Yoshida, H.; Machida, M.; Yamazoe, S.; Tsukuda, T.; Teramura, K.; Tanaka, T. Dynamic Behavior of Rh Species in Rh/Al2O3 Model Catalyst during Three-

Way Catalytic Reaction: An Operando X-Ray Absorption Spectroscopy Study. *Journal of the American Chemical Society* **2017**, *140* (1), 176–184.
(35) Wang, M.; Dimopoulos Eggenschwiler, P.; Franken, T.; Ferri, D.; Kröcher, O. Reaction Pathways of Methane Abatement in Pd-Rh Three-Way Catalyst in Heavy Duty Applications: A Combined Approach Based on Exhaust Analysis, Model Gas Reactor and DRIFTS Measurements. *Chemical Engineering Journal* **2021**, *422*, 129932.
(36) Keav, S.; Matam, S.; Ferri, D.; Weidenkaff, A. Structured Perovskite-Based Catalysts and Their Application as Three-Way Catalytic Converters—A Review. *Catalysts* **2014**, *4* (3), 226–255.
(37) Rodríguez, G. C. M.; Kelm, K.; Heikens, S.; Grünert, W.; Saruhan, B. Pd-Integrated Perovskites for TWC Applications: Synthesis, Microstructure and N 2O-Selectivity. In *Catalysis Today*; Elsevier, 2012; Vol. 184, pp 184–191.
(38) Alifanti, M.; Baps, B.; Blangenois, N.; Naud, J.; Grange, P.; Delmon, B. Characterization of CeO2−ZrO2 Mixed Oxides. Comparison of the Citrate and Sol−Gel Preparation Methods. *Chemistry of Materials* **2002**, *15* (2), 395–403.
(39) Liotta, L. F.; Macaluso, A.; Longo, A.; Pantaleo, G.; Martorana, A.; Deganello, G. Effects of Redox Treatments on the Structural Composition of a Ceria-Zirconia Oxide for Application in the Three-Way Catalysis. *Applied Catalysis A: General* **2003**, *240* (1–2), 295–307.
(40) Kozlov, A. I.; Do, H. K.; Yezerets, A.; Andersen, P.; Kung, H. H.; Kung, M. C. Effect of Preparation Method and Redox Treatment on the Reducibility and Structure of Supported Ceria-Zirconia Mixed Oxide. *Journal of Catalysis* **2002**, *209* (2), 417–426.
(41) He, H.; Dai, H. X.; Ng, L. H.; Wong, K. W.; Au, C. T. Pd-, Pt-, and Rh-Loaded Ce0.6Zr0.35Y0.05O2 Three-Way Catalysts: An Investigation on Performance and Redox Properties. *Journal of Catalysis* **2002**, *206* (1), 1–13.
(42) Li, P.; Chen, X.; Li, Y.; Schwank, J. W. A Review on Oxygen Storage Capacity of CeO2-Based Materials: Influence Factors, Measurement Techniques, and Applications in Reactions Related to Catalytic Automotive Emissions Control. *Catalysis Today* **2019**, *327*, 90–115.
(43) Dong, F.; Tanabe, T.; Takahashi, N.; Shinjoh, H. Investigation of the Effective Oxygen Storage and Release Performances on the Pt/CeO2-ZrO2 Catalysts by Breakthrough Method. *Catalysis Today* **2019**, *332*, 259–266.
(44) Wu, J.; O'Neill, A. E.; Li, C. H.; Jinschek, J. R.; Cavataio, G. Superior TWC Activity of Rh Supported on Pyrochlore-Phase Ceria Zirconia. *Applied Catalysis B: Environmental* **2021**, *280*, 119450.
(45) Kopelent, R.; Tereshchenko, A.; Guda, A.; Smolentsev, G.; Artiglia, L.; L. Sushkevich, V.; Bugaev, A.; I. Sadykov, I.; Baidya, T.; Bodnarchuk, M.; Anton van Bokhoven, J.; Nachtegaal, M.; V. Safonova, O. Enhanced Reducibility of the Ceria–Tin Oxide Solid Solution Modifies the CO Oxidation Mechanism at the Platinum–Oxide Interface. *ACS Catalysis* **2021**, *0* (0), 9435–9449.
(46) Yamamoto, T.; Suzuki, A.; Nagai, Y.; Tanabe, T.; Dong, F.; Inada, Y.; Nomura, M.; Tada, M.; Iwasawa, Y.; Yamamoto, T.; Suzuki, A.; Tada, M.; Iwasawa, Y.; Nagai, Y.; Tanabe, T.; Dong, F.; Inada, Y.; Nomura, M. Heterogeneous Catalysis Origin and Dynamics of Oxygen Storage/Release in a Pt/Ordered CeO2-ZrO 2 Catalyst Studied by Time-Resolved XAFS Analysis. *Angewandte Chemie - International Edition* **2007**, *119*, 9413–9416.
(47) Kondratenko, E. V.; Sakamoto, Y.; Okumura, K.; Shinjoh, H. Transient Analysis of Oxygen Storage Capacity of Pt/CeO2–ZrO2 Materials with Millisecond- and Second-Time Resolution. *Applied Catalysis B: Environmental* **2009**, *89* (3–4), 476–483.
(48) Shang, H.; Wang, Y.; Cui, Y.; Fang, R.; Hu, W.; Gong, M.; Chen, Y. Catalytic Performance of Pt-Rh/CeZrYLa+LaAl with Stoichiometric Natural Gas Vehicles Emissions. *Cuihua Xuebao/Chinese Journal of Catalysis* **2015**, *36* (3), 290–298.
(49) Schmitt, R.; Nenning, A.; Kraynis, O.; Korobko, R.; Frenkel, A. I.; Lubomirsky, I.; Haile, S. M.; Rupp, J. L. M. A Review of Defect Structure and Chemistry in Ceria and Its Solid Solutions. *Chem. Soc. Rev* **2020**, *49*, 554.

(50) Kubacka, A.; Iglesias-Juez, A.; Di Michiel, M.; Newton, M. A.; Fernández-García, M. Influence of the Ce-Zr Promoter on Pd Behaviour under Dynamic CO/NO Cycling Conditions: A Structural and Chemical Approach †. *Physical Chemistry Chemical Physics* **2013**, *15*, 8640.

(51) Rink, J.; Meister, N.; Herbst, F.; Votsmeier, M. Oxygen Storage in Three-Way-Catalysts Is an Equilibrium Controlled Process: Experimental Investigation of the Redox Thermodynamics. *Applied Catalysis B: Environmental* **2017**, *206*, 104–114.

(52) Dong, F.; Suda, A.; Tanabe, T.; Nagai, Y.; Sobukawa, H.; Shinjoh, H.; Sugiura, M.; Descorme, C.; Duprez, D. Dynamic Oxygen Mobility and a New Insight into the Role of Zr Atoms in Three-Way Catalysts of Pt/CeO2-ZrO2. In *Catalysis Today*; Elsevier, 2004; Vol. 93–95, pp 827–832.

(53) Laachir, A.; Perrichon, V.; Bernal, S.; Calvino, J. J.; Cifredo, G. A. Study of the COCeO2 Interaction in Presence of Highly Dispersed Rhodium. *Journal of Molecular Catalysis* **1994**, *89* (3), 391–396.

(54) Rao, G. R.; Kagpar, J.; Meriani, S.; Di Monte, R.; Graziani, M. *NO Decomposition over Partially Reduced Metallized CeO2-ZrO2 Solid Solutions*; 1994; Vol. 24.

(55) Li, C.; Xin, Q.; Gua, X.; Onishi, T. Surface Oxygen Species and Their Reactivities in the Oxidation of CH4, C2H6 and C2H4 Over Cerium Oxide at Mild Temperatures. *Studies in Surface Science and Catalysis* **1993**, *75* (C), 1955–1958.

(56) Kqpihski, L.; Wdcyrz, M.; Okal, J. *Effect of Chlorine on Microstructure and Activity of Pd/CeO, Catalysts*; 1995; Vol. 91.

(57) van Deelen, T. W.; Hernández Mejía, C.; de Jong, K. P. Control of Metal-Support Interactions in Heterogeneous Catalysts to Enhance Activity and Selectivity. *Nature Catalysis* **2019**, *2* (11), 955–970.

(58) Wakita, T.; Yashima, M. Structural Disorder in the Cubic Ce0.5Zr0.5O2 Catalyst: A Possible Factor of the High Catalytic Activity. *Applied Physics Letters* **2008**, *92* (10), 101921.

(59) Fan, J.; Wu, X.; Ran, R.; Weng, D. Influence of the Oxidative/Reductive Treatments on the Activity of Pt/Ce 0.67 Zr 0.33 O 2 Catalyst. *Applied Surface Science* **2005**, *245* (1–4), 162–171.

(60) Nagai, Y.; Hirabayashi, T.; Dohmae, K.; Takagi, N.; Minami, T.; Shinjoh, H.; Matsumoto, S. Sintering Inhibition Mechanism of Platinum Supported on Ceria-Based Oxide and Pt-Oxide-Support Interaction. *Journal of Catalysis* **2006**, *242* (1), 103–109.

(61) Nunan, J. G.; Robota, H. J.; Cohn, M. J.; Bradley, S. A. Physicochemical Properties of Ce-Containing Three-Way Catalysts and the Effect of Ce on Catalyst Activity. *Journal of Catalysis* **1992**, *133* (2), 309–324.

(62) Oyama, S. T.; Zhang, X.; Lu, J.; Gu, Y.; Fujitani, T. Epoxidation of Propylene with H2 and O2 in the Explosive Regime in a Packed-Bed Catalytic Membrane Reactor. *Journal of Catalysis* **2008**, *257* (1), 1–4.

(63) Rothensteiner, M.; Bonk, A.; Vogt, U. F.; Emerich, H.; Van Bokhoven, J. A. Structural Changes in Ce0.5Zr0.5O2-Δ under Temperature-Swing and Isothermal Solar Thermochemical Looping Conditions Determined by in Situ Ce K and Zr K Edge X-Ray Absorption Spectroscopy. *Journal of Physical Chemistry C*. 2016, pp 13931–13941.

(64) Izu, N.; Kishimoto, H.; Omata, T.; Ono, K.; Otsuka-Yao-Matsuo, S. Oxygen Release Behavior of Metastable Tetragonal T′meta-(Ce0.5Zr0.5)O2 Phases Prepared by Reduction and Successive Oxidation of T′ Phase. *Science and Technology of Advanced Materials* **2001**, *2* (2), 397–404.

(65) Zhang, F.; Chen, C.-H.; Hanson, J. C.; Robinson, R. D.; Herman, I. P.; Chan, S.-W. Phases in Ceria-Zirconia Binary Oxide (1Àx)CeO 2-XZrO 2 Nanoparticles: The Effect of Particle Size. *Journal of the American Ceramic Society* **2006**, *89* (3), 1028–1036.

(66) Pijolat, M.; Prin, M.; Soustelle, M.; Touret, O.; Nortier, P. *Thermal Stability of Doped Ceria : Experiment and Modelling*; 1995; Vol. 3.

(67) Nachimuthu, P.; Shih, W. C.; Liu, R. S.; Jang, L. Y.; Chen, J. M. The Study of Nanocrystalline Cerium Oxide by X-Ray Absorption Spectroscopy. *Journal of Solid State Chemistry* **2000**, *149* (2), 408–413.

(68) Paun, C.; V. Safonova, O.; Szlachetko, J.; M. Abdala, P.; Nachtegaal, M.; Sa, J.; Kleymenov, E.; Cervellino, A.; Krumeich, F.; A. van Bokhoven, J. Polyhedral CeO2 Nanoparticles: Size-Dependent Geometrical and Electronic Structure. *The Journal of Physical Chemistry C* **2012**, *116* (13), 7312–7317.

(69) Toscani, L. M.; Craievich, A. F.; Fantini, M. C. A.; Lamas, D. G.; Larrondo, S. A. Effects of the Incorporation

of Sc2O3 into CeO2-ZrO2 Solid Solution: Structural Characterization and in Situ XANES/TPR Study under H2 Atmosphere. *Journal of Physical Chemistry C* **2016**, *120* (42), 24165–24175.

(70) Yao, H. C.; Yao, Y. F. Y. Ceria in Automotive Exhaust Catalysts. I. Oxygen Storage. *Journal of Catalysis* **1984**, *86* (2), 254–265.

(71) Johnson, M. F. L.; Mooi, J. Cerium Dioxide Crystallite Sizes by Temperature-Programmed Reduction. *Journal of Catalysis* **1987**, *103* (2), 502–505.

(72) Madier, Y.; Descorme, C.; M. Le Govic, A.; Duprez, D. Oxygen Mobility in CeO2 and CexZr(1-x)O2 Compounds: Study by CO Transient Oxidation and 18O/16O Isotopic Exchange. *The Journal of Physical Chemistry B* **1999**, *103* (50), 10999–11006.

(73) Balducci, G.; Kašpar, J.; Fornasiero, P.; Graziani, M.; Islam, M. S.; Gale, J. D. Computer Simulation Studies of Bulk Reduction and Oxygen Migration in CeO2-ZrO2 Solid Solutions. *Journal of Physical Chemistry B*. 1997, pp 1750–1753.

(74) Kašpar, J.; Fornasiero, P.; Graziani, M. Use of CeO2-Based Oxides in the Three-Way Catalysis. *Catalysis Today* **1999**, *50* (2), 285–298.

(75) Wu, X.; Fan, J.; Ran, R.; Weng, D. Effect of Preparation Methods on the Structure and Redox Behavior of Platinum-Ceria-Zirconia Catalysts. *Chemical Engineering Journal*. 2005, pp 133–139.

(76) Karim, W.; Spreafico, C.; Kleibert, A.; Gobrecht, jens; VandeVondele, joost; Ekinci, yasin; van Bokhoven, jeroen A. Catalyst Support Effects on Hydrogen Spillover. *Nature Publishing Group* **2017**.

(77) Luo, M. F.; Zheng, X. M. Redox Behaviour and Catalytic Properties of Ce0.5Zr0.5O2-Supported Palladium Catalysts. *Applied Catalysis A: General* **1999**, *189* (1), 15–21.

(78) Fornasiero, P.; Di Monte, R.; Rao, G. R.; Kaspar, J.; Meriani, S.; Trovarelli, A.; Graziani, M. Rh-Loaded CeO2-ZrO2 Solid-Solutions as Highly Efficient Oxygen Exchangers: Dependence of the Reduction Behavior and the Oxygen Storage Capacity on the Structural-Properties. *Journal of Catalysis* **1995**, *151* (1), 168–177.

(79) Bazin, P.; Saur, O.; Lavalley, J. C.; Daturi, M.; Blanchard, G. FT-IR Study of CO Adsorption on Pt/CeO 2 : Characterisation and Structural Rearrangement of Small Pt Particles.

(80) Gajdo, M.; Eichler, A.; Hafner, J. CO Adsorption on Close-Packed Transition and Noble Metal Surfaces: Trends from *Ab Initio* Calculations. *Journal of Physics: Condensed Matter* **2004**, *16* (8), 1141–1164.

(81) Zeinalipour-Yazdi, C. D.; Cooksy, A. L.; Efstathiou, A. M. CO Adsorption on Transition Metal Clusters: Trends from Density Functional Theory. *Surface Science* **2008**, *602* (10), 1858–1862.

(82) Koleva, I. Z.; Aleksandrov, H. A.; Vayssilov, G. N. Influence of the Adsorption of CO on the Electronic Structure of Platinum Clusters and Nanowires Deposited on CeO2(111) and γ-Al2O3(001) Surfaces. *Catalysis Today*. Elsevier B.V. November 1, 2020, pp 442–452.

(83) Jing, Y.; Cai, Z.; Liu, C.; Toyao, T.; Maeno, Z.; Asakura, H.; Hiwasa, S.; Nagaoka, S.; Kondoh, H.; Shimizu, K. I. Promotional Effect of La in the Three-Way Catalysis of La-Loaded Al2O3-Supported Pd Catalysts (Pd/La/Al2O3). *ACS Catalysis* **2020**, *10* (2), 1010–1023.

(84) Jing, Y.; Wang, G.; Wei Ting, K.; Maeno, Z.; Oshima, K.; Satokawa, S.; Nagaoka, S.; Shimizu, K.; Toyao, T. Roles of the Basic Metals La, Ba and Sr as Additives in Al2O3-Supported Pd-Based Three-Way Catalysts. *Journal of Catalysis* **2021**.

(85) Yentekakis, I. V.; Vernoux, P.; Goula, G.; Caravaca, A. Electropositive Promotion by Alkalis or Alkaline Earths of Pt-Group Metals in Emissions Control Catalysis: A Status Report. *Catalysts* **2019**, *9* (2), 1–72.

(86) Gremminger, A.; Pihl, J.; Casapu, M.; Grunwaldt, J. D.; Toops, T. J.; Deutschmann, O. PGM Based Catalysts for Exhaust-Gas after-Treatment under Typical Diesel, Gasoline and Gas Engine Conditions with Focus on Methane and Formaldehyde Oxidation. *Applied Catalysis B: Environmental* **2020**, *265*, 118571.

(87) Fanson, P. T.; Horton, M. R.; Delgass, W. N.; Lauterbach, J. FTIR Analysis of Storage Behavior and Sulfur Tolerance in Barium-Based NOχ Storage and Reduction (NSR) Catalysts. *Applied Catalysis B: Environmental* **2003**, *46* (2), 393–413.

(88) A. Brown, W.; A. King, D. NO Chemisorption and Reactions on Metal Surfaces: A New Perspective. *The Journal of Physical Chemistry B* **2000**, *104* (12), 2578–2595.

(89) Sedlmair, C.; Seshan, K.; Jentys, A.; Lercher, J. A. Elementary Steps of NOx Adsorption and Surface Reaction on a Commercial Storage-Reduction Catalyst. *Journal of Catalysis* **2003**, *214* (2), 308–316.
(90) Nova, I.; Castoldi, L.; Lietti, L.; Tronconi, E.; Forzatti, P.; Prinetto, F.; Ghiotti, G. NOx Adsorption Study over Pt-Ba/Alumina Catalysts: FT-IR and Pulse Experiments. *Journal of Catalysis* **2004**, *222* (2), 377–388.
(91) Lietti, L.; Daturi, M.; Blasin-AubØ, V.; Ghiotti, G.; Prinetto, F.; Forzatti, P. Relevance of the Nitrite Route in the NO x Adsorption Mechanism over Pt-Ba/Al 2 O 3 NO x Storage Reduction Catalysts Investigated by Using Operando FTIR Spectroscopy. *ChemCatChem* **2012**, *4*, 55–58.
(92) Choudhary, V. R.; Srinivasan, K. R.; Singh, A. P. Temperature-Programmed Desorption of Aromatic Hydrocarbons on Silicalite-I and ZSM-5-Type Zeolites. *Zeolites* **1990**, *10* (1), 16–20.
(93) Trovarelli, A. Catalytic Properties of Ceria and CeO2-Containing Materials. *Catalysis Reviews - Science and Engineering* **1996**, *38* (4), 439–520.
(94) Nagai, Y.; Dohmae, K.; Ikeda, Y.; Takagi, N.; Tanabe, T.; Hara, N.; Guilera, G.; Pascarelli, S.; Newton, M. A.; Kuno, O.; Jiang, H.; Shinjoh, H.; Matsumoto, S. Heterogeneous Catalysis In Situ Redispersion of Platinum Autoexhaust Catalysts: An On-Line Approach to Increasing Catalyst Lifetimes?**.
(95) Gänzler, A. M.; Casapu, M.; Maurer, F.; Störmer, H.; Gerthsen, D.; Ferré, G.; Vernoux, P.; Bornmann, B.; Frahm, R.; Murzin, V.; Nachtegaal, M.; Votsmeier, M.; Grunwaldt, J. D. Tuning the Pt/CeO2 Interface by in Situ Variation of the Pt Particle Size. *ACS Catalysis* **2018**, *8* (6), 4800–4811.
(96) Haneda, M.; Nakamura, Y.; Yamada, T.; Minami, S.; Kato, N.; Iwashina, K.; Endo, Y.; Nakahara, Y.; Iwachido, K. Comprehensive Study of the Light-off Performance and Surface Properties of Engine-Aged Pd-Based Three-Way Catalysts. *Catalysis Science and Technology* **2021**, *11* (3), 912–922.
(97) Fujiwara, A.; Tsurunari, Y.; Yoshida, H.; Ohyama, J.; Yamada, T.; Haneda, M.; Miki, T.; Machida, M. Thermal Deactivation of Pd/CeO2-ZrO2Three-Way Catalysts during Real Engine Aging: Analysis by a Surface plus Peripheral Site Model. *ACS Omega* **2020**, *5* (44), 28897–28906.

Chapter 8

General Conclusion

In this research, I focused on the development of support materials to maximize the efficiency of PGM-based three-way catalysts. For this purpose, the role played by basic metal additives and oxygen storage in PGM-based three-way catalysts were investigated systematically. Basic metal additives, such as La, Ba, and Sr, which are used widely in three-way catalysts to enhance the thermal stability of support materials, were found to enhance the catalytic performance efficiently of PGM-based three-way catalysts. Pt/OSM catalyst with high content of CeO_2 exhibit higher three-way catalytic efficiency.

Chapter 2 and 3 conclude that a loading of 15 wt%, which is higher than that for the conventionally used industrial catalysts Pd/La(5)/Al_2O_3 (La = 5wt%) optimized to keep the high specific surface area, is more effective for the TWC process. Pd^0 species loaded on La-containing Al_2O_3 supports are more electron deficient than those on pristine Al_2O_3, which results in a higher reactivity toward NO and a suppression of the poisoning effect of CO. As a result, a higher NO conversion efficiency is attained over these Pd/La/Al_2O_3 catalysts. Pd/La/Al_2O_3 promotes NO conversion efficiently at low temperature via a disproportionation reaction to yield surface nitrite species and gas-phase N_2O.

Chapter 4 concludes that Pd/M/Al_2O_3 catalysts are superior in terms of promoting the reactions of NO, CO and C_3H_6 compared with the Pd/Al_2O_3 catalyst. Pd/La/Al_2O_3 was found to enhance NO reduction to a greater extent than the catalysts investigated in this work, while Pd/Ba/Al_2O_3 demonstrated superior catalytic performance during the oxidation of CO and C_3H_6. The presence of the atomically dispersed basic metals promoted the efficient formation of surface nitrite species, leading to the enhancement of $DeNO_x$ activity.

Chapter 5 showed that addition of Ba promotes the efficiency of reducing NOx, CO, and non-methane HCs in the standard TWC process using a vehicle powered by a gasoline engine. Efficient generation of surface reactive nitrate intermediates over Pd/Ba/Al_2O_3 catalyst and their subsequent reactions with H_2, CO, and C_3H_6, as reductants, also play key roles in the three-way catalytic process.

Chapter 6 demonstrated that Ba enhanced the catalytic activity of the Pt-based catalysts more efficiently than La and Sr. The Pt^0 species loaded on Ba/Al_2O_3 were more electron-rich than those loaded on Al_2O_3, thereby promoting the NO dissociation into N and O. Moreover, the efficient formation of surface N-containing species and their subsequent reaction with reductant gases promoted the effect of Ba in three-way catalytic processes.

Chapter 7 concludes that the Pt/OSM catalyst with high content of CeO_2 exhibit higher three-way catalytic efficiency. The Pt^0 species loaded on OSM(100%CeO_2) are electron-deficient, resulting in the resistance to CO poisoning over Pt/OSM catalysts.

In summary, support materials play an important role in enhancing the catalytic efficiency of PGM-based catalysts in three-way catalysts. Basic metal additives, such as La, Ba, and Sr, which are used widely in three-way catalysts to enhance the thermal stability of support materials, were found to enhance the catalytic performance efficiently via modifying the electronic state of metallic Pt/Pd species and enhancing the formation of reactive intermediate.